

FORWARD MUON PRODUCTION IN PROTON-ANTIPROTON COLLISIONS

AT $\sqrt{s} = 1.8$ TeV

John Erwin Skarha

Under the supervision of Professor Lee G. Pondrom

Results of the analysis of forward-produced ($1.95 < |\eta| < 2.80$) muons from $\bar{p}p$ collisions at $\sqrt{s} = 1.8$ TeV are presented. The data sample was collected during the 1987 run of the CDF detector at the Fermilab Tevatron collider and corresponds to an integrated luminosity of 0.80 nb^{-1} . The inclusive forward muon p_T spectrum is measured and compared to backgrounds. Several muon+jet events, consistent with the weak decay of the bottom quark, were found. In addition, from a larger data sample of 24.2 nb^{-1} , a candidate event for the first observation at $\sqrt{s} = 1.8$ TeV of the process $Z^0 \rightarrow \mu^+ \mu^-$ was discovered, where Z^0 is the uncharged mediator of the weak interaction.

Acknowledgements

Being a member of the Collider Detector at Fermilab (CDF) collaboration has been a fantastic experience. Doing state-of-the-art physics with state-of-the-art detectors, electronics, and computers is a real privilege. I believe that the experience and opportunity offered by a large experiment such as CDF is an excellent training ground for high energy physicists. If large collaborations are the way of the future, more power to them!

Literally hundreds of people have contributed in some way to my graduate physics education. I can only acknowledge but a few of them here. I start first with my advisor, Professor Lee G. Pondrom. He is, without a doubt, the greatest teacher I have ever known. He makes it a personal challenge that his students should learn. If the student's first attempt at understanding is unsuccessful, he has the patience, care, and determination to try again until finally the student catches on. I can recall many enjoyable conversations with him on a variety of topics, some related to physics and some not. His enthusiasm for and commitment to the field of high energy physics is outstanding and I thank him for the

opportunity to have been his student.

I offer my next thanks to Professor Duncan Carlsmith. I have benefited from his help, knowledge, and insight for many years. His energy and dedication, particularly during the construction of the experiment, has been a great source of lasting inspiration for me.

I have profited from discussions with many physicists over the years. I would especially like to express appreciation to Drs. Bob Handler, Adam Para, Marleigh Sheaff, and Dennis Theriot for significant contributions to my physics education. Conversations with Drs. Chris Wendt, John Huth, and Dan Amidei have also been very important to me.

Many people deserve mention and applause for their hard work during construction and installation of the forward muon system. I thank George Ott and Jesse Jaske for all their help and, in particular, for teaching me some of the more “practical aspects” of detector building. The efforts of Hugh Danforth, Mike Frankowski, and Bill Wickenberg are greatly appreciated as well. I also credit losing my fear of heights to climbing around on the forward muon toroids.

To my graduate student friends at Madison: Larry Rotter, Jim Allen, Masa Sano, Dale Tupa, and Bob Knudson; and the ones at Fermilab: Tom Westhusing, Dave Smith, and George Redlinger; the physics and non-physics we shared is fondly remembered.

Jim Catalanello drew most of the figures in this thesis and many thanks go to him.

Monica Skarha has been supportive of my graduate education in varying degrees and I acknowledge her assistance. I am very grateful to Tom Doud for helping to iron out some personal rough spots in recent years. Special thanks go to Meg Laidlaw for understanding and encouragement when I needed it most.

Finally, I acknowledge the many contributions of love and support from my mother, Doris, my sister, Rita, and my son, Justin. I dedicate this thesis to them.

This work was supported by the United States Department of Energy Contract DE-AC02-76ER00881.

Contents

Abstract	ii
Acknowledgements	iii
1 Introduction	1
1.1 The Standard Model	2
1.2 Muon Production in Proton-Antiproton Collisions	6
1.2.1 Single Muons	6
1.2.1.1 W^\pm Decay	6
1.2.1.2 Heavy Quark Decay	8
1.2.1.3 Other Sources	13
1.2.2 Dimuons	13
1.2.2.1 Z^0 Decay	14
1.2.2.2 Drell-Yan Production	14
1.2.2.3 Vector Meson Decay	16
1.2.2.4 Heavy Quark Cascade Decay	17

2	Experimental Setup	20
2.1	The Tevatron Collider	20
2.2	Overview of CDF	25
2.2.1	Vertex Time Projection Chamber	28
2.2.2	Forward Tracking Chambers	32
2.2.3	Endplug Electromagnetic Calorimeter	32
2.2.4	Endplug Hadron Calorimeter	35
2.2.5	Forward Electromagnetic Calorimeter	35
2.2.6	Forward Hadron Calorimeter	36
2.2.7	Beam-Beam Counters	37
2.3	The CDF Forward Muon System	38
2.3.1	General Features	40
2.3.2	The Toroids	40
2.3.3	The Drift Chambers	45
2.3.4	The Scintillation Counters	49
2.3.5	Survey and Alignment	50
2.3.6	Momentum Resolution	54
2.4	Forward Muon Electronics	64
2.4.1	Overview	64
2.4.2	The PSL Time-to-Digital Converter	71
2.4.3	RABBIT Electronics	75
2.4.4	The Half Octant Pattern Unit	77

2.5	The Forward Muon Trigger	79
2.5.1	Level 1	80
2.5.2	Level 2	82
3	The 1987 Collider Run	84
3.1	The 1987 Run Experience	84
3.2	Data Sample	94
4	Forward Muon Backgrounds	144
4.1	Cosmic Rays	145
4.2	Leakage Through Gaps in the Detector	145
4.3	Hadronic Shower Punchthrough	146
4.4	Misidentification	148
4.5	Delta Rays	150
4.6	Decays of Pions and Kaons in Flight	152
5	Inclusive Forward Muon Spectrum	169
5.1	Decay-in-flight Background Comparison	169
5.2	Inclusive Spectrum Normalization	181
5.3	CDF Charged Hadron Spectrum Comparison	185
5.4	UA1 Inclusive Muon Spectrum Comparison	185
6	$Z^0 \rightarrow \mu^+ \mu^-$ Candidate	192

7	Conclusions	203
A	CDF Coordinate System	206
B	Forward Muon Tracking Code	208
B.1	TDC Data Manipulations	208
B.2	Track-finding Procedure	222
B.3	Track-fitting Algorithm	226
C	Forward Muon Display	250
	Bibliography	255

List of Tables

1.1	Lepton and quark families within the Standard Model.	2
2.1	Radial distance from the beamline of sense wires in a front plane chamber.	47
3.1	Track-finding criteria.	96
4.1	Probabilities (in %) for having extra hits within the same cell as a fitted hit.	151
4.2	Probabilities (in %) for having extra hits within the 300% road but in a different cell than a fitted hit.	151
4.3	Properties of pions and kaons.	160
4.4	The three intervals used to perform the p_T integration.	160
4.5	Trigger efficiency values for the 1 - 5 GeV/c interval.	161
5.1	Forward muon invariant cross section for the interval $2.75 \leq p_T \leq$ 9.25 GeV/c.	183

5.2	Fit parameters for the forward muon and charged hadron p_T spectra to the form $A/(1 + p_T/p_0)^n$. Quoted errors are purely statistical.	183
5.3	The FMU and UA1 muon $d\sigma/dp_T dy$ spectra. The errors given are statistical.	188
6.1	$Z^0 \rightarrow \mu^+ \mu^-$ event parameters.	193
6.2	Z^0 event kinematic properties.	194
B.1	Mapping of RAM wire# to chamber wire#.	212
B.2	TDC data t_0 corrections.	227
B.3	Sample track hit positions.	227
B.4	Multiple scattering parameters.	242
B.5	dE/dx energy loss parameters.	242

List of Figures

1.1	Feynman diagrams for the first-order QCD production of weak bosons: a) gluon bremsstrahlung, b) QCD Compton scattering. .	9
1.2	Heavy quark production mechanisms: a) gluon fusion, b) gluon splitting, c) flavor excitation.	11
1.3	Drell-Yan production of dimuons.	15
1.4	Dimuons from $b\bar{b}$ production.	18
2.1	The Fermilab accelerator complex.	22
2.2	Perspective view of the CDF detector.	26
2.3	Side view of the CDF detector.	27
2.4	Two of the eight vertex time projection chamber (VTPC) modules. .	29
2.5	A 1.8 TeV $\bar{p}p$ collision as observed by the VTPC.	31
2.6	Illustration showing the radial wire layout for one of the two forward tracking chambers (FTC).	33
2.7	One plane of the beam-beam counter (BBC) system.	39
2.8	View of the CDF forward detectors.	41

2.9	Elements of the forward muon detector planes.	42
2.10	Toroid magnetic field measurements.	44
2.11	Schematic of the chamber cell geometry and materials. The dimensions given are that for the inner radius cells of a front plane chamber.	46
2.12	Schematic of the FMU survey procedure.	51
2.13	Ideal tooling ball (x,y) location.	53
2.14	The z position survey method.	55
2.15	Single toroid bend displacement calculation.	57
2.16	Momentum resolution estimation for the forward muon system. .	60
2.17	Multiple scattering displacement in the forward muon system. . .	63
2.18	Forward muon electronics.	65
2.19	Drift chamber pre-amplifier (a) and amplifier/discriminator (b) circuit diagrams.	67
2.20	Simplified operation of the trigger electronics.	69
2.21	Timing signals used by the FMU system.	72
2.22	Operation of the PSL TDC.	74
2.23	CDF RABBIT system block diagram.	76
2.24	RABBIT system timing signals.	78
2.25	A particle track satisfying the 100% trigger threshold.	81
2.26	Trigger efficiency for the 300%, 100%, and 50% trigger thresholds.	83

3.1	Collision hall picture showing the location of the low-beta quadrupole magnet relative to the forward muon system.	86
3.2	The FMU 300% Level 1 trigger rate as a function of luminosity. .	88
3.3	Beam fragment trigger with missing front and rear plane ambiguity wire hits.	90
3.4	Beam fragment trigger with a high multiplicity particle splash in the middle plane.	91
3.5	The beam-beam counter trigger rate.	92
3.6	The FMU(300%,outer HOPU region)·BBC Level 1 trigger rate. .	93
3.7	Flowchart of the data sample analysis.	95
3.8	Track-finding efficiency for simulated muons, including detector acceptance and energy loss range-out effects.	98
3.9	Forward muon momentum spectrum after track reconstruction. . .	100
3.10	Forward muon p_T spectrum after track reconstruction.	101
3.11	Trigger efficiency for the 300% trigger threshold.	102
3.12	Reconstructed p_T versus simulated p_T for Monte Carlo generated muons.	103
3.13	Monte Carlo p_T resolution as a function of p_T	104
3.14	Forward muon charge asymmetry after reconstruction.	105
3.15	Charge asymmetry observed in the Monte Carlo.	107

3.16 Electromagnetic energy in a 3×3 $\eta - \phi$ tower region centered on the forward muon track in the plug and forward calorimeters after track reconstruction.	108
3.17 Hadronic energy in a 3×3 $\eta - \phi$ tower region centered on the forward muon track in the plug and forward calorimeters after track reconstruction.	109
3.18 Projection of a forward muon track into a 3×3 calorimeter tower region.	110
3.19 Fake muon tracks typically have no calorimeter energy loss.	112
3.20 FMU/VTPC track matching.	113
3.21 Forward muon momentum spectrum after cuts.	116
3.22 Forward muon p_T spectrum after cuts.	117
3.23 Electromagnetic energy in a 3×3 $\eta - \phi$ tower region centered on the forward muon track in the plug and forward calorimeters after cuts.	118
3.24 Hadronic energy in a 3×3 $\eta - \phi$ tower region centered on the forward muon track in the plug and forward calorimeters after cuts.	119
3.25 Energy deposition in a 3×3 $\eta - \phi$ tower region centered on the forward muon track in the plug and forward electromagnetic and hadron calorimeters after cuts.	120

3.26	Pad pulse height distributions for each chamber plane show a minimum ionizing peak for muon tracks within our sample. Units are 10^3 ADC counts.	121
3.27	Polar angle match distribution between FMU and VTPC tracks. .	122
3.28	Azimuthal angle match distribution between FMU and VTPC tracks.	123
3.29	Event vertex distribution for our sample.	124
3.30	Front plane coordinate wire number distribution for our muon candidates.	125
3.31	Front plane coordinate wire number distributions for 2, 3, 4, and 5 GeV/c simulated muon tracks.	127
3.32	χ^2 distribution for FMU tracks in our sample.	128
3.33	Track residual distribution for our data sample.	130
3.34	Forward muon p_T spectrum after cuts. (linear scale)	131
3.35	Forward muon track pseudorapidity distribution.	132
3.36	Forward muon track phi distribution.	134
3.37	Forward muon octant occupancy distribution (west side).	135
3.38	Forward muon octant occupancy distribution (east side).	136
3.39	Reduced FMU system acceptance due to chamber dead channels.	137
3.40	Ratio of the number of tracks after correction due to trigger dead channels and chamber gain variations to that before correction. Octants 0-7 are on the west and 8-15 on the east side.	139

3.41	West side forward muon octant occupancy after corrections. . . .	140
3.42	East side forward muon octant occupancy after corrections. . . .	141
3.43	Forward muon p_T spectrum after corrections.	142
4.1	Interaction lengths of material versus polar angle in the forward region at CDF. Negative angles are used for the west side of the detector to show the east/west detector symmetry.	147
4.2	Integral probability distributions for hadronic shower punchthrough as a function of steel absorber thickness.	149
4.3	The p_T resolution for the two cases of extra hits (delta rays) and no extra hits.	153
4.4	The CDF inclusive charged hadron p_T spectrum.	154
4.5	Hadron decay path length in the forward region.	157
4.6	Procedure for determining the decay-in-flight background spec- trum via Monte Carlo simulation.	164
4.7	Forward muon decay-in-flight spectrum from a simulation of the CDF single particle inclusive spectrum.	168
5.1	Inclusive forward muon spectrum (solid line) compared to the sim- ulated decay-in-flight background (dashed line). The spectra are normalized to the data sample integrated luminosity of 0.80 nb^{-1}	170

5.2	Inclusive forward muon spectrum and simulated decay-in-flight background plotted on a semi-logarithmic scale with statistical errors.	172
5.3	Decay-in-flight background subtracted spectrum for $p_T > 4$ GeV/c muons including statistical errors.	173
5.4	Forward muon display for a candidate heavy quark decay event. .	174
5.5	Calorimetry lego display for a candidate heavy quark decay event.	175
5.6	Muon p_T spectrum for events containing jet activity and $p_T^\mu > 4$ GeV/c.	176
5.7	The $d\sigma/dy$ distributions for b quark production at center-of-mass energies of 630 GeV (a) and 1.8 TeV (b).	177
5.8	Muon transverse momentum relative to the nearest jet axis for $p_T^\mu > 5$ GeV/c.	179
5.9	UA1 muon transverse momentum relative to the nearest jet axis for $p_T^\mu > 10$ GeV/c and at least one jet of $E_T > 10$ GeV.	180
5.10	Invariant cross section for forward muon production in the interval $1.95 < \eta < 2.80$. The error bars are statistical only.	184
5.11	Comparison of charged hadron ($ \eta < 1.0$) and forward muon ($1.95 < \eta < 2.80$) inclusive spectra at CDF. The forward muon spectrum is plotted both at its actual values (lower curve) and at scaled values (upper curve) for shape comparison.	186

5.12	UA1 inclusive muon p_T distribution ($ \eta < 1.5$) before background subtraction (black circles). The background contribution from decay-in-flight is also shown (open triangles).	187
5.13	Comparison of the FMU ($1.95 < \eta < 2.80$) and UA1 ($ \eta < 1.5$) muon p_T spectra.	190
5.14	UA1 inclusive muon p_T distribution ($ \eta < 1.5$) after background subtraction.	191
6.1	Forward muon half of the Z^0 candidate event.	196
6.2	Central muon track inside the central tracking chamber.	197
6.3	E_T lego plot for the Z^0 event.	198
6.4	Forward muon track in the VTPC.	199
6.5	FTC azimuthal segment corresponding to the forward muon.	200
6.6	Muon energy deposition in the forward calorimeters.	201
6.7	CDF muon acceptance for W^\pm and Z^0 boson decay.	202
A.1	The CDF coordinate system.	207
B.1	Sample track to demonstrate the FMU track-fitting.	209
B.2	Hit time data as it appeared in the PSL TDC for our sample track.	210
B.3	Delay line operation and tap time offsets.	214
B.4	Reformatted TDC data stored in the FMUD bank for our sample track.	216

B.5	Method for obtaining the global t_0 offset and reciprocal drift velocity.	219
B.6	STOP signal arrival time variation for our data sample.	220
B.7	a) Strip hits consistent with a strip road of width 1. b)Strip hits failing a strip road of width 1 requirement.	225
B.8	Initial track parameter estimation.	228
B.9	Muon track propagation through the FMU system.	235
B.10	Iterative fit procedure flowchart.	237
B.11	Multiple scattering covariance calculation.	238
B.12	Residual distribution before including the multiple scattering correction.	244
B.13	Difference in the actual and fitted trajectories due to multiple scattering.	245
B.14	Residual distribution after the multiple scattering correction. (Same as Figure 3.33.)	248
C.1	A forward muon event picture	254

Chapter 1

Introduction

The Tevatron proton-antiproton collider at Fermilab has opened up a new energy regime for exploration in high energy physics with its operation at a center-of-mass energy of 1.8 TeV. For the first time, the “1 TeV barrier” is broken and new physics beyond the intermediate vector bosons W^\pm and Z^0 of the Glashow-Salam-Weinberg (GSW) electroweak theory [1] is possible. The Standard Model [2] will of course be tested in full detail at the new energy and an extensive search for the elusive top quark can be expected. It is an exciting time in the high energy physics field and results from the Tevatron collider will certainly help to shape the direction and course of the field for years to come.

This thesis is concerned with the particular topic of the production of forward-going muons at the collider and is based on data collected with the CDF (Collider Detector at Fermilab) detector [3] in 1987. “Forward-going” means muons pro-

leptons:	ν_e	ν_μ	ν_τ	$Q = 0$
	e	μ	τ	$Q = -1$
quarks:	u	c	(t)	$Q = +\frac{2}{3}$
	d	s	b	$Q = -\frac{1}{3}$

Table 1.1: Lepton and quark families within the Standard Model.

duced from proton-antiproton collisions at angles between 3° and 16° relative to the colliding beams. Several processes contribute to the single and double (di-) muon spectra at the collider and this makes muon studies a rich area for investigation.

In the remainder of this chapter, a few basic aspects of our current understanding of particle physics will be presented and the mechanisms for producing muons at proton-antiproton colliders will be examined.

1.1 The Standard Model

Major strides have been made in understanding the fundamental laws of nature over the last decade or so. Substantial evidence has been collected that supports a theoretical framework generally referred to as the “Standard Model”. The fundamental particles in this model are spin- $\frac{1}{2}$ fermions: six leptons and six quarks, which can be grouped into doublets of three families as shown in Table 1.1. As mentioned before, the top quark has not yet been discovered.

There exist three fundamental interactions (excluding gravity) between these elementary particles. They are mediated by the exchange of spin-1 gauge bosons and are known as:

- the electromagnetic interaction, mediated by the massless photon (γ), which couples to the electric charge;
- the strong interaction, mediated by eight massless gluons, which couple to a quantity called “color”;
- the weak interaction, mediated by the massive bosons W^\pm and Z^0 , which couple to the “weak isospin” and “weak hypercharge”.

The electromagnetic interaction has been well understood for some time. The classical theory of electromagnetism dates back to the last century and the quantum field theory of electrodynamics (QED) was introduced in the 1930's and 1940's.

In the 1970's, Quantum Chromodynamics (QCD), the quantum field theory of the strong or nuclear force, was developed in analogy to QED. Rather than coupling to electric charge, the strong force couples to a “color” charge existing in “blue”, “green”, and “red” varieties and to the corresponding “anticolors” as well. Quarks and gluons are the only particles which carry color and therefore experience the strong interaction. So far, only colorless particles have been observed in nature. The quarks are grouped either into mesons, which consist of a quark carrying color and an antiquark carrying anticolor, or into baryons, which consist of three quarks: a blue, a green, and a red one. Both combinations result

in a “white” or colorless state.

Theories of the weak interaction date back to the work of Fermi in the 1930’s, but development of a complete theory has been a relatively recent achievement. The vector bosons W^+ and W^- are the charged carriers of the weak interaction and induce transitions within a “weak isospin” doublet, i.e. an electron transforms into a ν_e , emitting a W^- . (Only left-handed fermions are in doublets. Right-handed fermions are grouped into singlets.) The weak interaction between quarks is slightly more complicated. The physical states d , s , and b are a mixture of the weak eigenstates d' , s' , and b' . Weak interactions of quarks can therefore occur between different families. A charm quark can decay into a strange quark or (less likely) into a down quark. The mixing is described by the Kobayashi-Maskawa (K-M) matrix [4]:

$$\begin{bmatrix} u \\ c \\ t \end{bmatrix} = \begin{bmatrix} V_{ud} & V_{us} & V_{ub} \\ V_{cd} & V_{cs} & V_{cb} \\ V_{td} & V_{ts} & V_{tb} \end{bmatrix} \begin{bmatrix} d \\ s \\ b \end{bmatrix}$$

The uncharged weak interaction mediator Z^0 induces neutral currents, i.e. $Z^0 \rightarrow \mu^+ \mu^-$. Neutral currents between members of different quark families are forbidden by the GIM mechanism [5]. In the currently-favored GSW electroweak theory, the Z^0 and γ are a mixture of neutral gauge bosons coupling to weak isospin (W^0) and to weak hypercharge (B^0). The mixing is described by the Weinberg angle θ_W and arises, together with the nonzero W^\pm and Z^0 masses,

from spontaneous symmetry breaking. The realization that the electromagnetic and weak interactions are not independent forces, but are actually a mixture of the weak isospin and weak hypercharge forces, was a major advance in particle physics in the 1960's.

Among its many features, the Standard Model proposes the existence of a scalar particle called the "Higgs". The Higgs field would lead to spontaneous symmetry breaking[6], making the W^\pm and Z^0 bosons massive. At the same time, it could be responsible for the nonzero fermion masses. The Higgs particle has not yet been discovered. The theory makes no predictions for its mass other than through a unitarity limit which requires it to be less than about 1 TeV.

Although the Standard Model describes the observed data very well, it is generally not believed to be the ultimate theory of Nature. It uses many parameters which have to be determined experimentally: 6 quark masses, 3 lepton masses (if neutrinos are massless), 3 Kobayashi-Maskawa angles, one phase of the K-M matrix, the electromagnetic coupling constant, the Weinberg angle, the vacuum expectation value of the Higgs field, the mass of the Higgs particle, and the QCD scale Λ . This results in 18 free parameters. A more fundamental theory would predict the values of these quantities. In addition, the Glashow-Salam-Weinberg model does not tell us why there appear to be three families of quarks and leptons. And finally, the Standard Model does not include gravity. Still, it is the best we have right now and the final theory of Nature cannot be too much different. It is up to experiment to provide the direction that the Standard Model should take.

1.2 Muon Production in Proton-Antiproton Collisions

Below we give a brief survey of muon production in $\bar{p}p$ collisions. We will consider standard production mechanisms and any available data at or near the current Tevatron center-of-mass energy of 1.8 TeV. At this time, the only experiment other than CDF investigating muon production in $\bar{p}p$ collisions is the UA1 experiment [7]. The UA1 detector has been in operation since 1981 and has produced many results, including discovery of the intermediate vector bosons W^\pm [8] and Z^0 [9]. In many ways, UA1 has set the pace and expectations for muon physics at CDF and their results will be mentioned frequently.

1.2.1 Single Muons

Single muons, whether isolated or near jet activity, are commonly produced in $\bar{p}p$ collisions. In the following, we will discuss several sources of single muons.

1.2.1.1 W^\pm Decay

The existence of the W^\pm bosons of the electroweak theory is no longer in question. Discovered in 1983 by UA1 and UA2 [10], CDF has already seen a significant signal in the electron channel $W \rightarrow e\nu$ [11] and several events in the lower acceptance muon channel.

The weak bosons (W^\pm and Z^0) are produced in hadron collisions by quarks and antiquarks with average fractional momenta $x = M_{W,Z}/\sqrt{s}$. It is important

to note that when \sqrt{s} is increased by a factor of ~ 3 (CERN collider energy of 630 GeV compared to 1800 GeV at the Tevatron), the average value of x shifts from about 0.130 at CERN to 0.045 at the Tevatron. The lower values of x (= quark p_L /beam p_L , in general) imply that sea quarks will play a significant role in the production features of weak bosons. In fact, at $\sqrt{s} = 1.8$ TeV, the W production cross section is ~ 2.5 times higher from valence-sea than from valence-valence quark annihilation. This is quite a reversal from the 630 GeV CERN energy where valence-valence annihilation is almost twice as probable as valence-sea.[12]

Because of the (V-A) coupling of the weak interaction, the W bosons produced from valence quark annihilation at the Tevatron are almost fully polarized along the antiproton direction. Again, owing to the (V-A) coupling of the W to its decay products, there will be a decay charge asymmetry in the emitted particles with respect to the beam direction. In the case of W decaying to $\mu + \nu$, the positively charged muons will be produced in the direction of the incoming antiprotons and likewise, the negatively charged muons are emitted in the proton direction. For a W boson produced at rest, this charge asymmetry should be measurable in the forward region. However, the forward muons from the W decay will be relatively low p_T (10 - 20 GeV/c) and some background contamination can be expected. For a W boson produced from quarks annihilating with different x values, the W will have non-zero longitudinal momentum. This will cause the normally centrally-produced high p_T (30 - 40 GeV/c) muon to be emitted into the forward region. The muon backgrounds at such transverse momenta are greatly

reduced and a charge asymmetry signal may be evident. Unfortunately, there is a competing production charge asymmetry with the opposite sign due to the harder fragmentation function of the u compared to the d quark. This causes more positively charged W bosons to be produced in the direction of the incoming protons and could cause the decay charge asymmetry to be unobservable. It remains to be seen if this production charge asymmetry can be unraveled from the decay asymmetry.

In addition to the usual formation of the weak bosons through quark-antiquark annihilation, higher-order QCD processes occur which involve the emission or absorption of gluons. In first-order QCD, one of the quarks radiates a gluon in the form of bremsstrahlung (Figure 1.1a), or in a Compton-type process a quark is scattered from a gluon followed by radiation of a weak boson (Figure 1.1b). At the Tevatron, gluon radiation dominates the Compton term simply because the quark-gluon system in the Compton process has to provide the energy necessary for weak boson formation. This is kinematically suppressed owing to the very soft structure function of the gluons in the proton.[13]

1.2.1.2 Heavy Quark Decay

Theoretical expectations are that the most important source of prompt single muons is from the semileptonic decay of heavy quark-antiquark pairs (charm, bottom, and possibly top) which are produced via the strong interaction. The

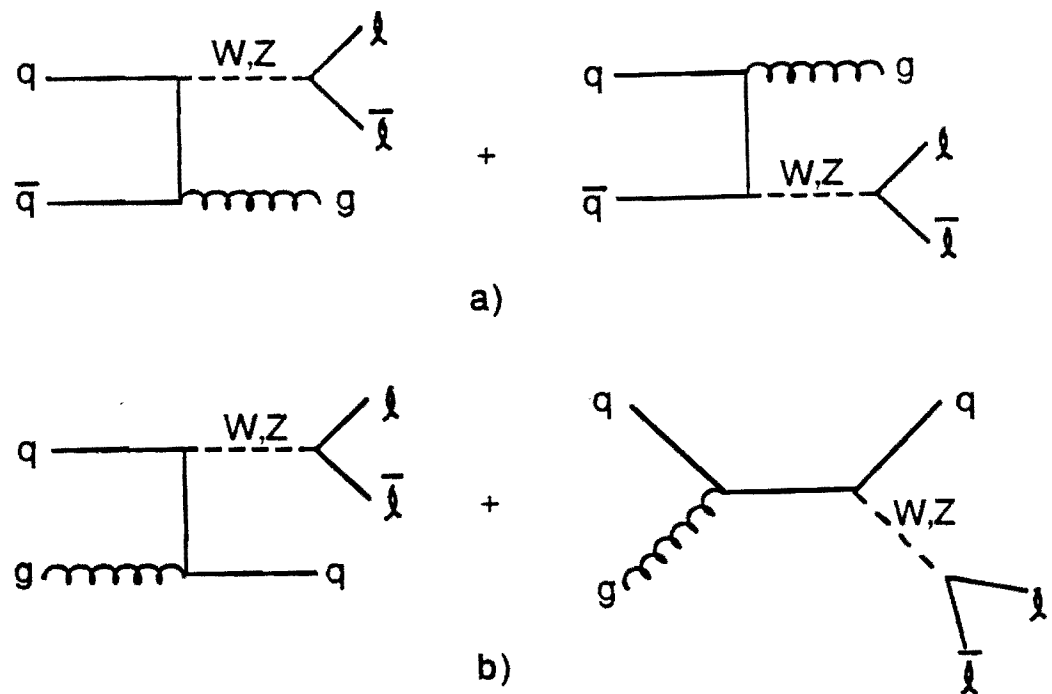


Figure 1.1: Feynman diagrams for the first-order QCD production of weak bosons:
a) gluon bremsstrahlung, b) QCD Compton scattering.

semileptonic decay of a heavy quark is mediated by a W^\pm , i.e.:

$$c \rightarrow sW^+(\text{virtual}) \rightarrow \mu^+ \nu_s$$

$$b \rightarrow cW^-(\text{virtual}) \rightarrow \mu^- \bar{\nu}_c$$

The heavy quark decay branching ratio into a final state muon is $\sim 10\%$.

Figure 1.2 shows the standard heavy quark production mechanisms involving gluons. Light quark-antiquark annihilation is a less important source of heavy quark pairs. The three processes known as gluon fusion, gluon splitting, and flavor excitation contribute approximately equally to heavy quark production.[14] However, UA1 reports that as a practical matter, the higher-order processes of gluon splitting and flavor excitation are kinematically suppressed for bottom quark decay by typical event selection requirements on the muon transverse momentum and on the dimuon mass (for the case of dimuons). In gluon splitting, the b quark and the \bar{b} quark tend to be collinear and cannot give rise to high-mass muon pairs. In flavor excitation, the “spectator” b quark normally has low p_T and cannot decay to give a high p_T muon.[15]

As discussed above, quarks are colored objects and as a result of color confinement they have to form into colorless mesons or baryons in the aftermath of a collision. In this step, the so-called “fragmentation process”, some fraction of the initial quark momentum is used to create (light) quark-antiquark pairs. A single light quark or quark-antiquark pair will combine with the heavy quark to form a colorless heavy hadron. The remaining light quarks form light hadrons.

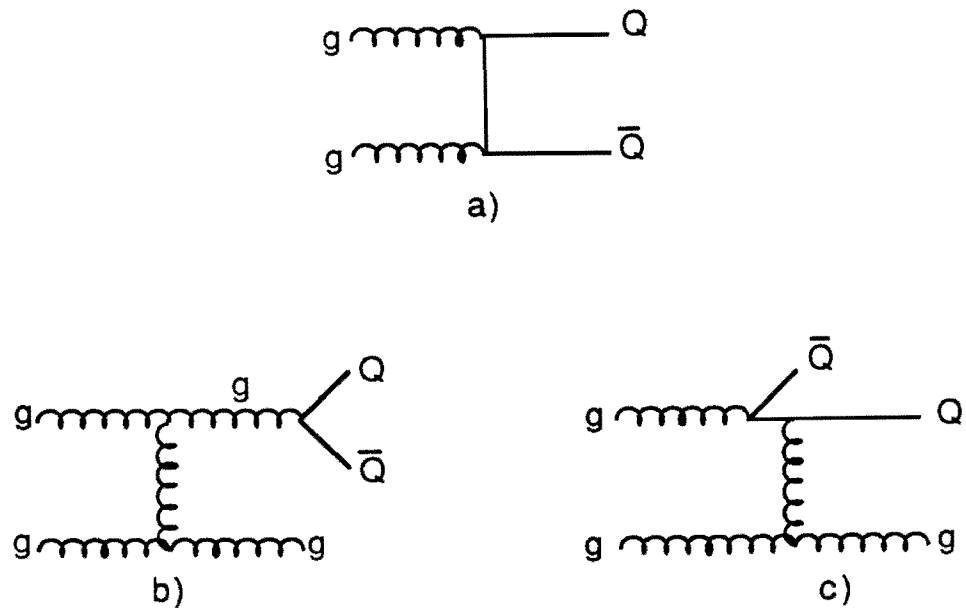


Figure 1.2: Heavy quark production mechanisms: a) gluon fusion, b) gluon splitting, c) flavor excitation.

Hence the heavy hadron is typically contained in a jet of particles. The heavy hadron will also keep a fraction of the original momentum of the heavy quark. This is expressed by the fragmentation variable z :

$$z = p_{||}/p_{\text{QUARK}},$$

where $p_{||}$ is the component of the hadron's momentum parallel to the initial quark direction. The distribution of the fragmentation variable z can be described by the Peterson heavy quark fragmentation function [16]:

$$D(z) = \frac{n}{z[1 - 1/z - \epsilon/(1 - z)]^2},$$

which depends on the single parameter ϵ .

Another source of heavy quarks is the decay of the W^\pm and Z^0 bosons:

$$Z^0 \rightarrow c\bar{c}, b\bar{b}, t\bar{t};$$

and

$$W^+ \rightarrow t\bar{b}, \quad W^- \rightarrow \bar{t}b.$$

Of course, the weak boson decays into the top quark are not possible if the top quark is too heavy. The weak production of heavy quarks is at a much lower rate than the direct QCD production. Although composed principally of light quarks, UA2 does claim to see a signal for the weak production of quark pairs in their 2-jet invariant mass distribution.[17] UA1 uses their single muon sample with associated jet production to study heavy flavor production [18] and to quote their best limit on the top quark mass, $m(t) > 44 \text{ GeV}/c^2$ [19].

1.2.1.3 Other Sources

Other potential sources of single muons include backgrounds such as pion and kaon decay-in-flight, hadronic shower punchthrough, cosmic rays, etc. These will be discussed in Chapter 4. A possibly serious background to the single muon signal at CDF is from dimuons where one muon is missed due to the limited muon coverage. It remains to be seen in the larger data samples of the coming runs if this is a problem.

1.2.2 Dimuons

Dimuons present a particularly clean signature at hadron colliders. The production process is usually rare so that the trigger rate is low (a big advantage) and the background, being the “square” of the single muon background, is also small. In addition, if the muons are produced from the decay of a single particle, the mass peak of this particle is usually quite evident above background.

Dimuon production falls into two general categories. The first is direct production via electroweak interactions, that is, weak production via Z^0 decay or Drell-Yan electromagnetic production via a virtual photon. The second mechanism for dimuon production is through the weak decays of heavy quarks (i.e. c , b , and t) which are produced by the strong or electroweak interactions. Since protons are composite, the $\bar{p}p$ collider is essentially a quark, antiquark, and gluon collider. All the possible initial production states, $q\bar{q}$, qg , and $g\bar{g}$ participate in processes that contribute to the dimuon spectrum.[20]

1.2.2.1 Z^0 Decay

First discovered by UA1 in 1983, the high-mass muon pair from the Z^0 provides a very distinctive signature with very little background. A few events of Z^0 decay into the muon channel have been seen at CDF and one particularly spectacular event with a forward and a central muon is described in detail in Chapter 6.

It should be noted that in contrast to the W^\pm case, only a small charge asymmetry is expected in the angular distribution of Z^0 decay leptons. This is because the parity-violating term is proportional to $(1 - 4\sin^2\theta_W)$, which is small due to $\sin^2\theta_W$ being close to 0.25. However, a measurement of the decay asymmetry provides an independent check on the value of $\sin^2\theta_W$ and would be an interesting result.

1.2.2.2 Drell-Yan Production

The Drell-Yan process is the annihilation of a quark and an antiquark pair into a virtual photon which decays into a lepton pair (Figure 1.3a).[21] The signature of such events are lepton pairs of opposite sign which are not accompanied by any nearby hadrons (jet activity) other than perhaps scattered fragments of the primary proton and antiproton. Hence, the muons from Drell-Yan production are isolated. This simple picture has to be modified slightly when higher-order QCD processes are taken into account as shown in Figures 1.3b and 1.3c. The radiated quark or gluon will show up as a jet. This jet may overlap with one of the muons but typically the jet is still far enough away that the muons remain

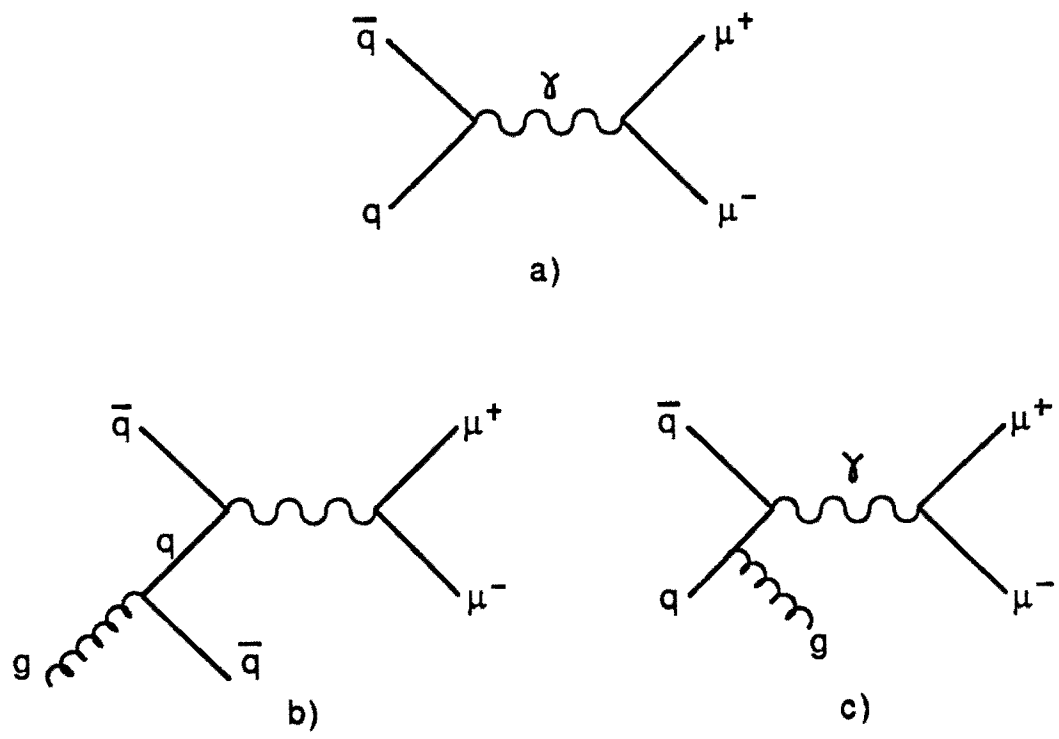


Figure 1.3: Drell-Yan production of dimuons.

relatively isolated. The muon pair from the higher-order processes will tend to have relatively high transverse momentum in order to balance the jet(s), while muon pairs from the lowest-order process are at rest in the transverse plane (except for some p_T on the order of 1 GeV/c from the Fermi motion of the quarks inside the proton). UA1 has presented results for the p_T distribution of low mass Drell-Yan pairs ($m(\mu\mu) < 2.5 \text{ GeV}/c^2$).[22]

1.2.2.3 Vector Meson Decay

Resonance production of dimuons is expected from the decay of the Υ and J/ψ particles. These vector mesons, consisting of a bound $b\bar{b}$ (Υ , $9.46 \text{ GeV}/c^2$ mass) or $c\bar{c}$ (J/ψ , $3.10 \text{ GeV}/c^2$ mass) state, can in principle be produced by the Drell-Yan process if the virtual photon converts into a bound quark-antiquark pair. They can also be produced by the strong interaction and this is expected to be the primary source at the Tevatron. Since the strong decays of the J/ψ and Υ are suppressed by the Zweig rule [23], a significant fraction of them decay electromagnetically into lepton pairs. UA1 has observed both the J/ψ [24] and the Υ [25] mass peaks in their dimuon sample and quote production cross sections at $\sqrt{s} = 630 \text{ GeV}$ for each particle. The UA1 dimuon sample required that each muon have a $p_T > 3 \text{ GeV}/c$ and thus the J/ψ 's in their sample were produced at high p_T ($p_T > 5 \text{ GeV}/c$). An important source of high p_T J/ψ 's may be the decay of beauty mesons. The branching ratio for $B \rightarrow J/\psi + X$ is about 1%.

1.2.2.4 Heavy Quark Cascade Decay

Cascade decays of heavy quarks are expected to be the dominant source of dimuons at the Tevatron. In particular, one can expect cascade decays to yield a substantial signal of like-sign muon pairs. For example in the case of $b\bar{b}$ production, muons can also come from the decay of a secondary charm quark. If the b quark decays directly into a μ^- and the \bar{b} decays into a \bar{c} which also decays into a μ^- , an event with a like-sign muon pair is created. In the case of the top quark, there are three decay steps which can produce a muon:

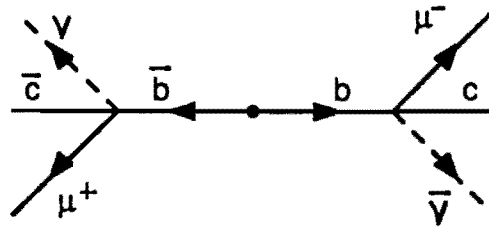
$$t \rightarrow b\mu^+\nu \text{ then } b \rightarrow c\mu^-\bar{\nu} \text{ and } c \rightarrow s\mu^+\nu.$$

Assuming the top quark is light enough, the $W \rightarrow t\bar{b}$ decay is especially interesting since it can produce a like-sign dimuon pair from two first generation decays.

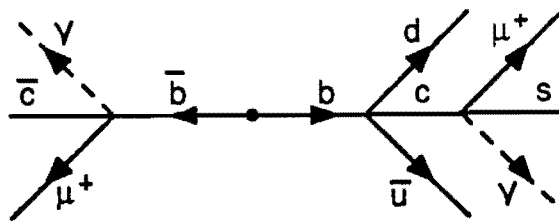
Since a cut on the muon transverse momentum is typically made, muons from secondary decays are heavily suppressed because they are produced with a softer p_T spectrum. Lacking copious top quark production and neglecting mass threshold effects so that the production cross section for $b\bar{b}$ and $c\bar{c}$ are the same, this means that $b\bar{b}$ rather than $c\bar{c}$ decays will be the principle source of dimuons from heavy quark decay (Figure 1.4).

Dimuon events from $b\bar{b}$ quark decay will generally have the following properties:

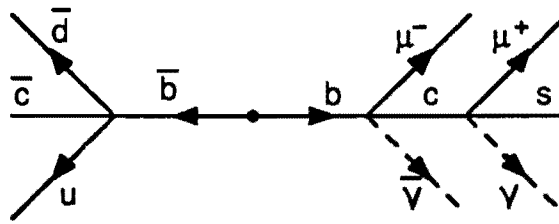
- The muons will be accompanied by hadrons from the heavy quark fragmenta-



a)



b)



c)

Figure 1.4: Dimuons from $b\bar{b}$ production.

tion and from its semileptonic decay. The muons will therefore not be isolated.

- The muons will predominantly have opposite signs, but some like-sign events from second generation decays are expected.
- The muons will usually be back-to-back in the transverse plane. Higher-order QCD effects can lead to a fraction of events with smaller azimuthal angles between the muons. These events will have additional jets.[26]

In their heavy quark analysis, UA1 has made thorough use of their dimuon data sample. They quote a $b\bar{b}$ production cross section for $p_T(b) > 5 \text{ GeV}/c$ [27] and have extended this measurement recently to give a value for the total cross section for bottom quark pair production [28]. They also see evidence for $B^0 - \bar{B}^0$ oscillations (mixing) [29] similar to that which has been observed in the $K^0 - \bar{K}^0$ system. The $B^0 - \bar{B}^0$ mixing signal is characterized by an excess of like-sign muon pairs above that expected from normal heavy quark cascade decays.

Chapter 2

Experimental Setup

2.1 The Tevatron Collider

In 1973, R. R. Wilson, the founding director of Fermi National Accelerator Laboratory, started a research and development program aimed at acquiring the technology of ramped superconducting magnets. In 1975, he was joined by Alvin Tollestrup, on leave from the California Institute of Technology, and several 0.6 m long model magnets were constructed. In 1976, an assembly line was created and full-scale magnets were assembled in a mass-production operation. The objective was to construct a new ring of superconducting magnets in the same tunnel which carried the 400 GeV conventional magnet Main Ring accelerator. The purposes of the new machine, known as the “Tevatron”, were to double the beam energy (400 to 800 GeV) and to save substantial amounts of electrical energy in the process (60 megawatts of magnet power reduced to 15 megawatts of refrigeration

power).

The U. S. Department of Energy authorized the project to proceed in July of 1979 and the installation of 776 dipole magnets each 6.2 m long, 226 quadrupole magnets each 4 m long, and 226 complex spool pieces containing beam diagnostics, correction windings, etc., was completed by April of 1983. At the same time, a mammoth cryogenics system was created to insure an ample supply of liquid helium to keep the 6.28 km ring of superconducting magnets at the required 4.5 °K liquid helium temperature. During the construction period, the physics goals of the Tevatron project were refined and two additional projects were started whose functions were to realize the physics potential of the accelerator. The new projects were labelled Tevatron I and Tevatron II. The Tevatron I project was to build an antiproton (\bar{p}) source and to modify the Fermilab accelerators in order to provide for proton-antiproton collisions at the maximum Tevatron energy. The Tevatron II program was charged with the upgrading of extraction, switchyard, and beamline components to operate fixed target experiments at beam energies up to 1 TeV.[30,31] Figure 2.1 shows the layout of the Fermilab accelerator complex.

During the 1987 proton-antiproton collider run, the Tevatron was operated at 900 GeV per beam or a 1.8 TeV center-of-mass energy. The number of antiprotons transferred in one operation was typically 1 to 2×10^{10} particles. These were bunched into approximately ten 19 nanosecond time intervals ("buckets") inside the accelerator. This operation was repeated twice, two minutes apart, with

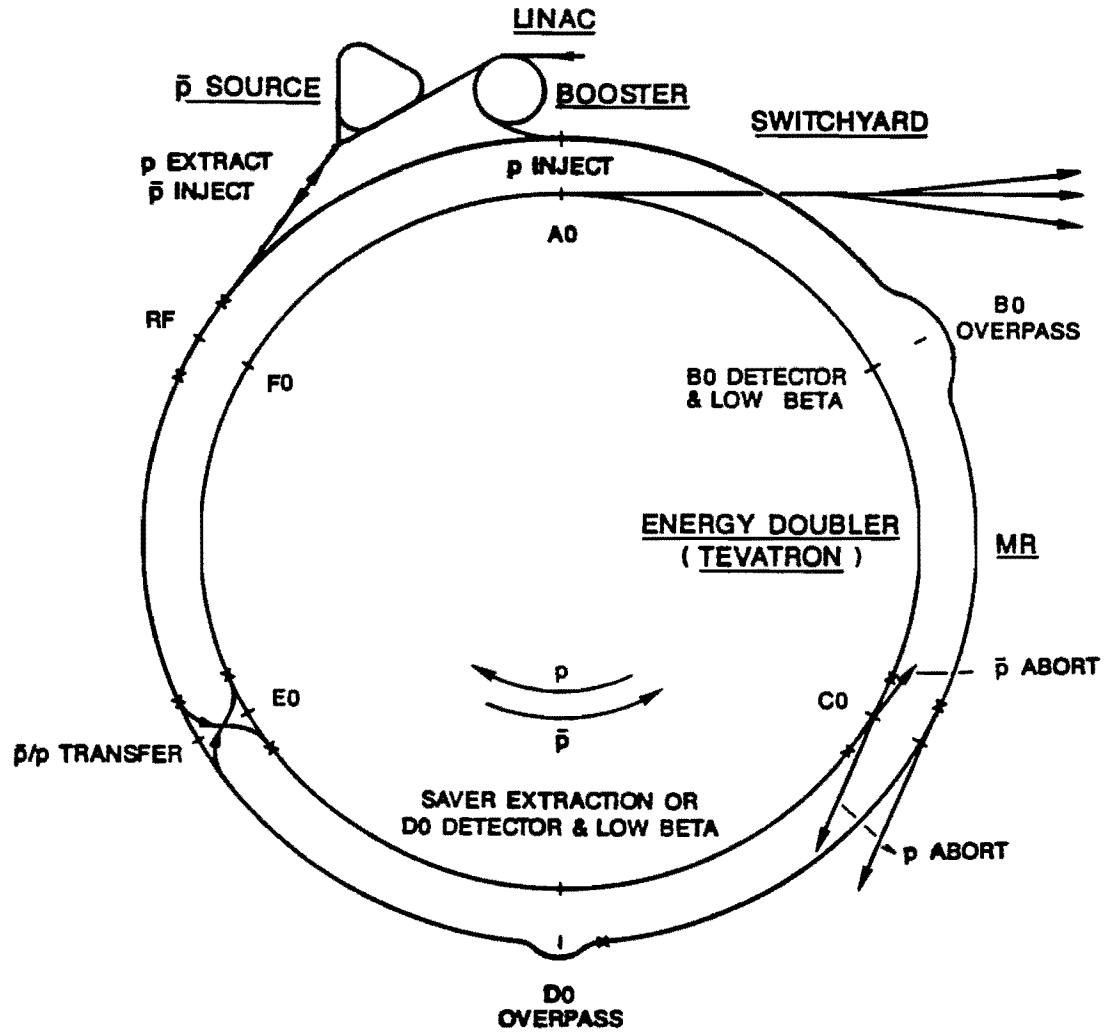


Figure 2.1: The Fermilab accelerator complex.

the three antiproton injections into the Tevatron then being followed by three proton bunches at an order of magnitude higher intensity. The ensemble was then accelerated to 900 GeV, moved (“cogged”) to collide at the interaction regions and focussed into a small spot (“squeezed”) by exciting low-beta quadrupole magnets to increase the interaction rate or luminosity.[32]

The entire procedure to establish colliding beams was a very complicated one. The whole process started when 120 GeV protons from the Main Ring struck a copper target, producing 8 GeV antiprotons. The \bar{p} 's were then focussed by a lithium lens and injected into the Debuncher ring. Radio-frequency (rf) bunch rotation was used to reduce the momentum spread of the \bar{p} 's. Stochastic cooling was also used to reduce the transverse emittance of the \bar{p} 's in the 3 seconds prior to the next \bar{p} production cycle. At the end of the 3 seconds, the partially cooled \bar{p} 's were transferred to the Accumulator ring where they were rf bunched and moved into the antiproton accumulation stack. Some six different cooling systems were used to reduce the antiproton transverse emittance. The antiproton accumulation (“stacking”) operation continued until a suitable stack of \bar{p} 's was achieved to attempt a “shot”, that is, to inject antiprotons and protons into the Tevatron to produce collisions. The \bar{p} production target and the Debuncher and Accumulator rings were referred to as the “ \bar{p} source” in Figure 2.1.

Upon attaining sufficient antiprotons, what occurred next can best be called “accelerator gymnastics” in which the end result was colliding protons and antiprotons at high luminosity. The antiprotons were extracted from the Accu-

mulator ring and injected into the Main Ring, which was then ramped to 150 GeV. Next the Main Ring rf was phase-locked to the Tevatron rf and a small frequency offset was introduced into the Main Ring rf which caused the antiproton bunches to move so that they would be in the correct position when transfer was made into the Tevatron. This last operation was known as "transfer cogging". The antiprotons were then injected into the Tevatron at 150 GeV. The 3 proton bunches were placed in the Tevatron through a similar process. With 6 bunches in the Tevatron (3 proton and 3 antiproton), a small frequency offset was introduced into the proton rf cavities relative to the antiproton rf cavities, which caused the protons to move in order to establish collisions at the interaction regions around the ring. This was known as "collision point cogging". The Tevatron was then ramped to 900 GeV. With a stable store at 900 GeV, the low-beta quadrupole magnets at the B0 interaction region (the location of the CDF detector) were turned on to focus the particle bunches to obtain more intense collisions and achieve a higher $\bar{p}p$ interaction rate. Data-taking then began and the Main Ring started its production cycle operation to produce antiprotons for the next shot.[33]

For the 1987 run, it was the intensity of the antiprotons which was the limitation on the highest luminosity attainable. The protons were readily available from hydrogen gas and the antiprotons were produced as secondaries from collisions of protons with a fixed target. The limitation on the number of antiprotons available for collisions came from the antiproton production cross-section, the

collection efficiency of antiprotons produced from the target, and the transfer efficiency from the Accumulator ring to collisions at low-beta. But it was of course the fact that the antiproton is the proton's antiparticle (same mass and opposite charge) that allowed one to produce collisions with only one accelerating ring and achieve a very high center-of-mass energy.

2.2 Overview of CDF

The Collider Detector at Fermilab (CDF) is a 5000-ton magnetic detector built to study 2 TeV $\bar{p}p$ collisions at the Fermilab Tevatron collider.[34] Figure 2.2 shows a perspective view and Figure 2.3 a side view of the CDF detector. Event analysis is based on charged particle tracking, magnetic momentum analysis, and energy deposition. The calorimetry, which had polar angle coverage from 2° to 178° and full azimuthal coverage for the 1987 run, consisted of electromagnetic shower counters and hadron calorimeters and was segmented into approximately 5000 projective "towers" or solid angle elements. Several tracking systems were used to cover the calorimeter acceptance and extend charged particle tracking down to 2 milliradians from the beam direction. Charged particle momenta in the central pseudorapidity region ($|\eta| < 1.0$) were analyzed in a 1.5 tesla solenoidal magnetic field, generated by a superconducting coil which was 3 m in diameter and 5 m in length. The central tracking chamber measured particle momentum with an approximate resolution $\Delta p_T/p_T^2 = 2 \times 10^{-3} \text{ (GeV/c)}^{-1}$ in

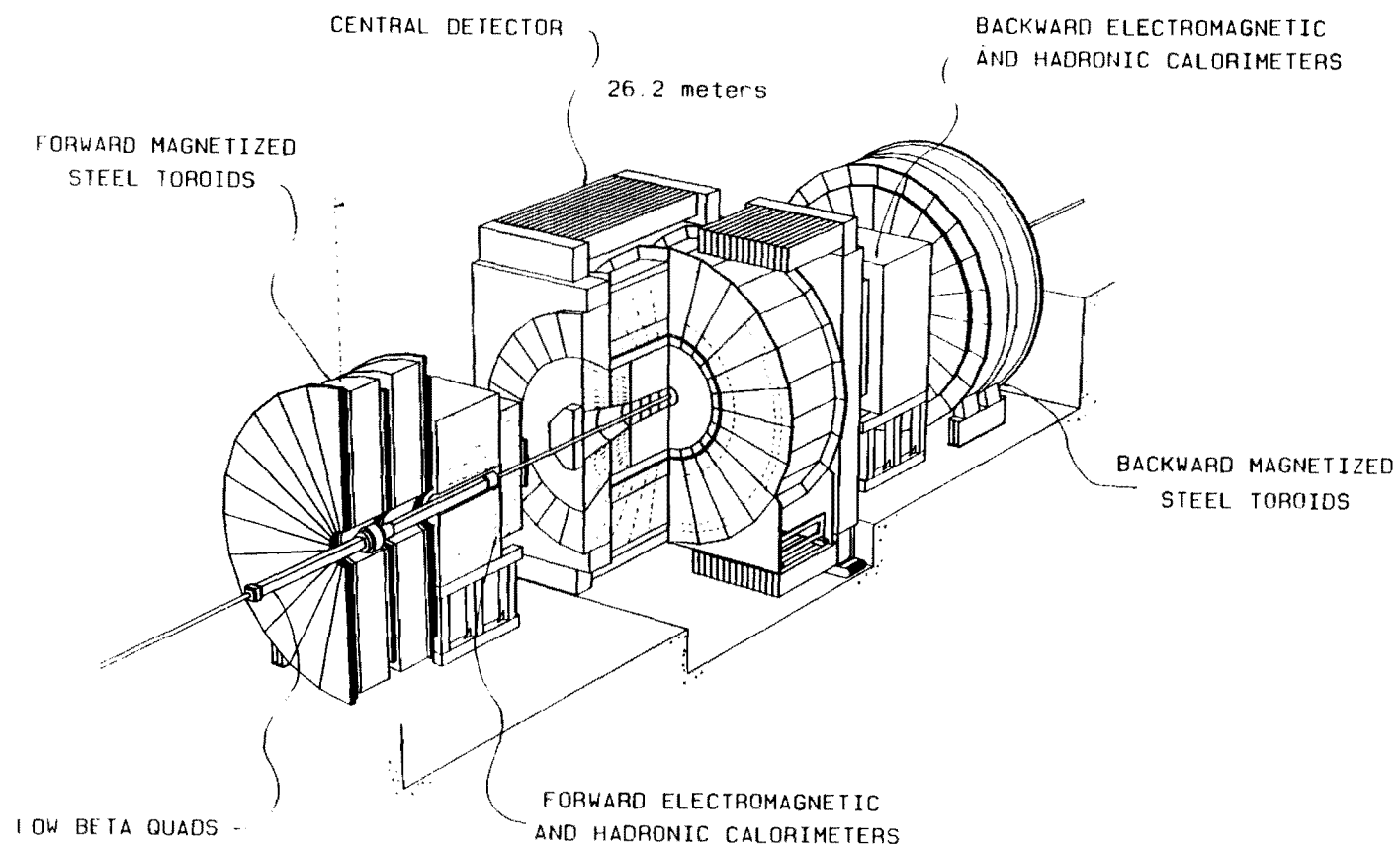


Figure 2.2: Perspective view of the CDF detector.

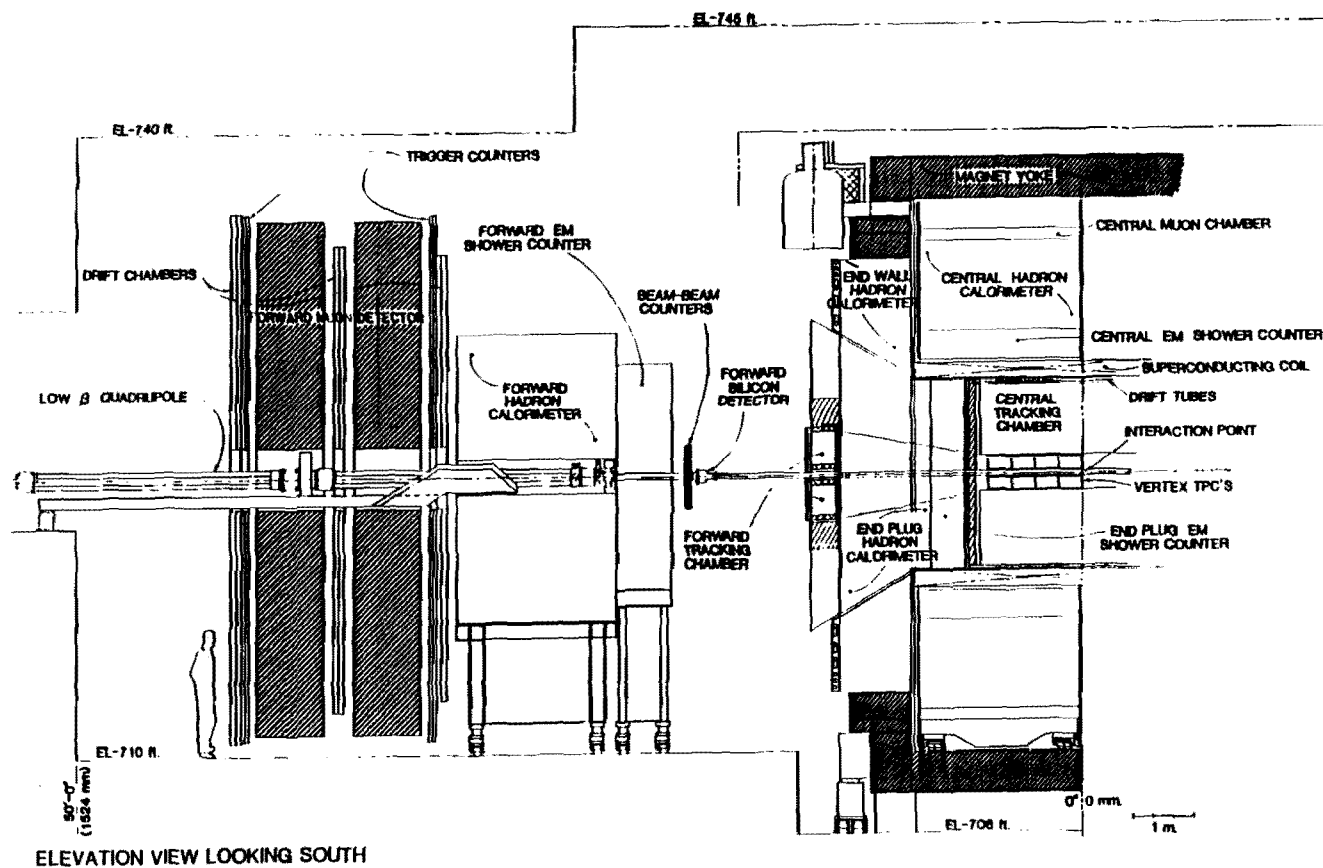


Figure 2.3: Side view of the CDF detector.

the region $40^\circ < \theta < 140^\circ$ and $\Delta p_T/p_T^2 = 4 \times 10^{-3}$ for $21^\circ < \theta < 40^\circ$ and $140^\circ < \theta < 159^\circ$. Muon coverage was provided by drift chambers in the region $56^\circ < \theta < 124^\circ$ and by two large forward toroid systems in the range $3^\circ < \theta < 16^\circ$ and $164^\circ < \theta < 177^\circ$. In addition, isolated high p_T muons have been identified in the intermediate angular region by a comparison of the tracking and calorimeter information in some cases. A custom front-end electronics system [35] followed by a large FASTBUS data acquisition network [36] provided the readout of the approximately 100,000 detector channels. A fast Level 1 trigger was used to pre-analyze the calorimetry and tracking information [37]. In the near future, a Level 2 trigger system will allow more sophisticated trigger options and a Level 3 system of online processors will do parallel processing of events [38].

In the rest of this chapter we will describe the CDF detector components which played a specific role in forward muon identification and then we will examine the forward muon system itself in great detail.

2.2.1 Vertex Time Projection Chamber

The vertex time projection chamber (VTPC) system consisted of eight double time projection chambers surrounding the beam pipe and mounted end-to-end along the beam direction. A picture of the VTPC is shown in Figure 2.4. The VTPC contributed both an event interaction vertex position and stand-alone tracking information. The chambers covered about seven units of pseudorapidity ($-3.5 < \eta < 3.5$) and were capable of handling the 30-35 charged particle tracks

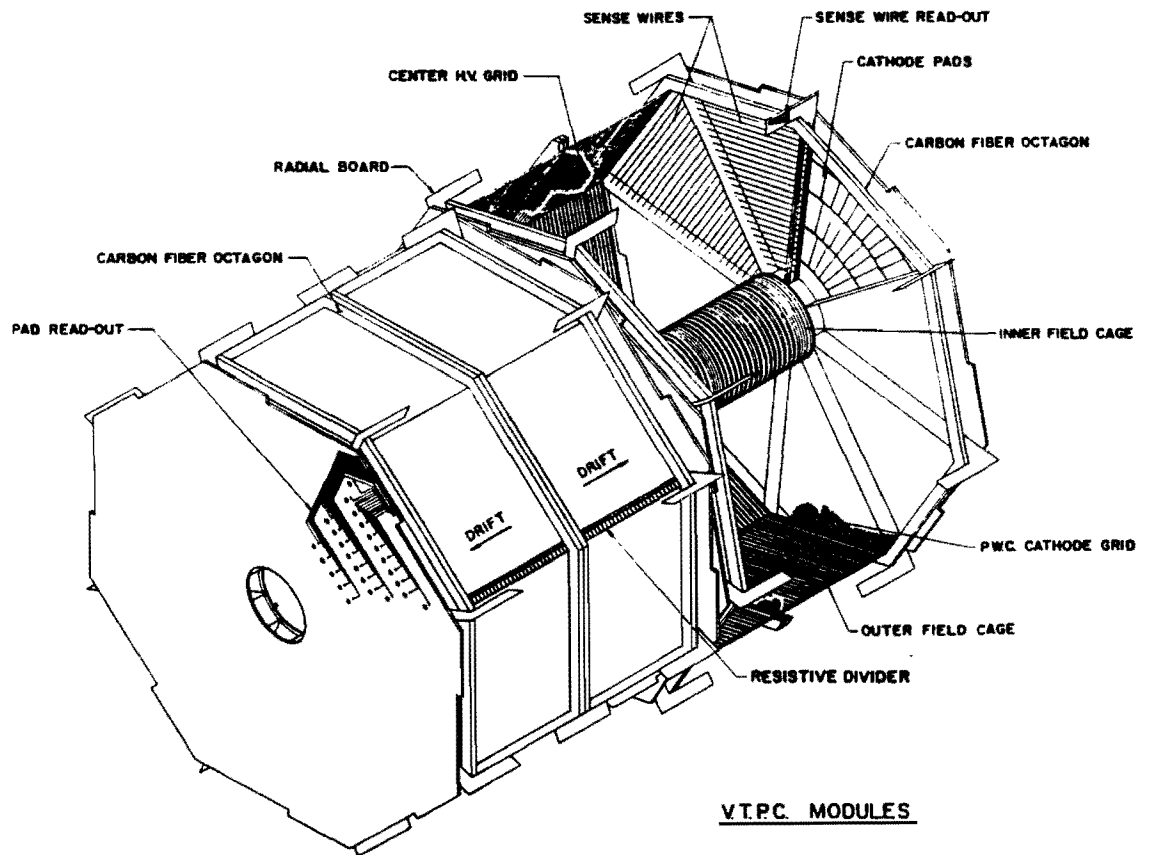


Figure 2.4: Two of the eight vertex time projection chamber (VTPC) modules.

produced by typical $\bar{p}p$ collisions at a center-of-mass energy of 1.8 TeV. The acceptance of the VTPC covered quite well the forward muon region.

Each of the eight octagonal VTPC modules had a central high voltage grid that divided it into two 15.25 cm long drift regions. It is eventually planned to operate the Tevatron in six bunch mode with $3.5 \mu\text{s}$ between crossings and the 15.25 cm drift length was chosen so that the maximum drift time would be less than $3.5 \mu\text{s}$. The ionization electrons in the VTPC drift away from the center grid until they pass through a cathode grid and enter one of the two proportional chamber endcaps. Each endcap was divided into octants, with 24 sense wires and 24 cathode pads in each octant. The arrival times of the electrons at the sense wires were read out using multi-hit time-to-digital converters (TDCs) and produced a picture of the event in the r - z plane (see Appendix A for the CDF coordinate system). In addition, the sense wires and pads in some endcaps were instrumented with an analog pulse height readout using flash analog-to-digital converters (FADCs) so that dE/dx and ϕ information was available for particles produced at angles between 5° and 25° with respect to each beam axis. Adjacent modules had a relative rotation angle of $\phi = 11.3^\circ$ about the beam axis. For tracks passing through at least two modules, this eliminated inefficiencies near octant boundaries and provided ϕ information from small angle stereo.[39] Figure 2.5 shows a typical $\bar{p}p$ collision event in the VTPC.

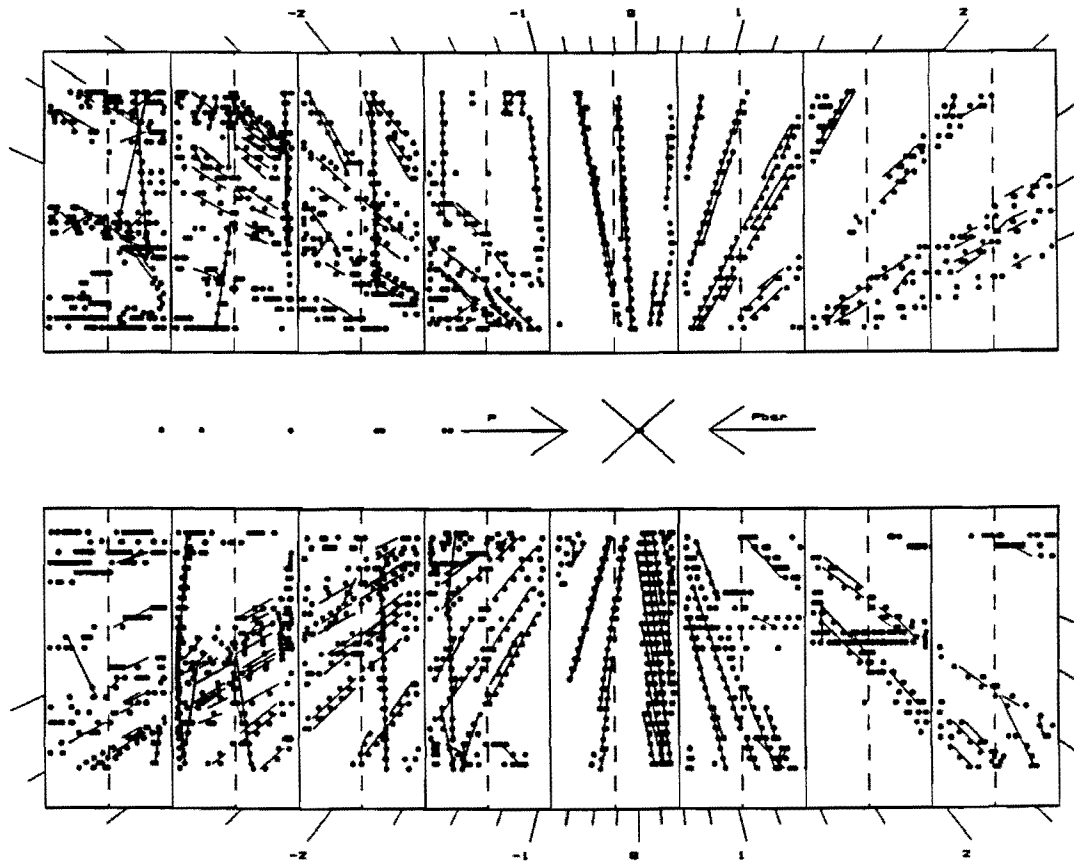


Figure 2.5: A 1.8 TeV $\bar{p}p$ collision as observed by the VTPC.

2.2.2 Forward Tracking Chambers

The forward tracking chambers (FTC) were radial wire drift chambers built to cover the forward/backward regions between 2° and 10° from the beamline. The chambers contained planes of anode and field shaping wires that alternated with planes of cathode strips (Figure 2.6). The wire planes and cathode planes of each 5° cell (72 total) were slanted at 2° relative to the beam axis so that left-right ambiguities could be resolved by demanding that tracks point back to the vertex. The anode plane had 21 active $50\ \mu\text{m}$ diameter sense wires and 26 field shaping wires $150\ \mu\text{m}$ in diameter that were strung approximately along the radial direction (normal to the beam axis). There were a total of 2736 active wires in the forward and backward chambers.

The drift spacing in the FTC varied from a minimum of 5.4 mm at a 12.5 cm radius to a maximum of 28.3 mm at a radius of 72.5 cm. Drift time information from the sense wires was read out using multi-hit TDCs. Two of the sense wires were instrumented with 30 MHz FADCs for current division measurement so that an r - ϕ - z position was determined for each track. The FTC thus provided tracking information for forward muons passing below 10° from the beamline.[40]

2.2.3 Endplug Electromagnetic Calorimeter

It was judged that a scintillator system like that used in the central region of CDF was not appropriate in the endplug and forward regions. Any type of light guides used to lead the scintillation light to the outside of the detector

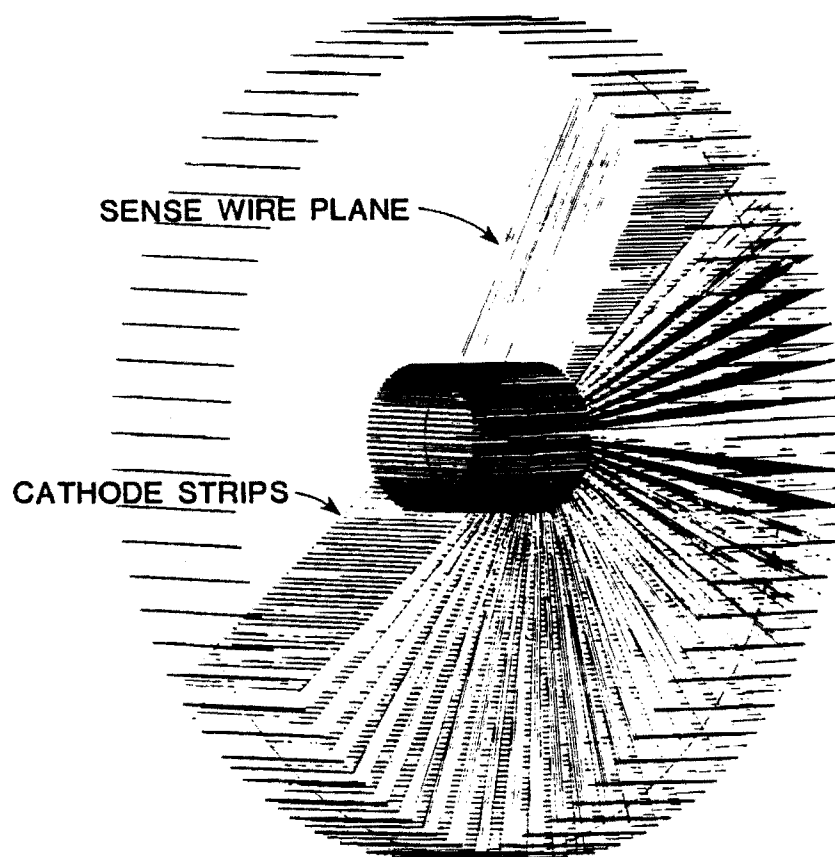


Figure 2.6: Illustration showing the radial wire layout for one of the two forward tracking chambers (FTC).

inevitably introduced a substantial dead/hot region if one tried to make a fine lateral segmentation and/or more than one longitudinal segment. In this angular region, it was also difficult to make a reasonably well-defined projective tower by using scintillators. In addition, radiation damage to the scintillator for angles near the beamline was a major concern. All of these considerations pointed towards a proportional chamber system. If the signals were read out from cathode pads and strips, patterns of any shape and size could be implemented virtually without any dead spaces. The longitudinal segmentation was also simply a matter of cabling.

The endplug electromagnetic calorimeter (PEM) covered both ends of the solenoidal magnet in the CDF central detector, leaving a 10° conical hole around the beamline on each end. Each of the two calorimeter modules occupied a cylindrical volume with an outer diameter of 280 cm and a length of 53 cm between 173 cm and 226 cm along the beam axis (see Figure 2.3). The polar angle coverage was from 10° to 36° , which corresponds to the pseudorapidity interval $1.1 < |\eta| < 2.4$. Thus, a forward muon between the angles of 10° and 16° would have penetrated and deposited energy in the endplug region.

The patterns of the pads and the strips in the PEM were defined by the coordinates η , ϕ , and z in order to form well-segmented projective towers. Longitudinally, each pad tower was divided into three segments. In terms of radiation lengths, the first and the last segments were relatively thin and the middle one was much longer in order to contain most of the electromagnetic shower energy.[41]

2.2.4 Endplug Hadron Calorimeter

The endplug hadron calorimeter (PHA) was located directly behind the endplug electromagnetic calorimeter on the central detector. The PHA was a gas sampling calorimeter consisting of 20 sampling layers, each separated by a 5 cm thick steel plate. The average number of interaction lengths was 6.5. The samples were made with gas proportional chambers with cathode pad readout. The projective tower segmentation followed that of the endplug electromagnetic calorimeter. For each hadronic tower, the longitudinal samples were ganged into a single depth segment. In addition, the gas proportional chambers were divided into 30° sectors in azimuth. All anode wires in a single chamber were ganged and read out to give longitudinal information from each of the 20 planes in a 30° sector.[42]

2.2.5 Forward Electromagnetic Calorimeter

Each of the two forward electromagnetic calorimeters (FEM) consisted of 30 sampling layers of proportional tube chambers with cathode pad readout. The layers were separated by lead sheets for a total calorimeter thickness of 25.5 radiation lengths. Each proportional tube chamber was constructed using a novel technique in which the insulating side of the cathode pad board was bonded to the proportional tube walls using resistive epoxy.

The FEM was segmented into bins of constant azimuthal angle and pseudo-rapidity to match the overall granularity of CDF. The distance from the collision point was chosen such that the smallest bins were matched to the average size

of an electromagnetic shower. The gas tubes were run at a nominal high voltage of 1900 volts, corresponding to the middle of the proportional region. Each calorimeter was ~ 3 m on a side and 1 m deep and weighed about 18 metric tons.

Each cathode pad in a layer subtended 0.1 units of pseudorapidity η and 5° in azimuthal angle ϕ . The pads were ganged longitudinally into towers with two depth segmentations, both of which were 15 layers thick. The cathode pads were scaled in size at every other layer so that the resultant towers projected back to the nominal beam-beam interaction point. There were 1440 pads per layer, resulting in a total of 5760 tower segments for the two ends. The anode wires were strung vertically and ganged together in five groups per chamber. These groups were read out independently for each layer, resulting in an additional 150 signals per quadrant. The anode information was installed primarily for diagnostic purposes but also provided a longitudinal profile of the energy deposition for each sector.[43]

2.2.6 Forward Hadron Calorimeter

The forward/backward hadron calorimeter of CDF was designed to detect and measure the energies and positions of hadrons in the pseudorapidity interval $2.2 \leq |\eta| \leq 4.2$ and with full azimuthal coverage around the beam axis. Hence, a forward muon between the angles of 3° and 10° would deposit energy in the forward calorimeters.

Each of the forward and backward hadron calorimeters were segmented into

four independent sections which, when stacked about the accelerator beam pipe, provided the necessary full azimuthal coverage. These calorimeter segments were each composed of alternating layers of 5 cm thick steel plates and ionization chambers for a total of 27 layers each. The entire assembly contained nearly 400 tons of steel plates and 216 ionization chambers.

The cathode surface of each of the ionization chambers was segmented into 20 bins in pseudorapidity ($\Delta\eta = 0.1$) and 18 bins in azimuth ($\Delta\phi = 5^\circ$). Cathode pads at fixed pseudorapidity and azimuth on each of the 27 ionization chambers formed a projective tower whose apex was the interaction point at a distance of 711 cm from the calorimeter face. The signals from each chamber pad at fixed η and ϕ were summed together to produce the total energy signal for a given projective tower. During the 1987 run, each calorimeter was instrumented with half of its normal complement of chambers.[44]

2.2.7 Beam-Beam Counters

The beam-beam counters (BBC) consisted of two planes of 16 time-of-flight scintillation counters, one on the east and one on the west side of the interaction region.[45] The counters were one inch thick and were arranged in four quadrants of four counters each. The dimensions of the four counters in each quadrant were such that each counter covered an approximately equal pseudorapidity interval of $\Delta\eta = 0.7$. The BBC system as a whole covered the region $3.2 < |\eta| < 5.9$. The smallest, innermost counter sat directly on the Tevatron beam pipe and the next

three counters were placed touching their nearest neighbors (Figure 2.7). The two planes of counters were equidistant from the center of the CDF detector and had a separation of 1182 cm.

Signals from each beam-beam counter were latched at two separate times. The first latch gate was timed for incoming beam halo particles, while the second latch gate coincided with the time at which outgoing particles from a beam-beam interaction would penetrate the counters. This information was recorded by the data acquisition system for each trigger. In addition, fast-out signals from the in-time latch were used to form an E-W coincidence signal. This signal detected the occurrence of a beam-beam collision and was used as the CDF “minimum-bias” trigger and luminosity monitor during the 1987 run. It was also combined with other detector-specific Level 1 signals to form different Level 1 triggers.

2.3 The CDF Forward Muon System

In investigating the dynamics of high-energy particle interactions, the identification of final-state muons is particularly important because they couple directly to the intermediate vector bosons which mediate the electroweak force. In addition, muons are a characteristic signature of the weak decays of heavy quarks. During the 1987 run, the CDF forward muon (FMU) system measured muon position and momentum for polar angles between 3° and 16° (the forward region) and between 164° and 177° (the backward region).[46]

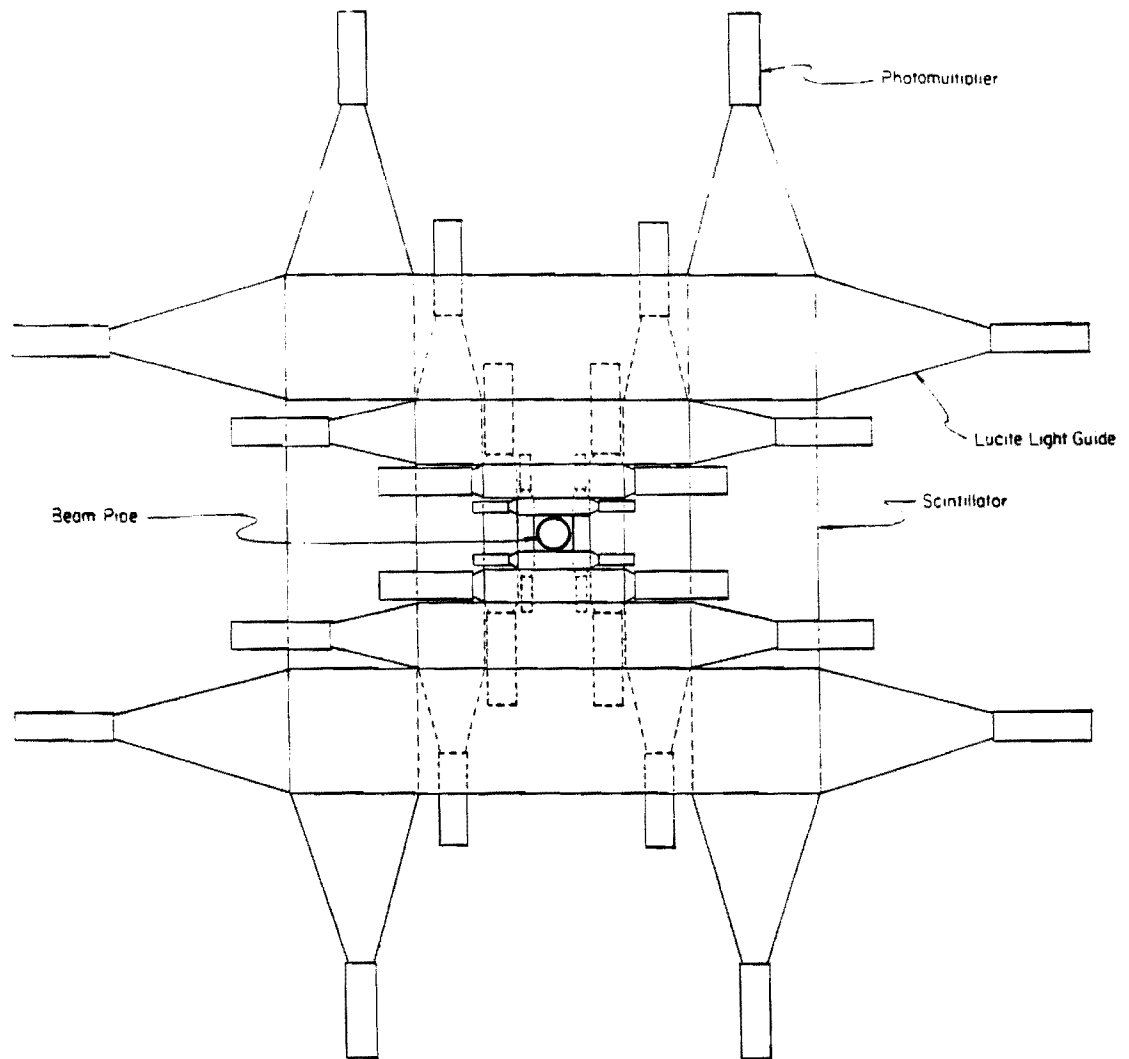


Figure 2.7: One plane of the beam-beam counter (BBC) system.

2.3.1 General Features

The CDF forward muon system consisted of a pair of magnetized iron toroids instrumented with three planes of drift chambers and two planes of scintillation trigger counters in each of the forward/backward regions (Figure 2.3).[47] Figure 2.8 shows the CDF forward region detectors during preparation for colliding beams. The front plane of chambers is seen just behind the forward calorimeters and the beam-beam counters. A given plane of chambers or counters formed a 24-sided figure with each wedge-shaped detector subtending an angle of 15° in azimuth as shown in Figure 2.9. Each wedge in a plane was staggered relative to its neighbors to form overlap regions which eliminated detector dead spots at the wedge boundaries. The drift chambers came in three different sizes depending on their distance from the beam crossing and were supported by a "spider-web" type structure hung from the top of the toroids. The counters were supported by mounts welded to the face of the magnets.

2.3.2 The Toroids

The forward muon analyzing magnets were 7.6 m o.d. x 1.0 m i.d. x 1.0 m wide toroids. Two of the 395 ton cast steel magnets were located in each of the forward and backward detector regions. Each toroid had 4 rectangular coils consisting of 28 turns of copper conductor to provide an azimuthal field in the steel. The toroids were built from 12 steel blocks ranging from 22 to 40 tons in weight. The blocks were constructed from 25 cm thick vertical slabs of continuous cast steel

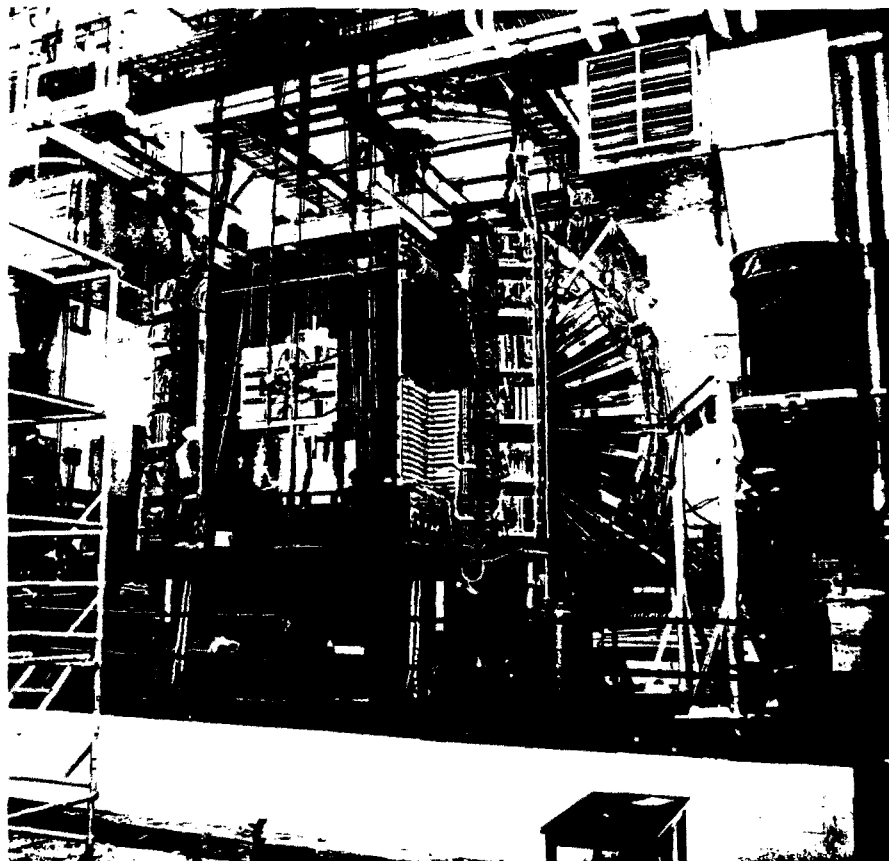


Figure 2.8: View of the CDF forward detectors.

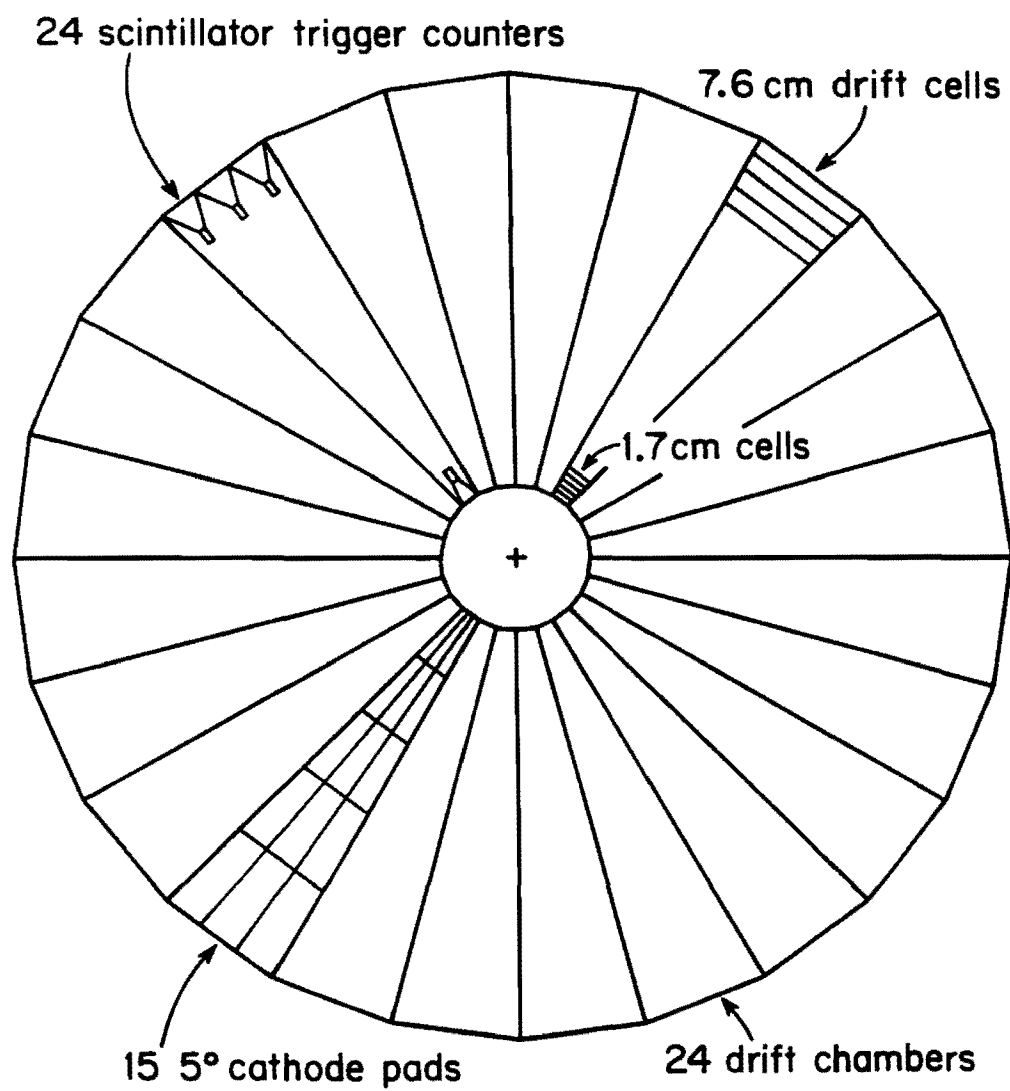


Figure 2.9: Elements of the forward muon detector planes.

and machined on the mating surfaces. The magnets were made in two halves which separated at the vertical centerline with a 3 mm gap at the top allowed for magnetic field measurements. At a current of 1000 amps through the coils a field of 1.8 tesla was produced at a radius of 2.1 m. The field varied from 2.0 tesla at the inner radius to 1.6 tesla at the outer radius.[48]

The magnetic field measurements were made with a Hall probe and with a fixed area loop. The Hall probe was mounted on a printed circuit board (50 in x 2 in x 1/16 in) to allow measurements to be made anywhere inside the 3 mm vertical gap between toroid halves. The probe itself was calibrated against an NMR probe at the Fermilab Magnet Test Facility. The fixed area loop was constructed by stringing two parallel thin steel wires 3.993 inches apart and gluing them on a 50 in x 5 in x 1/16 piece of G10 material. The charge integrating circuit used a precision 1 microfarad capacitor and a trimmed 1 megaohm resistor so that the output voltage in volts upon inserting the loop into the field was equal to the flux in MKS units or to 1/10 of the field integral in tesla-meters. Figure 2.10 shows an approximately 5% magnetic field variation among the four toroids. As viewed from the beam collision point, the magnetic field direction in the toroids was counterclockwise. Positively charged muons were therefore bent away from the beamline (defocussed) and negative muons were bent towards the beamline (focussed).

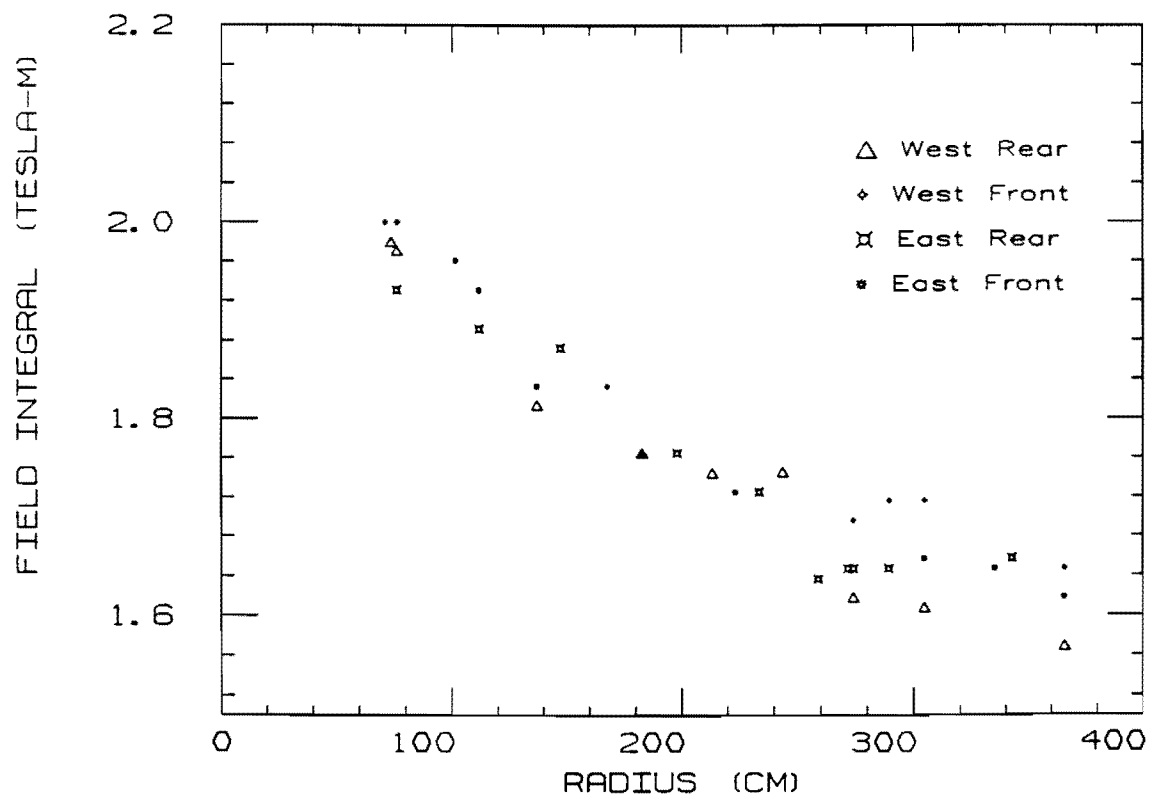


Figure 2.10: Toroid magnetic field measurements.

2.3.3 The Drift Chambers

The drift field in the FMU drift chambers was shaped by an equilibrium distribution of charges (positive ions) on the inside surfaces of the insulating chamber walls.[49] The time needed to establish the equilibrium charge distribution depended critically on the background radiation level. For a background source consisting of cosmic rays alone, several hours were needed to establish stable gain conditions inside the chamber cell. Typically, however, the Main Ring accelerator was operating to produce antiprotons and the radiation levels in the collision hall were sufficient to obtain efficient chamber operation in less than an hour.

Each chamber was composed of two planes of drift cells (Figure 2.11). The “coordinate” plane was closest to the beam crossing point and consisted of 56 cells. The “ambiguity” plane consisted of 40 cells staggered relative to the coordinate cells in order to resolve the left-right ambiguity of a particle track. There was one ambiguity cell for every two coordinate cells for the first 32 coordinate wires and one (staggered) ambiguity cell for every coordinate cell for the remaining 24 coordinate wires. Each drift cell contained a 63 micron diameter stainless steel anode wire which was strung along a chord of the wedge to provide a polar angle measurement of a passing muon. The wire locations in each chamber were measured on an optical table with a microscope. Table 2.1 gives the radial distance from the beamline of the coordinate (0-55) and ambiguity (56-95) wires in a front plane chamber. The two sides of a chamber shared a common copper

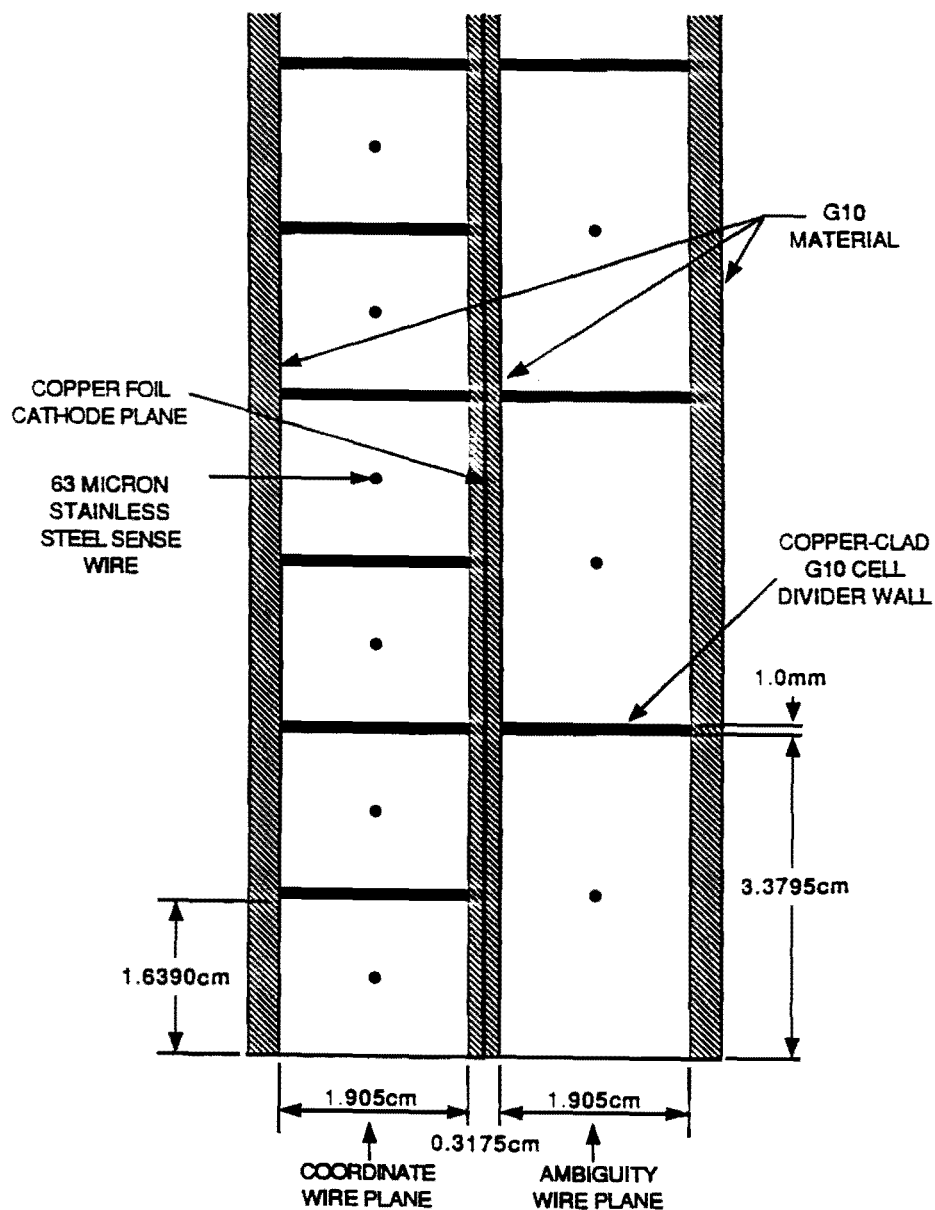


Figure 2.11: Schematic of the chamber cell geometry and materials. The dimensions given are that for the inner radius cells of a front plane chamber.

Wire #	Wire Loc.(cm)	Wire #	Wire Loc.(cm)	Wire #	Wire Loc.(cm)
0	49.8195	32	135.5735	64	83.6257
1	51.5601	33	140.3071	65	89.3664
2	53.3006	34	145.0406	66	95.1071
3	55.0412	35	149.7741	67	100.8479
4	56.7818	36	154.5077	68	107.4043
5	58.5223	37	159.2412	69	114.7764
6	60.2629	38	163.9747	70	122.1486
7	62.0035	39	168.7083	71	129.4527
8	63.9914	40	174.1144	72	136.6889
9	66.2265	41	180.1931	73	142.6738
10	68.4617	42	186.2718	74	147.4074
11	70.6969	43	192.3505	75	152.1409
12	72.9321	44	198.4292	76	156.8744
13	75.1673	45	204.5078	77	161.6080
14	77.4025	46	210.5865	78	166.3415
15	79.6377	47	216.6652	79	171.4113
16	82.1905	48	223.6076	80	177.1537
17	85.0608	49	231.4137	81	183.2324
18	87.9312	50	239.2198	82	189.3111
19	90.8016	51	247.0259	83	195.3898
20	93.6720	52	254.8320	84	201.4685
21	96.5423	53	262.6381	85	207.5472
22	99.4127	54	270.4442	86	213.6259
23	102.2831	55	278.2502	87	220.1364
24	105.5613	56	50.6898	88	227.5107
25	109.2474	57	54.1709	89	235.3168
26	112.9334	58	57.6520	90	243.1228
27	116.6195	59	61.1332	91	250.9289
28	120.3055	60	65.1089	92	258.7350
29	123.9916	61	69.5793	93	266.5411
30	127.6777	62	74.0497	94	274.3472
31	131.3637	63	78.5201	95	280.2018

Table 2.1: Radial distance from the beamline of sense wires in a front plane chamber.

foil cathode plane which was divided into 15 cathode pads. Each pad covered a region which was 5° in azimuth by $\sim 3^\circ$ in polar angle.

The chamber cells were graded (size proportional to polar angle) and projective. Each cell subtended a constant pseudorapidity bite of ~ 0.03 units. This configuration resulted in a roughly constant cell occupancy and provided for the simple high transverse momentum trigger described below. In actual practice, chamber cell sizes were averaged in groups of 8 yielding 7 different coordinate cell sizes and 5 different ambiguity sizes. The variation in the sense wire voltage was between 3.0 to 6.0 kilovolts and the maximum drift distance was ~ 5.0 cm in the largest rear plane cells. The time-to-distance relation in a 50/50 Argon-Ethane mixture was 193. nsec/cm and a position resolution of 130 microns has been achieved with a single prototype drift chamber cell in a test beam.[50]

The signal from each chamber cell was sent to a pre-amplifier circuit which was mounted on the chamber. After a $\times 40$ amplification, the signal was sent to an amplifier/discriminator board located on the "spider-web" supporting structure. A single channel of the amplifier/discriminator board actually received the inputs from cells at the same polar angle for three adjacent chambers (an octant of chambers). This provided a factor of three savings in electronics while the azimuthal resolution was reduced to 45° . The resolution was however restored to 15° by the scintillation counters in time for the trigger and improved to 5° by the cathode pads at readout time. The ECL (Emitter-Coupled Logic) pulse from the amplifier/discriminator board was then sent to a time-to-digital converter (TDC)

located ~ 75 m away in the counting room.

A pulse line, capacitively coupled to the ends of the sense wires opposite to the pre-amplifier, was placed on each chamber to test the chamber electronics. In addition, four wedges per plane contained ^{55}Fe sources (one for each cell size) and special readout electronics to monitor gain drifts.

2.3.4 The Scintillation Counters

The forward muon counters consisted of 13 mm thick 10% Napthalene-doped acrylic scintillator pieces instrumented with light pipes and photomultiplier tubes. Each wedge was 3.3 m long \times 1.0 m \times 14 cm at the large and small ends respectively. Three Amperex 2202B phototubes were coupled to the large end and one to the small end through a clear acrylic light pipe/180° bend combination. The use of the 180° bend allowed the light pipe/phototube/phototube shield package to rest on the scintillator surface which in turn satisfied space and mechanical constraints. Two thin high permeability μ -metal layers and a soft iron 1 cm wall cylinder surrounded each phototube to provide shielding against stray magnetic fields. The entire scintillator assembly was placed in a protective sheet metal box. The detection efficiency of the counters was measured to be $> 99.5\%$ over their entire surface.

A Schmitt-trigger circuit was placed in the phototube base of the forward muon counters to provide an ECL pulse for each anode pulse exceeding the 10 millivolt threshold. The signals from each of the four phototubes making up a

trigger counter were then sent to a logical "OR" circuit located inside the protective metal box. The output from this circuit was latched at the appropriate time to determine the presence of an in-time (beam crossing) or out-of-time (beam-halo) hit. The beam-halo window occurs ~ 75 nanoseconds (twice the distance from the rear counter plane to the interaction region) before the beam collision crossing and was useful for vetoing background particles which accompanied the beam but were outside the beam pipe. An "OR" signal of all front and rear plane counter pairs was also available to provide for a fast cosmic ray trigger. This fast signal was used during colliding beam operation as well to establish the Main Ring background radiation veto signal for the 1987 collider run.

In order to monitor the condition of the trigger counters, a light emitting diode (LED) pulsing scheme was implemented. The high voltage for one phototube in each counter was turned on, an LED which was optically coupled to the scintillator was fired and a phototube coincidence sought. This straightforward procedure helped to checkout the electronics and searched for dead phototubes.

2.3.5 Survey and Alignment

As described below, the forward muon trigger was based on vertex-pointing projective tower roads and so it was crucial that the chamber planes each be centered precisely on the beamline. This was done by measuring the (x,y) position of survey markers (tooling balls) attached to the inner radius edge of the chambers (Figure 2.12). These tooling balls were then referenced to precision located dowel

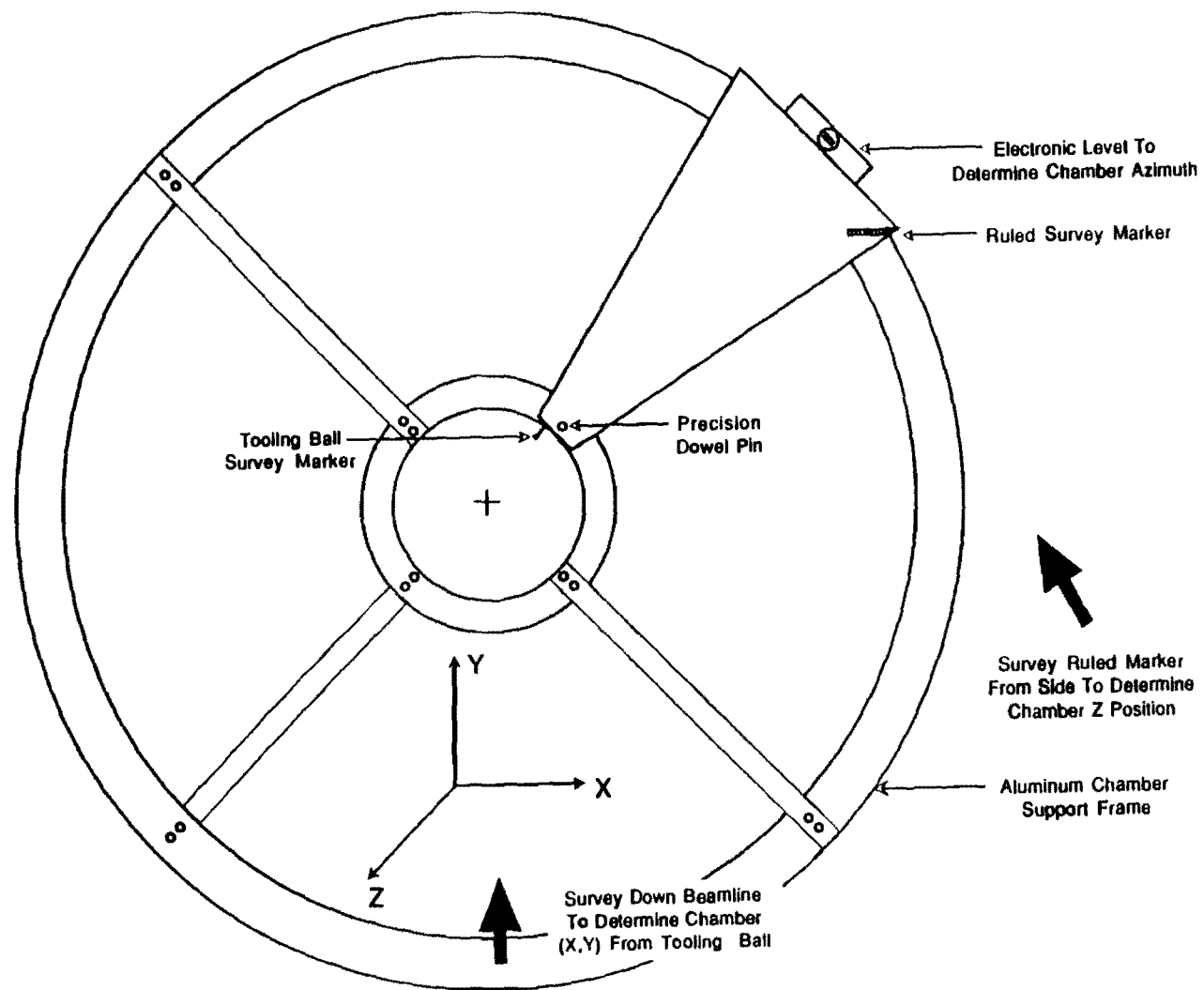


Figure 2.12: Schematic of the FMU survey procedure.

pins on the aluminum frame structure to which the chambers were attached. The required (x,y) location of the survey markers for beamline alignment was calculated in advance and the planes were adjusted accordingly. Figure 2.13 shows the geometry for the (x,y) survey. The inner edge of the drift chamber was designed to be at a radius of 18.000 inches. The tooling ball was located 2.000 inches along this edge and was 2.000 inches in length from that edge to its center. The (x,y) location of the center of the tooling ball in inches was then given by:

$$x = 16.000\cos\phi - 2.000\sin\phi, \quad (2.1)$$

$$y = 16.000\sin\phi + 2.000\cos\phi. \quad (2.2)$$

For example, for the drift chamber with its centerline at $\phi = 52.5^\circ$, the tooling ball center was at (x,y) = (8.153 inches, 13.911 inches). Typically, five tooling balls were surveyed per chamber plane and an overall setting error of 10 mils (10 thousandths of an inch or 254. microns) was achieved. Various fixtures were used to maintain the survey during the course of the run as chambers were taken down for repairs and reinstalled. The post-run survey agreed with the pre-run survey to within 20 mils (508. microns) typically.

In addition to their (x,y) position, the chambers were also precisely located azimuthally about the precision dowel pin and along the beamline (z position). For the azimuthal alignment, an electronic level was used along the outer radius edge of the chamber to set precisely the azimuth of each chamber individually. The z position survey was done using a standard surveyor's transit to sweep a

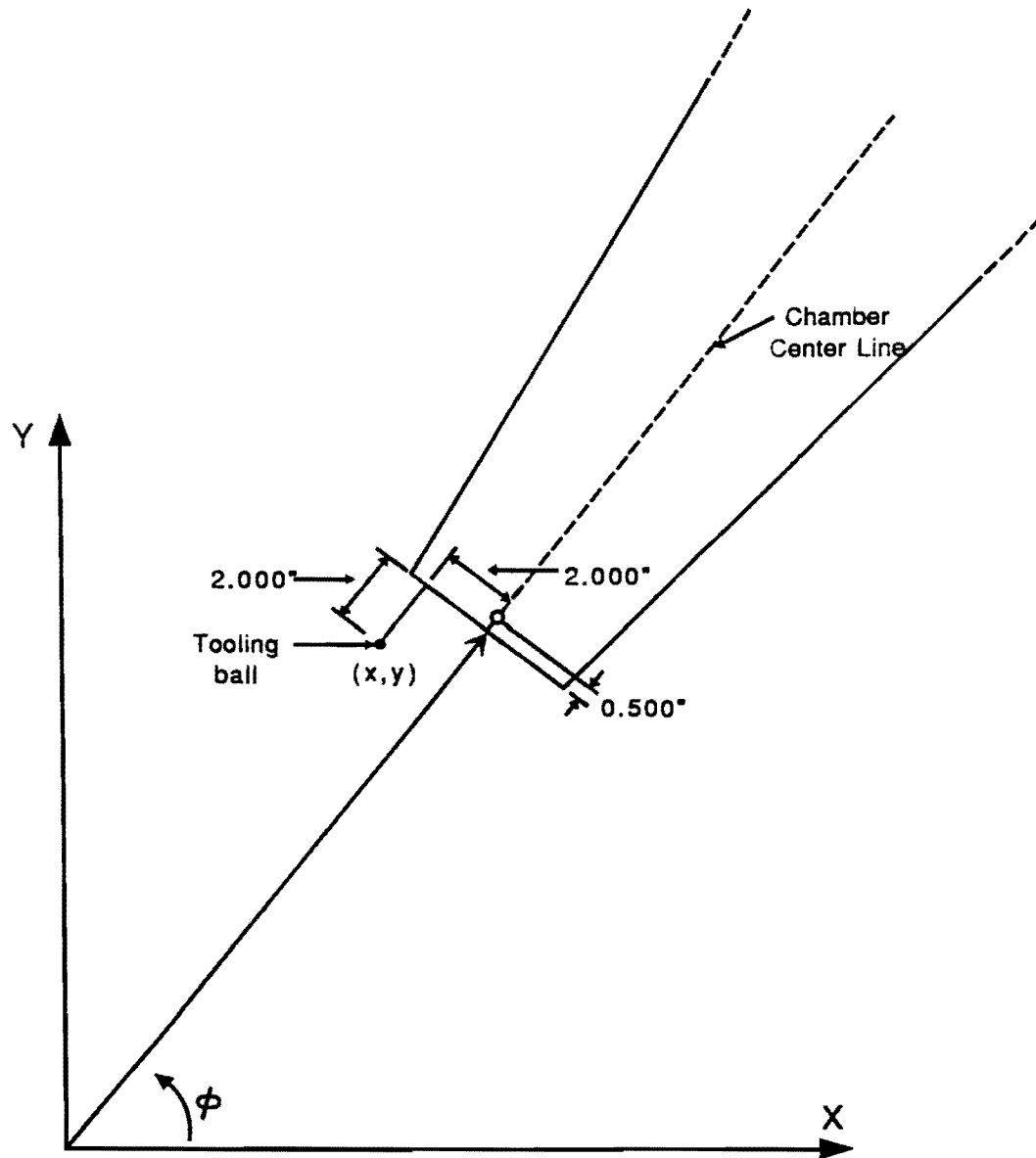


Figure 2.13: Ideal tooling ball (x,y) location.

plane perpendicular to the beamline and locate survey markers placed on each chamber plane. Each plane was then set in its correct position using adjusting fixtures placed at both the inner and outer radii of the chamber plane. Figure 2.14 shows the z position survey method. The center of each chamber plane was designed to be at a location Z_{REF} . A survey transit was setup to view the ruled targets, which were precision machinist rulers, placed on the chambers. Knowing the z position of the survey transit and the location of the rulers relative to Z_{REF} , the offset reading for the rulers, Z_{OFF} , was determined so that the center of the chamber plane was at the correct position Z_{REF} . For example, for $Z_{\text{REF}} = 382.35$ inches (front chamber plane) and a transit position of 378.00 inches, the reading in the outer radius ruler in inches should be:

$$Z_{\text{OFF}} = 382.35 - 378.00 - 1.814 = 2.54, \quad (2.3)$$

or $\sim 2 \frac{9}{16}$ inches in order for the plane to be in the correct position. Ten rulers were usually surveyed and a typical setting error for each plane in the z position was $1/16$ of an inch or 1.6 mm. This was comparable in position radius error, $\Delta r = \Delta z \tan \theta = 459$ microns at $\theta = 16^\circ$, to that obtained for the (x, y) survey.

2.3.6 Momentum Resolution

In this section, we want to make an estimate of the momentum resolution of the forward muon system. To this end, we first start with a calculation of the bend displacement ϵ_{\pm} of a μ^{\pm} after passing through a single toroid and then we extend

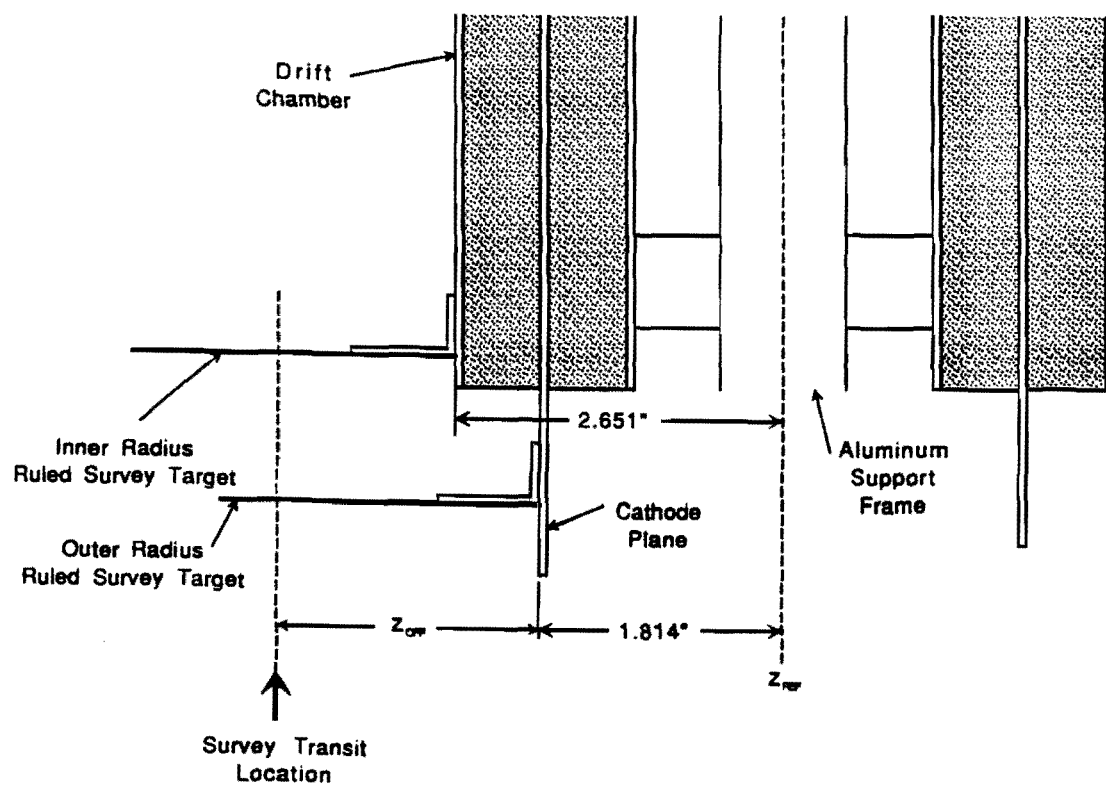


Figure 2.14: The z position survey method.

this calculation to the entire system. Figure 2.15 shows the bend displacement of a positive and a negative muon after passing through the front toroid. The estimate will assume the small angle approximation, $\tan\theta \approx \theta$, which holds in the forward region and that the radius of curvature is much greater than the toroid thickness, $R \gg l$, which is true for a typical muon momentum of 10 GeV/c. From Figure 2.15 we have that the chord of the trajectory for a positive and a negative muon is given by:

$$C_+ = R\theta_+ = \frac{l}{\cos(\alpha + \frac{\theta_+}{2})}, \quad (2.4)$$

$$C_- = R\theta_- = \frac{l}{\cos(\alpha - \frac{\theta_-}{2})}, \quad (2.5)$$

where α is the muon entrance angle and θ_{\pm} are defined in the figure. Using the trigonometric identity $\cos(\alpha + \theta) = \cos\alpha\cos\theta - \sin\alpha\sin\theta$, we obtain the transcendental equations:

$$\frac{l}{R} = \theta_+ (\cos\alpha \cos \frac{\theta_+}{2} - \sin\alpha \sin \frac{\theta_+}{2}), \quad (2.6)$$

$$\frac{l}{R} = \theta_- (\cos\alpha \cos \frac{\theta_-}{2} + \sin\alpha \sin \frac{\theta_-}{2}). \quad (2.7)$$

Substituting in the binomial expansion for sine and cosine and using the fact that $\alpha > \theta_{\pm}/2$ for most muons, we find

$$\frac{l}{R} \approx \theta_+ (1 - \frac{\alpha^2}{2} - \frac{\alpha\theta_+}{2}), \quad (2.8)$$

$$\frac{l}{R} \approx \theta_- (1 - \frac{\alpha^2}{2} + \frac{\alpha\theta_-}{2}). \quad (2.9)$$

And finally solving for θ_{\pm} , we have

$$\theta_+ = \frac{l}{R} (1 + \frac{\alpha^2}{2} + \frac{\alpha l}{2R}), \quad (2.10)$$

$$\theta_- = \frac{l}{R} \left(1 + \frac{\alpha^2}{2} - \frac{\alpha l}{2R} \right). \quad (2.11)$$

Now, referring again to Figure 2.15 and using the law of sines, we obtain the following expressions:

$$\epsilon_+ = \frac{C_+ \sin \theta_+}{2 \cos \frac{\theta_+}{2}} \frac{1}{\sin(\frac{\pi}{2} + \alpha)}, \quad (2.12)$$

$$\epsilon_- = \frac{C_- \sin \theta_-}{2 \cos \frac{\theta_-}{2}} \frac{1}{\sin(\frac{\pi}{2} - \alpha)}, \quad (2.13)$$

where ϵ_{\pm} are the bend displacements after passing through the front toroid for a positive and a negative muon and are defined relative to an infinite momentum muon. Making the small angle approximation and substituting in for C_{\pm} , we find

$$\epsilon_{\pm} \approx \frac{R \theta_{\pm}^2}{2}. \quad (2.14)$$

Using the binomial expansion for θ_{\pm}^2 and keeping only first-order terms, we obtain the final result for the bend displacement of a positive and a negative muon after one toroid:

$$\epsilon_+ = \frac{l^2}{2R} \left(1 + \alpha^2 + \frac{\alpha l}{R} \right), \quad (2.15)$$

$$\epsilon_- = \frac{l^2}{2R} \left(1 + \alpha^2 - \frac{\alpha l}{R} \right). \quad (2.16)$$

We see that there is a charge asymmetry in the bend displacement given by

$$\delta\epsilon = \epsilon_+ - \epsilon_- = \frac{\alpha l^3}{R^2}, \quad (2.17)$$

which is present only at low momentum (small R) and vanishes for normal incidence ($\alpha = 0$). Thus we find, as expected, that due to the finite muon incident angle α , positive muons undergo a larger displacement than negative ones.

We now want to calculate a value for the momentum resolution of the entire forward muon system (two toroids plus air gaps) and we use Figure 2.16 to do this. Remembering that the displacements are relative to an infinite momentum muon and noting that the entrance angle to the second toroid is $\alpha + \theta_+$ for a positive muon and $\alpha - \theta_-$ for a negative muon, we write for the total system bend displacements, $\epsilon_{\pm}^{\text{SYS}}$ (from Figure 2.16):

$$\begin{aligned} \epsilon_{\pm}^{\text{SYS}} = & \frac{l^2}{2R}(1 + \alpha^2 \pm \frac{\alpha l}{R}) + d\theta_{\pm} + l\theta_{\pm} + \\ & \frac{l^2}{2R}(1 + (\alpha \pm \theta_{\pm})^2 \pm \frac{(\alpha \pm \theta_{\pm})l}{R}) + t(\theta'_{\pm} + \theta_{\pm}), \end{aligned} \quad (2.18)$$

where θ_{\pm} are given by Equations 2.10 and 2.11 and for θ'_{\pm} we have

$$\theta'_{\pm} = \frac{l}{R}(1 + \frac{(\alpha \pm \theta_{\pm})^2}{2} \pm \frac{(\alpha \pm \theta_{\pm})l}{2R}). \quad (2.19)$$

Substituting in for θ_{\pm} and θ'_{\pm} and after some algebra, Equation 2.18 becomes

$$\begin{aligned} \epsilon_{\pm}^{\text{SYS}} = & \frac{l^2}{2R}\{4 + \frac{2(d + 2t)}{l} + \alpha^2(3 + \frac{(d + 2t)}{l}) \pm \frac{\alpha}{R}[5l + d + 4t + \alpha^2(l + t)] + \\ & \frac{2l(l + t)}{R^2}[1 + \frac{5}{4}\alpha^2] \pm \frac{3\alpha l^2}{2R^3}[l + t]\}. \end{aligned} \quad (2.20)$$

We see that the expression for the bend displacement charge asymmetry takes the form:

$$\delta\epsilon^{\text{SYS}} = \epsilon_+^{\text{SYS}} - \epsilon_-^{\text{SYS}} = \frac{\alpha l^2}{R^2}[5l + d + 4t + (\alpha^2 + \frac{3}{2}\frac{l^2}{R^2})(l + t)]. \quad (2.21)$$

Using the well-known formula for the momentum of a charged particle in a magnetic field [51]:

$$pcos\lambda = 0.3qBR, \quad (2.22)$$

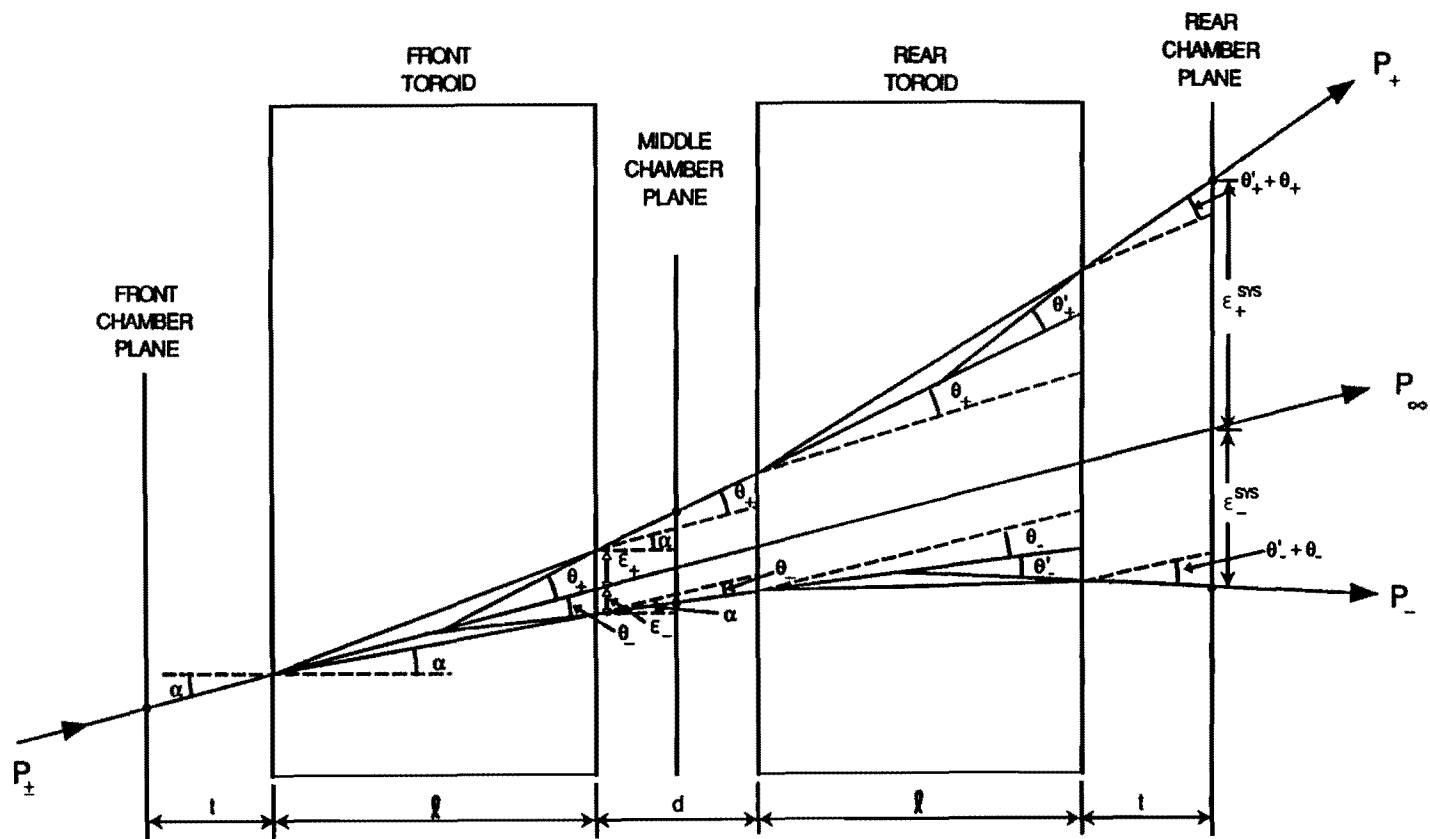


Figure 2.16: Momentum resolution estimation for the forward muon system.

where p is the momentum in GeV/c, λ is the pitch angle ($\cos\lambda \sim 1$ here), B is the magnetic field in tesla and R is the radius of curvature in meters, we can calculate the momentum resolution and bend displacement asymmetry. Keeping only the leading-order $1/R$ terms in Equation 2.20, which removes the charge dependence, we have

$$\epsilon^{\text{sys}} = \frac{0.3qBl^2}{2p} \left\{ 4 + \frac{2(d+2t)}{l} + \alpha^2 \left(3 + \frac{(d+2t)}{l} \right) \right\} \quad (2.23)$$

With $l = 100.$ cm, $d = 52.$ cm, $t = 42.$ cm, $q = 1.0$, $B = 1.8$ tesla and a typical value of α (10°), we find

$$\epsilon^{\text{sys}} = \frac{185.0 \text{ cm}}{p}. \quad (2.24)$$

At a nominal value of 10 GeV/c momentum ($R = 18.5$ m) and $\alpha = 10^\circ$, the bend displacement difference due to the muon charge sign is

$$\delta\epsilon^{\text{sys}} = 0.37 \text{ cm}, \quad (2.25)$$

which is not insignificant. This charge asymmetry will be discussed further in Chapter 3.

The uncertainty in the particle deflection (and hence the momentum resolution) is due almost entirely to multiple scattering up to momenta of 200 GeV/c where survey errors become non-negligible. The mean square plane-projected scattering angle $\langle\Delta\theta^2\rangle$ from the multiple scattering of a charged particle in a material medium is given by the equation [52]:

$$\langle\Delta\theta^2\rangle = \frac{1}{2}\theta_s^2, \quad (2.26)$$

where θ_s^2 is the mean square space scattering angle per unit length and x is the thickness of the material traversed. The value of θ_s^2 is obtained from the expression:

$$\theta_s^2 = \left(\frac{0.021}{\beta p}\right)^2 \frac{1}{X_o}, \quad (2.27)$$

where β and p are the velocity (in units of c) and momentum (in GeV/ c) of the muon and X_o is the average radiation length over the scattered distance. As shown in Figure 2.17, we are considering the displacement of the muon from infinite momentum due to multiple scattering. An infinite momentum muon travels from point A at the front chamber plane to point B at the rear plane whereas a typical muon scatters and arrives at point C with a mean square displacement $\langle \Delta y^2 \rangle$ given by

$$\langle \Delta y^2 \rangle = \frac{1}{6} \theta_s^2 x^3. \quad (2.28)$$

The average radiation length over the path of the muon is larger than that for iron due to the air gaps in front, between, and behind the toroids. With $L = 336$ cm and $X_{Fe} = 1.76$ cm, we calculate X_o :

$$X_o = \frac{336}{200} 1.76 = 2.96 \text{ cm}. \quad (2.29)$$

Substituting this into Equation 2.27 and taking $\beta = 1$, we obtain

$$\theta_s^2 = \frac{1.49 \times 10^{-4}}{p^2} \text{ cm}^{-1}. \quad (2.30)$$

Inserting this into Equation 2.26, setting $x = L$, and taking the square root, we

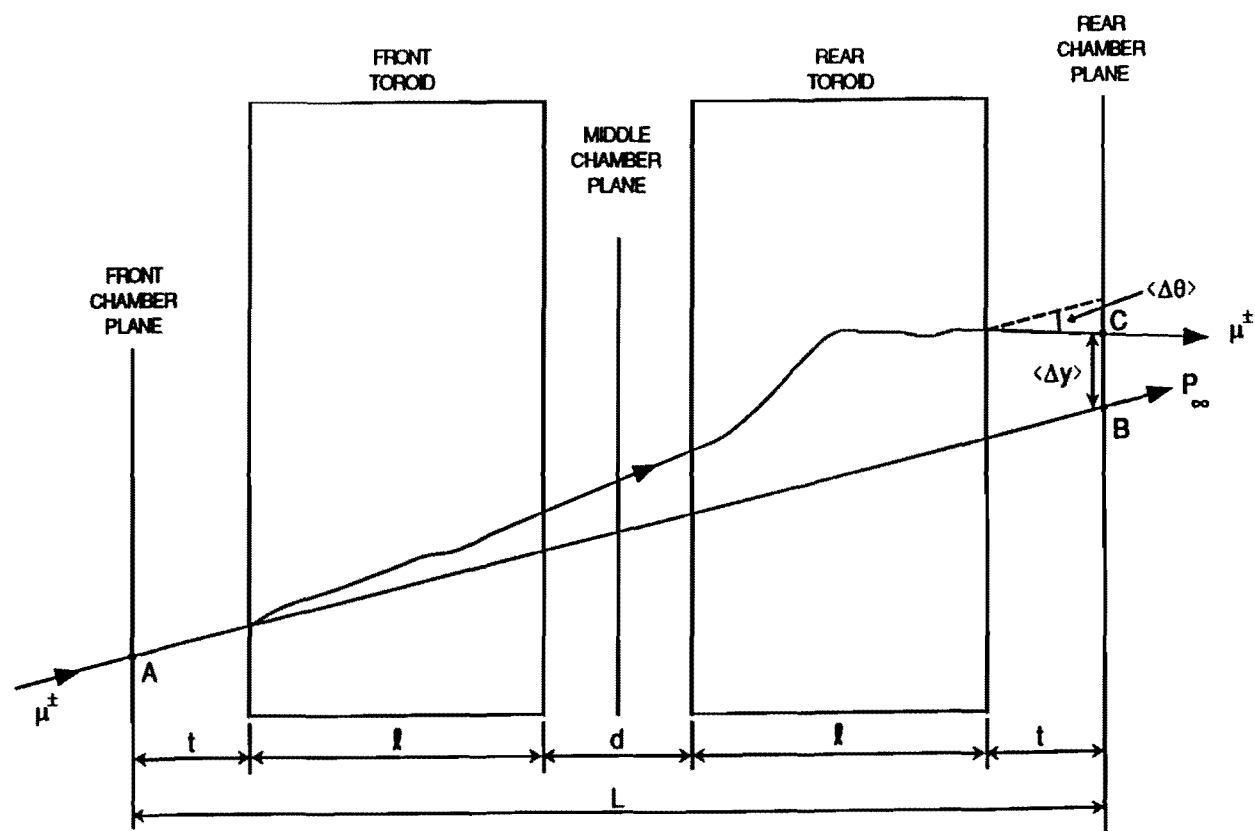


Figure 2.17: Multiple scattering displacement in the forward muon system.

find the mean plane-projected space angle (in radians) to be

$$\langle \Delta\theta \rangle = \frac{0.16}{p}. \quad (2.31)$$

And similarly, the mean displacement $\langle \Delta y \rangle$ over the distance $x = L$ is

$$\langle \Delta y \rangle = \frac{30.7 \text{ cm}}{p}, \quad (2.32)$$

where p is in GeV/c. Using error propagation, it can be shown that $\Delta p/p = \Delta\epsilon/\epsilon$, where $\Delta\epsilon = \langle \Delta y \rangle$ and $\epsilon = \epsilon^{\text{SYS}}$ given in Equation 2.24. The momentum resolution $\Delta p/p$ of the FMU system is then estimated to be

$$\frac{\Delta p}{p} = 16.6\%, \quad (2.33)$$

independent of momentum for typical muon momenta between 5 and 200 GeV/c. We will compare this result with that obtained from a Monte Carlo simulation in Chapter 3.

2.4 Forward Muon Electronics

Below we describe the electronics used in the forward muon system. We start with a overview of the data acquisition system and then discuss several of the most important electronics modules in detail.

2.4.1 Overview

Figure 2.18 shows schematically the electronics that were involved in testing and reading out various components of the FMU system. The modules are shown as

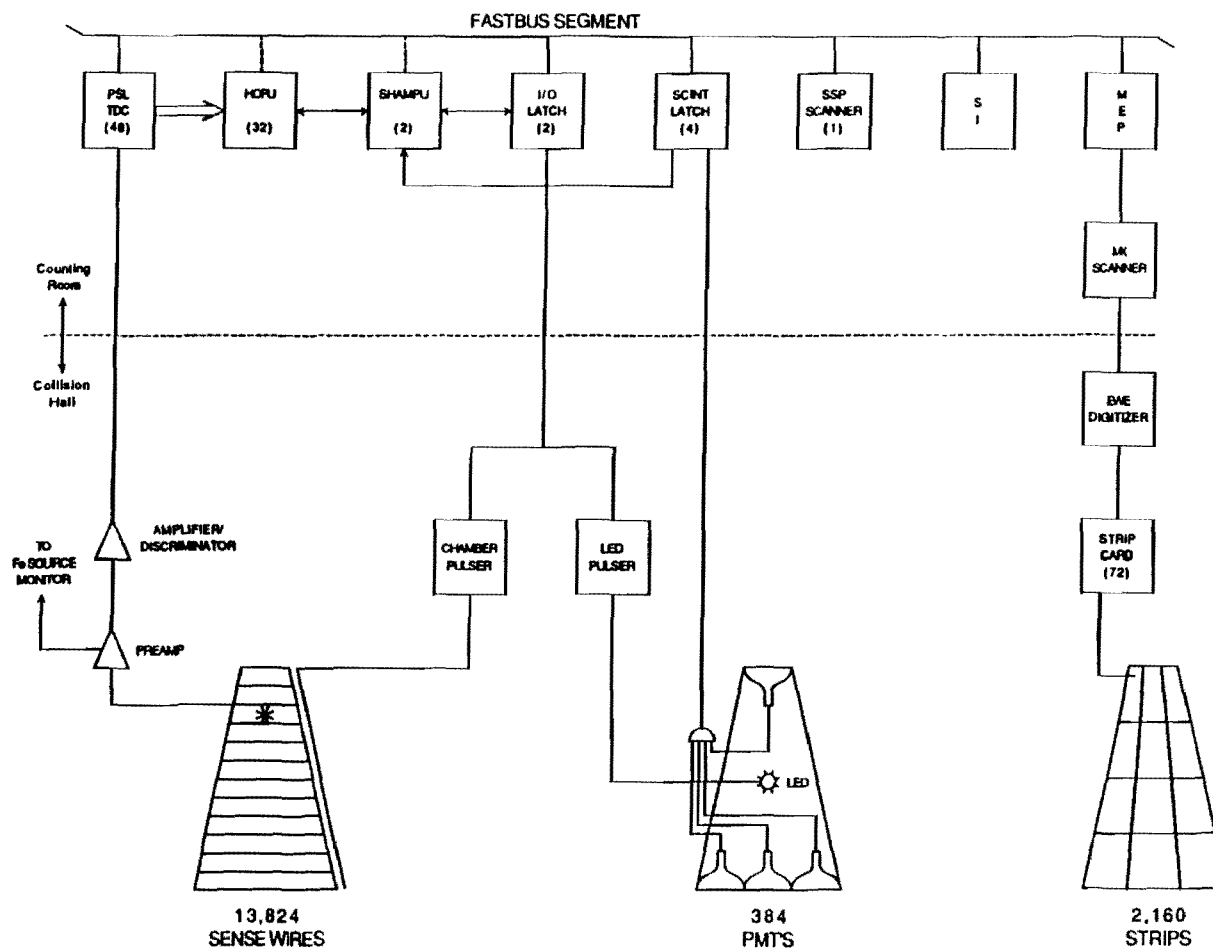


Figure 2.18: Forward muon electronics.

they appeared within the larger CDF FASTBUS-based data acquisition system. They were grouped together as a subsystem (also known as a "FASTBUS segment"). In the upper left-hand corner of the figure are located the 48 PSL (for the Physical Sciences Laboratory of the University of Wisconsin which built the units) TDC modules. There was one TDC unit for each chamber octant ($8 \text{ octants} \times 6 \text{ planes} = 48 \text{ octants total}$). These modules were located in the counting room and measured the drift times of muon hits recorded in the collision hall. The signals received by the TDCs were differential ECL digital signals produced in the collision hall by pre-amplifier (Figure 2.19a) and amplifier/discriminator (Figure 2.19b) electronics acting on the incident muon ionization signal. As shown in the figure and mentioned before, special electronics also made use of pre-amplified signals from various ^{55}Fe sources located in the system to monitor the chamber gain stability. The hit time information measured by the TDCs for an event was read out through the FASTBUS segment by a single SSP (SLAC Scanner Processor) module located on the right side of the figure. The SSP is itself a microcomputer which is capable of reading and writing information to any module with a FASTBUS interface located on the FASTBUS segment. Modules with a FASTBUS interface are denoted by a solid line connection to the FASTBUS segment in the figure. During the event readout, the SSP copies the TDC hit information into its memory, re-orders it into a more useful format (as described in Appendix B), and sends it to the data acquisition computer (in this case a Digital Equipment Corporation VAX-785 computer) to be written onto

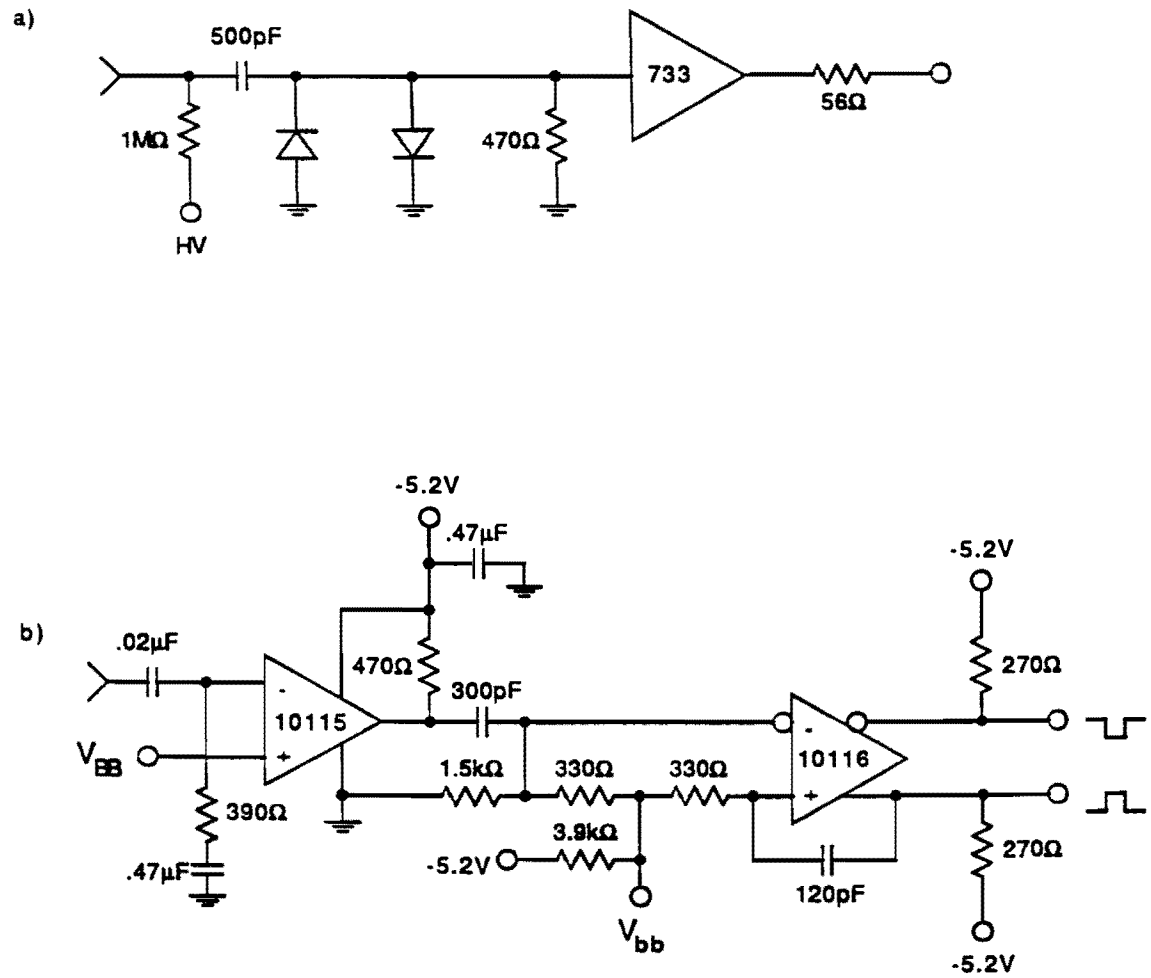


Figure 2.19: Drift chamber pre-amplifier (a) and amplifier/discriminator (b) circuit diagrams.

magnetic tape.

In addition to the drift time information, the TDCs also provided signals for those wires which had hits during an event. This wire hit information was sent directly to and latched by the 32 HOPU (Half Octant Pattern Unit) modules located nearby. The HOPU units formed the Level 1 forward muon trigger for an event during the 1987 run. This was done by searching for a pattern of hit wires consistent with the passage of a muon within a vertex-pointing road in the three chamber planes. If such a pattern was found, this information was passed onto the SHAMPU (Scintillator Hodoscope And Muon Pattern Unit) trigger controller module. The SHAMPU received from the HOPUs the location of the octants containing hits satisfying the trigger hit pattern and it searched for scintillator counter pair coincidences within those octants. If a matched counter pair was found, the forward muon trigger was satisfied and a bit was set in a FASTBUS I/O latch indicating this fact. This information was then available to the CDF trigger system via FASTBUS to decide whether to take the time to readout all CDF detectors and write the event onto magnetic tape (thereby being unable to record data from successive beam-beam crossings until this task was completed) or to reset the electronics and prepare for the next beam-beam crossing.

Figure 2.20 shows a simplified view of the trigger electronics operation. As seen in the figure, chamber hit time information was sent to the TDCs and the pattern of hit wires was passed to the HOPUs where a coincidence between latched signals from the vertex-pointing cells was sought. Such a coincidence is

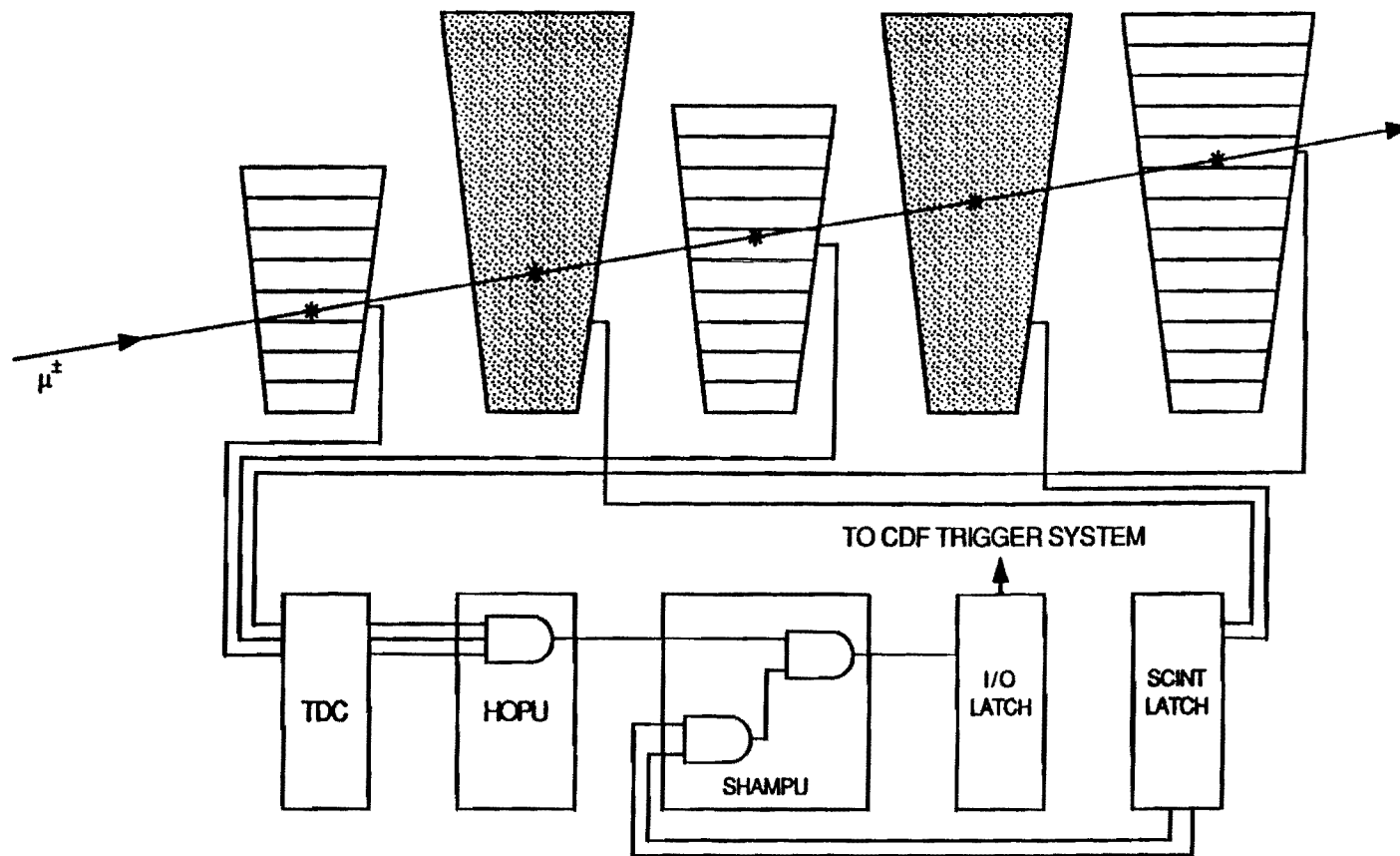


Figure 2.20: Simplified operation of the trigger electronics.

represented by the "AND" gate in the figure. If a coincidence was found, then this signal was sent to the SHAMPU. Here it was "AND"ed with any same-azimuth counter pair coincidence in the octant. If such a counter pair existed, then the trigger was satisfied and this information was latched and sent to the CDF trigger system.

Returning to Figure 2.18, we see that the scintillator hit signals (both beam-beam and beam-halo) were recorded in four (one per plane) latches which were also read out by the SSP during each event. In addition, another I/O latch was used to drive chamber and LED pulsing circuits in the collision hall to test the drift chamber and scintillation counter operation. Continuing towards the right of the figure, we encounter the SI or Segment Interconnect module. This module was the interface of the forward muon subsystem to the rest of the CDF FASTBUS network and was used for all FASTBUS operations (module initialization, diagnostic testing, etc.) that didn't involve the SSP. Finally, in the upper right-hand corner, we encounter the RABBIT (Redundant Analog Bus Based Information Transfer) system used to record the cathode pad (or strip) signals from a passing muon. This system consisted of seventy-two strip cards located in the collision hall which amplified the analog cathode pad signals before sending them to be digitized in the EWE (Event Write Enable) digitizing boards. The digitized signals were then read out by the MX scanner processor which was interfaced to the FASTBUS system through the MEP (Multiple Event Port) module and sent to magnetic tape during event readout.

Figure 2.21 shows the timing signals used by the forward muon system during data acquisition. All timing signals were derived from the "CLR" and "STOP" signals generated by the CDF master clock which was itself synchronized to the Tevatron clock. As shown, both CLR and STOP arrive well before the beam crossing at a patch panel located near the FMU electronics. These signals were then fanned out and delayed using standard NIM electronics. The TDCs were operated in what is known as "Clear/Stop" mode whereby the CLR signal was used to start the TDC clock and then the STOP signal caused the clock to run for a preset number of cycles (=128 cycles or 1.280 microseconds for the 1987 run). The CLR signal was also used to clear the scintillator hit latches before the collision as well as to generate the beam-halo and beam-beam gate windows.

2.4.2 The PSL Time-to-Digital Converter

The University of Wisconsin Physical Sciences Laboratory (PSL) has developed a time-to-digital converter (TDC) for general use in high energy physics and this device was used by the FMU system in the 1987 collider run.[53] The particular features of the PSL TDC include a time resolution of 1 nanosecond, sparse read-out, multi-hit capability and a FASTBUS interface [54]. In addition, a dynamic range of up to 40 microseconds is available.

The TDC board itself was a multiwire board using a double ground/supply plane to ensure low noise. A single board had 8 TDC units each of which could accept 12 inputs. The 96 channels of TDC per board were thus nicely matched

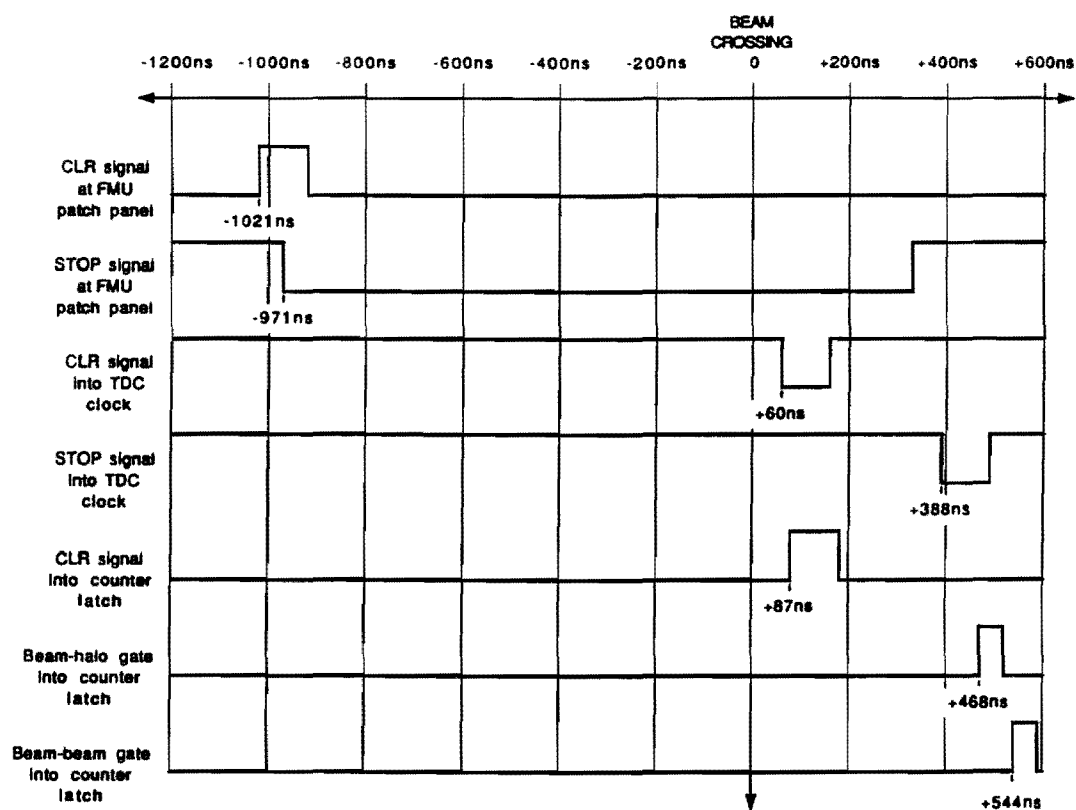


Figure 2.21: Timing signals used by the FMU system.

to the 96 cells in each drift chamber.

The operation of the PSL TDC starts with a discriminated pulse arriving from a chamber, entering the unit and being sent along a 100 ohm impedance tapped delay line which had a 16 nsec delay with 16 taps (Figure 2.22). In each of the 8 units on a board, a 16 bit deep x 40 bit wide RAM was clocked regularly (every 10 nsec) to record:

- a) 12 bits of a counter (incremented by 1 each clock). This recorded the time 0-4095 counts (i.e. up to 40 microseconds). As an option, only 8 bits need be used for a full dynamic range of 2.5 microseconds.
- b) 16 bits from the tapped delay line. This acted as a vernier to divide the 10 nsec clock period into 1 nsec intervals since the leading edge of an incoming pulse was recorded as it propagated along the delay line.
- c) 12 bits from the incoming pulse lines. This was to record which line or lines had hits.

If a pulse was seen on a delay line, the RAM address was incremented so that the current hit information was retained and new memory was made available for successive hits. Typically, only 15 nsec was needed between hits into a TDC unit in order that no information be lost. In addition to the above, a bit was set for each TDC unit that received hits. These 8 bits were checked before reading out the RAMs. The CDF version of the SLAC Scanner Processor (SSP) [55] was used to read out and reformat the hit information from the TDCs.

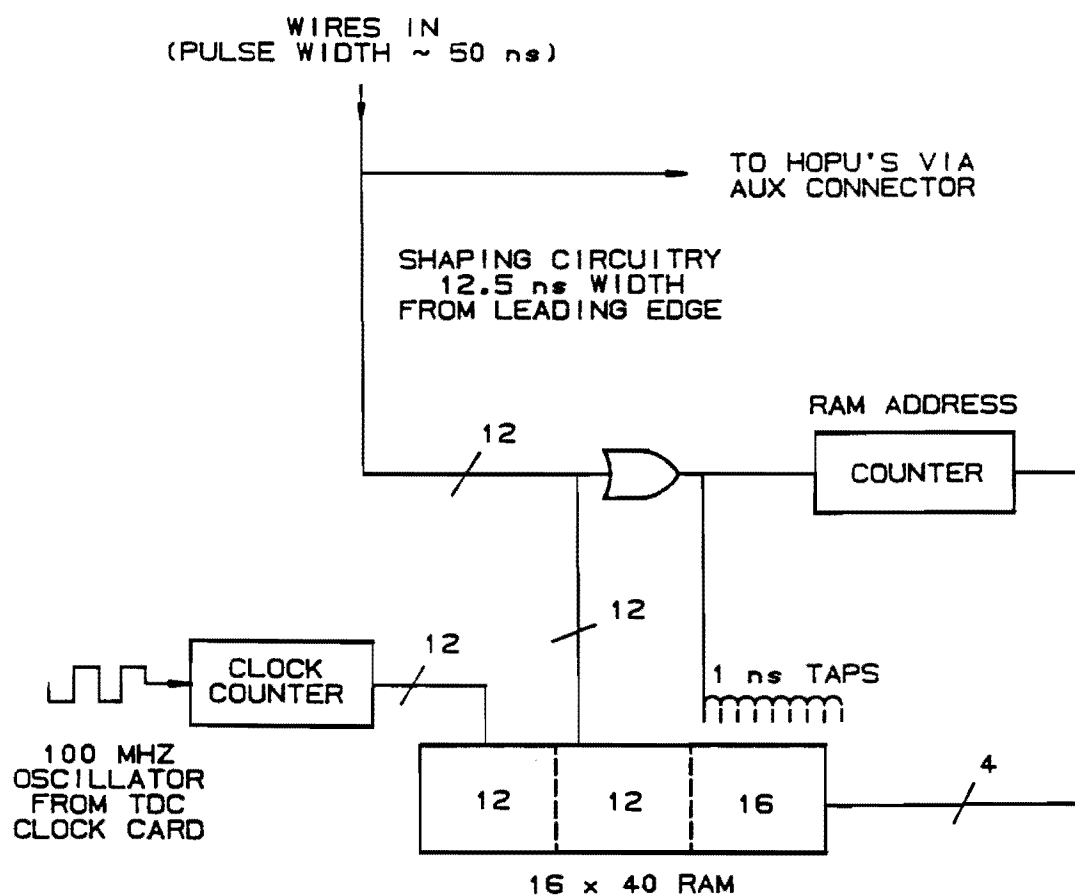


Figure 2.22: Operation of the PSL TDC.

2.4.3 RABBIT Electronics

The forward muon system used RABBIT electronics to read out and perform analog-to-digital conversion of the cathode pad signals from the drift chambers.[56] The good sensitivity of the RABBIT strip cards (65535 counts per picoCoulomb) was well matched to the small pad signals. In the future it may be possible to use the pad pulse height information to flag multiple hits on single pad. A total of seventy-two strip cards and associated readout electronics were used in the pad system.

Figure 2.23 shows a block diagram of the RABBIT data acquisition system. The instrumentation modules typically contain several channels (up to 32) of discrete component, cascode type charge-integrating amplifiers. The amplifier itself consists of a low-noise JFET input transistor followed by a common base stage and two emitter-follower output drivers. An open loop gain of 5000 and a gain-bandwidth product of ~ 10 MHz are standard. In conjunction with the charge-integrating amplifiers, a novel sample-and-hold measurement scheme was used in the high rate $\bar{p}p$ collision environment. There were two sample-and-hold circuits on each integrator, one of which ("BEFORE") sampled the amplifier output just before the beam crossing and the other ("AFTER") sampled the output after the charge from the event had been integrated. The Before After Timer (BAT) module provided the necessary timing signals to open and close switches to the two sample-and-hold circuits. Figure 2.24 shows the timing signals

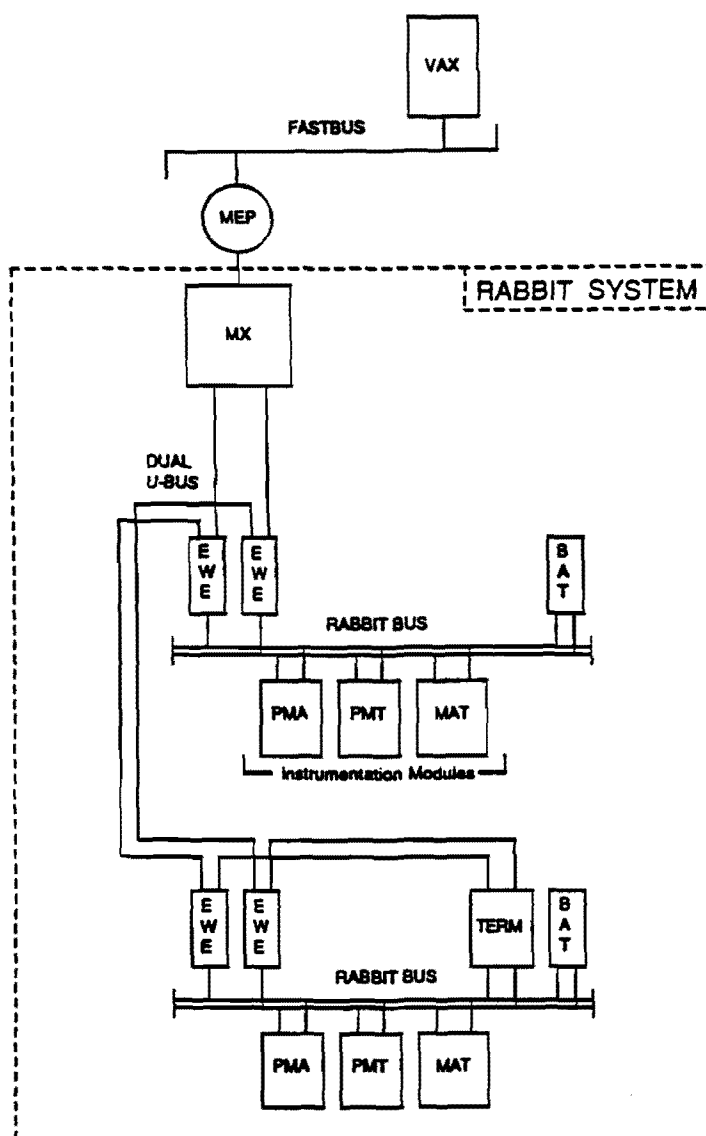


Figure 2.23: CDF RABBIT system block diagram.

used by the RABBIT system. The CLEAR & STROBE signal was generated by the CDF trigger system to be precisely timed relative to the beam-beam collision crossing. The leading or CLEAR edge of the CLEAR & STROBE signal was used by the BAT to generate the BEFORE gate and the trailing or STROBE edge was used to generate the AFTER gate. The difference between the BEFORE and AFTER sample-and-hold signal values was then a good measure of the charge (energy) deposited in the event. This difference was multiplexed to the Event Write Enable (EWE) module which contained a high-speed 16-bit ADC and the analog signal was digitized. The data was subsequently read out by a dedicated processor board (MX), buffered into a FASTBUS slave device (MEP), and written to tape using a VAX mainframe computer. Other features of the RABBIT system included online pedestal subtraction and sparse readout.

2.4.4 The Half Octant Pattern Unit

The Half Octant Pattern Unit or HOPU contained the Level 1 trigger coincidence logic for the FMU system. This custom multiwire device received wire pulses from the TDCs via the FASTBUS auxiliary connector for the inner 28 or outer 28 cells (= half octant) of the 56 cell coordinate wire plane for three same azimuth octants of chambers (one in each chamber plane). The pulses were sent to a gated latch in the HOPU and coincidence circuits searched for hit patterns corresponding to the 1-3-3 (300%), 1-1-1 (100%), and 1-1-.5 (50%) trigger roads described below. The wire trigger road signals were then logically "OR"ed into five pseudorapidity

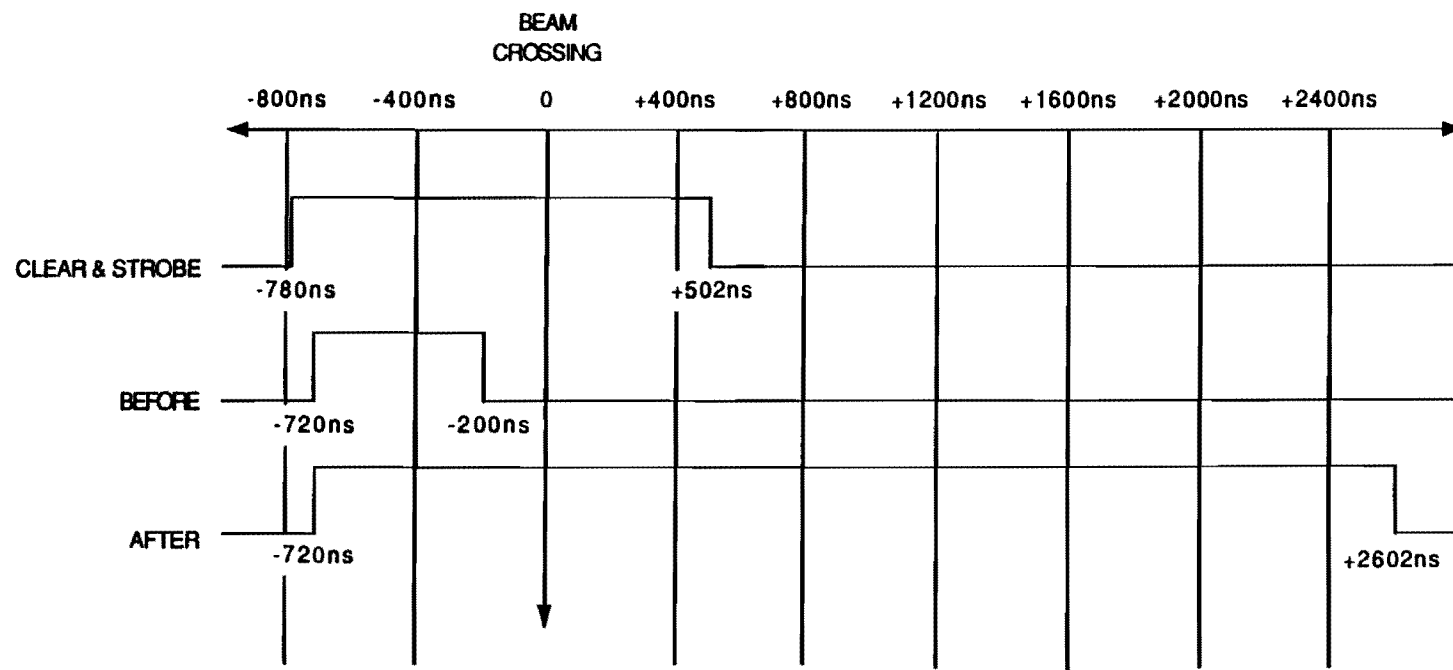


Figure 2.24: RABBIT system timing signals.

towers ($\Delta\eta = 0.2$) which gave a reduced segmentation that corresponded to the standard trigger tower geometry (in preparation for a Level 2 trigger). These five tower triggers were next put in coincidence with the three in-time counter pairs for the octant. This was done in the Scintillator Hodoscope And Muon Pattern Unit (SHAMPU) module. The “OR” of the resulting 15 counter coincidence circuit outputs constituted the single muon trigger for that half octant. An analog current summing circuit was used to generate a multiple muon Level 1 trigger. The single and multiple muon triggers were formed for each of the three trigger types and the SHAMPU provided a single Level 1 trigger signal to the CDF trigger system. This signal could have been for a single muon at a particular threshold or a multiple muon at a different threshold in the same or different octants. In addition, the HOPU provided to the FMU level 2 trigger boards the location of the level 1 trigger in the standard CDF pseudorapidity-azimuth trigger tower geometry. The HOPU boards were tested by using a FASTBUS latch to generate the different trigger hit patterns.

2.5 The Forward Muon Trigger

The primary background to direct muon production in the forward region arises from decay-in-flight of pions and kaons. The spectrum of such secondary muons is a steeply falling function of their transverse momentum. The trigger rate can be reduced to a tolerable level by the imposition of a transverse momentum threshold

of a few GeV/c. By virtue of the drift chamber design, this was accomplished by simple coincidence logic.

2.5.1 Level 1

Three Level 1 trigger thresholds have been implemented in the HOPU module for the forward muon system. They are known as:

- a) the 300% trigger threshold. This required a coincidence between hits in the n th cell of an octant in the 1st plane and hits in either the $n+1$ th, the n th, or the $n-1$ th cells in planes 2 and 3. This was the lowest p_T trigger threshold.
- b) the 100% trigger threshold. This consisted of a coincidence between hits in the n th cell of an octant in each chamber plane. Figure 2.25 shows a particle track satisfying the 100% trigger threshold.
- c) the 50% trigger threshold. This was identical to the 100% trigger threshold except that the threshold was increased with a drift time gating scheme by requiring that the hit in the rear chamber cell be less than some fraction of the maximum drift time. This allowed one to have a variable trigger threshold with an increase in threshold (and thus reduced trigger rate) gained at the expense of efficiency.

This simple scheme provided a constant transverse momentum trigger due to the projective and graded nature of the chamber cells. Each trigger coincidence

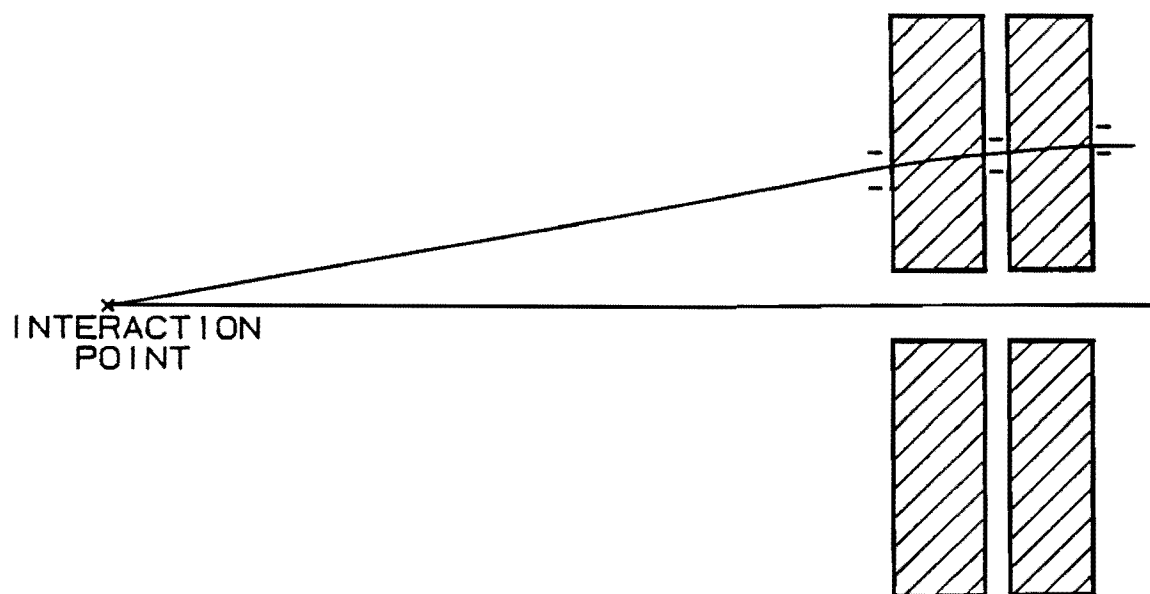


Figure 2.25: A particle track satisfying the 100% threshold trigger.

required a minimum momentum in order that a track not be bent outside the trigger cell in the rear chamber. Since the cell size was proportional to the polar angle, a constant threshold in transverse momentum resulted. Figure 2.26 shows a Monte Carlo calculation of the trigger efficiency as a function of muon transverse momentum for each of the three trigger thresholds.[57] For the 50% trigger threshold, the muon hit in the last plane was required to be within half the maximum drift time.

2.5.2 Level 2

The forward muon level 2 cards make available to the CDF Level 2 trigger system the trigger threshold (300%, 100%, 50%) for any muon track in each of 480 trigger towers. Thus one can correlate forward muons with forward jets, with central muons, etc. to study specific physics processes. While CDF did not use a Level 2 trigger in the 1987 run, it is expected to play a major role in future runs.

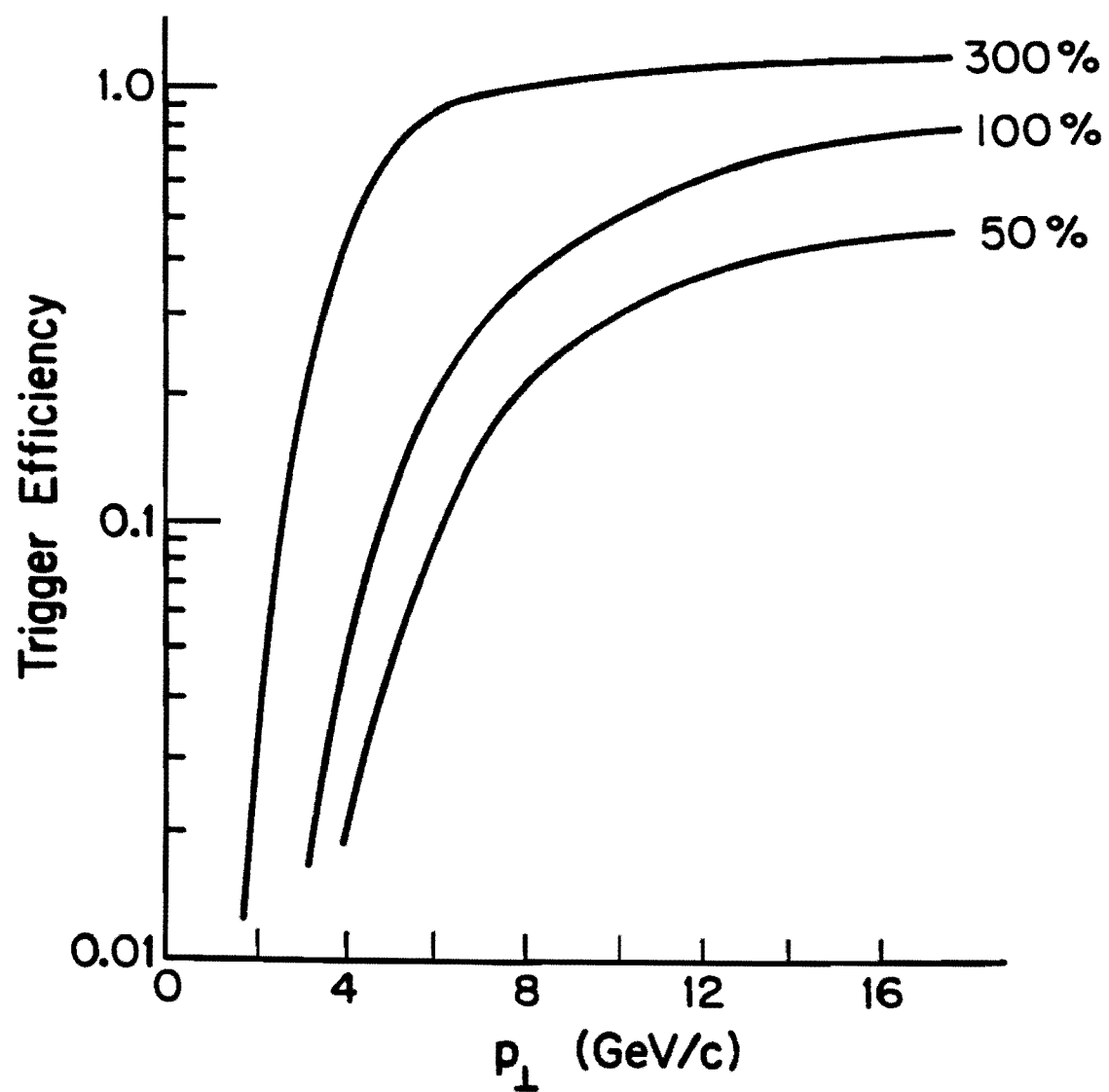


Figure 2.26: Trigger efficiency for the 300%, 100%, and 50% trigger thresholds.

Chapter 3

The 1987 Collider Run

In this chapter we first describe the overall experience of operating the forward muon system in its first data-taking run. We then outline the steps used to obtain our data sample and subsequent selection criteria used to improve the muon content of the sample.

3.1 The 1987 Run Experience

Bringing up a new detection system for the first time is no easy task. Preparing the forward muon system for the 1987 Tevatron collider run proved to be no exception. As described in Chapter 2, it was a rather large system (the largest in CDF by both number of channels and weight!), using brand-new state-of-the-art electronics, and operating in a new region (between 3° and 16° from the beamline) at a $\bar{p}p$ collider. The UA1 experiment [58,59] tried to trigger and take data on

muons in that region and they were unsuccessful.[60,61,62] As will be evident in the following, it is not a simple task.

The first difficulty to emerge during the run start-up was background radiation from the Main Ring beam pipe which runs through the collision hall, near the ceiling, at a distance of ~ 12 meters from the Tevatron accelerator. The FMU counters were in fact the first detectors to observe the unexpectedly large Main Ring beam losses which at this time continue to be a factor in terms of absorbed radiation dose and trigger deadtime for CDF as a whole. The large pulse heights in the photomultipliers of the FMU counters from the Main Ring beam losses caused modification of the 384 phototube bases to include protection diodes and reinstallation of the 96 counters on two separate occasions. This came as a bit of a surprise as low light levels had always been the rule in the large area counters. Initial indications were that the collision hall was *not* a friendly environment.

Of course, the real difficulty in the forward region, and the one UA1 had trouble with, is direct radiation from the colliding beam accelerator. While the low-beta quadrupole magnets are indispensable for providing the luminosity necessary to observe the rare physics processes of interest, the steel return yokes of these magnets provide a substantial target to the 900 GeV large-rapidity beam particles produced in hadronic collisions. Figure 3.1 shows that the forward muon toroidal magnets fit quite snugly around the focussing magnets, with the first chamber cell starting at a radius of only 49 centimeters from the beam. Secondaries, produced by beam particles striking the quadrupole magnets, scattered up into the for-

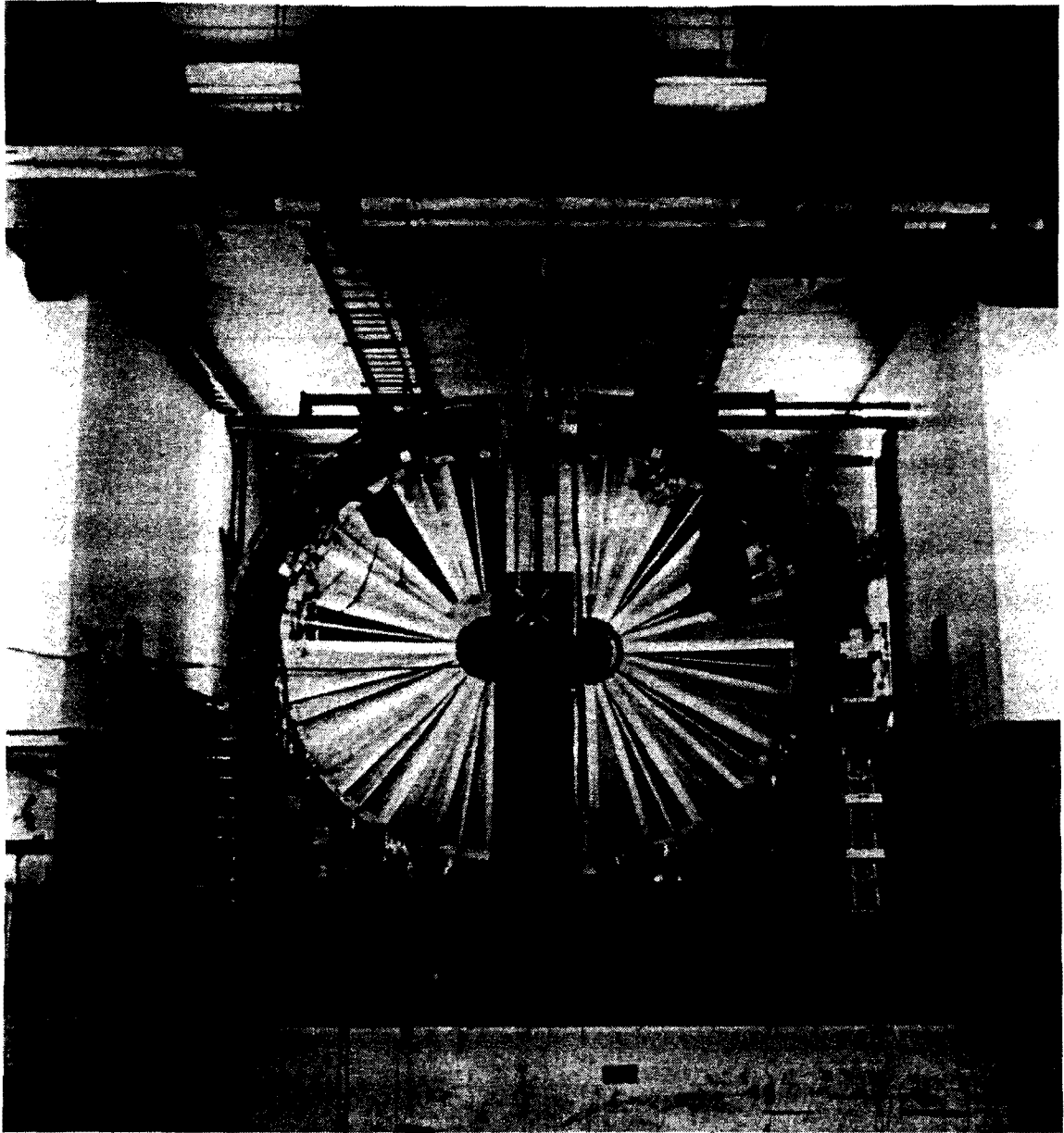


Figure 3.1: Collision hall picture showing the location of the low-beta quadrupole magnet relative to the forward muon system.

ward muon system and were sometimes of sufficient multiplicity and distribution to satisfy the 300% trigger threshold used in the 1987 collider run. This was a particularly severe problem for the “inner HOPU region”, which consisted of the first 28 out of 56 coordinate wires nearest to the beamline and corresponded to the pseudorapidity interval $2.80 < |\eta| < 3.68$. The rate was 10 times lower for the “outer HOPU region” ($1.95 < |\eta| < 2.80$) and it was only in this region that the trigger was used. A forward muon scintillation counter coincidence was not required in the trigger since typically most of the large-area counters had hits due to beam fragment secondaries and their ability to improve the azimuthal position of a single forward muon was significantly reduced. Even in the outer HOPU region, the FMU trigger rate was still unfortunately dominated by the beam fragment triggers which had a rate of 3.0 Hz at a luminosity of $1.0 \times 10^{29} \text{ cm}^{-2} \text{ sec}^{-1}$. This was substantially above the expected decay-in-flight background and completely unacceptable to the CDF collaboration which had to allocate the 1-2 Hz tape writing rate among numerous triggers. The end result was that the FMU trigger was rate-limited to a constant 0.05 Hz, giving a luminosity-dependent prescale factor which had a value of 60 at $1.0 \times 10^{29} \text{ cm}^{-2} \text{ sec}^{-1}$ instantaneous luminosity. This fact yielded a limited forward muon data sample.

The forward muon 300% Level 1 trigger before “AND”-ing with a beam-beam counter coincidence is shown in Figure 3.2. The trigger rate does scale with luminosity as expected, but there is a 2.0 Hz offset. This corresponds to FMU triggers which occurred during non-beam-beam collision crossings due to

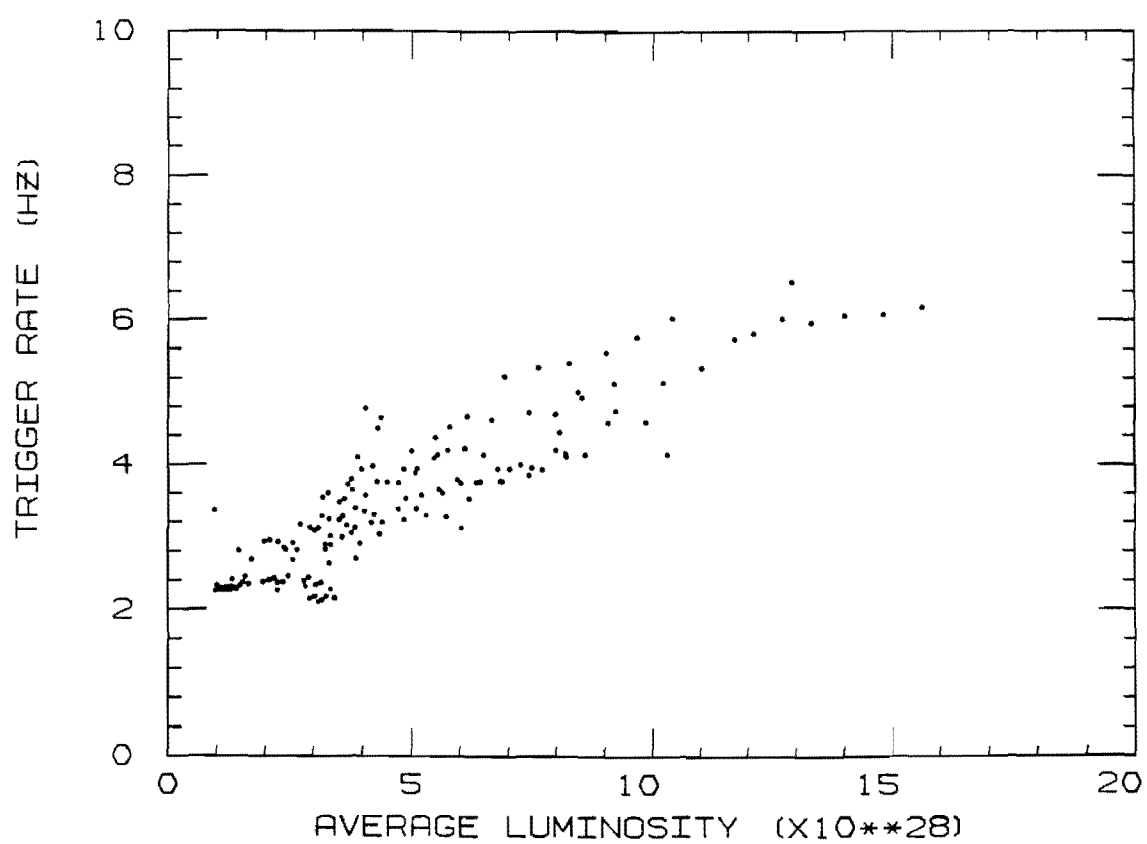


Figure 3.2: The FMU 300% Level 1 trigger rate as a function of luminosity.

the beam fragment background. Figures 3.3 and 3.4 show some typical beam fragment trigger events. (See Appendix C for a description of the forward muon display.) In both cases, particles have managed to scatter up into the system to satisfy the 3 out of 6-hit 300% trigger. In Figure 3.3, the ambiguity wire hits which would be expected for a good muon track are missing in both the front and rear planes. A high multiplicity particle splash, also not consistent with the passage of a single muon, is evident in the middle plane of Figure 3.4.

Figure 3.5 shows the trigger rate as a function of luminosity for the beam-beam counters. The beam-beam counter rate determines the instantaneous luminosity at CDF through the relation:

$$R = \sigma L, \quad (3.1)$$

where R is the beam-beam counter $E \cdot W$ coincidence rate, $\sigma = 43 \pm 6$ millibarns is the estimated cross section for a beam-beam counter coincidence [63], and L is the instantaneous luminosity. By definition, the points on this plot should lie on a straight line and the scatter in the points is from run-to-run accidental coincidence corrections. Figure 3.6 gives the rate for the actual trigger used, $\text{FMU}(300\%, \text{outer HOPU region}) \cdot \text{BBC}$. We find that the offset goes away since we are requiring a beam-beam collision and the solid line shows the expected trigger rate from the decay-in-flight of pions and kaons (see Chapter 4 for this background calculation). The spurious background trigger rate from beam fragments is seen to be ~ 15 times the decay-in-flight rate. This was the situation for the 1987 run and it is expected that future modifications to the Level 1 trigger, such as

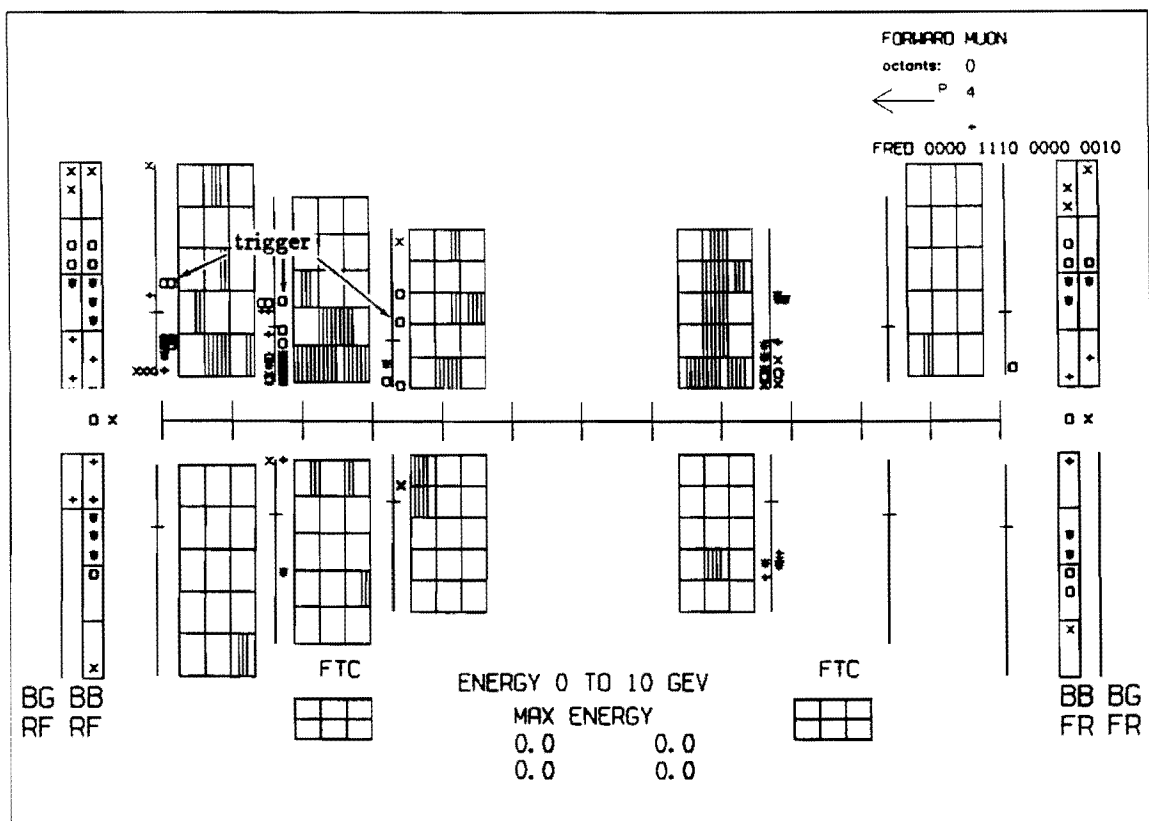


Figure 3.3: Beam fragment trigger with missing front and rear plane ambiguity wire hits.

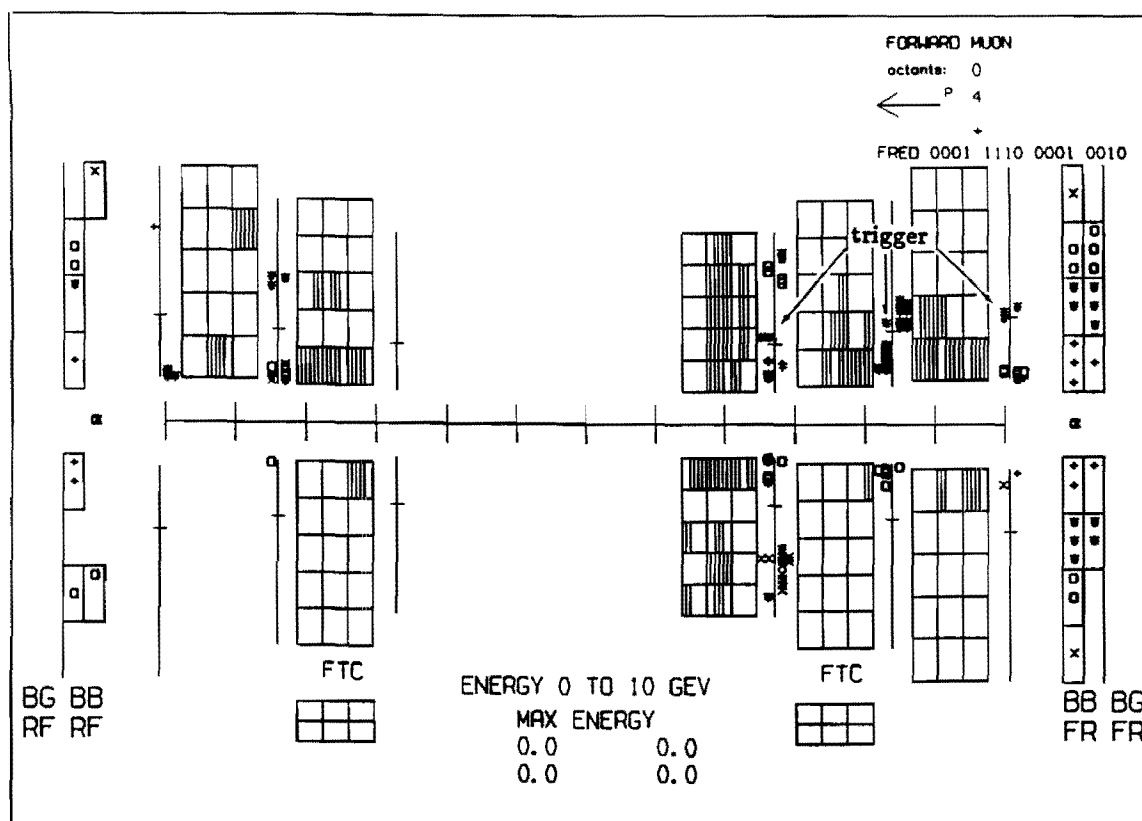


Figure 3.4: Beam fragment trigger with a high multiplicity particle splash in the middle plane.

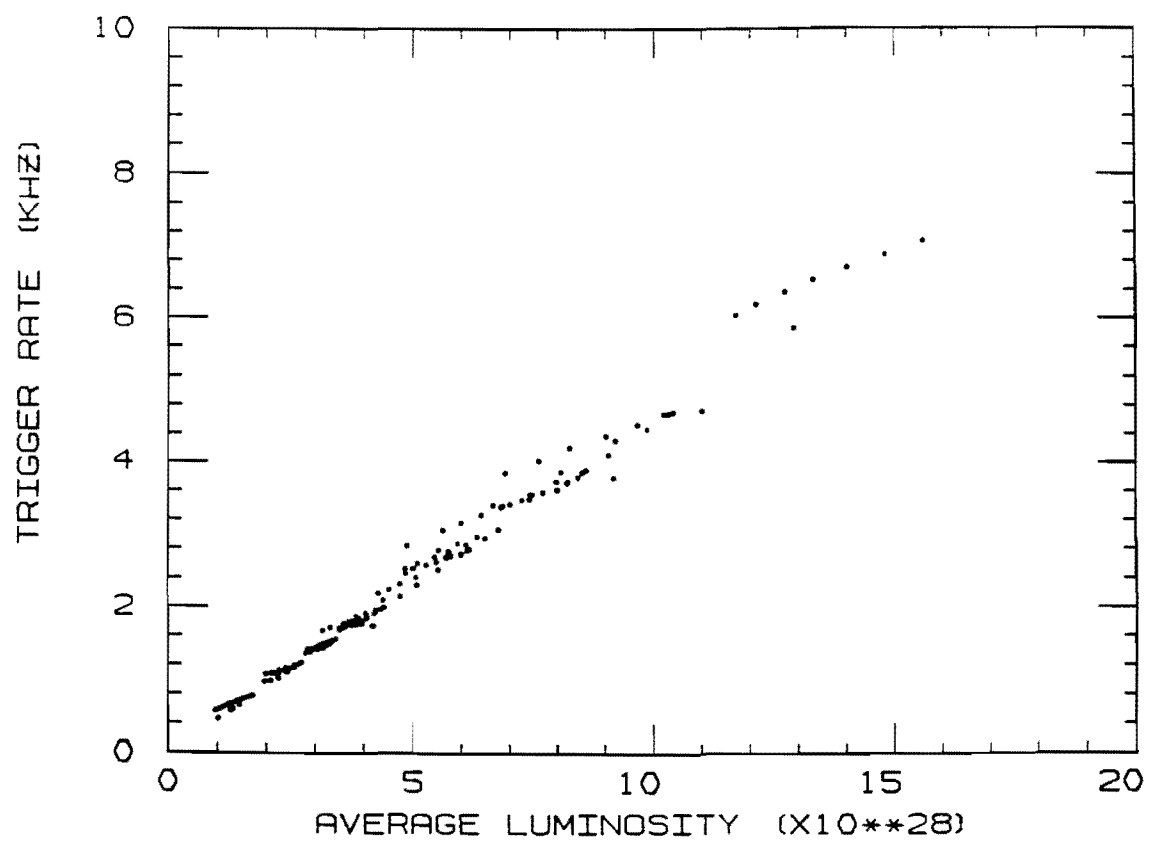


Figure 3.5: The beam-beam counter trigger rate.

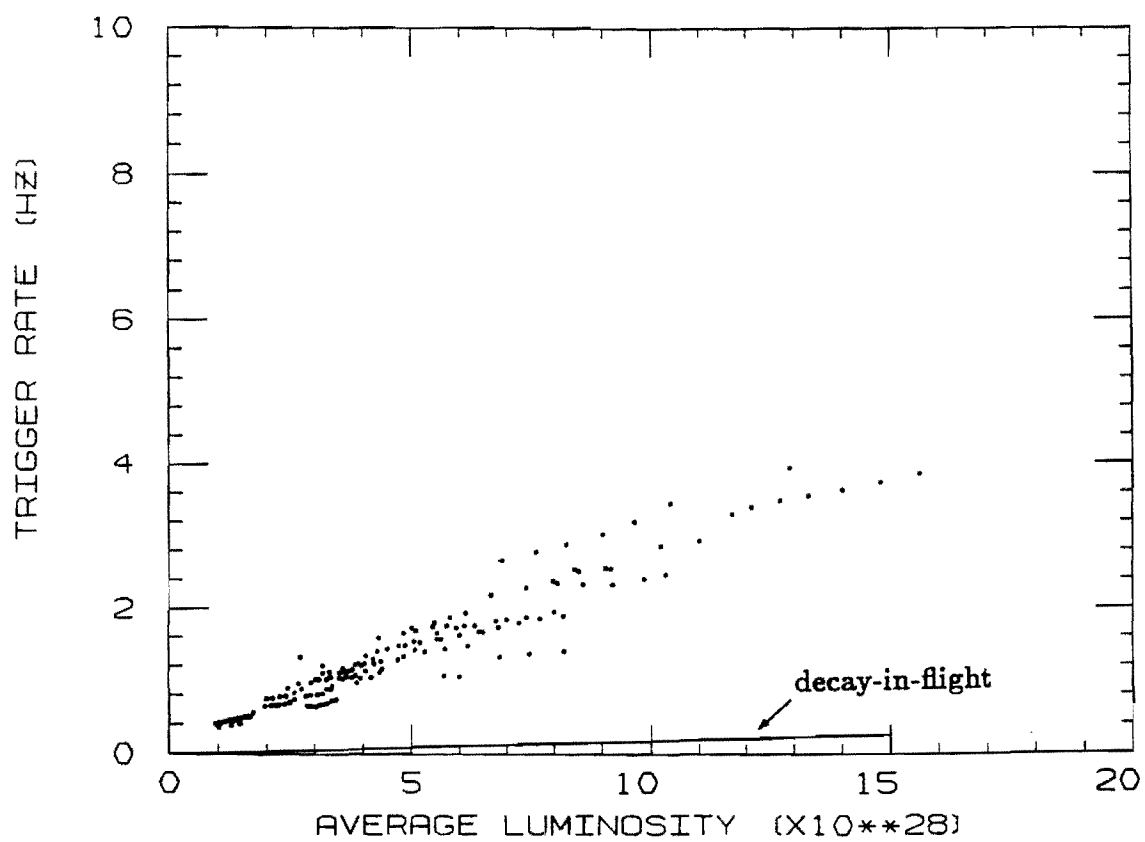


Figure 3.6: The FMU(300%,outer HOPU region)-BBC Level 1 trigger rate.

requiring the full 6 out of 6 hits on a track, will reduce the background trigger rate.

3.2 Data Sample

For this analysis, we consider a sample of 23,282 forward muon triggered events in the region $1.95 < |\eta| < 2.80$ (outer HOPU region). This corresponds to an integrated luminosity of $0.80 \pm .12$ nanobarns⁻¹, where the error ($\pm 14\%$) is due to the uncertainty in the cross section for triggering the beam-beam counters given above.

We first apply a beam-beam event filter to our data sample to insure that we are considering only beam-beam collision events. The requirement for the beam-beam counters to trigger was simply a single in-time hit in both the east and west plane of counters. There was no veto on out-of-time hits and it is possible for a beam-gas event to trigger the beam-beam counters. A software filter was developed for general use in CDF [64] which had an efficiency of 99% for beam-beam collision events. This filter was used to reject beam-gas events. An event vertex position cut was also necessary to insure good detector acceptance to beam-beam collision events and a cut on the vertex position along the beamline of $|z| < 80$. cm was made. This cut accepted $>95\%$ of all beam-beam collision events. Figure 3.7 shows that the effect of these requirements cause the data sample to be reduced by $\sim 7\%$.

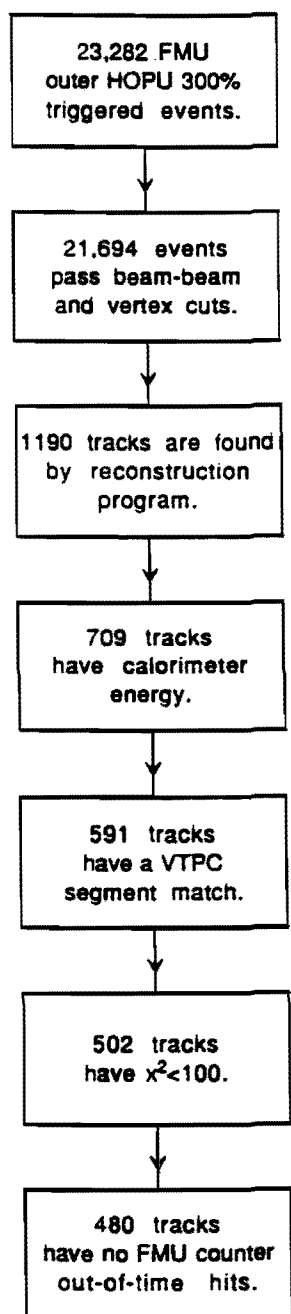


Figure 3.7: Flowchart of the data sample analysis.

- | |
|--|
| <ol style="list-style-type: none"> 1. Track-finding region consistent with trigger region. 2. Track-finding road consistent with trigger road. 3. Require at least 5 hits on the reconstructed track. 4. Coordinate/ambiguity hit pairs should match to within 0.5 cm. 5. The multiplicative product of the number of hit positions per chamber plane within the trigger road should be < 100. 6. Chamber resolution of 500 microns. 7. Include multiple scattering errors in the fit. 8. Include the VTPC vertex position in the fit. |
|--|

Table 3.1: Track-finding criteria.

We next use the forward muon tracking code to search for muon candidates within the data sample. In Appendix B we describe in detail the tracking algorithm used to find forward muons. Certain assumptions and criteria on the muon candidates were made before the reconstruction program would attempt to fit a track and determine the muon momentum. These are listed in Table 3.1. Since the reconstruction program loops through all possible hit combinations, criterion #5 was used to avoid wasting computer time on high multiplicity background events. In the calculation of the multiplicative product of the number of hit positions, a single unmatched hit contributed two hit positions since the left-right ambiguity was unresolved for such a hit.

From the handscanning of $\sim 10\%$ of the data (2500 events) distributed uniformly throughout the sample, the cuts listed in Table 3.1 were found to have nearly 100% efficiency for detecting muons. Several independent scans were done to reduce any scanning bias.[65] This high efficiency is confirmed by Monte Carlo simulation in Figure 3.8 where the track reconstruction efficiency is plotted as a function of track p_T for simulated tracks. At the lowest p_T , the effects of energy loss range-out cause the muon to be absorbed in the toroid steel before passing completely through the system and result in a reduced track-finding efficiency given the criteria of Table 3.1. Near 3 GeV/c p_T , muon range-out is no longer important and the detector acceptance establishes a reconstruction efficiency of $>95\%$. This acceptance includes both the chamber cell walls which are dead regions and can cause hit detection inefficiency and the finite geometrical acceptance of the system in which a muon can be bent outside the rear chamber plane cells at the inner and outermost radii. As will be seen, the cuts given in Table 3.1 are in fact relatively loose and a fair amount of fake muon tracks due to the accidental alignment of spurious hits are reconstructed and will have to be removed by subsequent cuts.

The result of the track-finding produced a sample of 1190 tracks. The requirements of Table 3.1 thus yielded 1 reconstructed track for every 20 triggers. The more than 20,000 triggers which failed to produce a muon track were due to the beam fragment background discussed above. The momentum and transverse momentum spectra of the reconstructed tracks are shown in Figures 3.9

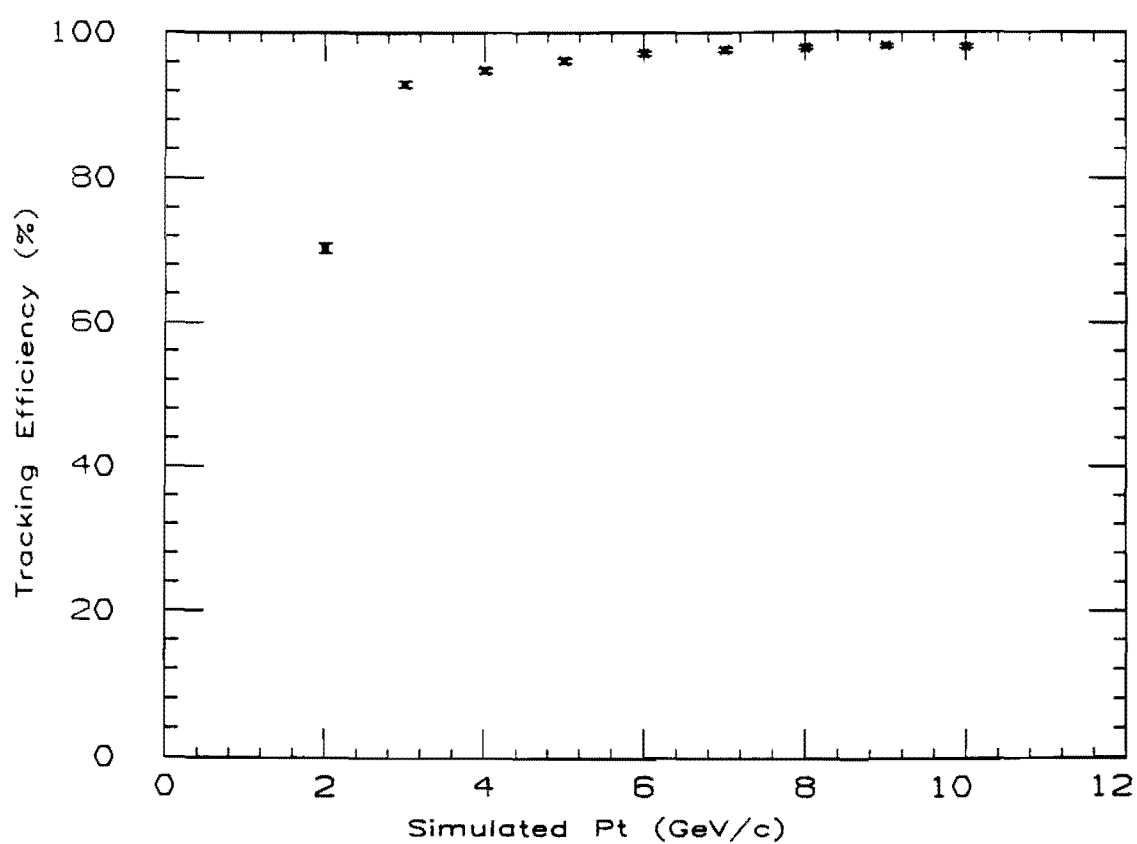


Figure 3.8: Track-finding efficiency for simulated muons, including detector acceptance and energy loss range-out effects.

and 3.10. We see that the transverse momentum spectrum is sharply peaked between 2 and 3 GeV/c. While the forward muon trigger was not very efficient at such transverse momentum values (Figure 3.11), there are expected to be a lot of hadrons (pions and kaons, principally) which could decay to muons and give such a spectrum. This hypothesis will be examined in subsequent chapters.

To check that the muons in our sample are being reconstructed with the correct transverse momentum, a Monte Carlo program was used in which muons of known p_T were generated, simulated, and reconstructed. Figure 3.12 shows that the simulated muons were reconstructed correctly over a wide range of transverse momenta and that the error bars are consistent with the 16.6% momentum resolution calculated in Chapter 2. Figure 3.13 shows a Monte Carlo calculation of the p_T resolution as a function of p_T . The p_T resolution is approximately constant as expected and is in good agreement with the hand-calculated value of $\Delta p_T/p_T \simeq \Delta p/p = 16.6\%$. At 2.0 GeV/c transverse momentum, the trigger efficiency is low ($\sim 5\%$) and those muons which do happen to satisfy the trigger and are reconstructed have undergone large multiple scattering deflections and this results in a somewhat poorer p_T resolution. The gentle slope in the p_T resolution is due to the increasing significance of the chamber resolution at higher p_T where the error due to multiple scattering is diminishing. We see also in Figure 3.14 that the data contain the charge asymmetry (more negatives than positives at low p_T) which was predicted by the hand-calculation of Chapter 2. This asymmetry is also observed in the Monte Carlo (Figure 3.15), and within

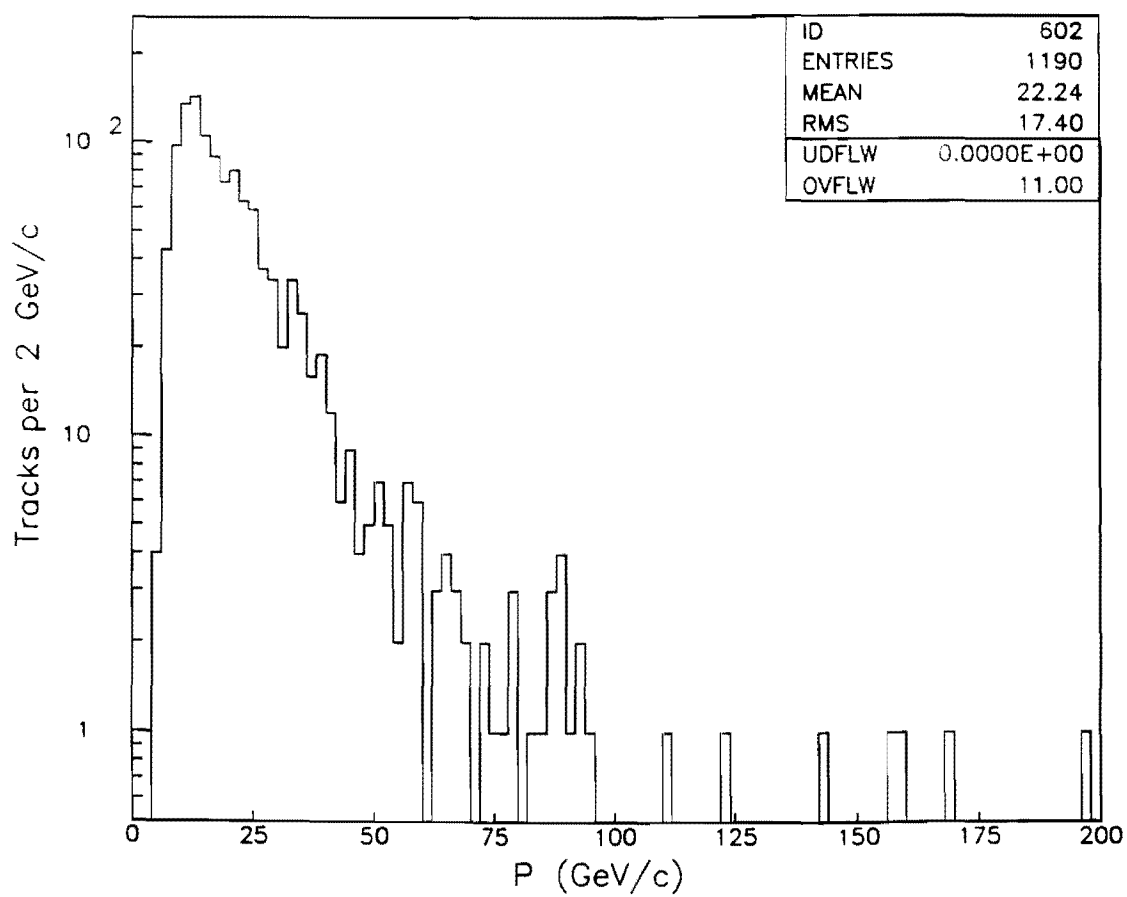


Figure 3.9: Forward muon momentum spectrum after track reconstruction.

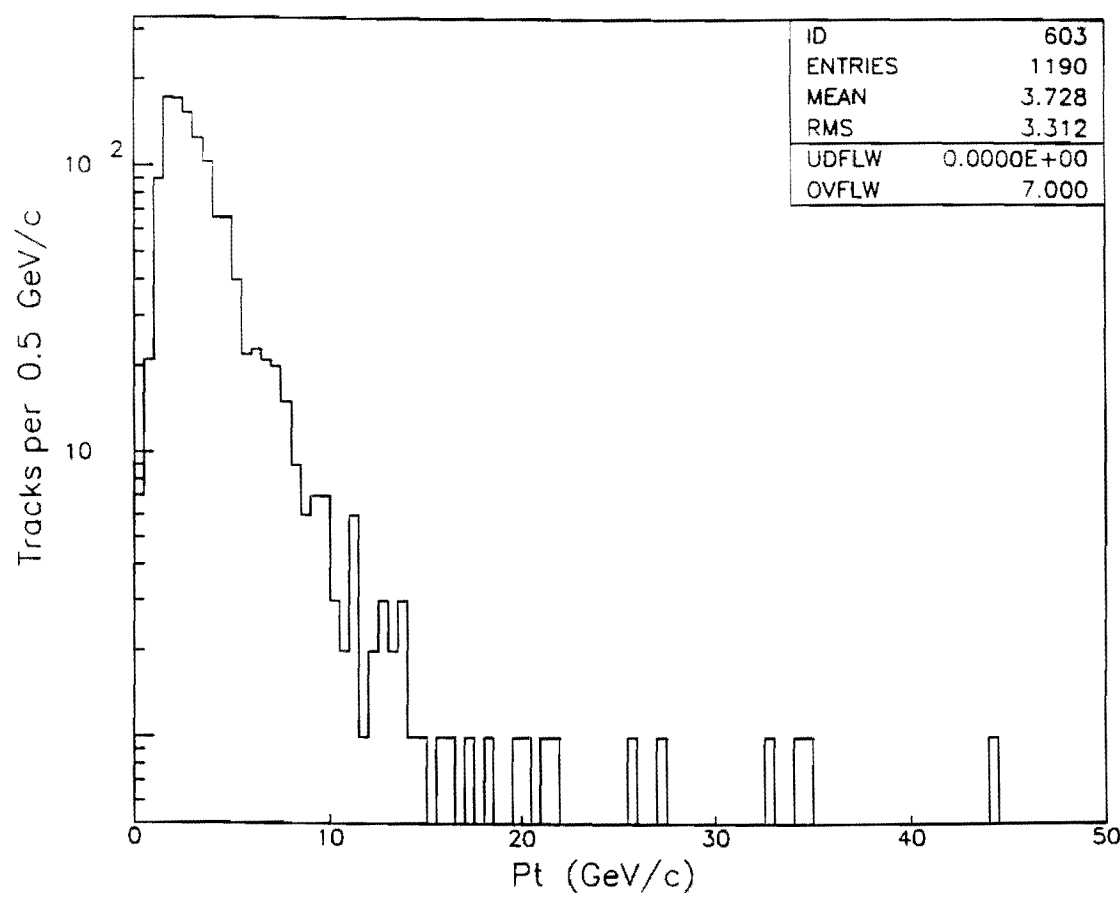


Figure 3.10: Forward muon p_T spectrum after track reconstruction.

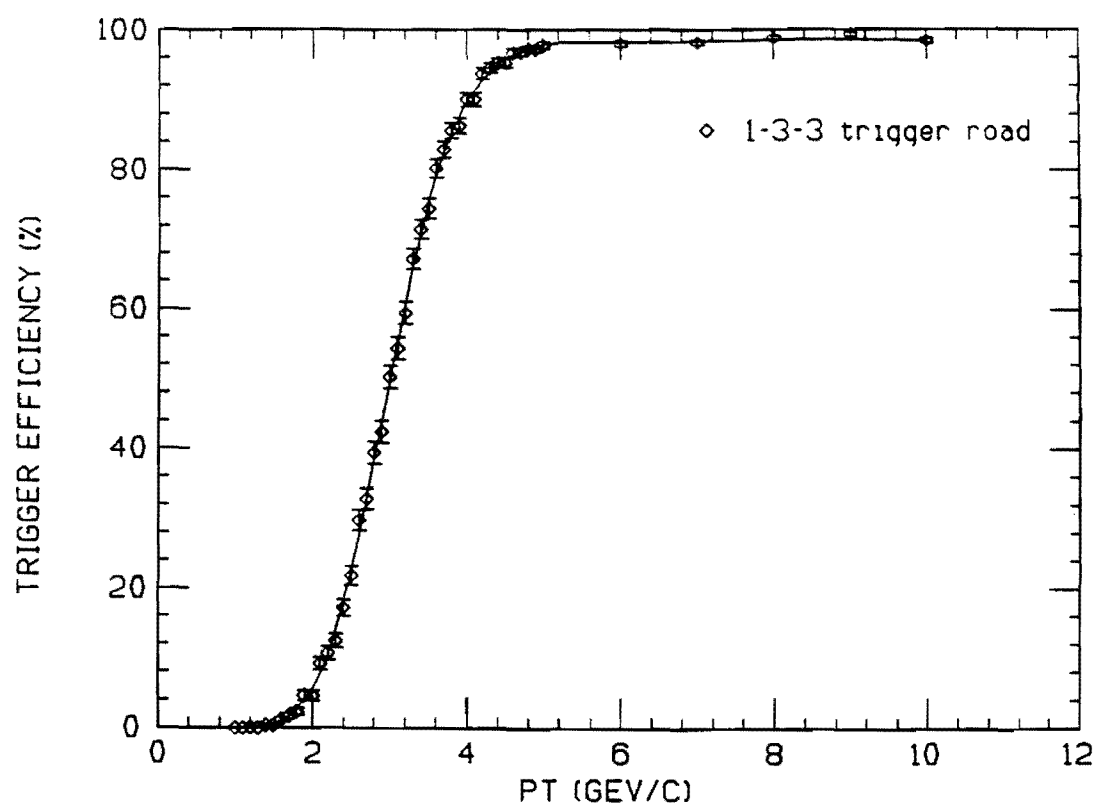


Figure 3.11: Trigger efficiency for the 300% trigger threshold.

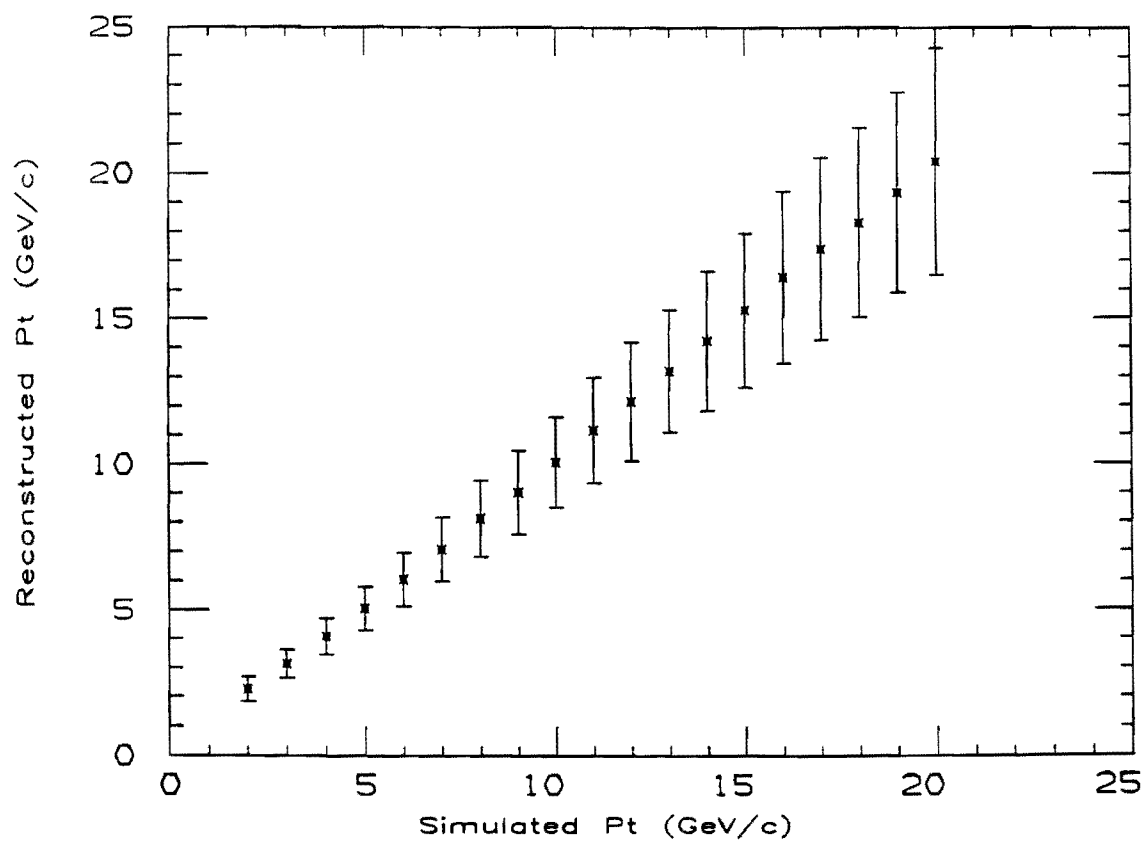


Figure 3.12: Reconstructed p_T versus simulated p_T for Monte Carlo generated muons.

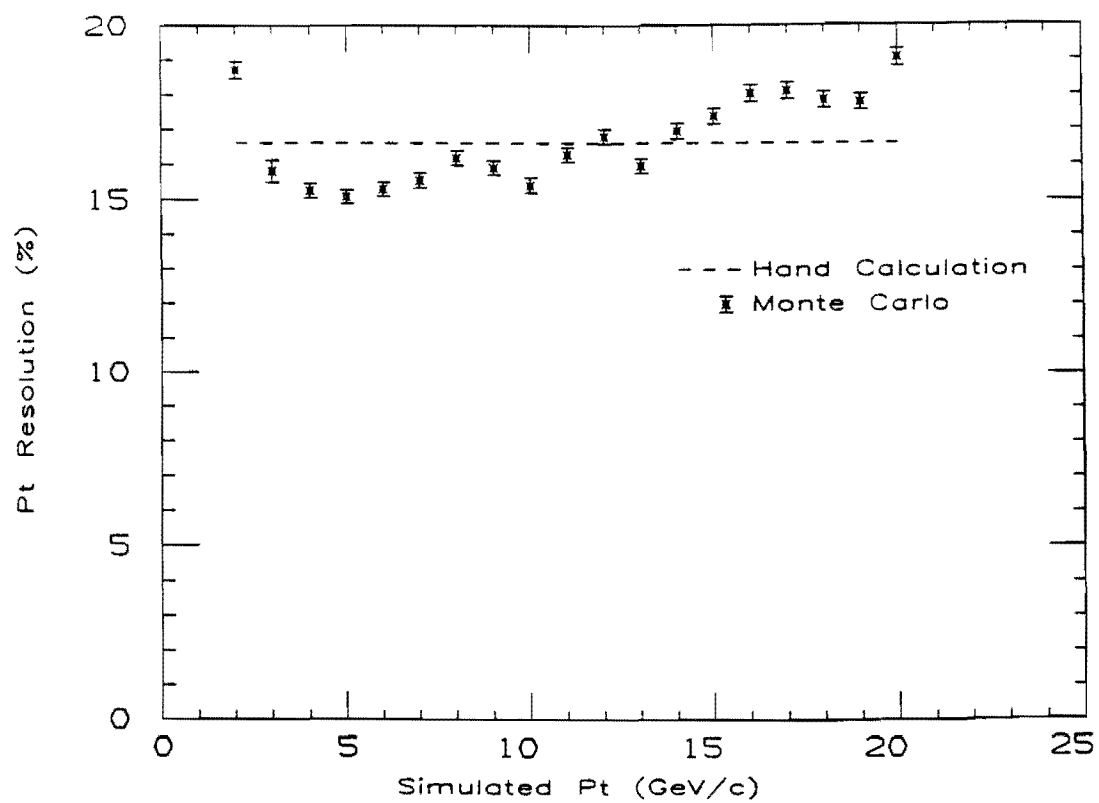


Figure 3.13: Monte Carlo p_T resolution as a function of p_T .

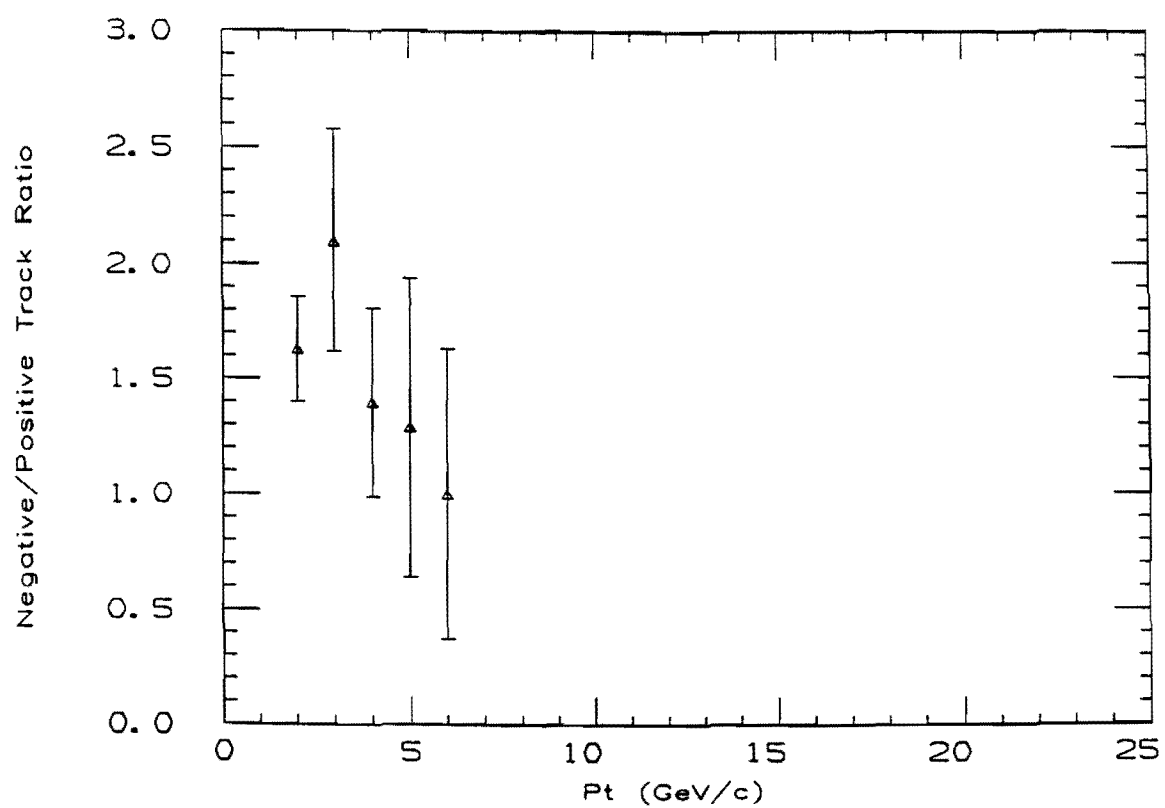


Figure 3.14: Forward muon charge asymmetry after reconstruction.

statistics the data and Monte Carlo are in agreement.

The transverse momentum spectrum of Figure 3.10 contains an unexpectedly large number of events at high transverse momentum (>10 GeV/c) given the integrated luminosity of the sample and the known physics processes discussed in Chapter 1. This is taken as an indication of the presence of fake tracks mentioned above which were found by the reconstruction program in events containing a chance alignment of random hits in the chamber planes. Recall that the forward muon trigger rate was completely dominated by the beam fragment background described previously and thus an ample source of fake muon tracks exists. To reduce the number of fake tracks, we apply additional cuts that a real forward muon would be expected to pass.

Depending on its polar angle, one expects a forward muon to deposit some energy in either the plug or forward electromagnetic shower counters and hadron calorimeters. Figures 3.16 and 3.17 show the electromagnetic and hadronic energy in a 3×3 $\eta - \phi$ tower region centered about the trajectory of the muon track. This 3×3 tower region corresponds on average to a 2σ error in the space projection of the muon track to the front face of the calorimeter under consideration. Figure 3.18 shows schematically the projection of the muon track into the corresponding calorimeters. There is some indication of the expected minimum ionizing energy loss from muons in both Figures 3.16 and 3.17 and the energy loss is at the values expected from test beam results.[66] There is also a clear excess of zero energy loss, corresponding to fake tracks which the reconstruction program

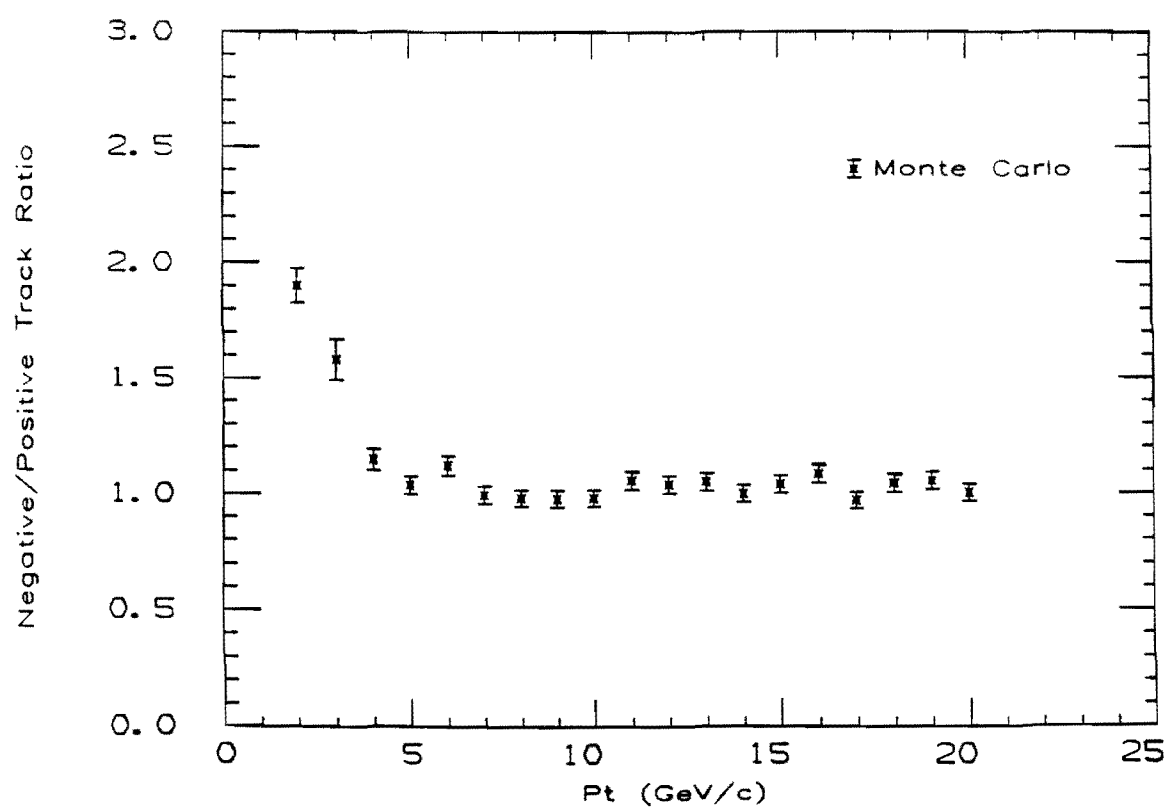


Figure 3.15: Charge asymmetry observed in the Monte Carlo.

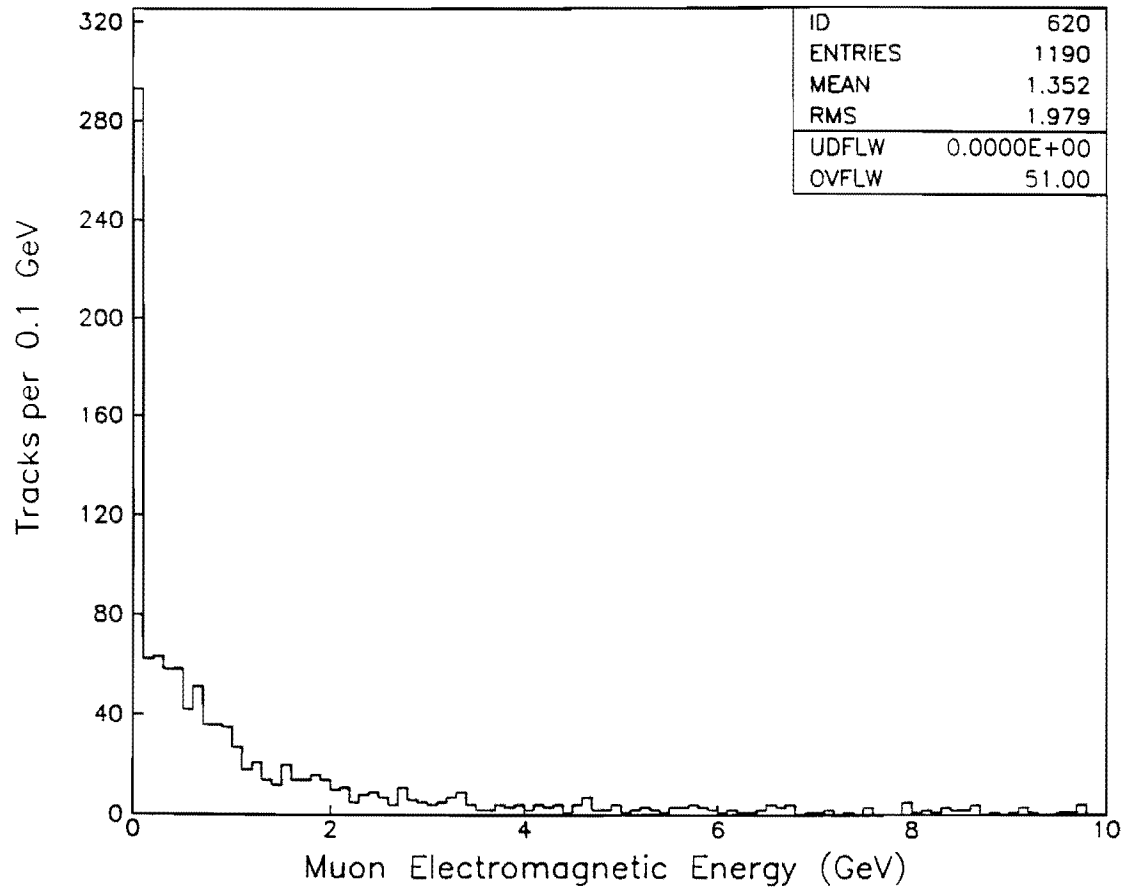


Figure 3.16: Electromagnetic energy in a 3×3 $\eta - \phi$ tower region centered on the forward muon track in the plug and forward calorimeters after track reconstruction.

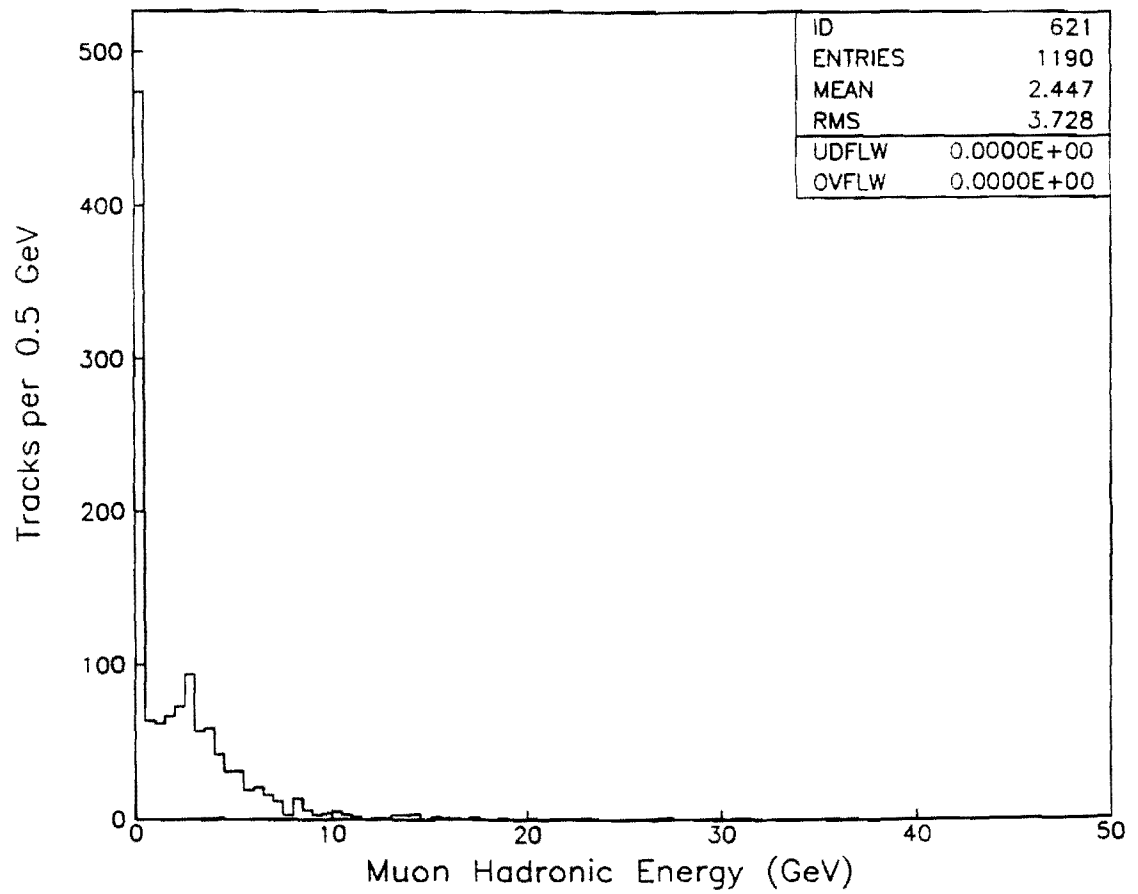


Figure 3.17: Hadronic energy in a 3×3 $\eta - \phi$ tower region centered on the forward muon track in the plug and forward calorimeters after track reconstruction.

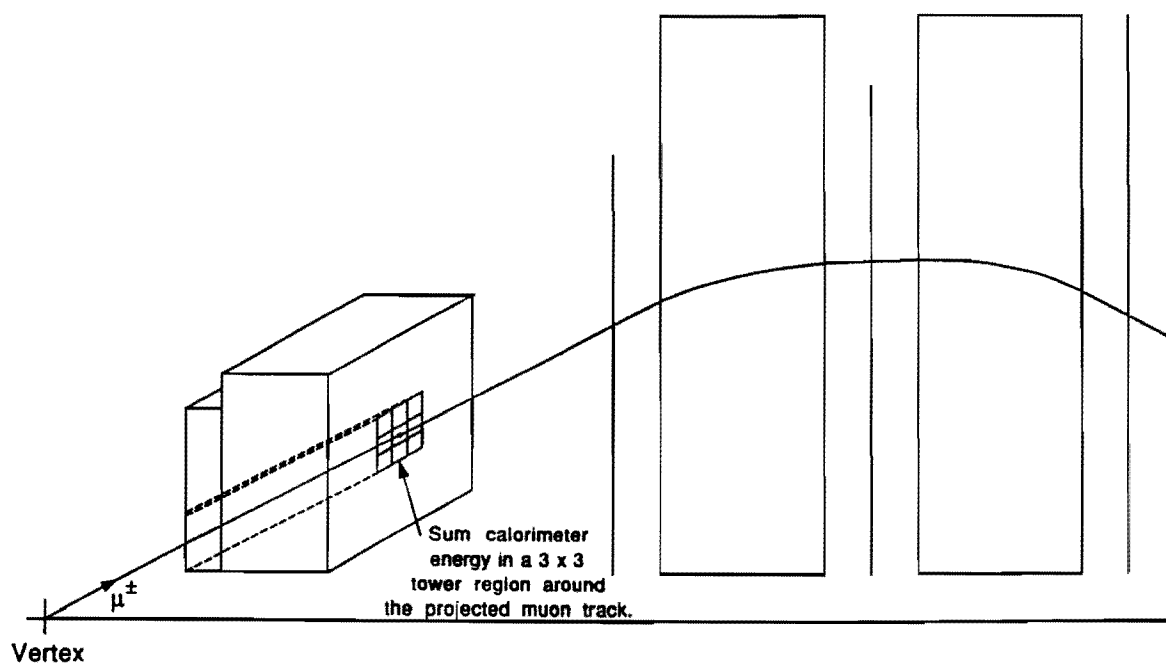


Figure 3.18: Projection of a forward muon track into a 3x3 calorimeter tower region.

has managed to find. We wish to eliminate these fake tracks from our sample and to do so we make the simple requirement that both non-zero electromagnetic and hadronic energy be found in the muon projected tower region. As a practical matter, we require a minimum energy loss of 2 ADC counts or 11.6 MeV. As shown in Figure 3.7 this cut reduces the sample by 481 tracks. A handscan of the 1190 tracks prior to this cut reveals that clearly fake tracks, which have a high multiplicity of hits within the trigger road such as the track in Figure 3.19, usually have no calorimeter energy loss.

Another muon selection criterion is available based on the fact that the forward muon acceptance is well-matched to a region of the vertex time projection chamber for which it has high efficiency. Thus, there should be a VTPC track at nearly the same polar and azimuth angle as a real forward muon track. Figure 3.20 shows schematically the situation. Referring to this figure, the difference in polar angle between the forward muon and VTPC tracks is given by:

$$\Delta\theta = \theta_M - \theta_V, \quad (3.2)$$

with error:

$$\delta\theta = \sqrt{\delta\theta_M^2 + \delta\theta_V^2}. \quad (3.3)$$

The difference, in units of the expected error, between the polar angles of the FMU and VTPC tracks is then:

$$\sigma_\theta = \frac{\Delta\theta}{\delta\theta}. \quad (3.4)$$

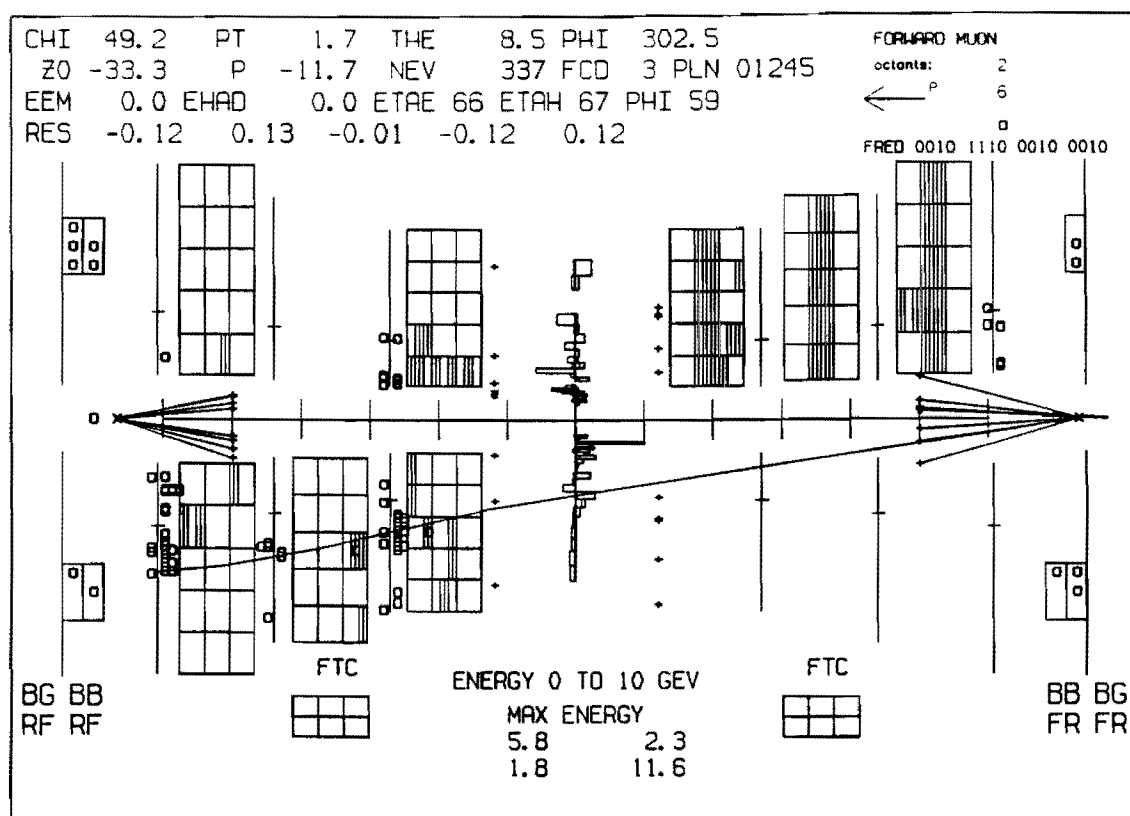


Figure 3.19: Fake muon tracks typically have no calorimeter energy loss.

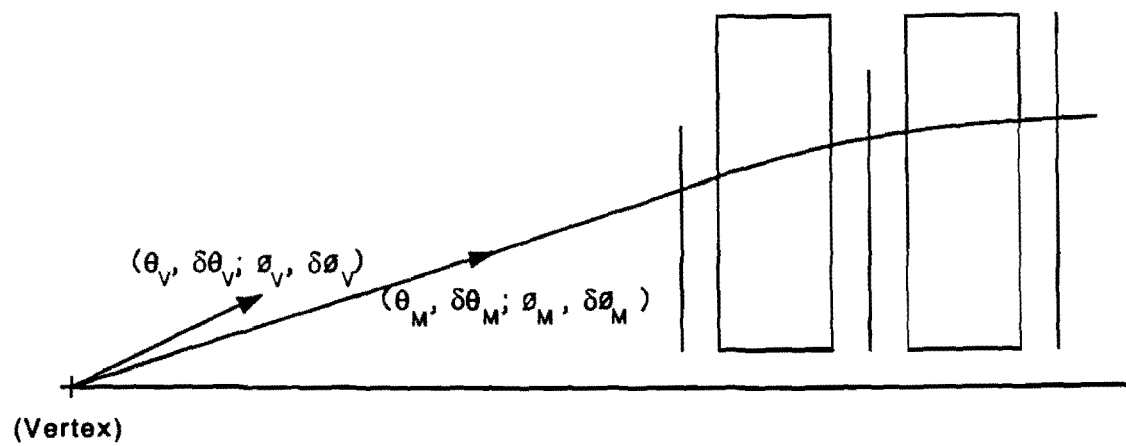


Figure 3.20: FMU/VTPC track matching.

A similar calculation yields the normalized azimuthal angle deviation σ_ϕ for our FMU/VTPC track pair. Requiring a match within 5σ in both θ and ϕ , we can eliminate more fake tracks from our sample and significantly enhance the muon content. This requirement further reduces the sample by 118 tracks. We note that in Figure 3.19 we eliminated a fake track which had no calorimeter energy loss but did in fact have a VTPC track match. There also is a class of fake tracks containing non-zero calorimeter energy in the muon tower region due to pedestal fluctuations or neighboring hadrons and no VTPC track match. This FMU/VTPC track matching cut eliminates these tracks with good efficiency.

A further handscan of the resulting 591 tracks reveals that some fake track background is present in the form of an overlap between a real hadron and a fake muon track due to spurious hits. A loose cut on the χ^2 of the fitted track ($\chi^2 < 100$) eliminates a good portion of these tracks. There still remain however a few events containing fake tracks due to beam-gas collisions which can occur in our system without striking the beam-beam counters. These events are eliminated by requiring no out-of-time hits in the forward muon trigger counters. This requirement brings us to our final sample of 480 tracks.

It should be mentioned that for angles between 3° and 10° to the beamline, one would expect a forward tracking chamber track to match in azimuth with a forward muon candidate. In its first data-taking run the FTC unfortunately experienced difficulties operating in an environment which contained a substantial amount of albedo coming from the plug calorimeter. The FTC wire high voltage

was thus reduced during some of the run to avoid chamber breakdown. Hence it was not fully efficient for our data sample [67] and we choose not to require a FMU/FTC track match.

Figures 3.21 and 3.22 show the momentum and transverse momentum spectra of the forward muon tracks in our sample after all cuts. The selection criteria applied above have removed much of the (expected fake) high p_T tail seen in Figures 3.9 and 3.10. Figures 3.23 and 3.24 now show much more distinct muon energy loss peaks in the electromagnetic and hadron calorimeters. In fact, muon energy loss peaks can be seen in all four calorimeters (Figure 3.25). As shown in Figure 3.26, minimum ionizing peaks can also be found in the FMU chamber cathode pad pulse height distributions. The pad information was not however used in this analysis. Figures 3.27 and 3.28 show the polar and azimuthal angle matching between forward muon and VTPC tracks. The match is quite good in both coordinates with very little background.

Figure 3.29 shows the event vertex distribution for tracks within our sample. The average vertex position and rms value are consistent with that found in data samples taken with other triggers during the run. No gross alignment error or trigger bias is observed. The front plane coordinate wire number for our muon candidates is seen to be peaked toward the inner radius of the outer HOPU region (wires 28-55) in Figure 3.30. Because the chamber cells were built to subtend equal regions of pseudorapidity, one would expect this distribution to be flat. There are two effects which can give rise to such a shape. Assuming a

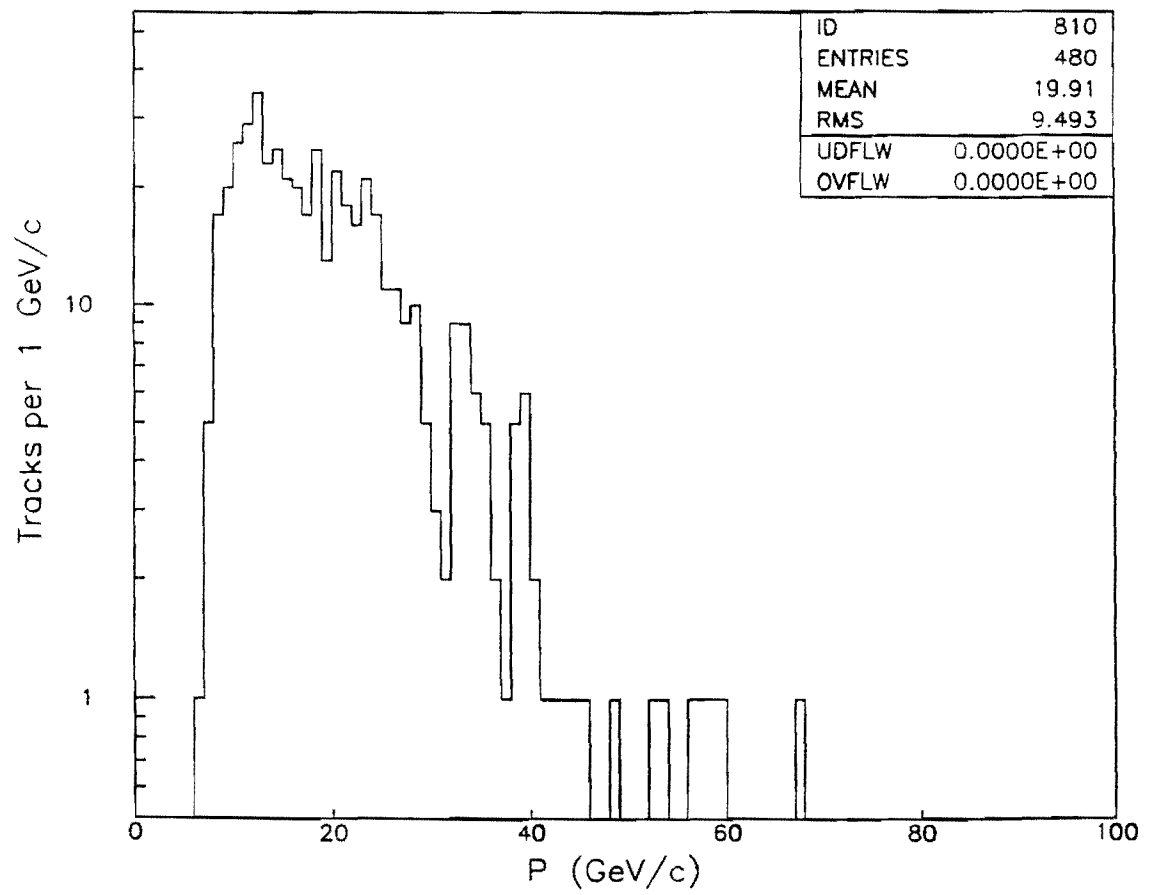


Figure 3.21: Forward muon momentum spectrum after cuts.

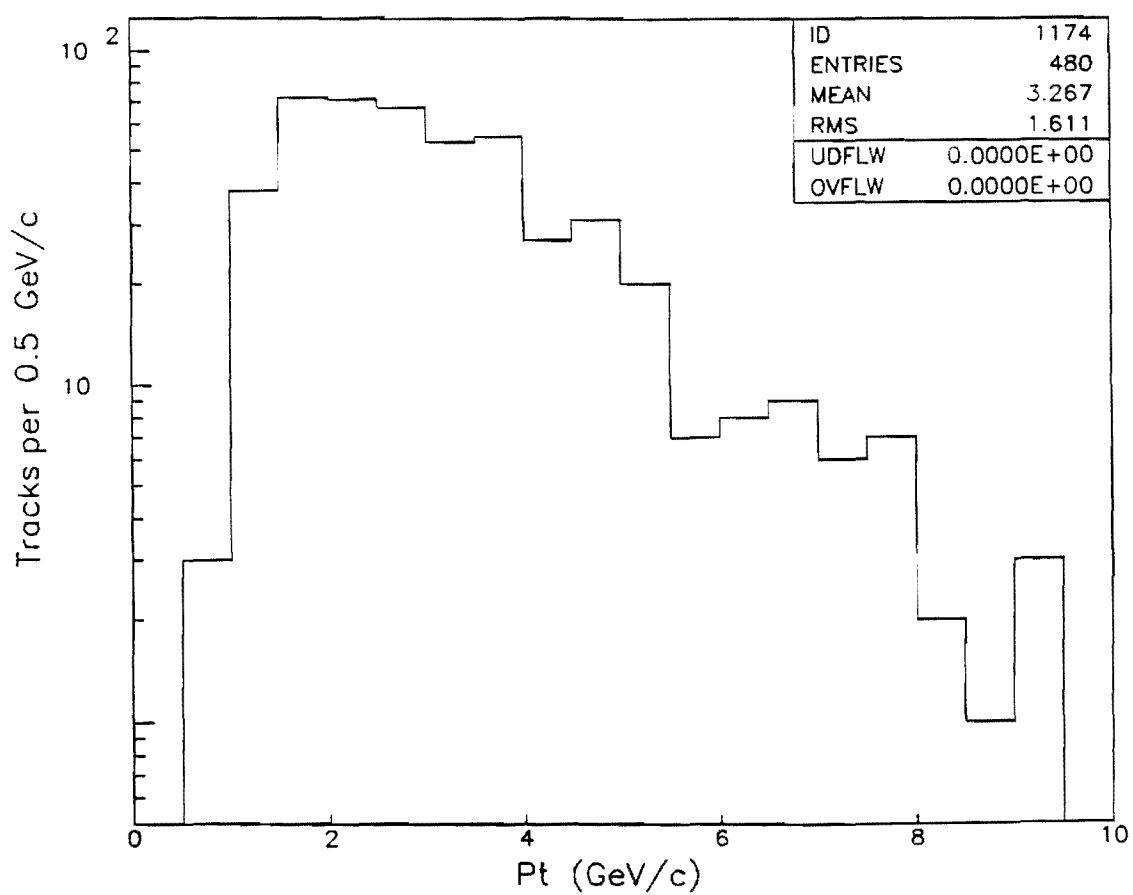


Figure 3.22: Forward muon p_T spectrum after cuts.

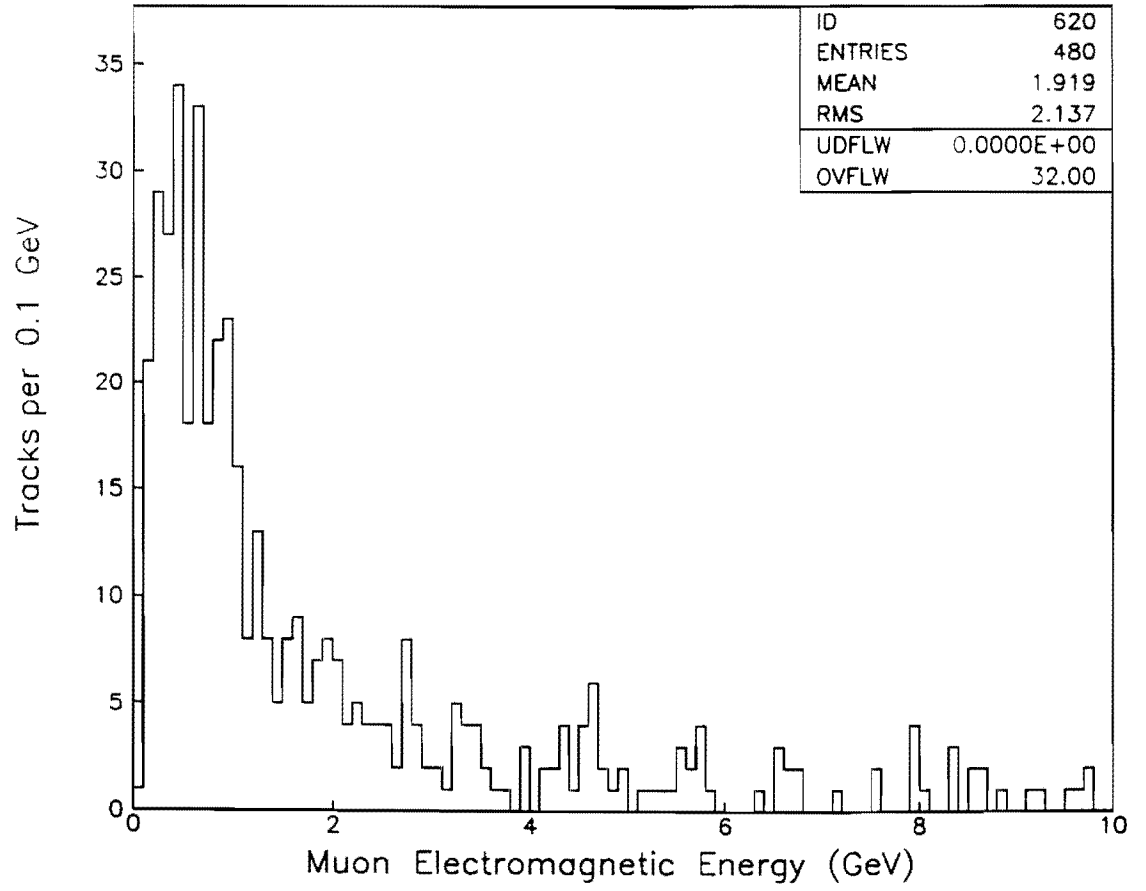


Figure 3.23: Electromagnetic energy in a 3×3 $\eta - \phi$ tower region centered on the forward muon track in the plug and forward calorimeters after cuts.

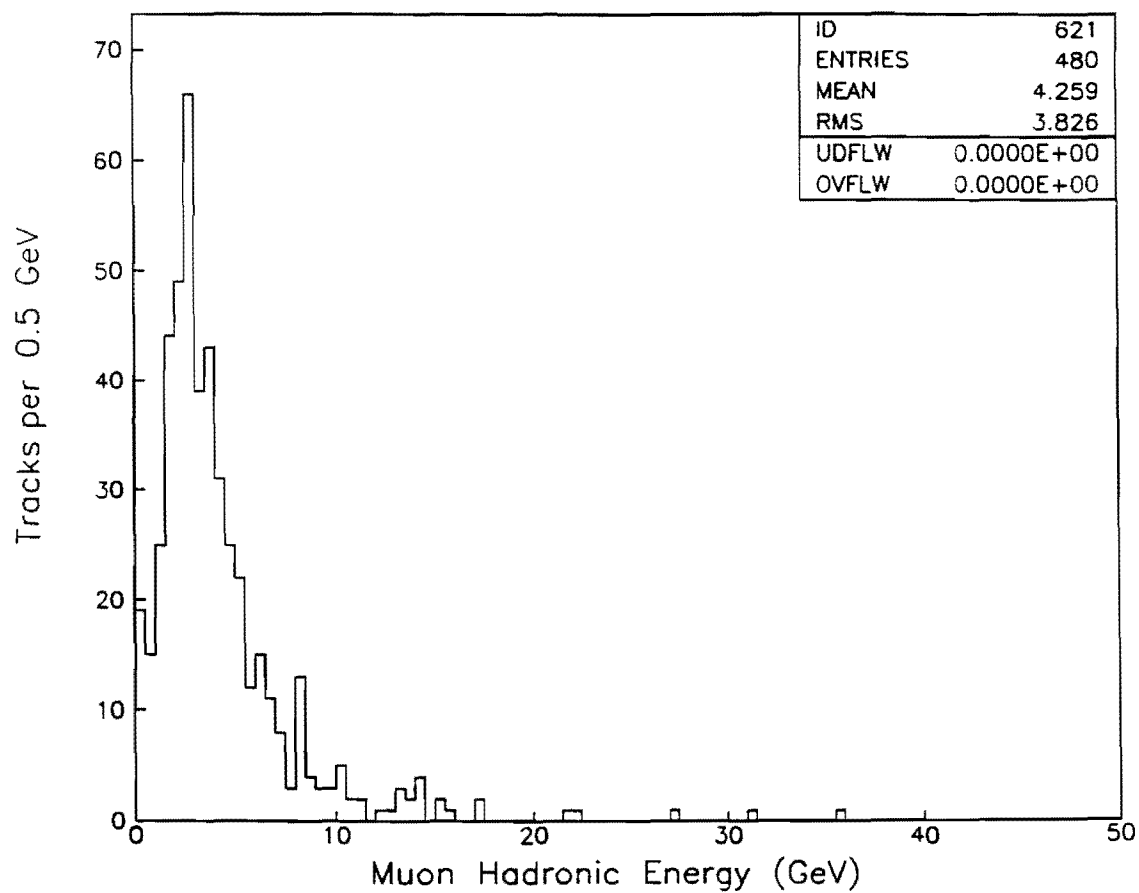


Figure 3.24: Hadronic energy in a 3×3 $\eta - \phi$ tower region centered on the forward muon track in the plug and forward calorimeters after cuts.

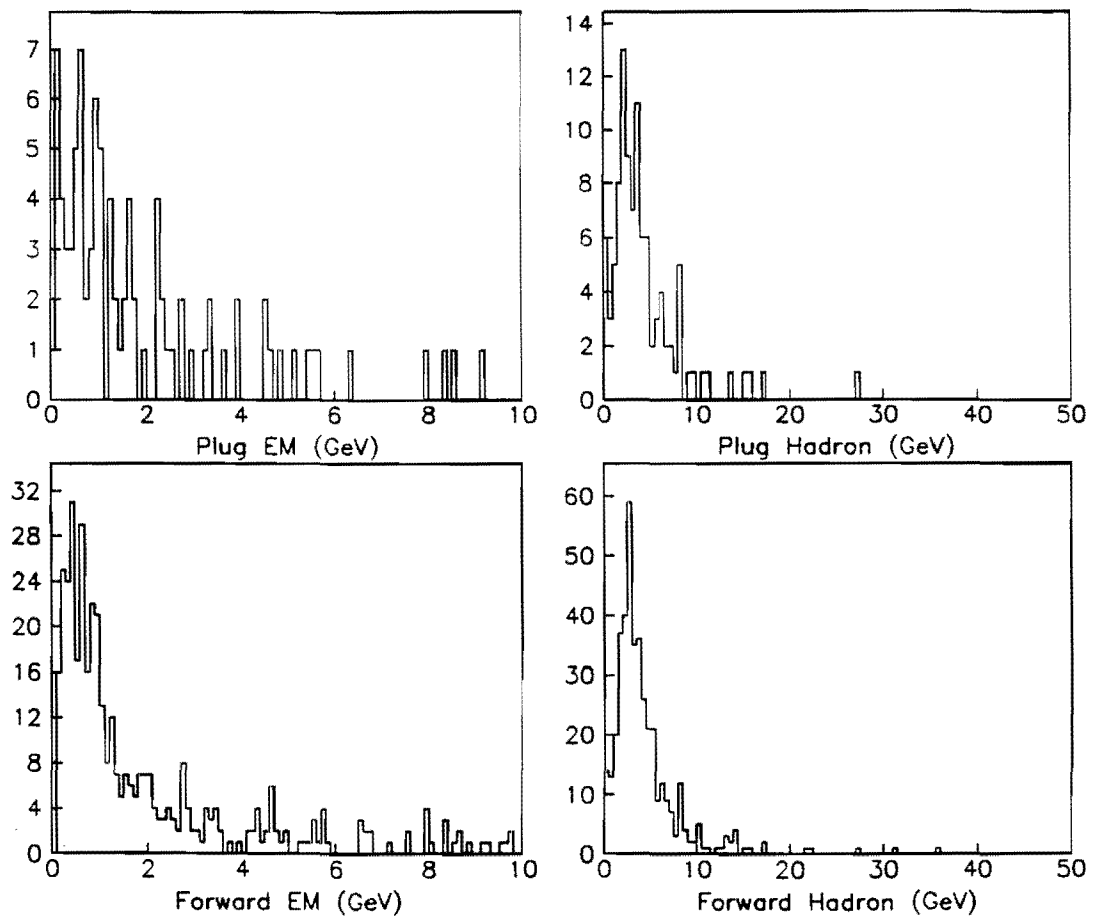


Figure 3.25: Energy deposition in a 3x3 η - ϕ tower region centered on the forward muon track in the plug and forward electromagnetic and hadron calorimeters after cuts.

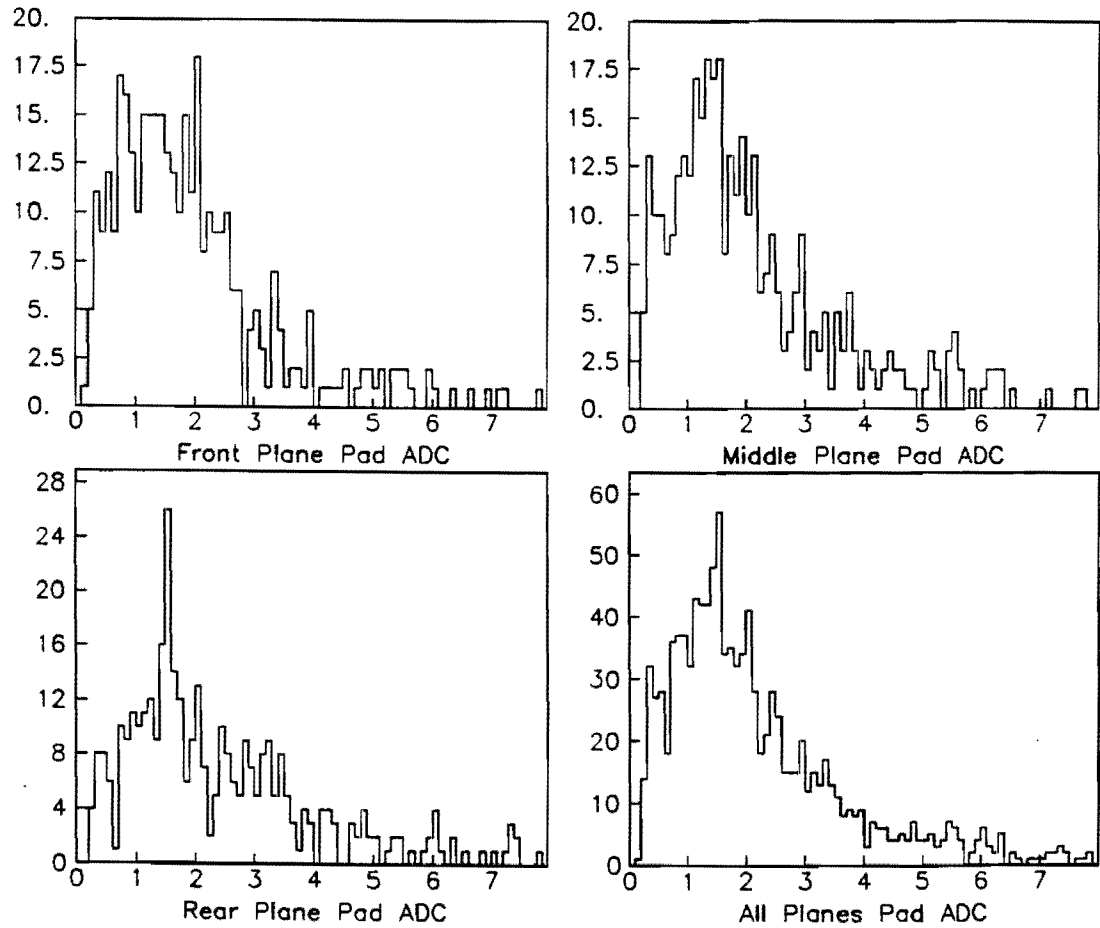


Figure 3.26: Pad pulse height distributions for each chamber plane show a minimum ionizing peak for muon tracks within our sample. Units are 10^3 ADC counts.

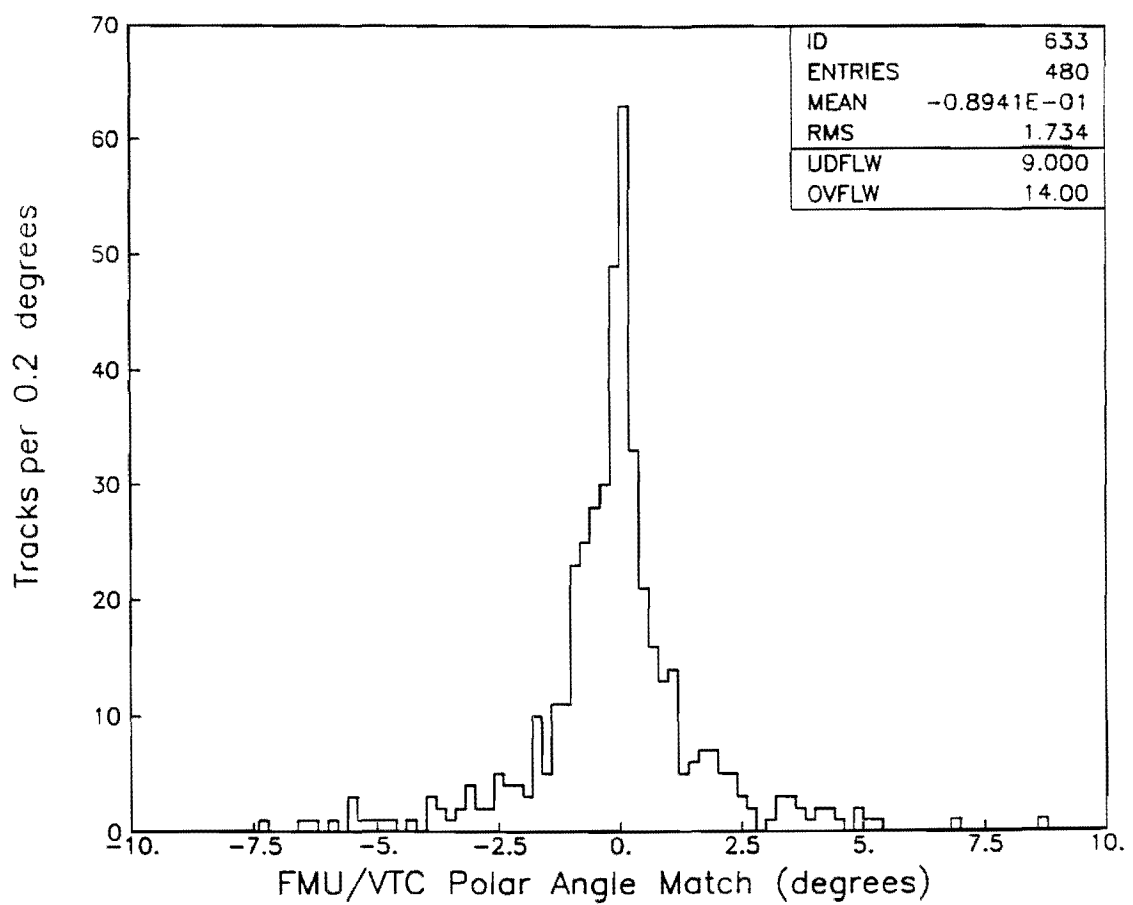


Figure 3.27: Polar angle match distribution between FMU and VTPC tracks.

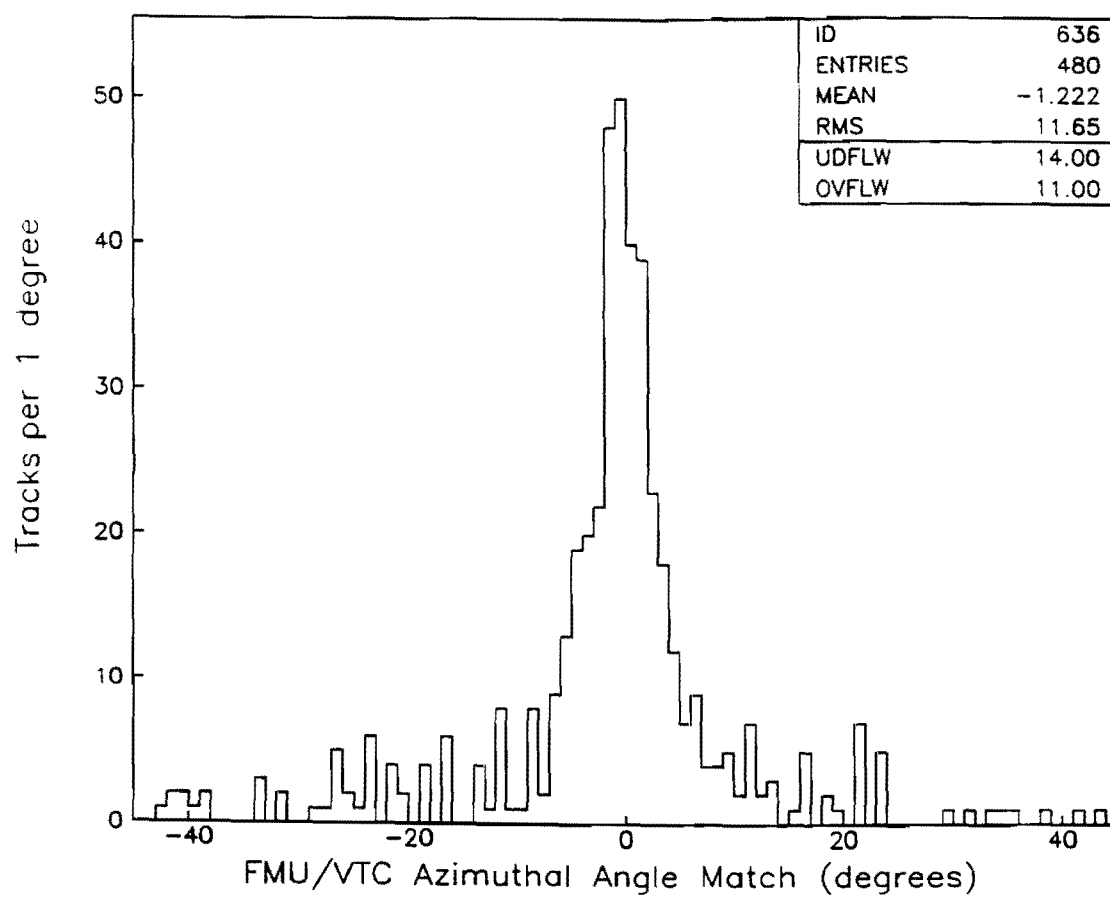


Figure 3.28: Azimuthal angle match distribution between FMU and VTPC tracks.

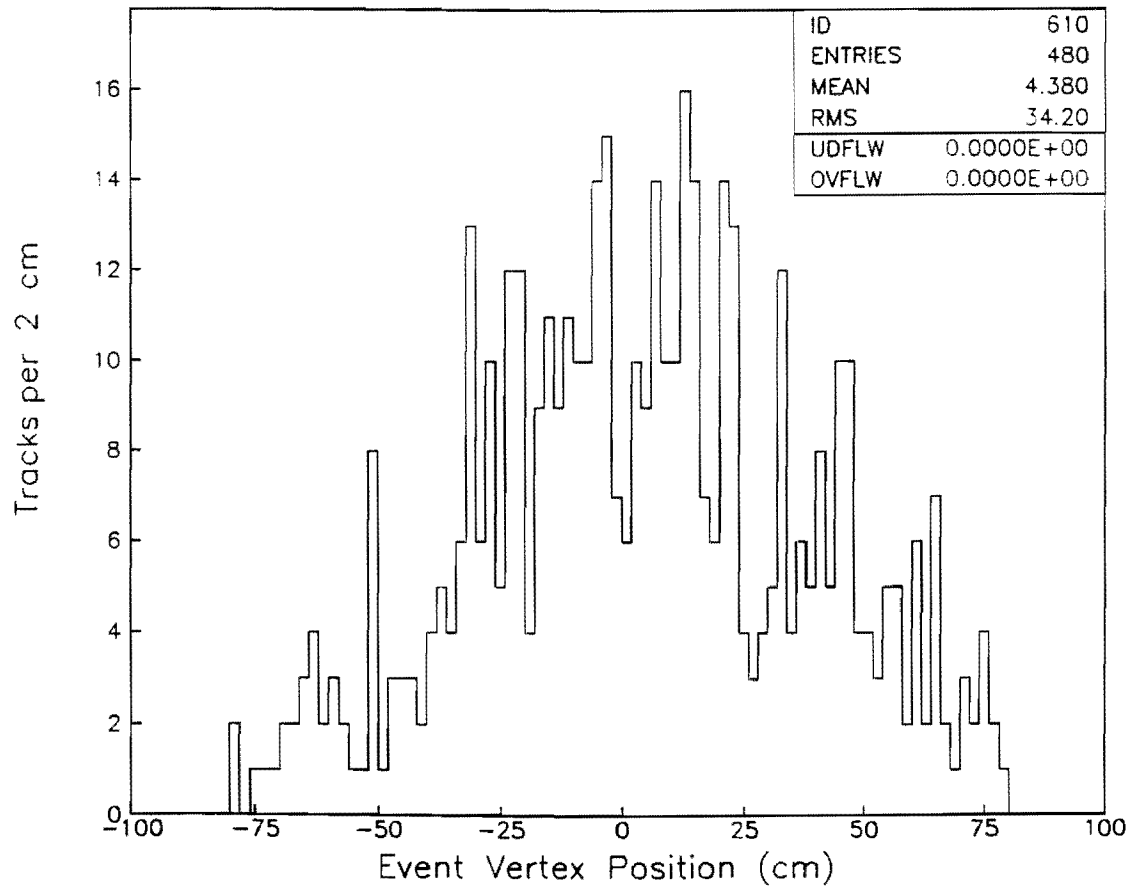


Figure 3.29: Event vertex distribution for our sample.

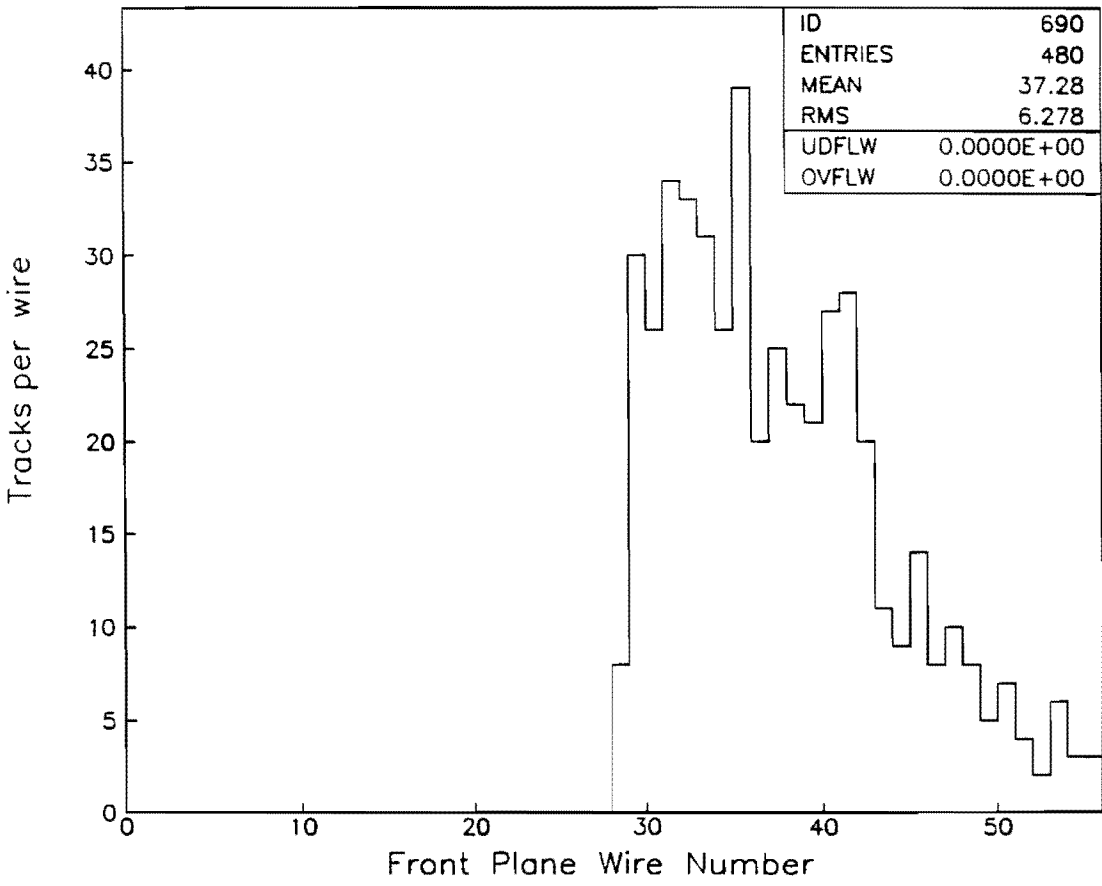


Figure 3.30: Front plane coordinate wire number distribution for our muon candidates.

substantial source of decay-in-flight muons, the first effect is due to the different hadron decay path lengths in the plug (2.2 m) and the forward (7.1 m) regions. As will be discussed in more detail in Chapter 4, the cut-off between the two regions is at a polar angle of $\sim 10^\circ$ and this corresponds roughly to the depleted region of tracks starting at wire number 43. The second effect was discovered using the Monte Carlo simulation and is shown in Figure 3.31. For low p_T tracks, the trigger transverse momentum threshold is found not to be uniform over the acceptance of the system due to the increased path length through the toroids (and thus the increased bend displacement and multiple scattering) at the larger polar angles. Since our distribution contains mostly 2 and 3 GeV/c tracks, the wire number distribution is also distorted by this effect. We see that for 4 and 5 GeV/c p_T tracks the trigger threshold is essentially uniform over the outer HOPU region. This polar angle variation of the trigger threshold at low p_T is included in the acceptance-averaged trigger efficiency curve of Figure 3.11.

The χ^2 distribution for the forward muon tracks in our sample is shown in Figure 3.32. Since we are considering 5- and 6-hit FMU tracks which include the vertex position, we have 6 or 7 measured points on a track. Combine this with a 3-parameter tracking algorithm and the number of degrees of freedom for our tracks is between 3 and 4. Thus, the mean value of χ^2 should be between 3 and 4 and this is the value observed for simulated tracks. On a statistical basis, one would then expect $>99\%$ of the tracks in our sample to have a $\chi^2 < 12$. Since we believe our sample to contain nearly all good muons, the χ^2 distribution of Figure 3.32 is

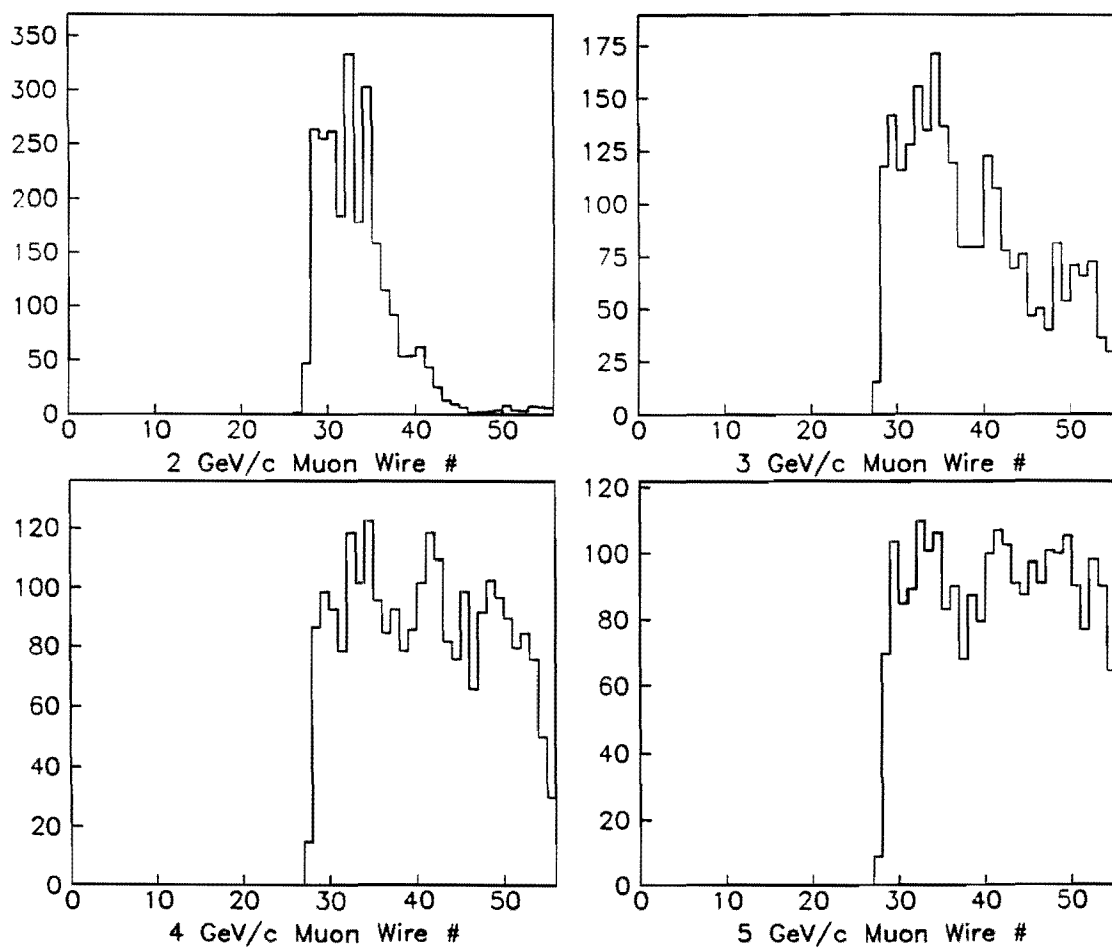


Figure 3.31: Front plane coordinate wire number distributions for 2, 3, 4, and 5 GeV/c simulated muon tracks.

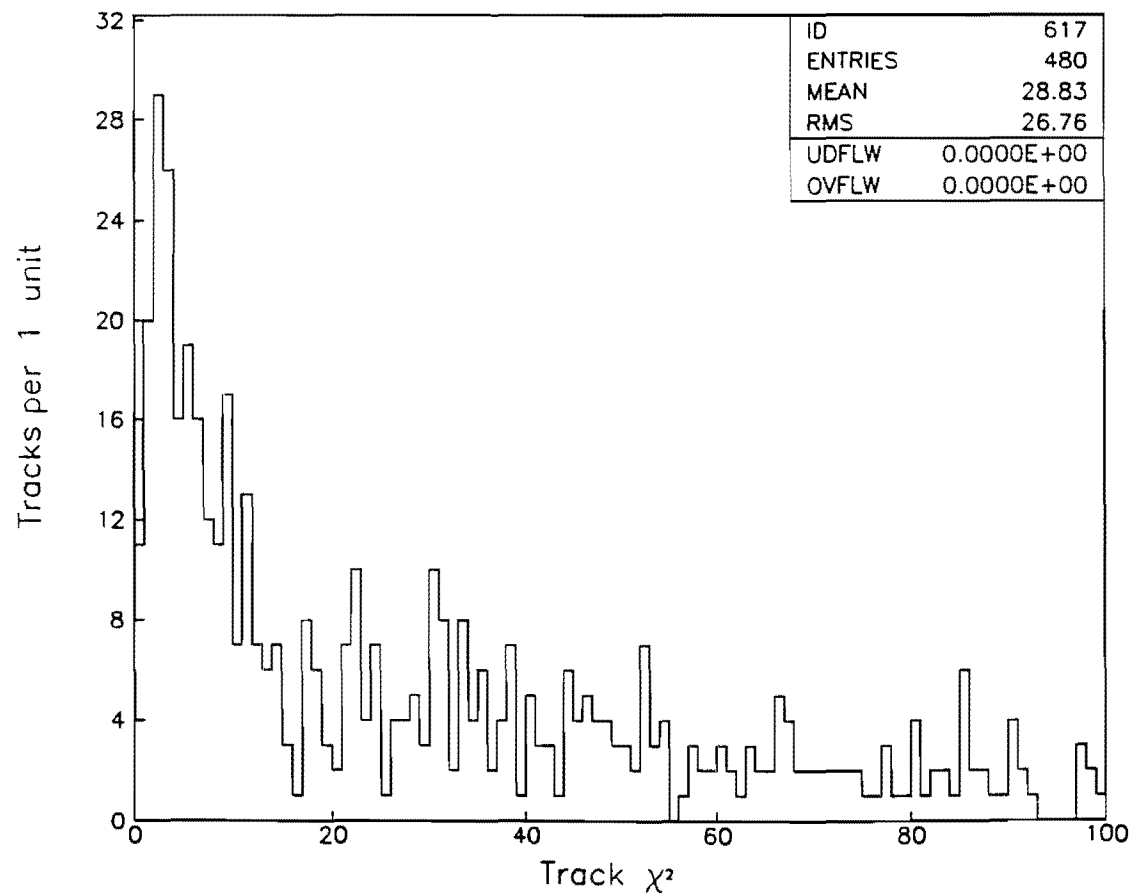


Figure 3.32: χ^2 distribution for FMU tracks in our sample.

not correctly normalized and indicates additional measurement error. The loose $\chi^2 < 100$ cut described above was however very useful in rejecting fake tracks which managed to satisfy both the calorimetry energy and VTPC matching cuts.

Figure 3.33 shows the track residual distribution for our sample. The residual distribution is very well-centered and has an rms value of 864. microns. The width of the residual distribution also indicates some measurement error beyond that of the chamber resolution, but this error is still negligible compared to multiple scattering effects for the relatively low momentum tracks considered in our sample (from Equation 2.32, $\Delta y = 864.$ microns for $p = 355$ GeV/c). Sources of this additional measurement error include alignment errors, t_0 offset variations, and drift velocity fluctuations.

Our primary interest is in the inclusive forward muon transverse momentum spectrum, shown on a linear scale in Figure 3.34. We need to apply a few corrections to this spectrum before we can consider its source. The first correction is one of detector acceptance due to dead channels. Figure 3.35 shows the pseudorapidity distribution for tracks in our sample. By symmetry, one would expect equal numbers of tracks with negative (west side) and positive (east side) pseudorapidities. After cuts, our sample contains 269 tracks (56.0%) on the west side and 211 tracks (44.0%) on the east side. The difference in the number of east and west tracks is due to dead channel and chamber gain fluctuations. Because of the large number of electronic channels in the FMU system, the channels were multiplexed to reduce cost. The disadvantage of a multiplexing scheme is that a

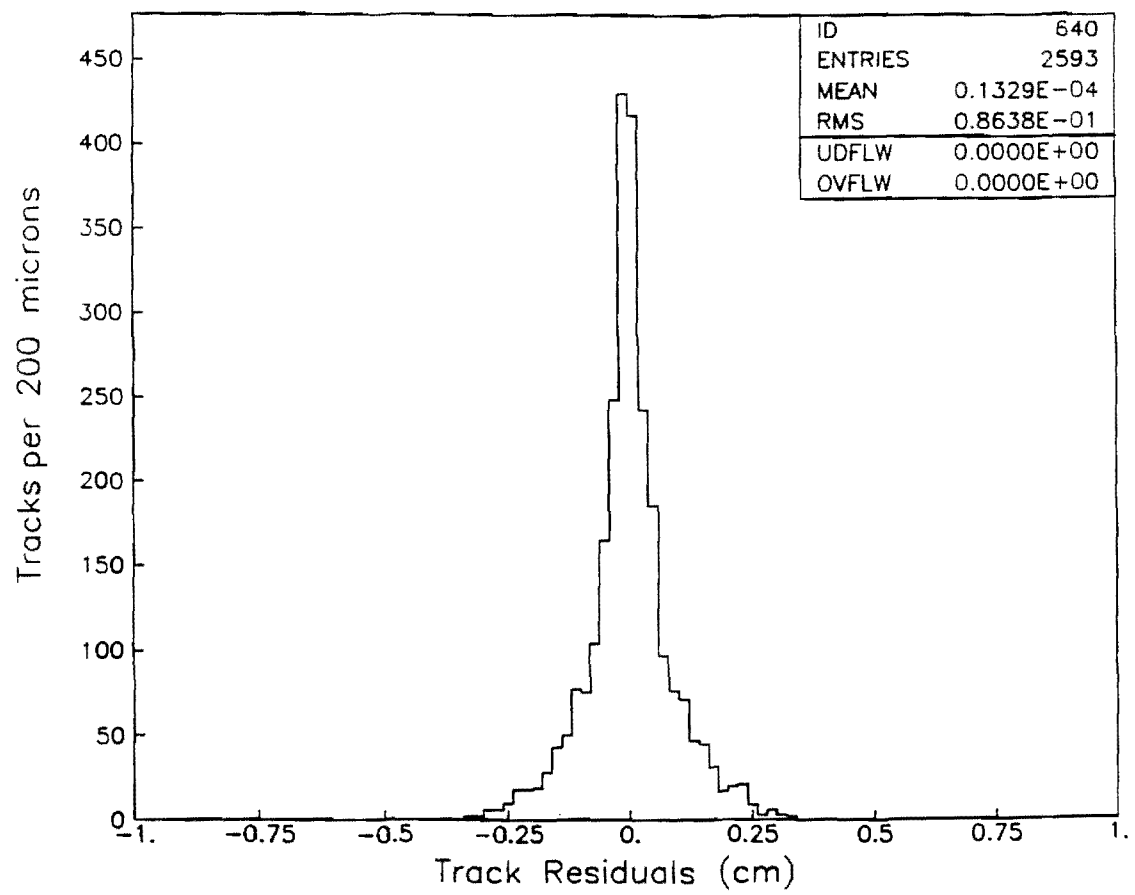


Figure 3.33: Track residual distribution for our data sample.

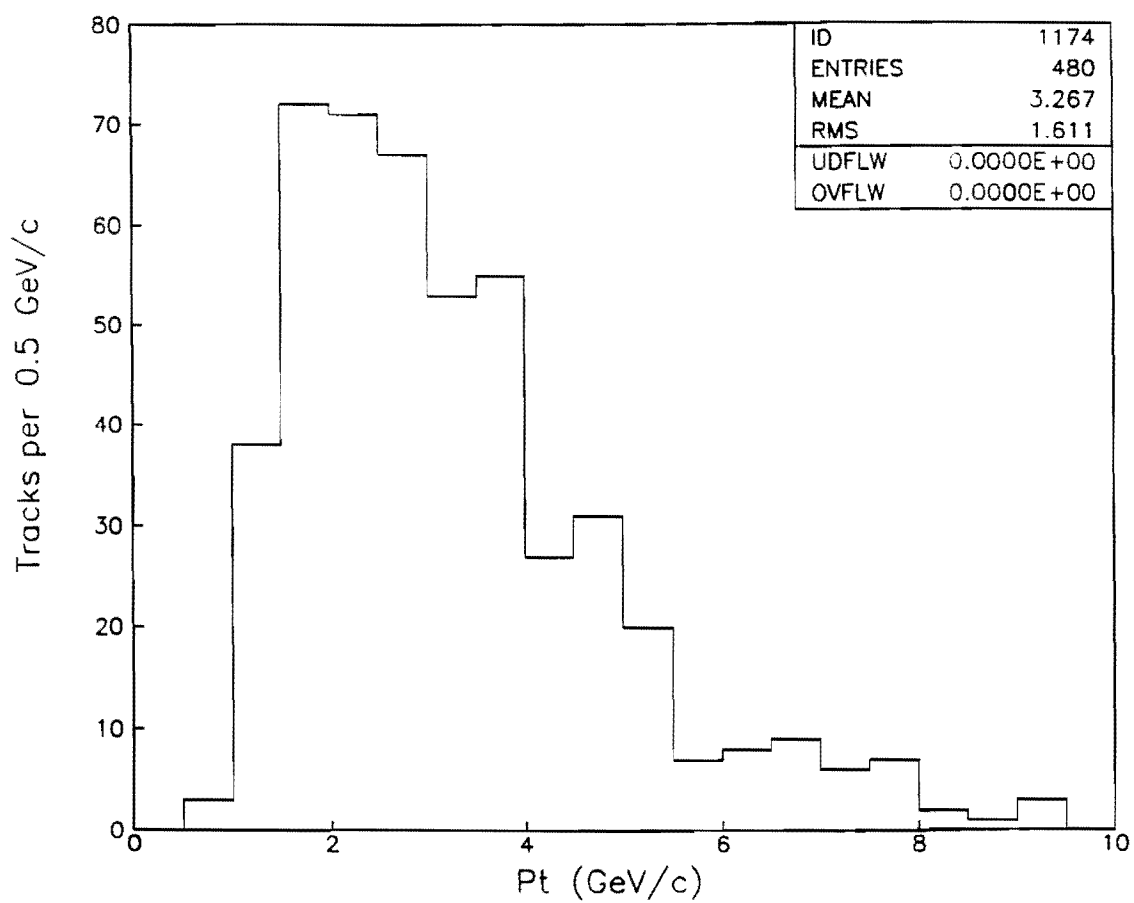


Figure 3.34: Forward muon p_T spectrum after cuts. (linear scale)

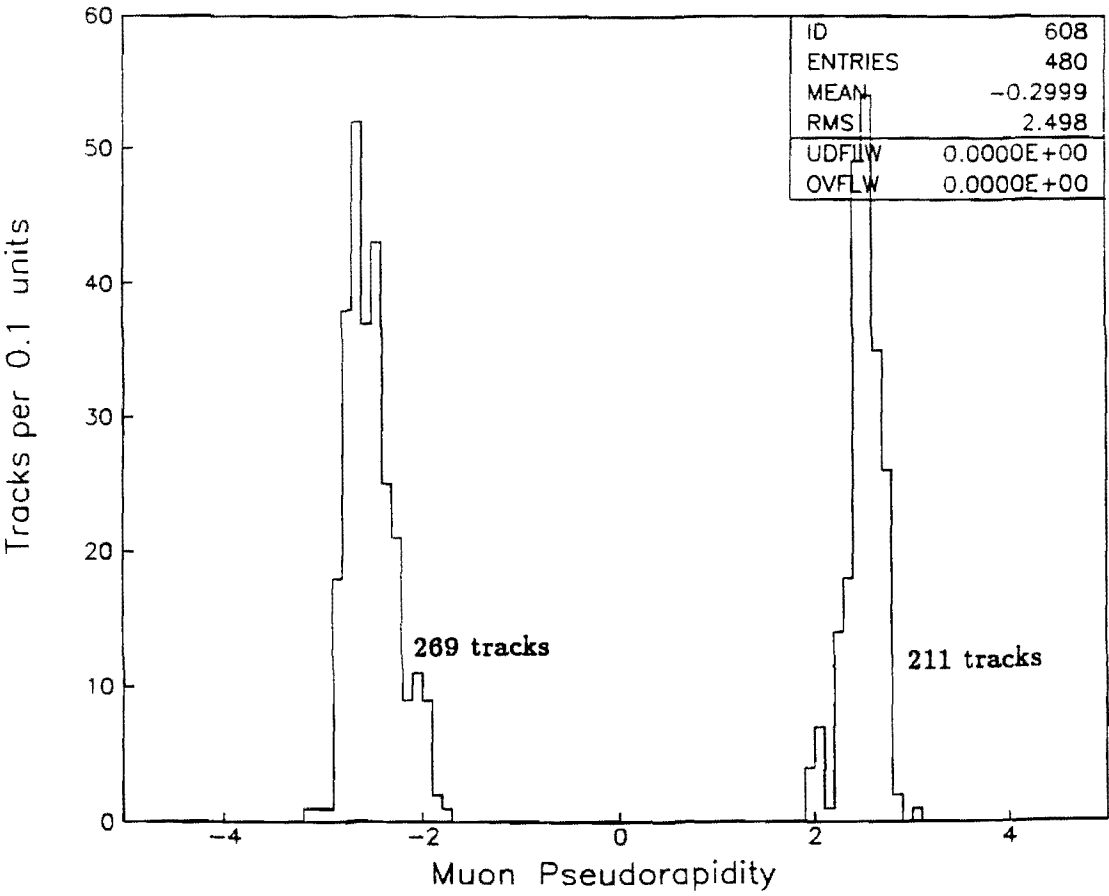


Figure 3.35: Forward muon track pseudorapidity distribution.

few dead or hot channels will often disable many times their number and cause significant fluctuations in acceptance. These acceptance variations are also seen in the azimuthal angle or phi distribution of our tracks (Figure 3.36), which is expected to be uniform. This is most dramatically observed in the variation in octant occupancy on the east and west side separately, shown in Figures 3.37 and 3.38, since chamber dead channels tended to come in units of octants or fractions thereof.

Figure 3.39 shows the reduced forward muon system acceptance due to known chamber dead channels as a function of run number. These dead channels were determined from gaps in the wire hit multiplicity distributions. A correction was made run-by-run for this reduced system acceptance and this resulted in a $\sim 15\%$ increase in the total number of tracks. The total number of tracks after chamber dead channel corrections is 565.

There still remains a correction due to trigger dead channels and chamber gain variations. This correction was determined from a sample of 10,003 muon tracks taken during special zero toroid field data runs to accumulate a large sample of forward muons. By turning off the toroid magnetic field, the p_T threshold of the 300% trigger was reduced substantially and the rate for decay-in-flight muons overwhelmed the fake track background. After correcting the zero toroid field sample for chamber dead channels, the percentage increase necessary for those octants lacking less than the average number of tracks to obtain the average number was computed. It is believed that since the zero toroid field data and our

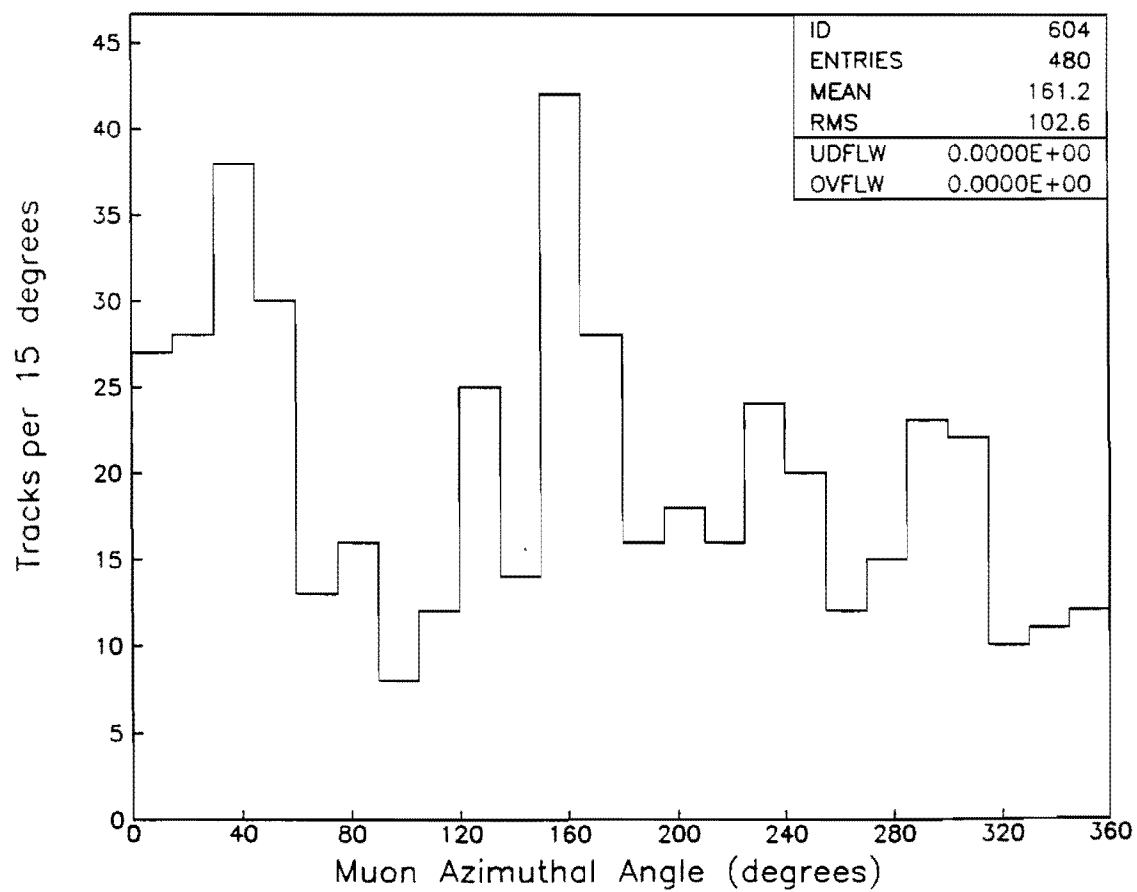


Figure 3.36: Forward muon track phi distribution.

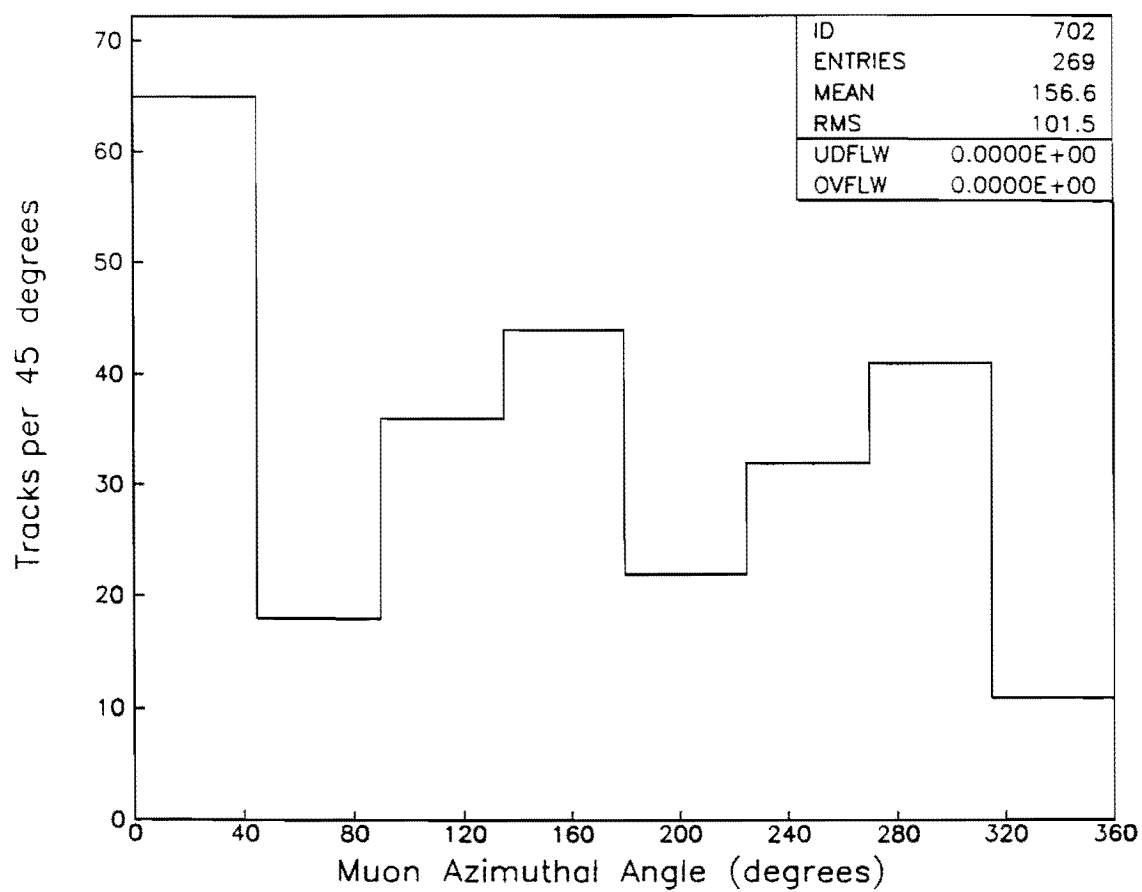


Figure 3.37: Forward muon octant occupancy distribution (west side).

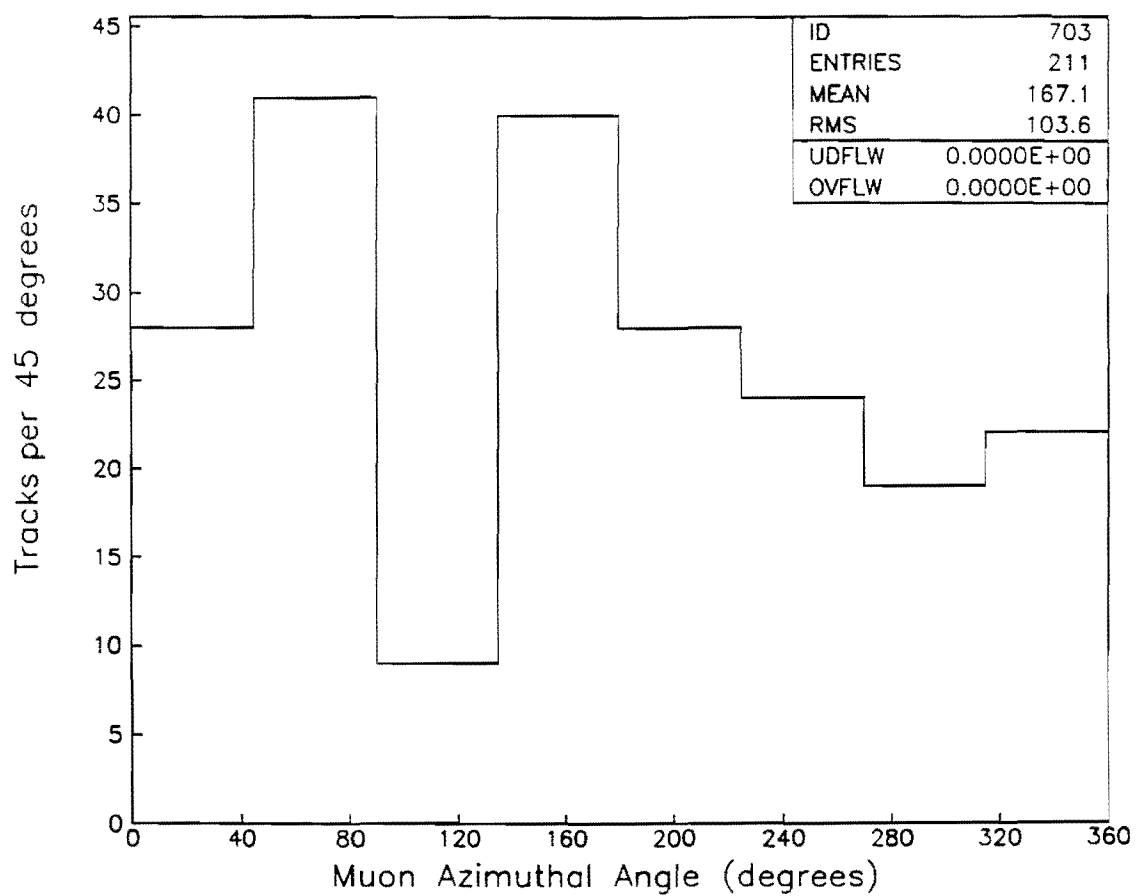


Figure 3.38: Forward muon octant occupancy distribution (east side).

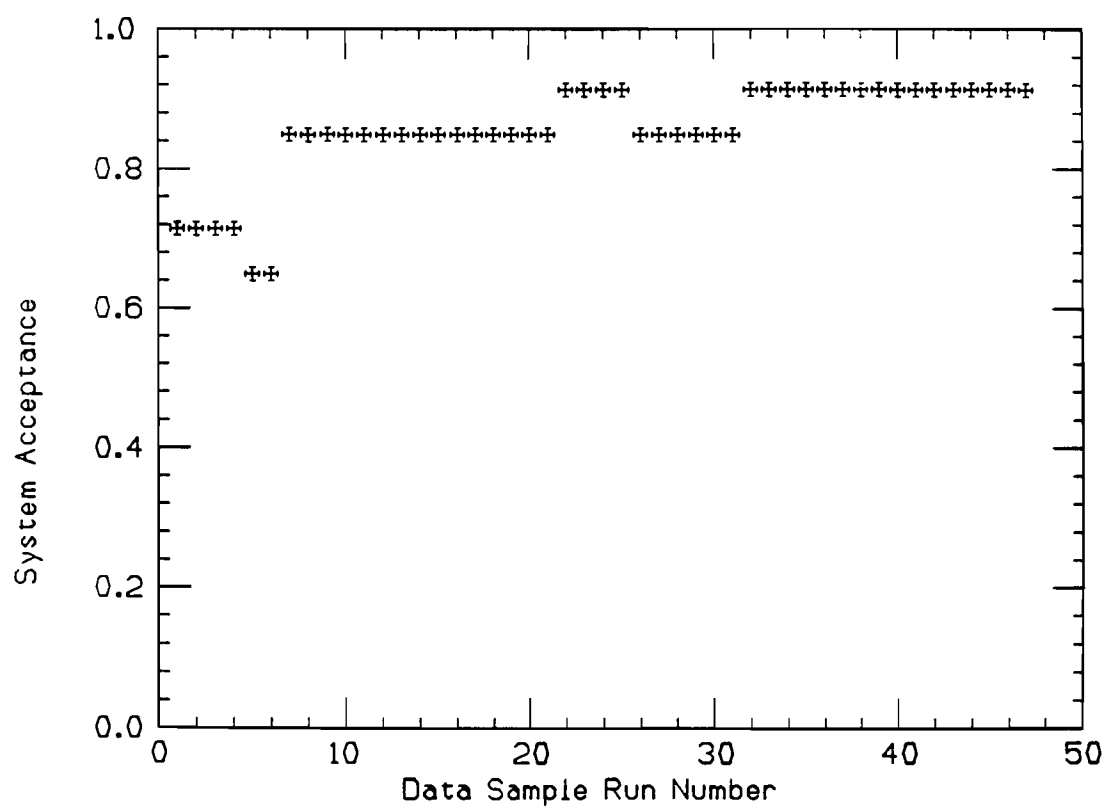


Figure 3.39: Reduced FMU system acceptance due to chamber dead channels.

data sample contain mostly real muons, those octants lacking tracks compared to the average number of tracks/octant were suffering from trigger dead channel and chamber gain variations. These percentage increase values were then applied to our data sample and the ratio of the number of tracks after the increase to that before the increase is given in Figure 3.40.

Figures 3.41 and 3.42 show that the west and east phi distributions after the above corrections are relatively flat. The total number of tracks in our sample has increased to 713 with 377 tracks (52.9%) on the west side and 336 tracks (47.1%) on the east side.

The next corrections to our transverse momentum distribution have to do with chamber detection efficiency. Using the zero toroid field data described above, a handscan of 1000 events found 646 tracks with 3 ambiguity cell hits and 215 tracks with 2 ambiguity cell hits. This was in addition to the 3 coordinate cell hits required by the trigger. Applying binomial statistics to these numbers, the chamber single cell detection efficiency was calculated to be $90.1 \pm .8\%$. The trigger requirement of 3 out of a possible 6 hits then had an efficiency of $(0.901)^3 = 73.1\%$. Given that the trigger needed 3 out of 6 hits, the tracking algorithm then required at least 2 of the remaining 3 hits. Again from binomial statistics, this requirement has a good efficiency of 97.3%. Including a correction for the trigger requirement only, the total number of tracks expected in our sample rises to 975 ± 44 . Figure 3.43 shows our p_T spectrum after corrections. The corrections were all p_T -independent and have increased the number of tracks in our sample

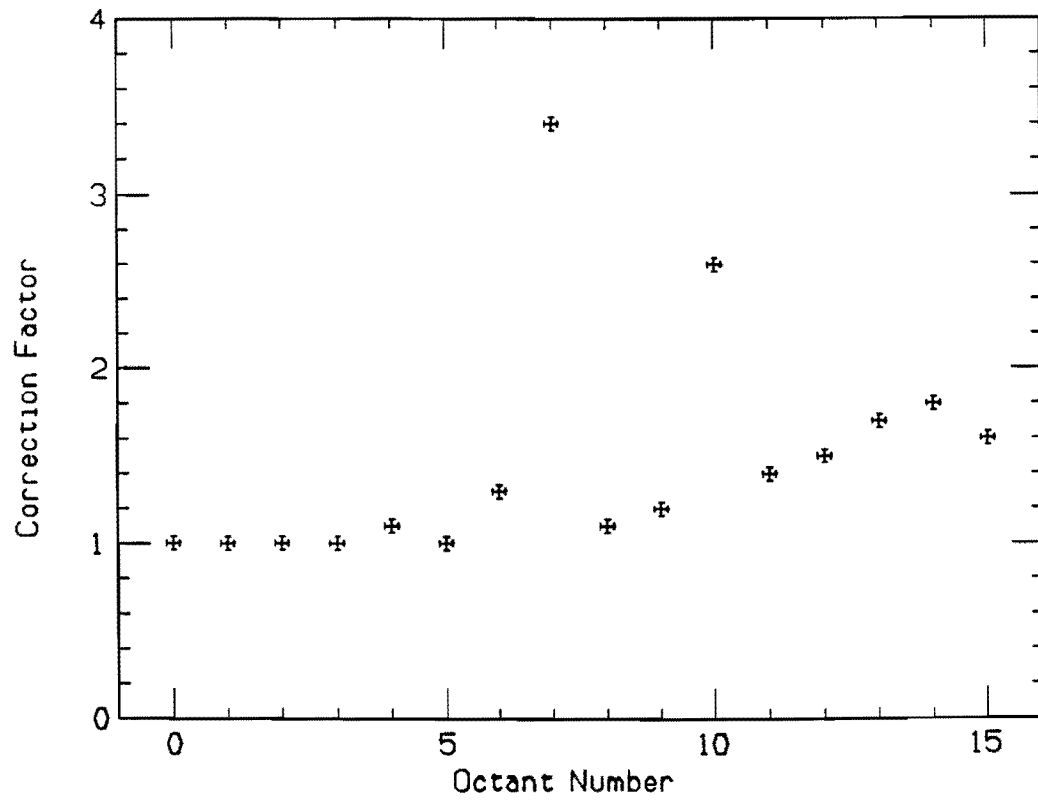


Figure 3.40: Ratio of the number of tracks after correction due to trigger dead channels and chamber gain variations to that before correction. Octants 0-7 are on the west and 8-15 on the east side.

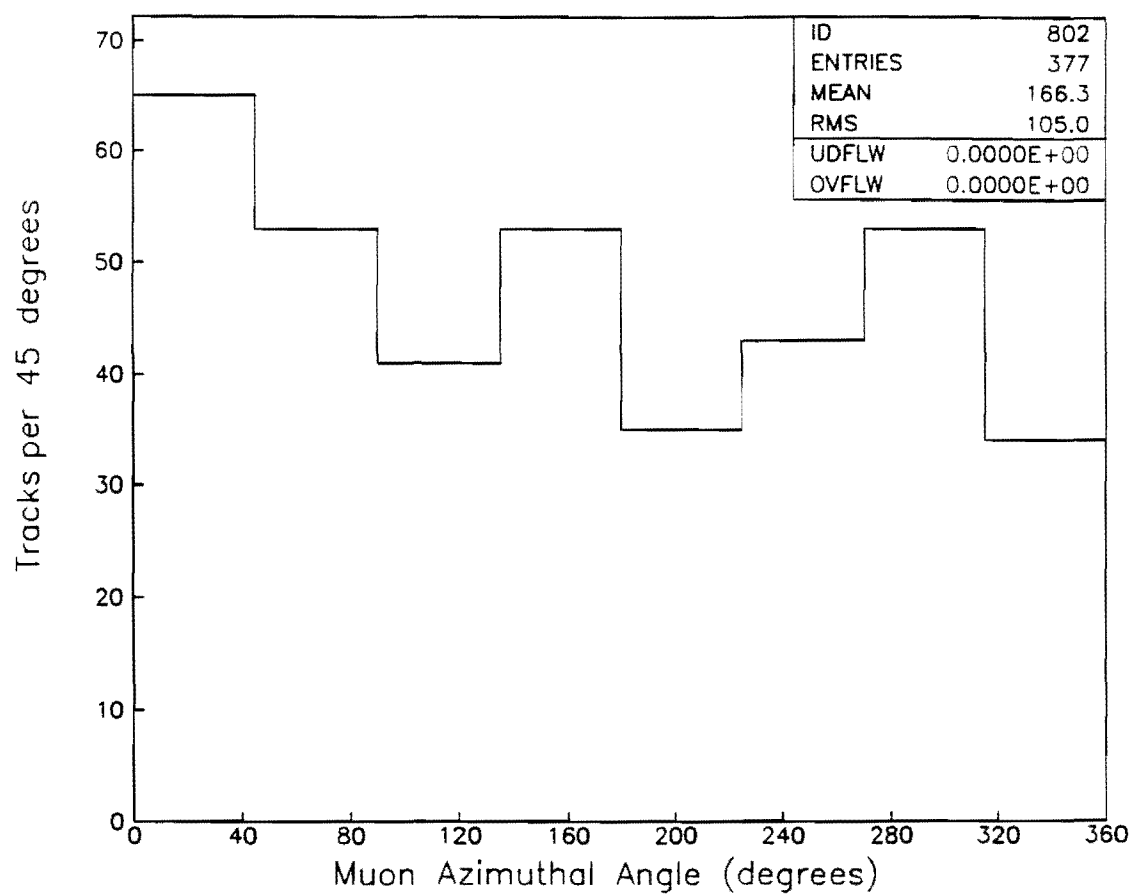


Figure 3.41: West side forward muon octant occupancy after corrections.

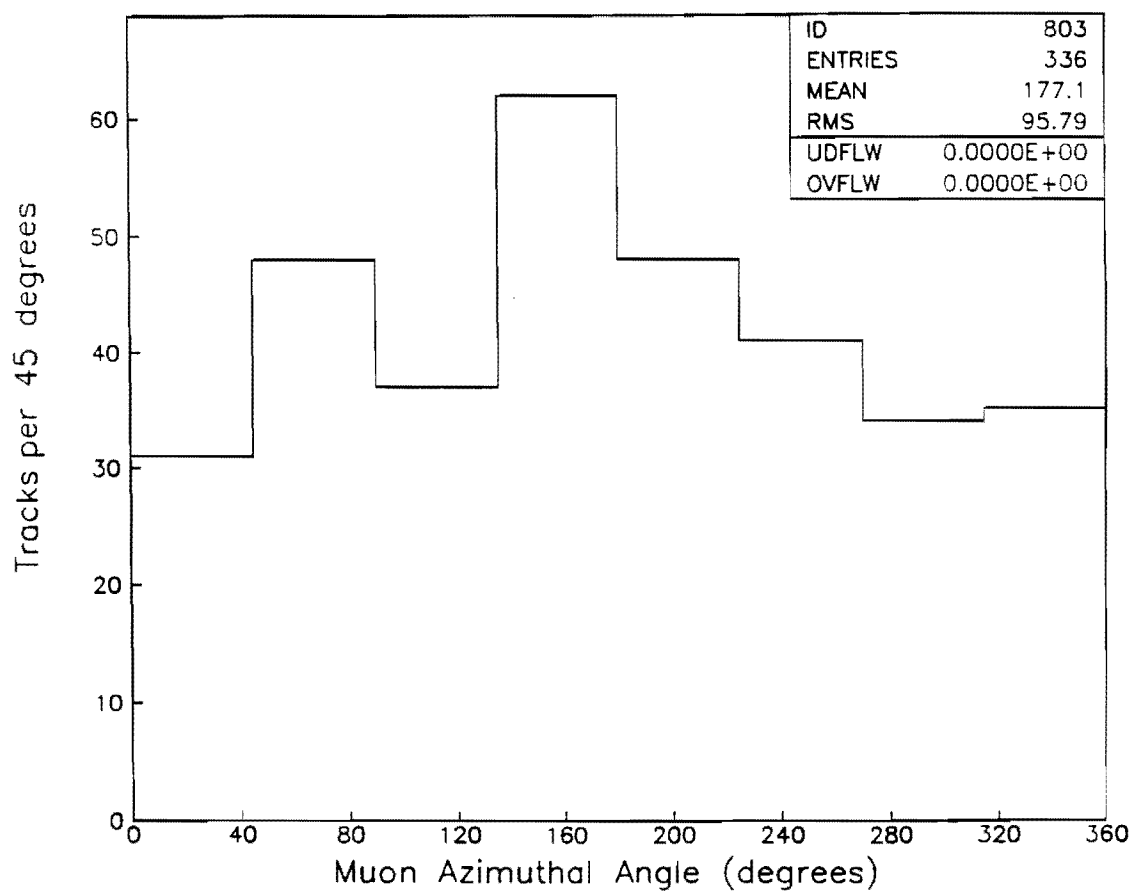


Figure 3.42: East side forward muon octant occupancy after corrections.

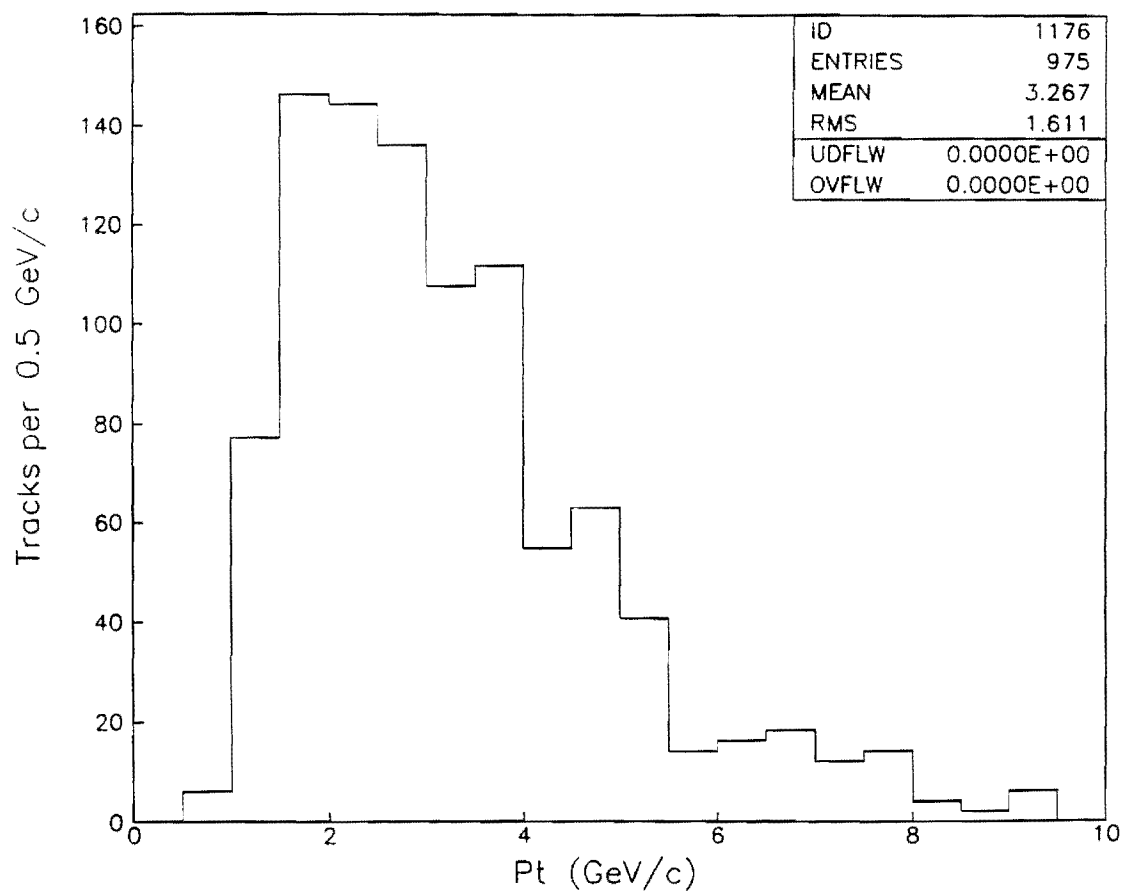


Figure 3.43: Forward muon p_T spectrum after corrections.

by almost exactly a factor of 2 (975 tracks after corrections compared to 480 before). We now consider possible background sources to this spectrum in the next chapter.

Chapter 4

Forward Muon Backgrounds

In this chapter we want to investigate the muon backgrounds in the forward region. The identification of a forward muon depends mainly on the fact that it can penetrate the material of the calorimeters and toroids. There are several possible sources of fake and non-prompt muons and we will consider contributions from the following:

- Cosmic rays;
- Leakage through gaps in the detector;
- Hadronic shower punchthrough;
- Misidentification;
- Delta rays;
- Decays of pions and kaons in flight.

4.1 Cosmic Rays

To determine the background contribution from cosmic rays, dedicated beam-off cosmic ray data was taken early in the run under the same trigger conditions, except for the BBC requirement, as our sample (300% trigger threshold, outer HOPU region). This data consisted of 1500 cosmic ray triggers over a 2696 second time period. Of these 1500 triggers, only 16 muon tracks were reconstructed with a vertex position less than 80.0 cm and would have therefore made it into our sample. During colliding beam data-taking cosmic rays have only a 60 nanosecond time window in which to be accepted and this window occurs only every 7.7×10^{-4} seconds, which corresponds to a beam-beam counter trigger rate of 1.3 kHz at the sample average instantaneous luminosity of $2.8 \times 10^{28} \text{ cm}^{-2} \text{ sec}^{-1}$. Including the standard factor of 2 in the accidental coincidence calculation and with a 2.90×10^4 second livetime for our sample, we compute the following number of background cosmic ray events in our data:

$$\frac{1500 \text{ triggers}}{2696 \text{ s}} \times \frac{16 \text{ tracks}}{1500 \text{ triggers}} \times \frac{2 \cdot 60. \times 10^{-9} \text{ s}}{7.7 \times 10^{-4} \text{ s}} \times 2.90 \times 10^4 \text{ s} = 2.7 \times 10^{-2}, \quad (4.1)$$

which is negligible.

4.2 Leakage Through Gaps in the Detector

As described in Chapter 2, great effort was made to reduce the dead areas in the forward muon system. The chambers and counters were designed to overlap, resulting in full coverage in azimuth. The chamber cell walls compose the principle

dead regions and account for only $\sim 3\%$ of the total detection area. Therefore, muon leakage through gaps in the detector may be neglected.

4.3 Hadronic Shower Punchthrough

In the central region at CDF, hadronic shower punchthrough is in fact a very important background. There are only 5 interaction lengths of material in the central calorimeter wedges. This results in 1 out of every 140 pions of 10 GeV/c transverse momentum punching through the calorimeter and being recorded as a muon candidate.[68] In the forward region, however, this is not a problem. Figure 4.1 shows the number of interaction lengths as a function of polar angle encountered by a forward-produced particle. The minimum amount is 17 interaction lengths. The non-interaction or punchthrough probability for hadrons is given by:

$$P(x) = e^{-x/\lambda}, \quad (4.2)$$

where λ is the interaction length of the material and x is distance traveled by the hadron measured in interaction lengths. Thus, we have that e^{-17} or 1 out of every 24 million hadrons of suitable p_T would have punched through the calorimeters and toroids and been recorded as a muon. As a practical matter, however, such a rejection factor (4×10^{-6}) would never be achieved since a hadron shower contains a small fraction of muons from the weak decay-in-flight of unstable hadrons and these decay muons have enormous penetrating power.[69] Figure 4.2

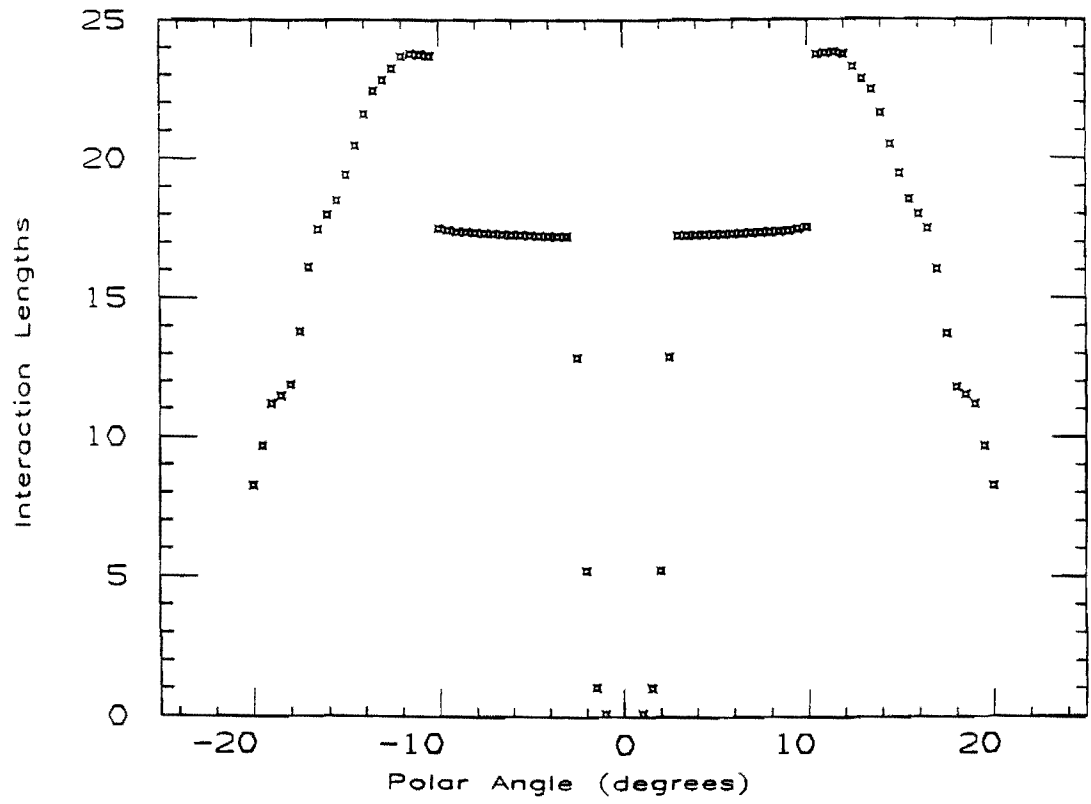


Figure 4.1: Interaction lengths of material versus polar angle in the forward region at CDF. Negative angles are used for the west side of the detector to show the east/west detector symmetry.

shows the punchthrough probability for different momentum hadrons as a function of steel absorber thickness.[70] Because muons penetrate matter much more effectively than hadrons, the probability distributions are characterized by two distinct regions of exponential falloff. In the region immediately after the flat top, the majority of punchthrough particles are hadrons whose non-interaction probability is given by Equation 4.2. In the second region, the dominant source of punchthrough particles is decay muons. Since the average muon momentum for our data sample is 19.9 GeV/c (Figure 3.21) and 17 interaction lengths of steel corresponds to 286. cm of steel, the 25 GeV/c curve of Figure 4.2 gives $\sim 4 \times 10^{-4}$ punchthrough probability. Using the charged hadron spectrum given in Equation 4.25, we calculate that 8.6×10^4 hadrons will be produced with $p_T > 4.3$ GeV/c, corresponding to $p > 25$ GeV/c at $\theta = 10^\circ$, for our integrated luminosity of 0.80 nb^{-1} and $\Delta y = 1.7$ acceptance. This gives 34 punchthrough background events in our sample. The actual number of punchthrough events will be much smaller than this due to the p_T threshold and vertex-pointing requirement in the trigger. We conclude that the background contribution from hadronic shower punchthrough may also be neglected.

4.4 Misidentification

As discussed in Chapter 3, there was a substantial source of fake muon tracks due to the accidental alignment of spurious hits. A set of cuts was outlined

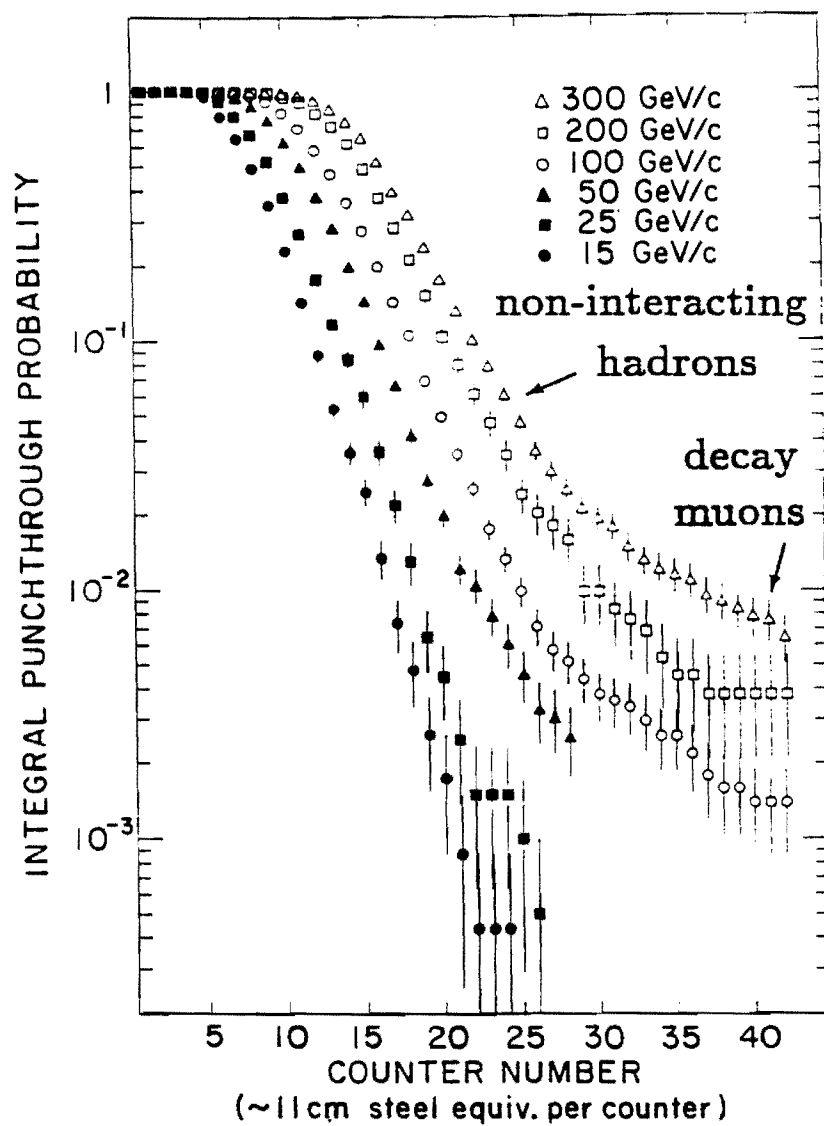


Figure 4.2: Integral probability distributions for hadronic shower punchthrough as a function of steel absorber thickness.

in Figure 3.7 to remove the fake track background and extract a signal of real forward muons. From extensive handscanning and the distributions shown in Chapter 3, specifically Figures 3.27 and 3.28, the misidentification background from fake tracks is $<10\%$ of the total sample.

4.5 Delta Rays

Delta rays may be produced by a forward muon in its passage through the toroids and cause extra hits in the drift chambers which might result in the misreconstruction of the muon momentum due to the wrong hits being used by the tracking program. This background was investigated by determining the extra hit multiplicity and time distributions for each wire plane within the 300% road for muon tracks reconstructed in our data sample and adding such extra hits to Monte Carlo simulated tracks to see the effect on the track-finding and fitting. The time distribution of the extra hits was found to be reasonably flat. The extra hit probabilities were separated into two categories: a) the probability of finding an extra hit within the same cell as a hit used on a fitted track (Table 4.1); and b) the probability of finding an extra hit within the trigger road but in a different cell than the hit used on the reconstructed track (Table 4.2). Examination of the reconstructed p_T spectrum of simulated tracks over the range 2 - 20 GeV/c shows some mismeasurement of tracks at low p_T due to the addition of extra hits. This is indicated in Figure 4.3 where we plot the p_T resolution for the two

Wire Plane	0 Extra Hit Prob.	1 Extra Hit Prob.	2 Extra Hit Prob.	3 Extra Hit Prob.	≥ 4 Extra Hit Prob.
0	90.84	8.06	1.10	0.00	0.00
1	92.31	6.59	1.10	0.00	0.00
2	92.67	6.96	0.37	0.00	0.00
3	94.50	4.40	0.73	0.19	0.18
4	91.95	5.49	2.56	0.00	0.00
5	94.87	4.40	0.73	0.00	0.00

Table 4.1: Probabilities (in %) for having extra hits within the same cell as a fitted hit.

Wire Plane	0 Extra Hit Prob.	1 Extra Hit Prob.	2 Extra Hit Prob.	3 Extra Hit Prob.	≥ 4 Extra Hit Prob.
0	93.77	4.76	1.10	0.37	0.00
1	95.97	4.03	0.00	0.00	0.00
2	92.31	5.49	1.83	0.13	0.24
3	90.11	6.22	1.83	1.47	0.37
4	90.11	8.06	1.10	0.73	0.00
5	94.50	3.30	1.83	0.19	0.18

Table 4.2: Probabilities (in %) for having extra hits within the 300% road but in a different cell than a fitted hit.

cases of extra hits and no extra hits. The tracking program misreconstructed a 2 GeV/c track to have a $p_T > 4$ GeV/c with a probability of 6.6% when extra hits were included. This is compared to a 2.9% probability with no extra hits. Thus, some mismeasurement of tracks can be expected due to the presence of extra hits.

4.6 Decays of Pions and Kaons in Flight

The most important background source of forward muons is the decay of pions and kaons in flight. In order to estimate this decay-in-flight background we use the spectrum of charged hadrons produced in the central region ($|\eta| < 1.0$) at CDF [71]. This spectrum, shown in Figure 4.4, was fit to the form:

$$E \frac{d^3\sigma^h}{d^3p^h} = \frac{A}{(1 + p_T^h/p_0)^n}, \quad (4.3)$$

where $A = 0.45 \times 10^{-24} \text{ cm}^2 \text{ c}^3 \text{ GeV}^{-2}$, $p_0 = 1.30 \text{ GeV/c}$, and $n = 8.28$. For our calculation we assume that this measurement also holds in the forward region ($1.95 < |\eta| < 2.80$). There is some indication that this may be true since $dN/d\eta$, the number of charged tracks per unit of pseudorapidity, is constant at a preliminary value of 4.3 for the entire interval $|\eta| < 3.0$. [72]

With $d^3p = dp_x dp_y dp_z = p_T dp_T d\phi dp_{||}$ and $dp_{||} = (E/c)dy$, we can write:

$$c \frac{d^3\sigma^h}{p_T^h dp_T^h d\phi dy} = \frac{A}{(1 + p_T^h/p_0)^n}. \quad (4.4)$$

Integrating both sides of this equation, the inclusive charged hadron production

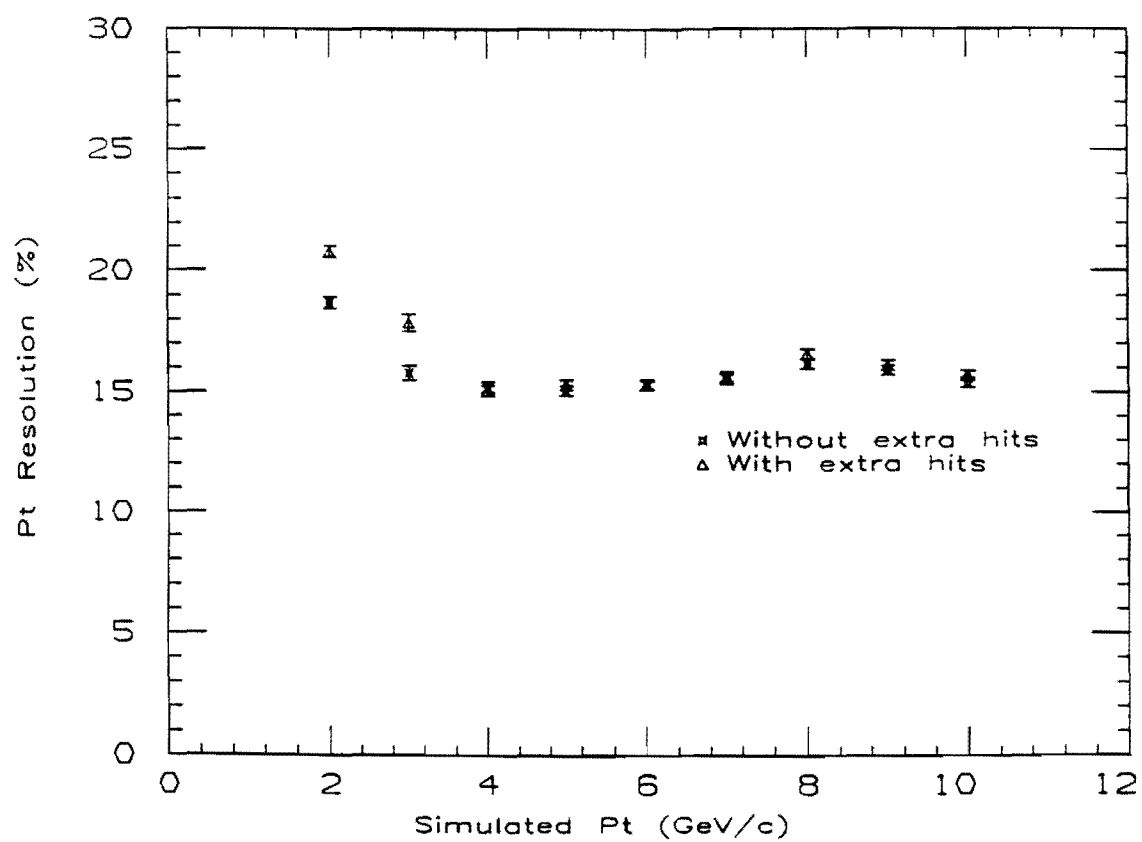


Figure 4.3: The p_T resolution for the two cases of extra hits (delta rays) and no extra hits.

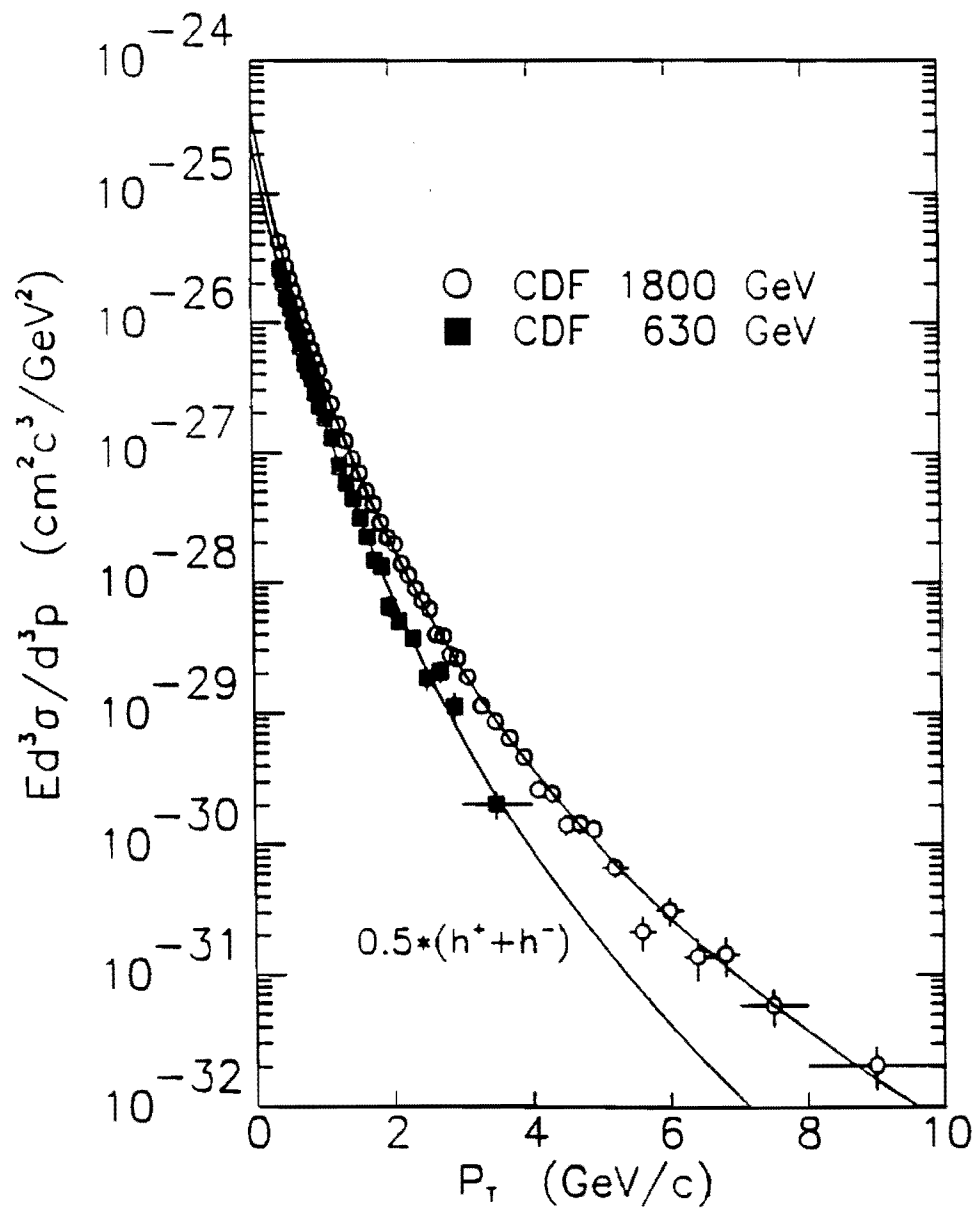


Figure 4.4: The CDF inclusive charged hadron p_T spectrum.

cross section is given by:

$$\sigma^h = \frac{1}{c} \int \int \int \frac{A p_T^h}{(1 + p_T^h/p_0)^n} dp_T^h dy d\phi. \quad (4.5)$$

Now, to go from hadrons to decay muons, we need to consider the following factors:

- 1) $\epsilon_1(\pi/K, p_T^h, \theta)$ = hadron decay probability;
- 2) $\epsilon_2(p_T^\mu)$ = muon trigger efficiency;
- 3) $\epsilon_3(\pi/K)$ = hadron branching ratio to muons;
- 4) $\epsilon_4(\pi/K)$ = hadron species composition percentage in the charged hadron spectrum.

There is also a factor of 2 which needs to be included since we are considering muons of both charge signs and the values for the fitted hadron spectrum are for charge-averaged data. Our cross section for muon production then takes the form:

$$\sigma^\mu = \frac{2}{c} \int \int \int \frac{A p_T^h}{(1 + p_T^h/p_0)^n} \epsilon_1(\pi/K, p_T^h, \theta) \epsilon_2(p_T^\mu) \epsilon_3(\pi/K) \epsilon_4(\pi/K) dp_T^h dy d\phi. \quad (4.6)$$

The decay probability factor $\epsilon_1(\pi/K, p_T^h, \theta)$ is given by the standard exponential decay formula:

$$\epsilon_1(\pi/K, p_T^h, \theta) = 1 - \exp(-x/\lambda), \quad (4.7)$$

where $\lambda = \beta\gamma c\tau = p^h\tau/m$ with values for $c\tau$ and the mass m given in Table 4.3. The maximum value of x is ~ 7 meters and $p^h > 5$ GeV/c typically so that

$x/\lambda \ll 1$ and we can write:

$$\epsilon_1(\pi/K, p_T^h, \theta) = \frac{mx}{p_T^h \tau} = \frac{mx \sin \theta}{p_T^h \tau}. \quad (4.8)$$

Substituting this into Equation 4.6 and integrating over ϕ , we have:

$$\sigma^\mu = \frac{4\pi A}{c} \int \int \frac{1}{(1 + p_T^h/p_0)^n} \frac{mx \sin \theta}{\tau} \epsilon_2(p_T^\mu) \epsilon_3(\pi/K) \epsilon_4(\pi/K) dp_T^h dy. \quad (4.9)$$

To do the rapidity integral, we realize from the following equation [73]:

$$\cosh^2 y = \frac{m^2 + p_T^2 \cosh^2 \eta}{m^2 + p_T^2}, \quad (4.10)$$

that for the particle masses and transverse momentum ($p_T > 1.0$ GeV/c) considered here, $y = \eta$ to a good approximation. Under this assumption, we can use the relation:

$$y = \ln\left(\frac{1 + \cos \theta}{1 - \cos \theta}\right)^{\frac{1}{2}}, \quad (4.11)$$

so that $|dy| = d\theta/\sin \theta$. The angular integral then simplifies to just the polar angle interval over the region considered and Equation 4.9 becomes:

$$\sigma^\mu = \frac{4\pi A}{c} \int \frac{1}{(1 + p_T^h/p_0)^n} \frac{m}{\tau} x \Delta \theta \epsilon_2(p_T^\mu) \epsilon_3(\pi/K) \epsilon_4(\pi/K) dp_T^h. \quad (4.12)$$

We now note that x has two distinctly different values within the forward muon acceptance. This is shown in Figure 4.5 where we have simulated pions and measured their flight path before showering in the plug or forward calorimeters. The error bars indicate 1σ fluctuations in the flight path due to variations in the calorimeter penetration depth in the Monte Carlo simulation before showering. Between 3° and 10° , forward-going hadrons will exit the 10° hole in the

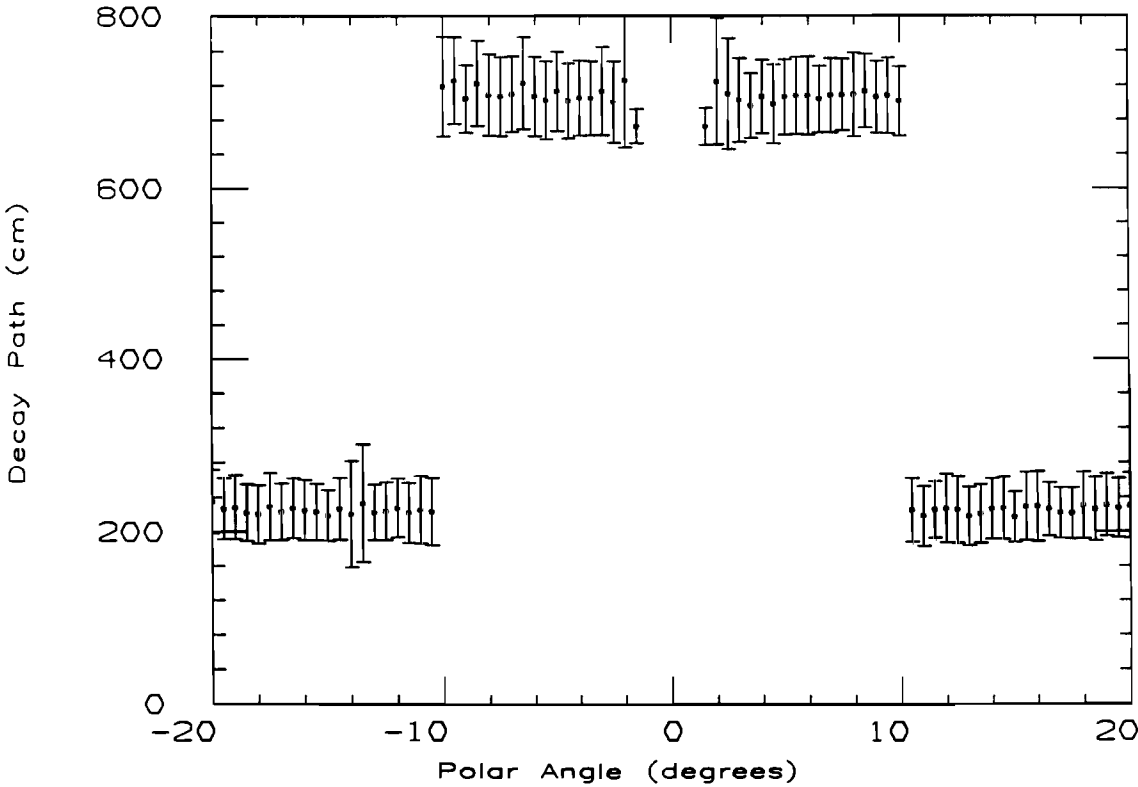


Figure 4.5: Hadron decay path length in the forward region.

plug calorimeter and travel an additional 5.0 meters before striking the forward calorimeter (see Figure 2.3). Above 10° , hadrons strike the plug calorimeter on the central detector. The characteristic distance is 2.2 m and 7.1 m for the plug and forward calorimeters, respectively. So, for the outer HOPU region ($7^\circ < \theta < 16^\circ$), the decay-in-flight path length has the two values:

$$x = 7.1 \text{ m for } 7^\circ < \theta < 10^\circ,$$

$$x = 2.2 \text{ m for } 10^\circ < \theta < 16^\circ.$$

The product $x\Delta\theta$ for both ends of the detector then takes on the value:

$$x\Delta\theta = 2(7.1 \text{ m} \cdot 3^\circ + 2.2 \text{ m} \cdot 6^\circ) \frac{\pi}{180^\circ} = 1.2 \text{ m radians.} \quad (4.13)$$

Equation 4.12 then becomes:

$$\sigma^\mu = 4\pi A(1.2\text{m}) \int \frac{1}{(1 + p_T^h/p_0)^n} \frac{m}{c\tau} \epsilon_2(p_T^\mu) \epsilon_3(\pi/K) \epsilon_4(\pi/K) dp_T^h. \quad (4.14)$$

A muon from pion decay can have a momentum value in the range $0.57p_\pi \leq p_\mu \leq p_\pi$ and one from kaon decay has the range $0.05p_K \leq p_\mu \leq p_K$. If we take the average muon momentum in both cases and consider the tranverse momentum values, then we have that $p_T^\mu = 0.79p_T^\pi$ and $p_T^\mu = 0.53p_T^K$. Splitting up the p_T integral into separate ones over pions and kaons and performing the above change of variables, we have:

$$\begin{aligned} \sigma^\mu = 4\pi A(1.2\text{m}) [& \int \frac{1}{(1 + p_T^\mu/0.79p_0)^n} \frac{m_\pi}{c\tau_\pi} \epsilon_2(p_T^\mu) \epsilon_3(\pi) \epsilon_4(\pi) \frac{dp_T^\mu}{0.79} + \\ & \int \frac{1}{(1 + p_T^\mu/0.53p_0)^n} \frac{m_K}{c\tau_K} \epsilon_2(p_T^\mu) \epsilon_3(K) \epsilon_4(K) \frac{dp_T^\mu}{0.53}]. \end{aligned} \quad (4.15)$$

To calculate the p_T^μ integral, we break it up into the three intervals shown in Table 4.4. For the 1 - 5 GeV/c range, we approximate the integral by a Riemann sum with $\Delta p_T^\mu = 0.1$ GeV/c and $\epsilon_2(p_T^\mu)$ given in Table 4.5. Substituting in values for the various constants, the pion decay-in-flight cross section becomes:

$$\begin{aligned} \sigma^\mu(\pi \rightarrow \mu) = & \frac{4\pi}{0.79}(0.45 \times 10^{-24} \text{cm}^2 \text{c}^3 \text{GeV}^{-2})(1.2\text{m})(1.00)(0.58) \frac{0.1396 \text{GeV}/\text{c}^2}{7.803\text{m}} \\ & \left[\int_0^1 \frac{0.0}{(1 + p_T^\mu/1.03)^{8.28}} dp_T^\mu + \sum_{p_T^\mu=1}^5 \frac{\epsilon_2(p_T^\mu)(0.1 \text{GeV}/\text{c})}{(1 + p_T^\mu/1.03)^{8.28}} + \right. \\ & \left. \int_5^\infty \frac{0.98}{(1 + p_T^\mu/1.03)^{8.28}} dp_T^\mu \right], \end{aligned} \quad (4.16)$$

where from Table 4.3, the branching ratio for pions into muons is $\epsilon_3(\pi) = 1.0$ and the percentage of charged hadrons which are pions is $\epsilon_4(\pi) = 0.58 \pm .12$ [74]. The 20% systematic error associated with the hadron composition percentages is due to the uncertainty in the measured total hadron and pion cross sections by UA2 [75] and the kaon cross section by UA5 [76] at a center-of-mass energy of 540 GeV. There are preliminary indications that the composition percentages are unchanged at $\sqrt{s} = 1800$ GeV.[77]

To determine the error in the muon yield based on the uncertainty in the hadron composition, we start with the following equation for the muon yield, N_μ :

$$\begin{aligned} N_\mu = & N_{\text{HADRON}} \cdot f_\pi \cdot \epsilon_{\text{RECON}}(\pi) \cdot \epsilon_{\text{DECAY}}(\pi) \cdot \epsilon_{\text{BR}}(\pi) + \\ & N_{\text{HADRON}} \cdot f_K \cdot \epsilon_{\text{RECON}}(K) \cdot \epsilon_{\text{DECAY}}(K) \cdot \epsilon_{\text{BR}}(K), \end{aligned} \quad (4.17)$$

where N_{HADRON} is the total number of hadrons in the sample; f_π , f_K are the hadron composition percentages; $\epsilon_{\text{RECON}}(\pi)$, $\epsilon_{\text{RECON}}(K)$ are the probabilities of

Particle	Mass (GeV/c ²)	$c\tau$ (m)	B.R. to μ (%)	Hadron Comp. (%)	Forw. Region Decay Prob. *1/p _T (%)	Plug Region Decay Prob. *1/p _T (%)
π^\pm	0.1396	7.803	100.0	$58 \pm 12.$	1.9	0.9
K^\pm	0.4936	3.709	63.5	$21. \pm 4.$	14.0	6.6

Table 4.3: Properties of pions and kaons.

p_T^μ interval	Trigger efficiency
0 - 1 GeV/c	0.0%
1 - 5 GeV/c	$\epsilon_2(p_T^\mu)$
> 5 GeV/c	98.0%

Table 4.4: The three intervals used to perform the p_T integration.

p_T^μ	$\epsilon_2(p_T^\mu)(\%)$	p_T^μ	$\epsilon_2(p_T^\mu)(\%)$	p_T^μ	$\epsilon_2(p_T^\mu)(\%)$
1.0	0.0	2.4	17.2	3.8	85.6
1.1	0.0	2.5	21.8	3.9	86.3
1.2	0.1	2.6	29.8	4.0	90.0
1.3	0.0	2.7	32.9	4.1	90.0
1.4	0.4	2.8	39.4	4.2	93.7
1.5	0.4	2.9	42.4	4.3	94.5
1.6	1.2	3.0	50.2	4.4	95.2
1.7	1.7	3.1	54.3	4.5	95.3
1.8	2.3	3.2	59.4	4.6	96.7
1.9	4.6	3.3	67.2	4.7	96.8
2.0	4.5	3.4	71.5	4.8	97.3
2.1	9.1	3.5	74.5	4.9	97.2
2.2	10.6	3.6	80.2	5.0	97.8
2.3	12.4	3.7	82.9		

Table 4.5: Trigger efficiency values for the 1 - 5 GeV/c interval.

getting a reconstructed muon; $\epsilon_{\text{DECAY}}(\pi)$, $\epsilon_{\text{DECAY}}(K)$ are the average hadron decay probabilities; and $\epsilon_{\text{BR}}(\pi)$, $\epsilon_{\text{BR}}(K)$ are the decay branching ratios. For a simulated sample of 8,000 hadrons containing 4,000 pions and 4,000 kaons, the reconstructed muon probabilities were 81/4,000 for pions and 29/4,000 for kaons, respectively. The average decay probabilities were $\epsilon_{\text{DECAY}}(\pi) = 1/133$ and $\epsilon_{\text{DECAY}}(K) = 1/18$. With the hadron composition and branching ratio values given in Table 4.3, we have:

$$N_\mu = 8,000 \left(0.58 \cdot \frac{81}{4,000} \cdot \frac{1}{133} \cdot 1.0 + 0.21 \cdot \frac{29}{4,000} \cdot \frac{1}{18} \cdot 0.635 \right) = 1.136, \quad (4.18)$$

for the actual number of decay muons. Using error propagation, the muon yield uncertainty based on the hadron composition error $\sigma(N_\mu)$ is given by:

$$\begin{aligned} \sigma^2(N_\mu) &= \left(\frac{\partial N_\mu}{\partial f_\pi} \right)^2 \sigma^2(f_\pi) + \left(\frac{\partial N_\mu}{\partial f_K} \right)^2 \sigma^2(f_K) \\ &= N_{\text{HADRON}}^2 [(\epsilon_{\text{RECON}}(\pi) \cdot \epsilon_{\text{DECAY}}(\pi) \cdot \epsilon_{\text{BR}}(\pi) \cdot \sigma(f_\pi))^2 + \\ &\quad (\epsilon_{\text{RECON}}(K) \cdot \epsilon_{\text{DECAY}}(K) \cdot \epsilon_{\text{BR}}(K) \cdot \sigma(f_K))^2], \end{aligned} \quad (4.19)$$

where $\sigma(f_\pi) = 0.2 \times f_\pi$ and $\sigma(f_K) = 0.2 \times f_K$. Substituting in the numbers, we find:

$$\sigma(N_\mu) = 0.165, \quad (4.20)$$

for the uncertainty on the muon yield. The systematic error on the muon yield due to the hadron composition uncertainty is then:

$$\frac{\sigma(N_\mu)}{N_\mu} = 14.5\%. \quad (4.21)$$

Performing the integrals of Equation 4.16, we find then find that:

$$\sigma^\mu(\pi \rightarrow \mu) = 1.43 \pm .21 \times 10^{-30} \text{ cm}^2, \quad (4.22)$$

where we include the 14.5% systematic error described above. And, similarly for kaons, we obtain:

$$\sigma^\mu(K \rightarrow \mu) = 0.31 \pm .04 \times 10^{-30} \text{ cm}^2. \quad (4.23)$$

Combining these two values, we have:

$$\sigma^\mu(\pi/K \rightarrow \mu) = 1.74 \pm .25 \times 10^{-30} \text{ cm}^2, \quad (4.24)$$

for the total cross section for muon production from decay-in-flight for our sample. Multiplying this value by the 0.80 inverse nanobarn integrated luminosity for our sample, we obtain $1392 \pm 37 \pm 278$ muons from decay-in-flight, where the first error is statistical and the second reflects the 14% error in the integrated luminosity in quadrature with the 14.5% hadron composition uncertainty to give a total systematic error of $\pm 20\%$. We see that the total yield of 975 ± 44 tracks for our sample is nearly consistent within statistics with a decay-in-flight source.

To compare the shape of our data sample p_T spectrum with that from decay-in-flight and to check our decay-in-flight calculation as well, we use a Monte Carlo simulation. Figure 4.6 outlines the procedure. We start with the measured charged hadron spectrum given in Equation 4.3 and write it in the form:

$$\frac{dN^h}{dp_T^h} = \frac{2\pi A \Delta y L}{c} \frac{p_T^h}{(1 + p_T^h/p_0)^n}, \quad (4.25)$$

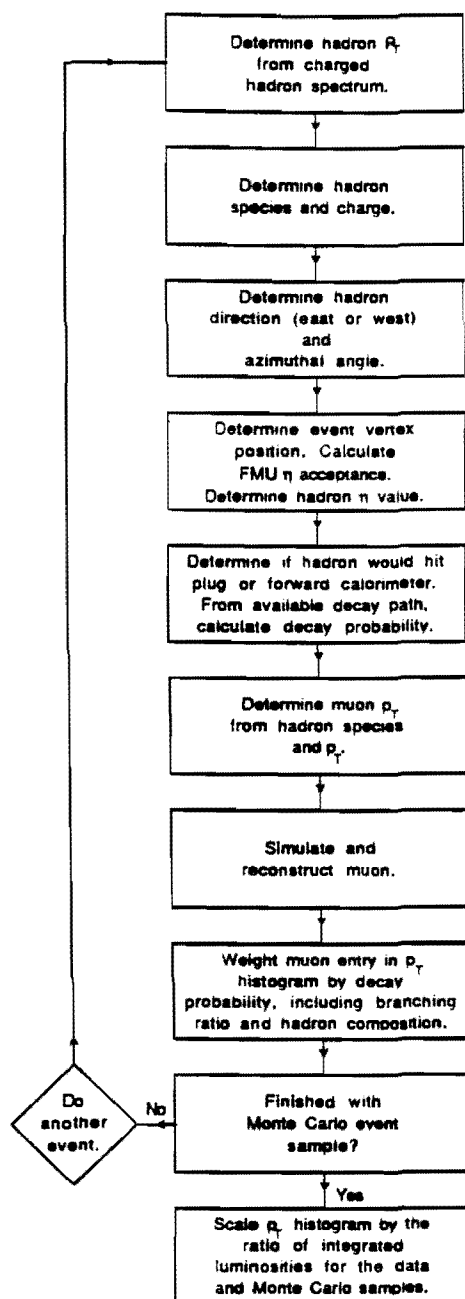


Figure 4.6: Procedure for determining the decay-in-flight background spectrum via Monte Carlo simulation.

where we have integrated over ϕ and expressed the rapidity integral as an interval Δy . We now want to simulate a sample of hadrons whose transverse momentum values are distributed according to Equation 4.25. We do this by using a popular Monte Carlo technique. Consider the normalized integral equation:

$$F(x) = \int_{x_0}^x f(x') dx' / \int_{x_0}^{\infty} f(x') dx'. \quad (4.26)$$

By definition, the slope of the $F(x)$ distribution is $dF(x)/dx = f(x)$. This looks like the equation of a straight line with zero intercept, $y/x = m$, or more commonly, $y = mx$, where m is the slope. Given a value of $F(x)$ between 0 and 1 from a random number generator, then x will necessarily follow the slope or shape of $f(x)$. Using this technique for our hadron spectrum, we have:

$$\text{RAN\#} = \int_{p_N}^{p_T} \frac{p_T}{(1 + p_T/p_0)^n} dp_T / \int_{p_N}^{\infty} \frac{p_T}{(1 + p_T/p_0)^n} dp_T, \quad (4.27)$$

where p_N is the p_T value for which we normalize the spectrum. With this formula we can generate the p_T spectrum of charged hadrons given by Equation 4.25. We choose to normalize to $p_N = 1 \text{ GeV}/c$ transverse momentum to avoid wasting computer time simulating particles which won't contribute to the decay-in-flight spectrum due to the trigger and range-out thresholds of the FMU system. Substituting in for p_N , p_0 , and n and performing the integrals of Equation 4.27, we obtain:

$$\text{RAN\#} = 440.98 \left[\frac{1}{6.28(1 + p_T/1.30)^{6.28}} + \frac{-1}{7.28(1 + p_T/1.30)^{7.28}} \right], \quad (4.28)$$

with p_T in GeV/c . Since we can't solve for p_T explicitly, we throw a random number and search for the p_T value satisfying this equation. Having obtained

the transverse momentum value of our simulated hadron, we next, through a series of random number tosses, determine the hadron species, the charge of the hadron, the direction it is heading (east or west), and its azimuthal angle. The hadron species is obtained using a K/π ratio of $0.21/0.58 = 0.36$. The event vertex position is then found from a Gaussian distribution with a standard deviation of 40.0 cm. Using this vertex position, the pseudorapidity acceptance of the FMU system is determined and the η of the hadron is obtained from a random number throw within this acceptance. The hadron is then projected to the plug and forward calorimeters to determine its available decay path. From this decay path, the decay probability of the hadron is calculated and it is forced to decay. The transverse momentum of the decay muon is then obtained from a random number toss over its allowed range and the muon is simulated and reconstructed. The simulation includes dE/dx energy loss, multiple scattering, the complete detector geometry including survey information, and extra hits (delta rays) distributed according to our data sample. The selection criteria used by the reconstruction program were identical to those used for our data. Since we forced our simulated hadron to decay, it is necessary to weight the reconstructed muon track by the decay probability, including branching ratio and hadron composition percentage. The resulting p_T histogram is then scaled by the ratio of the luminosities for our data and simulated samples. The luminosity of our 30,000 track simulated sample is obtained from Equation 4.25 by integrating over p_T from 1 GeV/c to ∞ and solving for L . Doing so, we find $L = 1.63 \times 10^{-3} \text{ nb}^{-1}$ for our simulated sample

so that the ratio of the luminosities is $0.80/(1.63 \times 10^{-3}) = 491$. This results in our simulated sample containing $790 \pm 28 \pm 158$ tracks, where the first error is statistical and the second error is the $\pm 20\%$ systematic uncertainty described above. The muon yield is lower than the value obtained from the hand-calculation and this is to be expected since the hadron decay kinematics are done correctly and multiple scattering effects are included in the simulation. The agreement with our data sample yield of 975 ± 44 tracks is somewhat improved. Figure 4.7 shows the simulated p_T spectrum. The shape of this spectrum was found to be essentially independent of the mixture of kaons and pions (K/π ratio) used in the simulation. In the next chapter, we will compare this decay-in-flight spectrum with the p_T spectrum from our data sample.

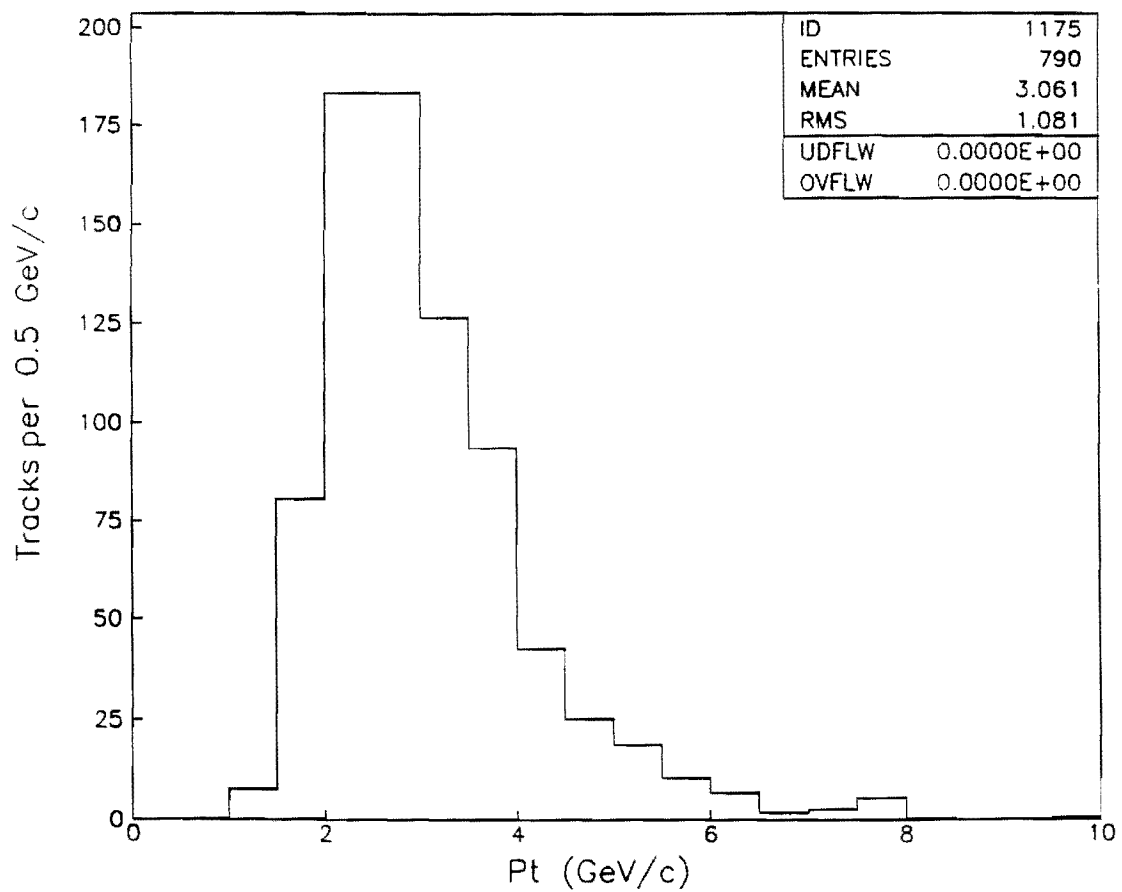


Figure 4.7: Forward muon decay-in-flight spectrum from a simulation of the CDF single particle inclusive spectrum.

Chapter 5

Inclusive Forward Muon Spectrum

In this chapter, we compare our data sample p_T spectrum with that obtained from a Monte Carlo simulation of the expected decay-in-flight background. We then normalize this inclusive spectrum and compare it to the CDF charged hadron and UA1 muon inclusive spectra.

5.1 Decay-in-flight Background Comparison

Figure 5.1 shows a comparison of our inclusive forward muon spectrum obtained in Chapter 3 (Figure 3.43) with that of the Monte Carlo simulated decay-in-flight background from Chapter 4 (Figure 4.7). We cannot really make a meaningful comparison of the two spectra below ~ 3 GeV/c p_T due to the substantial trigger

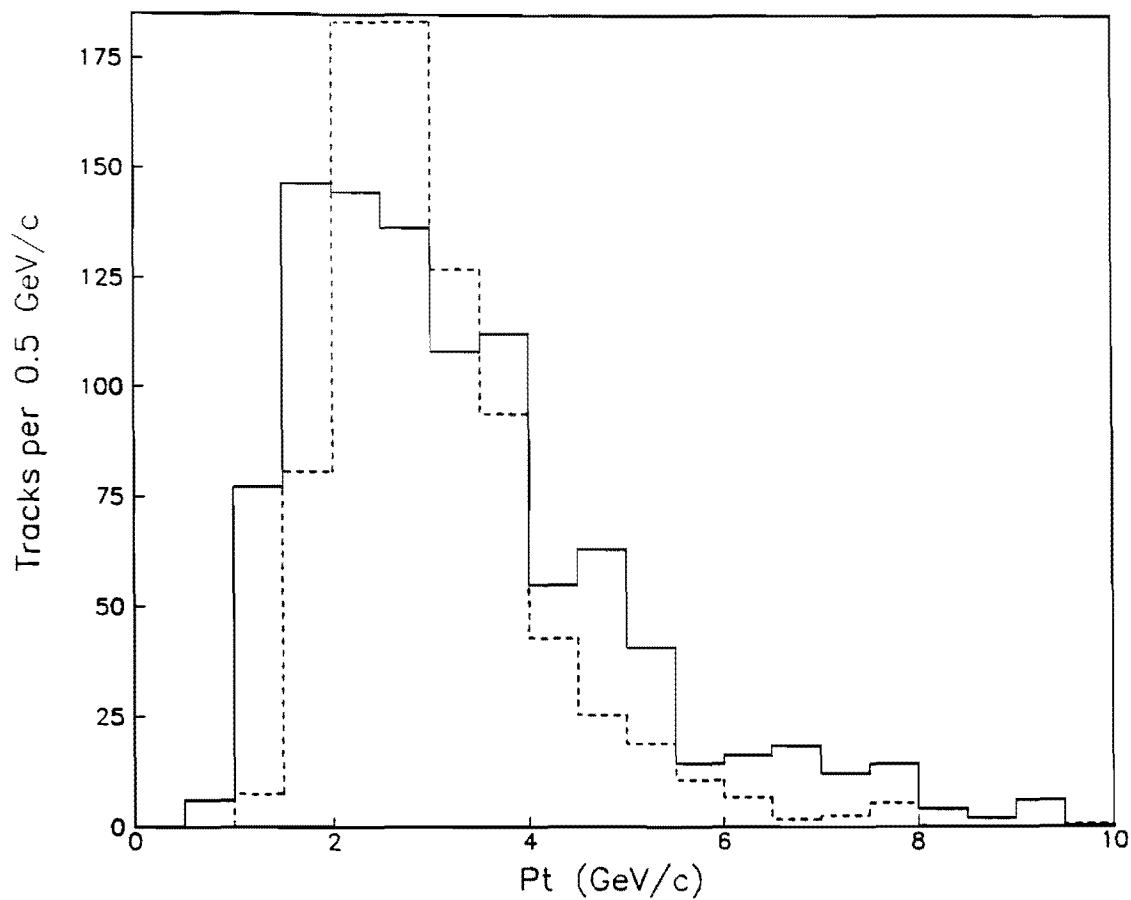


Figure 5.1: Inclusive forward muon spectrum (solid line) compared to the simulated decay-in-flight background (dashed line). The spectra are normalized to the data sample integrated luminosity of 0.80 nb^{-1} .

threshold and range-out effects experienced by these soft muons. Above 4 GeV/c transverse momentum, we do note however an excess of muons beyond those expected from decay-in-flight. This is also seen in Figure 5.2 where we include statistical errors and plot the two spectra on a semi-logarithmic scale. Figure 5.3 shows the background subtracted p_T spectrum above 4 GeV/c. This spectrum contains 131 ± 25 tracks. Investigating these $p_T > 4$ GeV/c muon events, we find that 8 events have jet activity in the calorimetry. As discussed in Chapter 1, this may indicate the presence of muons from heavy quark decay. Figures 5.4 and 5.5 show the forward muon track and calorimetry lego for a candidate heavy quark decay event. In Figure 5.4, the forward muon is very near one of the jets and this would be expected from the weak decay of a bottom quark.

In Figure 5.6, we show the muon p_T spectrum for the 8 events containing jet activity. We can estimate the number of muon+jet events we might expect by using the UA1 result [78] of Figure 5.14. In this figure the differential cross section $d\sigma/dp_T^\mu$ for $p\bar{p} \rightarrow \mu + \geq 1 \text{ Jet}$ ($E_T^{\text{Jet}} > 12 \text{ GeV}$) at $\sqrt{s} = 630 \text{ GeV}$ and $|\eta| < 1.5$ is given. From this curve, we calculate that:

$$\sigma(p\bar{p} \rightarrow \mu + \geq 1 \text{ Jet}; E_T^{\text{Jet}} > 12 \text{ GeV}) = 28.1 \pm 9.5 \text{ nanobarns}, \quad (5.1)$$

for $p_T^\mu > 5 \text{ GeV/c}$. To apply this result to $\sqrt{s} = 1.8 \text{ TeV}$ and $1.95 < |\eta| < 2.80$, we assume $\eta \simeq y$ and use the $d\sigma/dy$ distributions for b quark production at the two center-of-mass energies given in Figure 5.7.[79] From these two curves, we determine the ratio for the total b quark production cross section between the

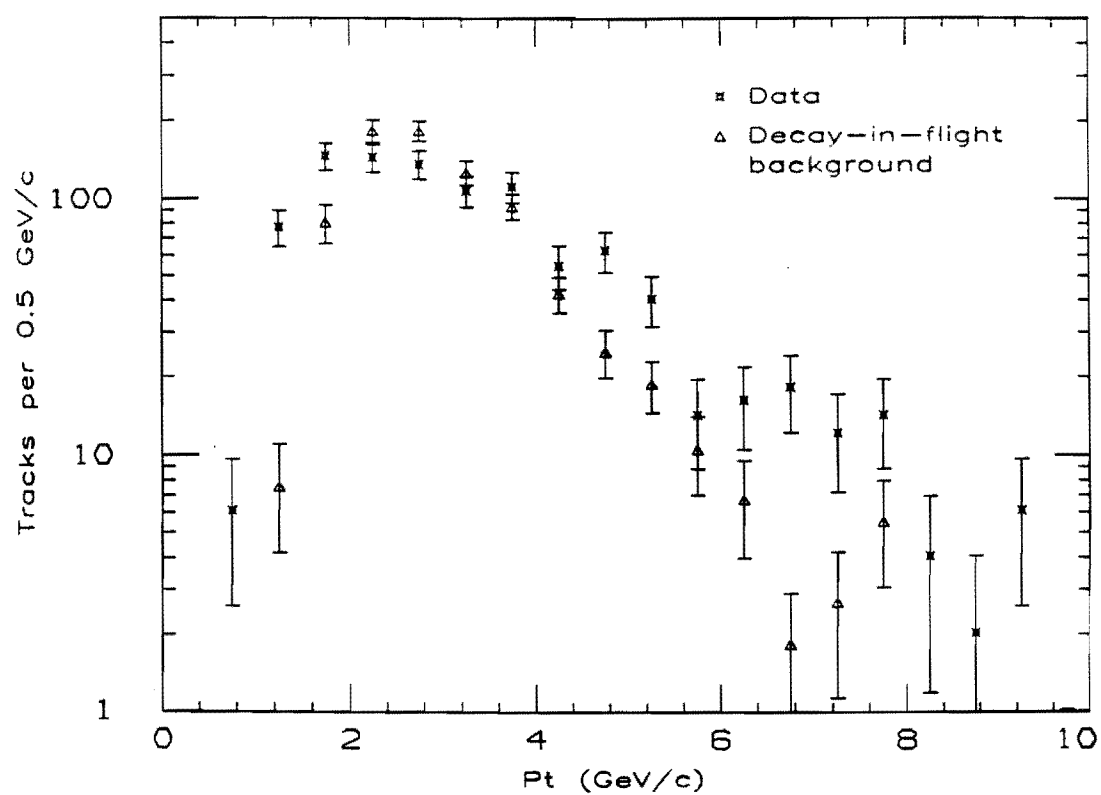


Figure 5.2: Inclusive forward muon spectrum and simulated decay-in-flight background plotted on a semi-logarithmic scale with statistical errors.

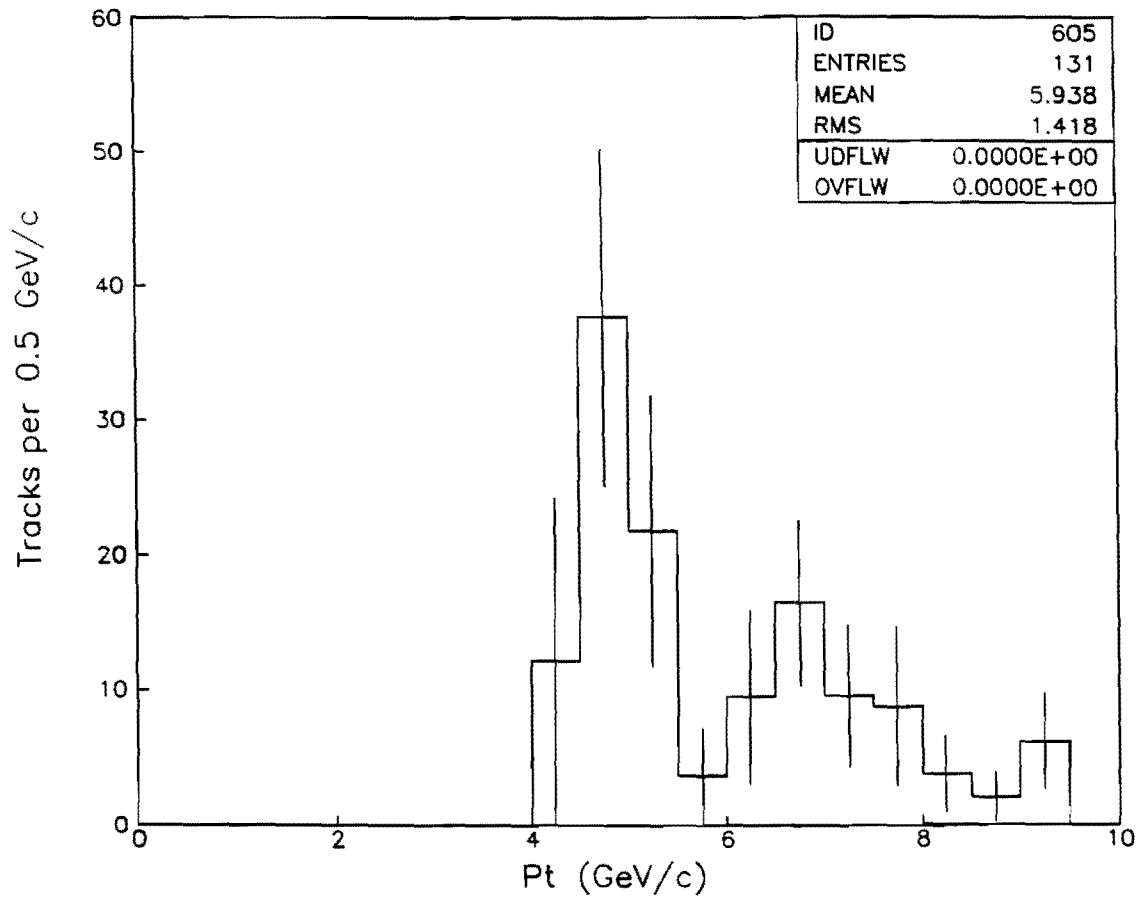


Figure 5.3: Decay-in-flight background subtracted spectrum for $p_T > 4$ GeV/c muons including statistical errors.

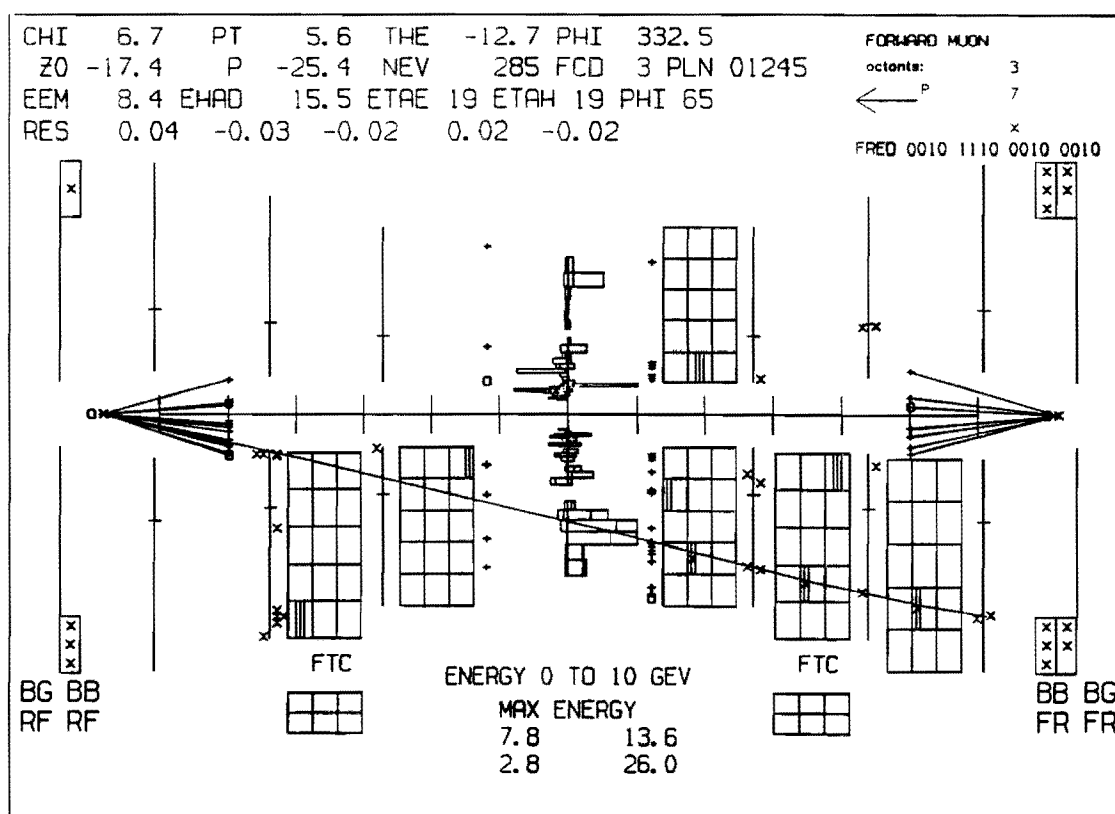


Figure 5.4: Forward muon display for a candidate heavy quark decay event.

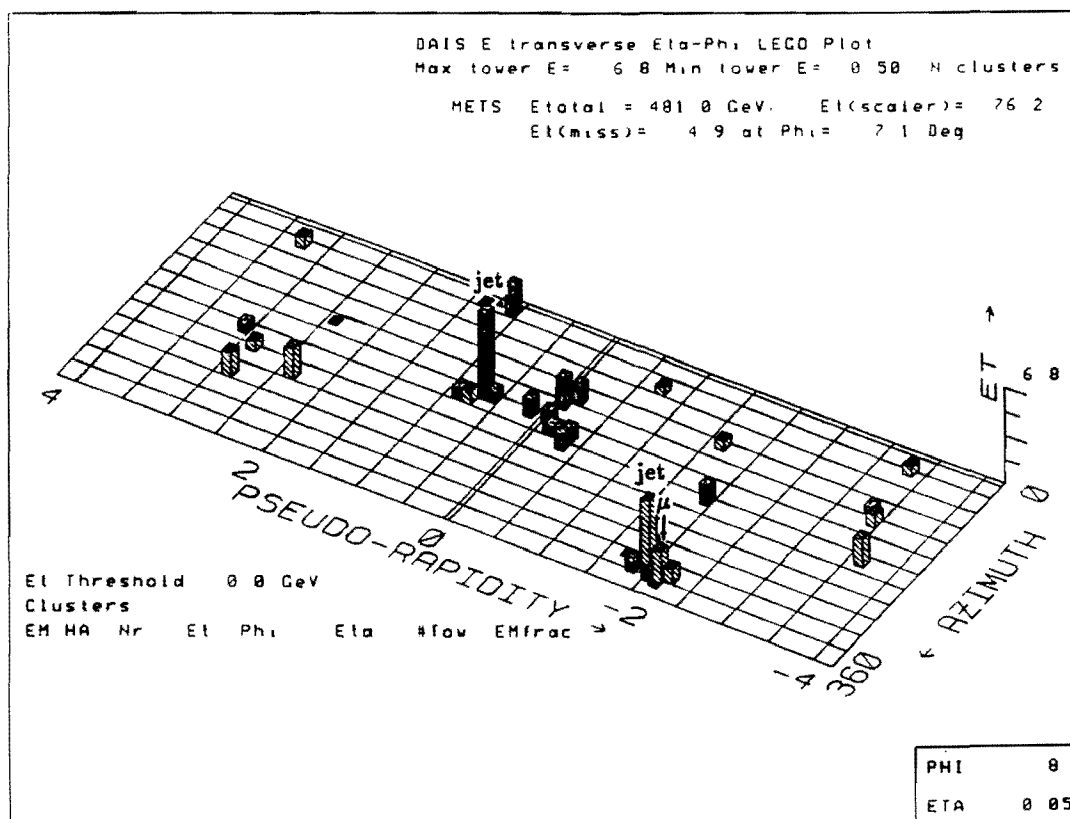


Figure 5.5: Calorimetry lego display for a candidate heavy quark decay event.

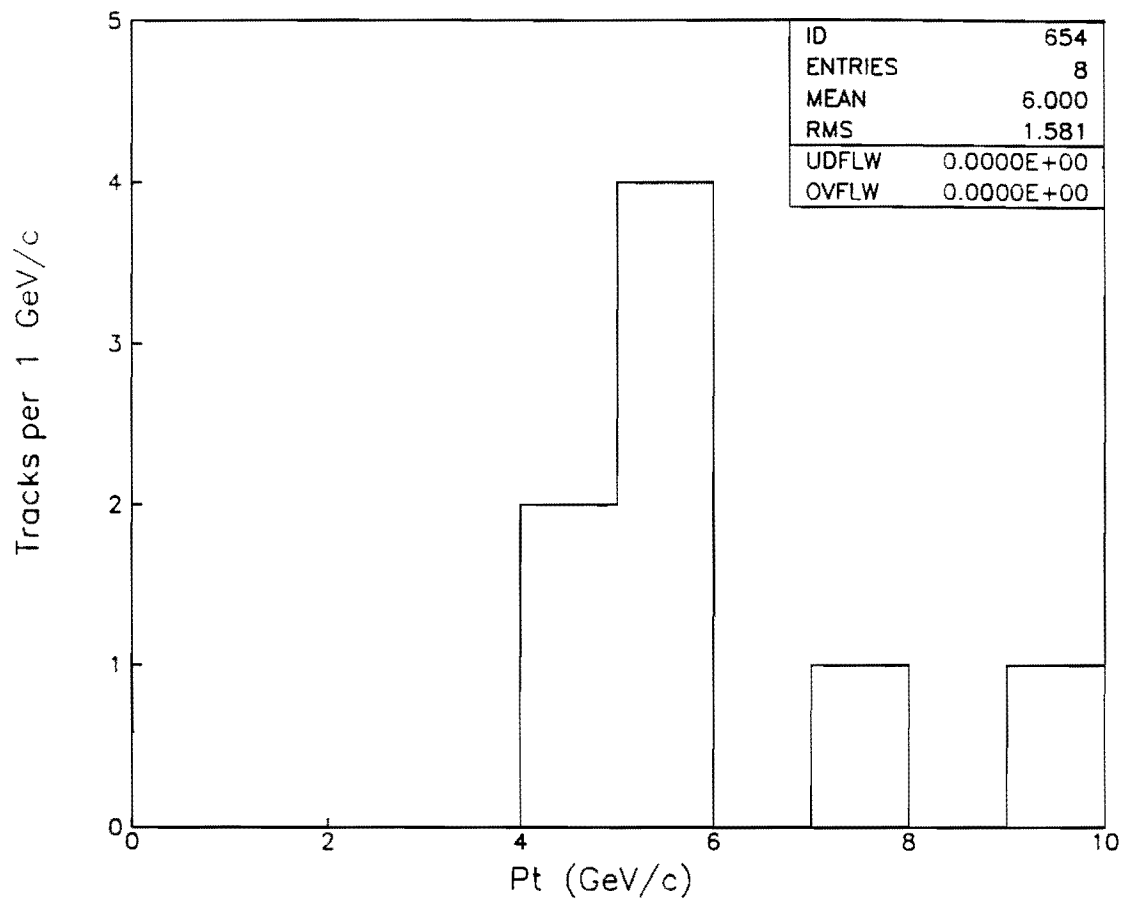


Figure 5.6: Muon p_T spectrum for events containing jet activity and $p_T^\mu > 4$ GeV/c.

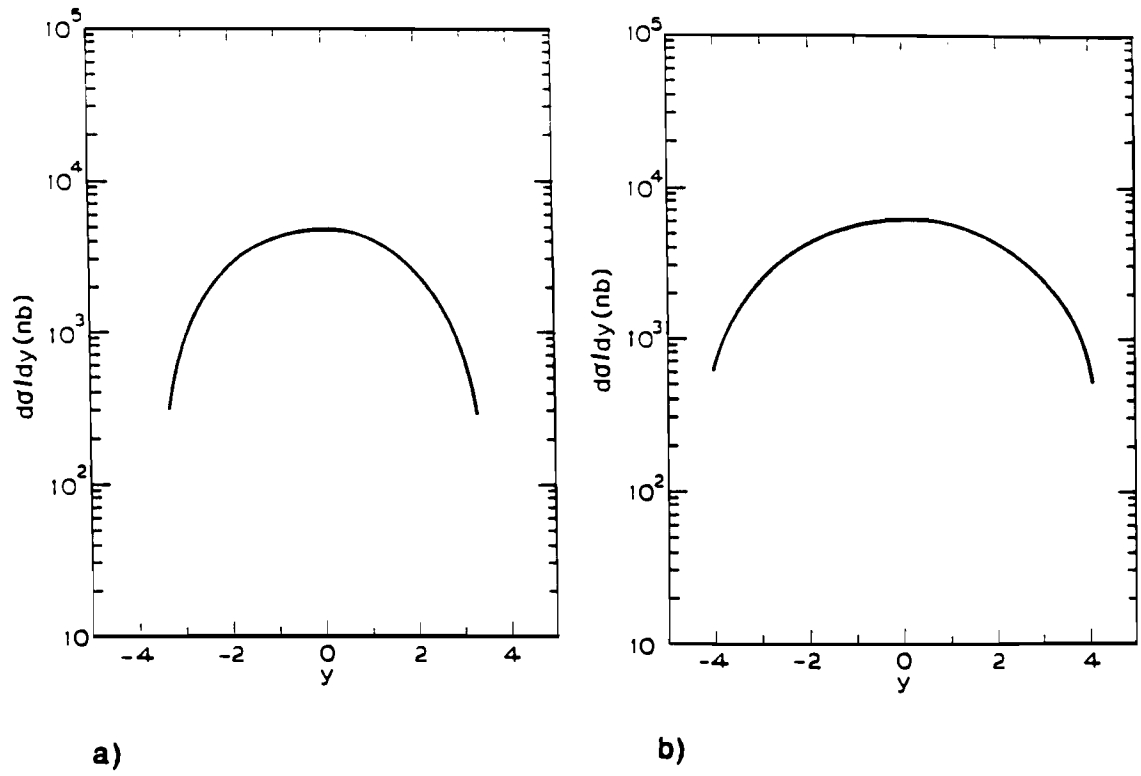


Figure 5.7: The $d\sigma/dy$ distributions for b quark production at center-of-mass energies of 630 GeV (a) and 1.8 TeV (b).

two collision energies and detector acceptance intervals:

$$\frac{\sigma(p\bar{p} \rightarrow b + \bar{b} + X; \sqrt{s} = 1.8 \text{ TeV}; 1.95 < |\eta| < 2.80)}{\sigma(p\bar{p} \rightarrow b + \bar{b} + X; \sqrt{s} = 630 \text{ GeV}; |\eta| < 1.5)} = \frac{5.9 \mu\text{b}}{12.8 \mu\text{b}} = 0.46. \quad (5.2)$$

The muon+jet cross section in the forward muon system for $p_T^\mu > 5 \text{ GeV}/c$ is then:

$$\sigma(p\bar{p} \rightarrow \mu + \geq 1 \text{ Jet}; E_T^{\text{Jet}} > 12 \text{ GeV}) = 12.9 \pm 4.4 \text{ nanobarns}. \quad (5.3)$$

In our data sample of 0.80 nb^{-1} , we would expect:

$$(12.9 \pm 4.4 \text{ nb}) \cdot 0.80 \text{ nb}^{-1} = 10.3 \pm 3.5 \text{ muon} + \text{jet events} \quad (5.4)$$

with $p_T^\mu > 5 \text{ GeV}/c$ and at least one jet with $E_T > 12 \text{ GeV}$. In our 8 observed events with $p_T^\mu > 4 \text{ GeV}/c$, we find that all of them have at least one jet with $E_T > 12 \text{ GeV}$ and that 6 of them have $p_T^\mu > 5 \text{ GeV}/c$. As described in Chapter 3, various corrections were made which resulted in a factor of 2 increase in the number of tracks in our sample (480 observed tracks increased to 975 tracks after corrections). We would then expect $6 \times 2 = 12$ muon+jet events for full system acceptance. This agrees well with the 10.3 ± 3.5 events calculated above. Figure 5.8 shows the muon transverse momentum relative to the nearest jet axis for our 6 muon+jet events with $p_T^\mu > 5 \text{ GeV}/c$. We include the muon in the calculation of the jet axis in order to compare to the same distribution from UA1 (Figure 5.9). We see that the two p_T^{REL} spectra are in good agreement and that our muon+jet events are consistent with a bottom quark decay source. While we cannot make a quantitative statement about muon+jet production, we have observed the first muon+jet events in the forward region at $\sqrt{s} = 1.8 \text{ TeV}$.

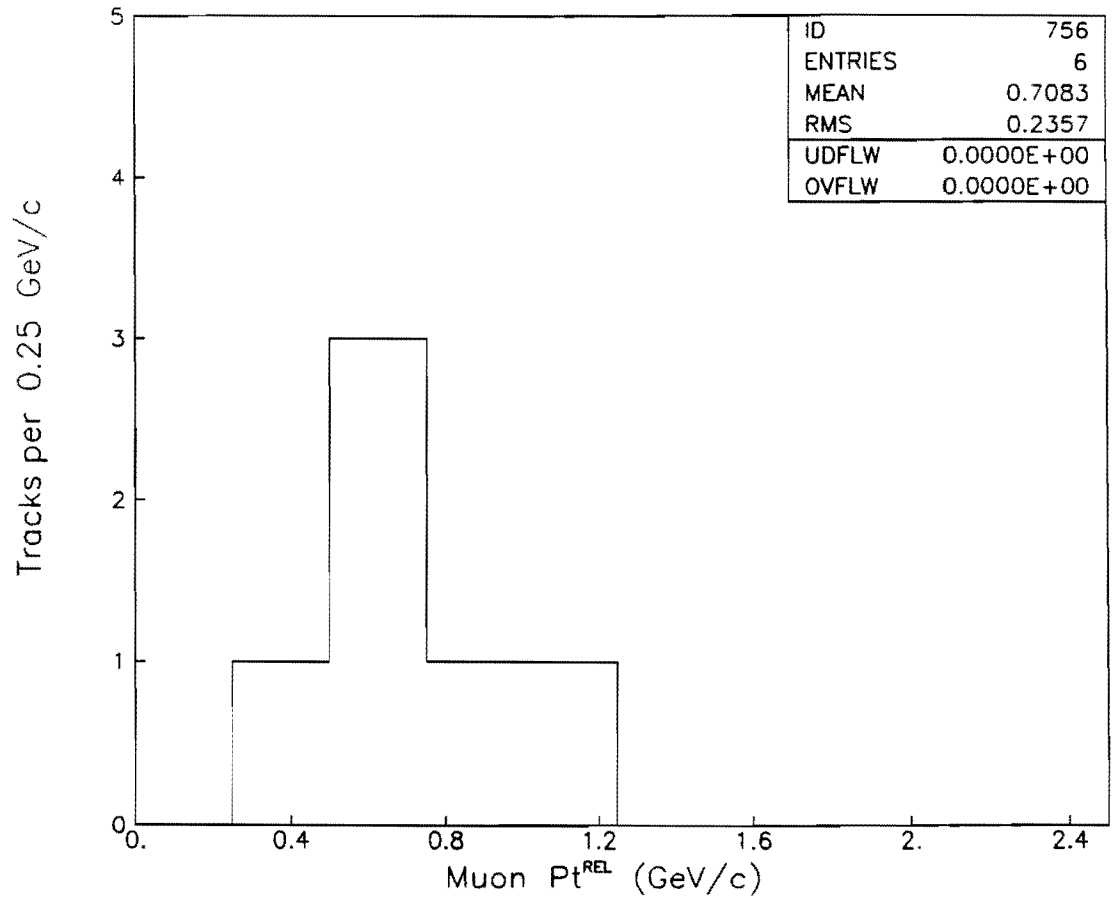


Figure 5.8: Muon transverse momentum relative to the nearest jet axis for $p_T^\mu > 5$ GeV/c.

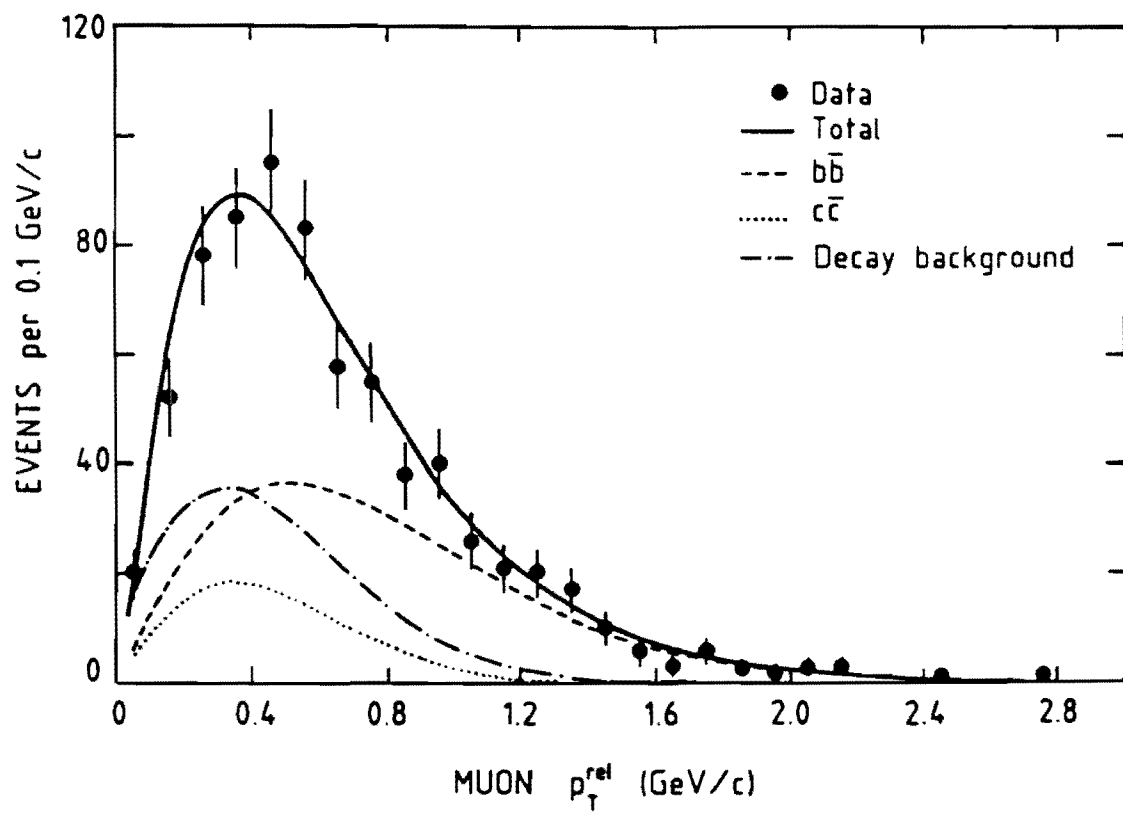


Figure 5.9: UA1 muon transverse momentum relative to the nearest jet axis for $p_T^\mu > 10 \text{ GeV}/c$ and at least one jet of $E_T > 10 \text{ GeV}$.

Subtracting off the 12 muon+jet events, the remaining 119 ± 25 events in the background subtracted spectrum of Figure 5.3 contain no doubt some “feed-down” from lower p_T tracks which were mismeasured due to extra hits. There are also very likely some additional muons from heavy quark decays which produce softer, less-observable jets.

5.2 Inclusive Spectrum Normalization

It is useful for comparisons to normalize our transverse momentum spectrum and express it in terms of an invariant cross section. Recall that for the invariant cross section, $E d^3\sigma/d^3p$, we can write:

$$E \frac{d^3\sigma}{d^3p} = E \frac{d^3\sigma}{p_T dp_T d\phi dp_{||}} = c \frac{d^3\sigma}{p_T dp_T d\phi dy}, \quad (5.5)$$

where we have used $dp_{||} = (E/c)dy$. With $N = \sigma L$, where N is the total number of forward muons produced and L is the integrated luminosity for our sample, we have the expression:

$$\frac{dN}{dp_T} = L \frac{d\sigma}{dp_T}. \quad (5.6)$$

Assuming that the shape of the p_T spectrum is independent of y and ϕ , we can write:

$$E \frac{d^3\sigma}{d^3p} = \frac{c}{2\pi\Delta y p_T} \frac{d\sigma}{dp_T} = \frac{c}{2\pi\Delta y L p_T} \frac{dN}{dp_T}. \quad (5.7)$$

With $dN/dp_T = (N(p_T + \Delta p_T) - N(p_T))/\Delta p_T = N(p_T + \Delta p_T, p_T)/\Delta p_T$, the above equation becomes:

$$E \frac{d^3\sigma}{d^3p} = \frac{c}{4\pi\Delta y L p_T} \frac{N(p_T + \Delta p_T, p_T)}{\Delta p_T}, \quad (5.8)$$

where we divide by 2 in order to calculate a charge-averaged invariant cross section. For the outer HOPU region, $\Delta y \simeq \Delta\eta = 0.85 \times 2 = 1.70$ and $L = 0.80 \text{ nb}^{-1}$ for our sample so that:

$$E \frac{d^3\sigma}{d^3p} = \frac{5.85 \times 10^{-2} \text{ GeV}^{-2} \text{ c}^3 \text{ nb}}{p_T} \frac{N(p_T + \Delta p_T, p_T)}{\Delta p_T}, \quad (5.9)$$

gives the invariant cross section for forward muon production. For the input spectrum we use our data sample as shown in Figure 3.43, which has a bin width $\Delta p_T = 0.5 \text{ GeV}/c$. To insure good tracking efficiency (Figure 3.8), we consider only tracks with $p_T > 2.5 \text{ GeV}/c$. For tracks with transverse momentum below $4.0 \text{ GeV}/c$, we correct for the trigger efficiency using Table 4.5. Table 5.1 lists the invariant cross section for the p_T interval 2.75 to 9.25 GeV/c . In Figure 5.10, we plot the invariant cross section and fit it to the standard form:

$$E \frac{d^3\sigma}{d^3p} = \frac{A}{(1 + p_T/p_0)^n}. \quad (5.10)$$

Using the MINUIT fitting package [80] and fixing $p_0 = 1.30 \text{ GeV}/c$, we find that $A = 2.05 \times 10^{-4} \text{ nb GeV}^{-2} \text{ c}^3$ and $n = 6.34$ give the best fit with a $\chi^2/\text{dof} = 1.43$ (Table 5.2). As mentioned previously, there is a $\pm 14\%$ error in the overall normalization due to the uncertainty in the luminosity.

p_T (GeV/c)	# Tracks before corr.	Trigger eff. corr. factor	# Tracks after corr.	$E \, d^3\sigma/d^3p$ (nb GeV ⁻² c ³)
2.75	136.09 \pm 16.63	3.04	413.71 \pm 50.56	17.6 \pm 2.2
3.25	107.66 \pm 14.79	1.68	180.87 \pm 24.85	6.5 \pm 0.89
3.75	111.72 \pm 15.06	1.21	135.18 \pm 18.22	4.2 \pm 0.57
4.25	54.84 \pm 10.55	1.00	54.84 \pm 10.55	1.5 \pm 0.29
4.75	62.97 \pm 11.31	1.00	62.97 \pm 11.31	1.6 \pm 0.28
5.25	40.63 \pm 9.08	1.00	40.63 \pm 9.08	0.91 \pm 0.20
5.75	14.22 \pm 5.37	1.00	14.22 \pm 5.37	0.29 \pm 0.11
6.25	16.25 \pm 5.75	1.00	16.25 \pm 5.75	0.30 \pm 0.11
6.75	18.28 \pm 6.09	1.00	18.28 \pm 6.09	0.32 \pm 0.11
7.25	12.19 \pm 4.98	1.00	12.19 \pm 4.98	0.20 \pm 0.080
7.75	14.22 \pm 5.37	1.00	14.22 \pm 5.37	0.21 \pm 0.081
8.25	4.06 \pm 2.87	1.00	4.06 \pm 2.87	0.058 \pm 0.041
8.75	2.03 \pm 2.03	1.00	2.03 \pm 2.03	0.027 \pm 0.027
9.25	6.09 \pm 3.52	1.00	6.09 \pm 3.52	0.077 \pm 0.044

Table 5.1: Forward muon invariant cross section for the interval $2.75 \leq p_T \leq 9.25$ GeV/c.

Spectrum	Fit interval (GeV/c)	A (nb GeV ⁻² c ³)	p_0 (GeV/c)	n	χ^2	N_{dof}
FMU	2.75-9.25	$2.07 \pm .80 \times 10^4$	1.30 fixed	$6.35 \pm .26$	17.1	12
Hadron	0.4-10.0	$0.45 \pm .01 \times 10^9$	1.30 fixed	$8.28 \pm .02$	103	65

Table 5.2: Fit parameters for the forward muon and charged hadron p_T spectra to the form $A/(1 + p_T/p_0)^n$. Quoted errors are purely statistical.

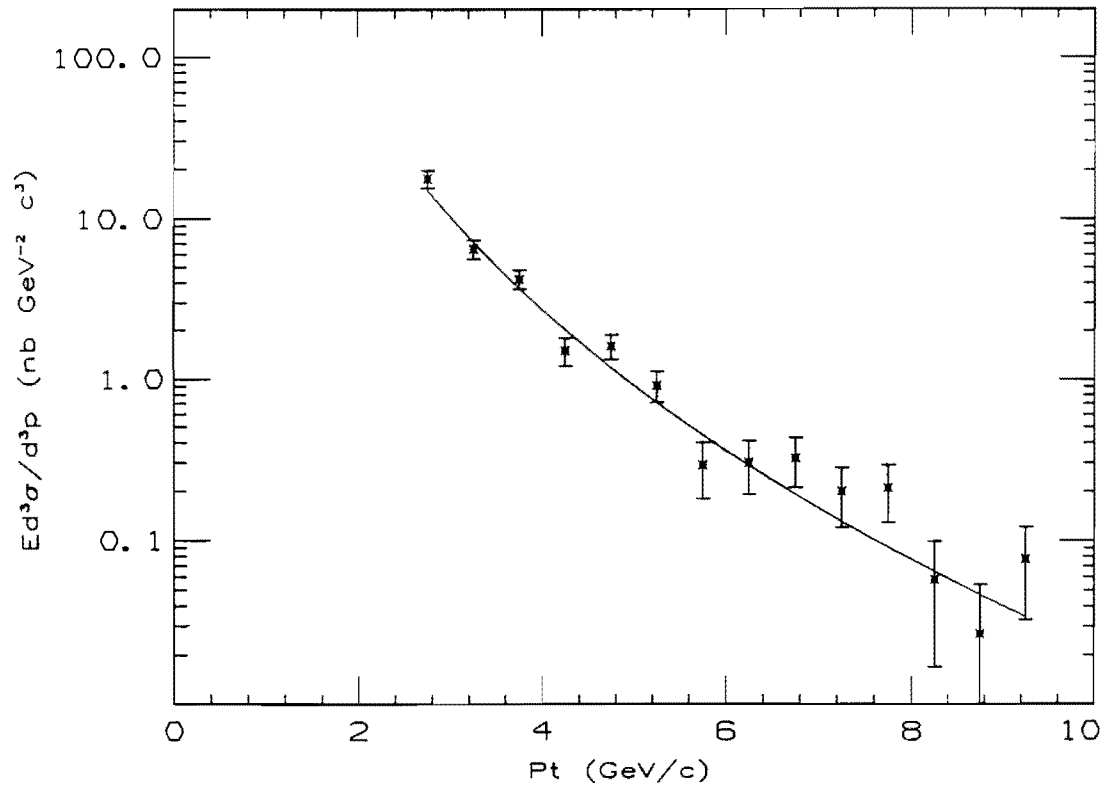


Figure 5.10: Invariant cross section for forward muon production in the interval $1.95 < |\eta| < 2.80$. The error bars are statistical only.

5.3 CDF Charged Hadron Spectrum Comparison

In Figure 5.11, we compare our spectrum to the CDF charged hadron spectrum of Figure 4.4. The forward muon spectrum is plotted both at its actual values (lower curve) and at scaled values (upper curve) to allow better shape comparison with the charged hadron spectrum. We see that the forward muon spectrum falls less rapidly than the charged hadron spectrum. This can also be seen in Table 5.2 by comparing the power-law dependence of the two spectra. This spectral shape difference is due to a loss of muons at low p_T from trigger threshold and range-out effects and from mismeasurement “feed-down” and the heavy quark decay source mentioned above.

5.4 UA1 Inclusive Muon Spectrum Comparison

The inclusive muon spectrum as measured by the UA1 experiment at a center-of-mass energy of 630 GeV is given in Figure 5.12. The figure corresponds to a data sample of 556 nb^{-1} . We see that below 10 GeV/c p_T , the UA1 inclusive muon spectrum is also dominated by a π/K decay-in-flight background. As a check, it is useful to compare our p_T spectrum with that from UA1. We would expect to have more muons due to the larger charged hadron cross section at our higher center-of-mass energy and to the longer decay path in the CDF forward region compared to the UA1 central region. To do the comparison, we calculate $d\sigma/dydp_T$ for the two data samples (Table 5.3). In Figure 5.13, we see that in

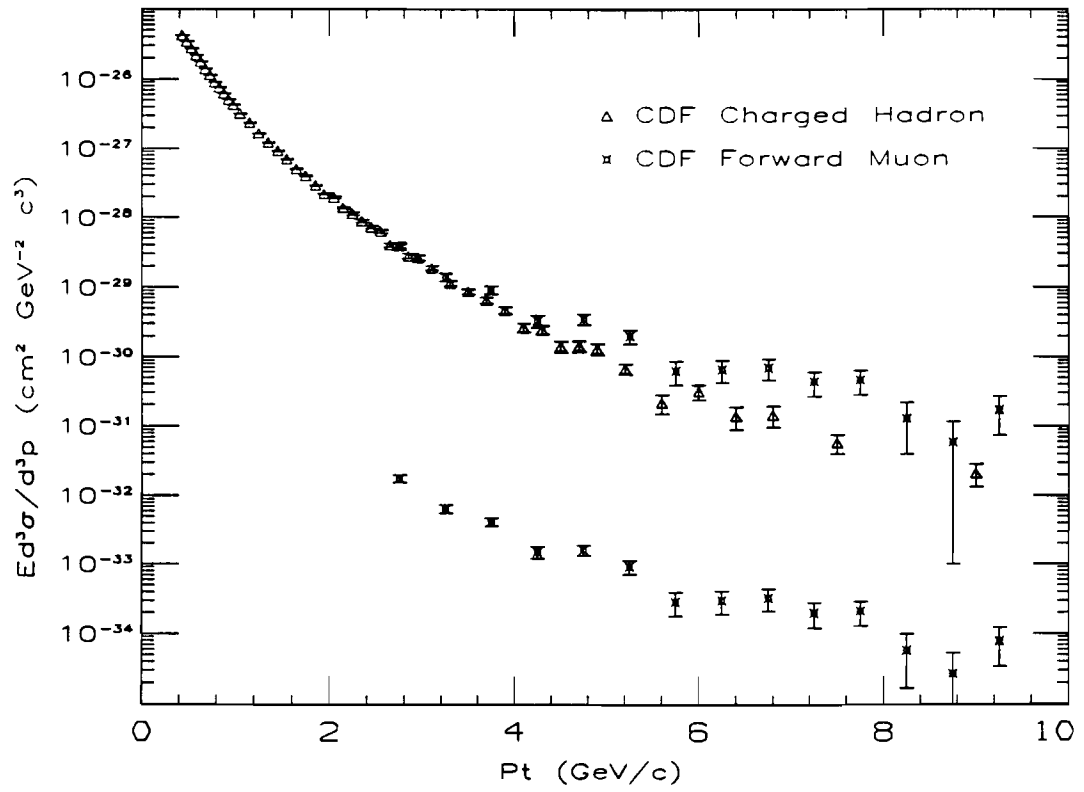


Figure 5.11: Comparison of charged hadron ($|\eta| < 1.0$) and forward muon ($1.95 < |\eta| < 2.80$) inclusive spectra at CDF. The forward muon spectrum is plotted both at its actual values (lower curve) and at scaled values (upper curve) for shape comparison.

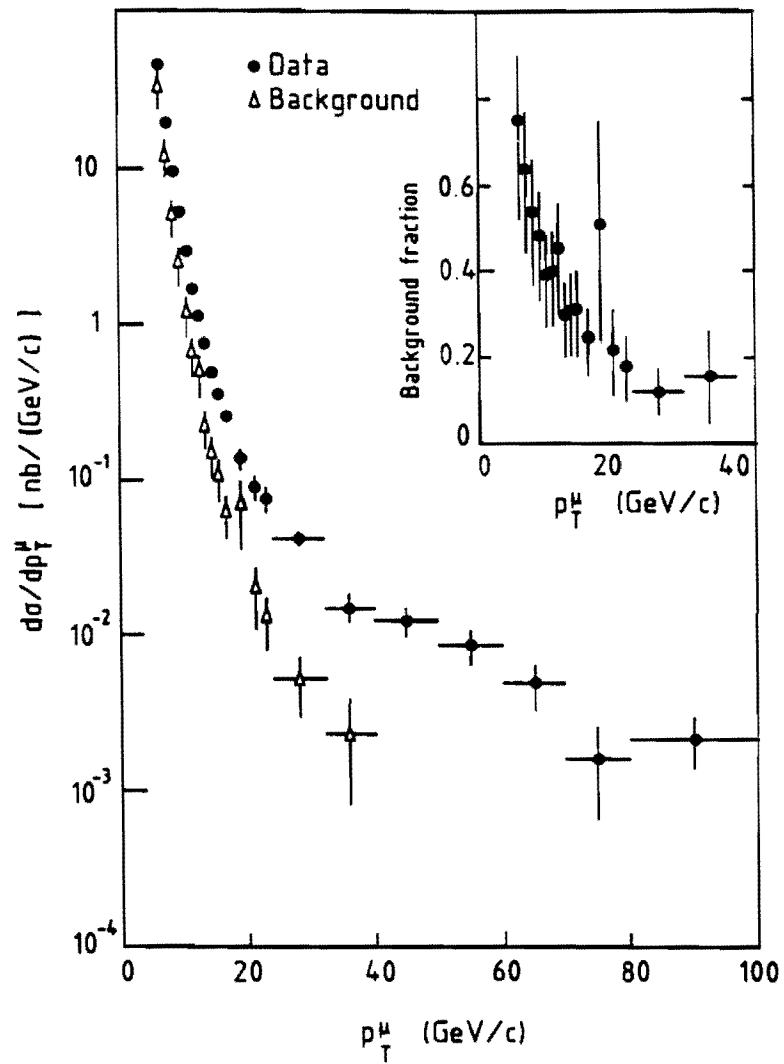


Figure 5.12: UA1 inclusive muon p_T distribution ($|\eta| < 1.5$) before background subtraction (black circles). The background contribution from decay-in-flight is also shown (open triangles).

p_T (GeV/c)	FMU $d\sigma/dp_T dy$ [nb/(GeV/c)]	p_T (GeV/c)	UA1 $d\sigma/dp_T dy$ [nb/(GeV/c)]
2.75	608.4 ± 74.4	6.50	15.53 ± 11.72
3.25	266.0 ± 36.5	7.50	6.71 ± 3.10
3.75	198.8 ± 26.8	8.50	3.29 ± 1.06
4.25	80.6 ± 15.5	9.50	1.65 ± 0.41
4.75	92.6 ± 16.6		
5.25	59.8 ± 13.4		
5.75	20.9 ± 7.9		
6.25	23.9 ± 8.5		
6.75	26.9 ± 9.0		
7.25	17.9 ± 7.3		
7.75	20.9 ± 7.9		
8.25	6.0 ± 4.2		
8.75	3.0 ± 3.0		
9.25	9.0 ± 5.2		

Table 5.3: The FMU and UA1 muon $d\sigma/dp_T dy$ spectra. The errors given are statistical.

fact the forward muon cross section is slightly higher than that of UA1. Due to limited statistics the distinction is not very clear but the FMU curve does appear to have the stiffer slope of the two curves as was expected.

The muon physics analysis has been very fruitful for UA1 in providing physics results. We see in Figure 5.14 the UA1 background subtracted inclusive muon p_T spectrum. Curves are given for the contribution from different physics processes and are in good agreement with the data. In larger data samples from future CDF runs, it is hoped that the forward muon system can go after much of this physics as well.

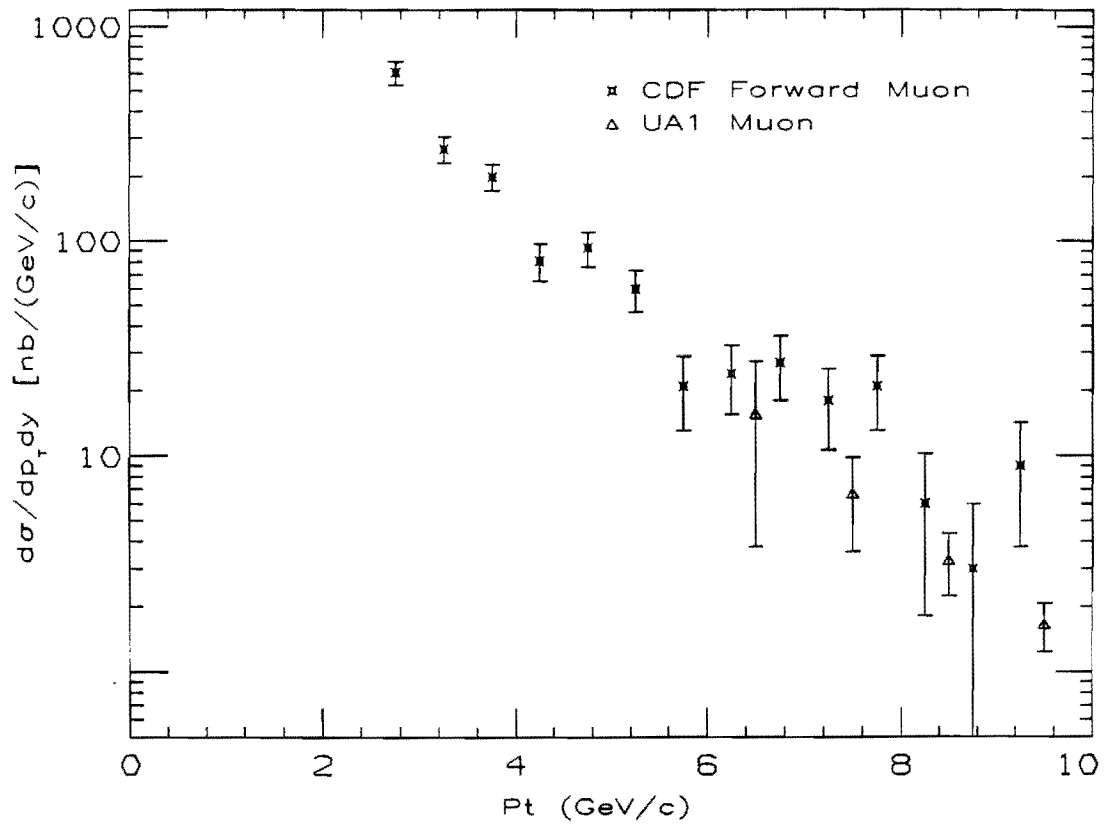


Figure 5.13: Comparison of the FMU ($1.95 < |\eta| < 2.80$) and UA1 ($|\eta| < 1.5$) muon p_T spectra.

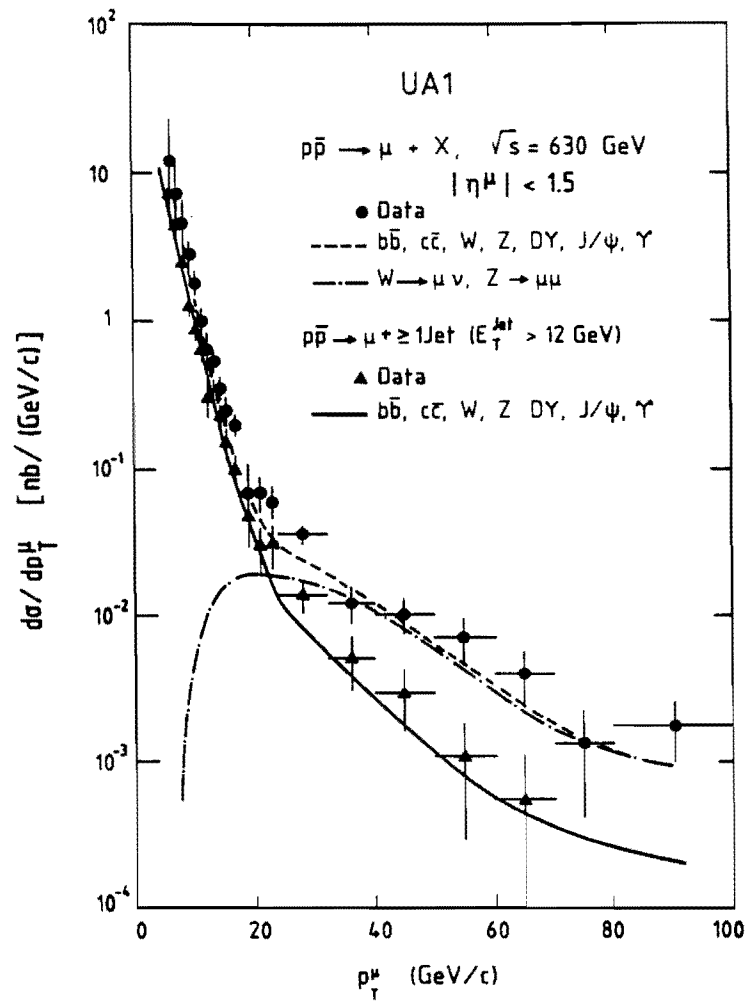


Figure 5.14: UA1 inclusive muon p_T distribution ($|\eta| < 1.5$) after background subtraction.

Chapter 6

$Z^0 \rightarrow \mu^+ \mu^-$ Candidate

In the entire 1987 data sample, one of the most interesting events was the observation of a $Z^0 \rightarrow \mu^+ \mu^-$ event in which a muon was seen in both the central and forward muon systems. Table 6.1 lists the parameters of the event. This was one of only two $Z^0 \rightarrow \mu^+ \mu^-$ events observed in the 1987 run. The other event was a central-endwall muon pair.[81]

Figure 6.1 shows the forward muon half of the Z^0 candidate. It is clearly a clean, well-measured high transverse momentum muon. The muon is actually located in the inner HOPU region so it did not trigger the forward muon system. The event was triggered by the central muon detector and is part of a larger $24.2 \pm 3.4 \text{ nb}^{-1}$ data sample. Figure 6.2 shows the central muon track inside the central tracking chamber. It is composed of several clean hit segments, as shown in the display window, and is also well-measured. Figure 6.3 shows the

	Forward muon	Central muon
charge	+1	-1
p_T	15.5 GeV/c	21.6 GeV/c
p	157.6 GeV/c	25.3 GeV/c
θ	174.4°	121.4°
η	-3.0	-0.58
ϕ	342.5°	161.0°
invariant mass = 68.1 ± 6.8 GeV/c ²		
$E_T^{\text{MISS}} = 7.8$ GeV at $\phi = 355.1^\circ$		

Table 6.1: $Z^0 \rightarrow \mu^+ \mu^-$ event parameters.

η - ϕ calorimetry transverse energy lego plot. There is very little activity and the missing E_T is quite low. This is expected for a $Z^0 \rightarrow \mu^+ \mu^-$ event since there are no neutrinos in the final state and for the lowest-order production process the Z^0 has very little p_T . Figure 6.4 shows a VTPC 3-dimensional track segment and Figure 6.5 shows a FTC azimuthal segment which both match the forward muon track. The energy deposition in the forward calorimeters (Figure 6.6) is also consistent with a muon candidate.

Of course, with only one event, it is difficult to be sure that it is due to the Z^0 boson predicted by the electroweak model and observed by UA1. One can however examine some kinematic properties of the event and these are listed in Table 6.2. They are all consistent with a Z^0 boson decay. The mass of the muon pair is a little low compared to the expected value of around 91.0 GeV/c². If

Event property	Value
Z^0 p_T	6.2 GeV/c
Z^0 rapidity	-1.6
Z^0 Feynman x	0.19
muon $\cos\Theta^*$	0.80
parton Feynman x values	0.20, 7.25 $\times 10^{-3}$

Table 6.2: Z^0 event kinematic properties.

we require p_T balance in the event and modify the forward muon momentum appropriately, the mass of the dimuon pair goes up to 80.9 GeV/c². The only other known source of such a high-mass $\mu^+\mu^-$ event is the Drell-Yan process. If there is substantial Drell-Yan production, one would expect to see a rapidly falling spectrum of dimuon masses. The data sample was checked for other forward-central dimuon events in which the central muon had at least 5 GeV/c transverse momentum. After applying standard quality cuts and requiring opposite sign muons, the only event to survive is the Z^0 candidate event presented here. A background calculation using the scaling form for Drell-Yan production [82]:

$$m^3\left(\frac{d^2\sigma}{dm dy}\right)_{y=0} = (3.8 \pm 1.4) \times 10^{-32} e^{-(15.7 \pm 1.6)\sqrt{\tau}} \text{cm}^2 \text{GeV}^2, \quad (6.1)$$

where $\tau = m^2/s$, yields $< 10^{-2}$ FMU-CMU Drell-Yan events in the mass range 50 - 100 GeV/c².

Figure 6.7 shows the CDF muon acceptance for W^\pm and Z^0 boson production from a lowest-order ISAJET V6.02 calculation.[83] We see that a FMU-CMU Z^0

has almost twice the acceptance of a completely central Z^0 due to the relatively limited central muon coverage ($|\eta| < 0.63$). With a 13.9% acceptance for our event, a calculation of the cross section times branching ratio for $Z^0 \rightarrow \mu^+\mu^-$ yields:

$$\begin{aligned}\sigma \cdot \text{BR}(Z^0 \rightarrow \mu^+\mu^-) &= \frac{1}{24.2\text{nb}^{-1}} \frac{1}{0.139} \\ &= 0.3 \pm 0.3 \pm 0.05\text{nb},\end{aligned}\tag{6.2}$$

where the first error is statistical and the second is systematic ($\pm 14\%$ luminosity uncertainty). The measured value is in fact not too far from expectations. From the 1987 $Z^0 \rightarrow e^+e^-$ event sample, a value of:

$$\sigma \cdot \text{BR}(Z^0 \rightarrow e^+e^-) = 0.4 \pm 0.2 \pm 0.1\text{nb},\tag{6.3}$$

has been presented.[84] Assuming lepton universality, these values should agree and within the large errors they do. Thus, the forward muon system has seen a hint of electroweak physics in the 1987 collider run.

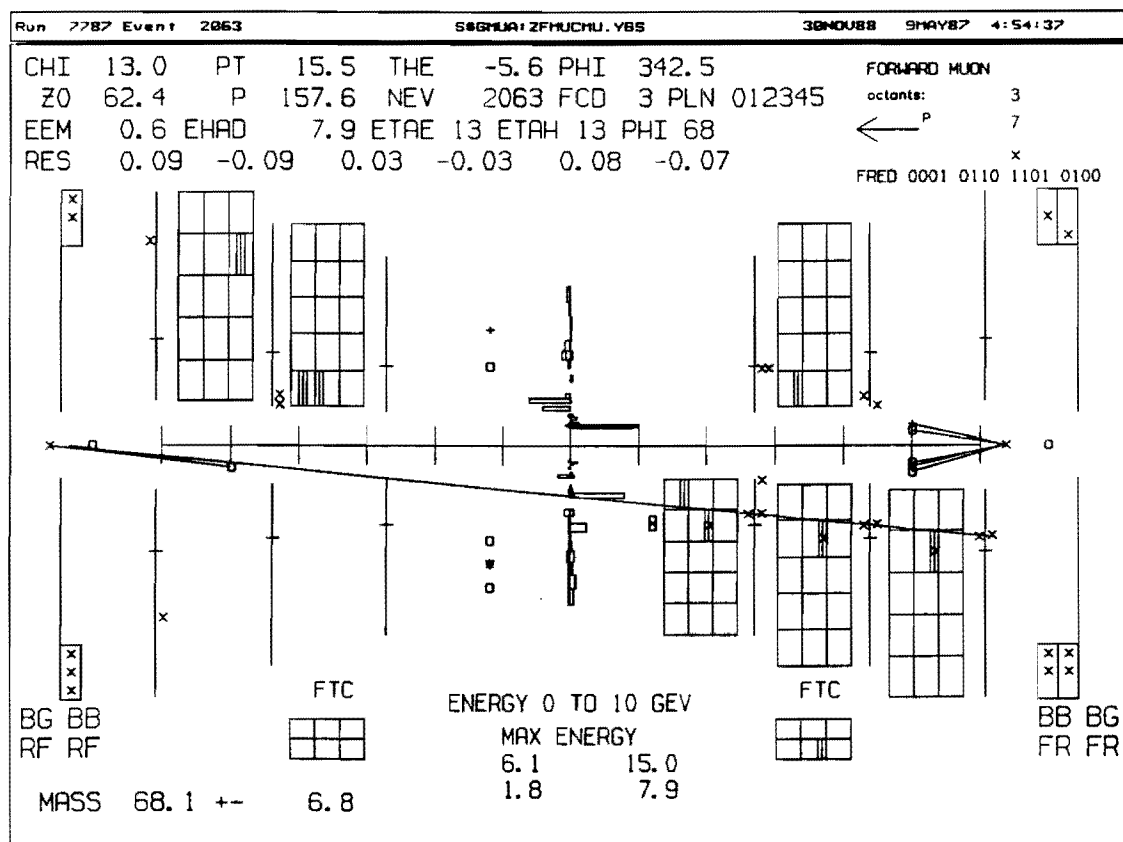


Figure 6.1: Forward muon half of the Z^0 candidate event.

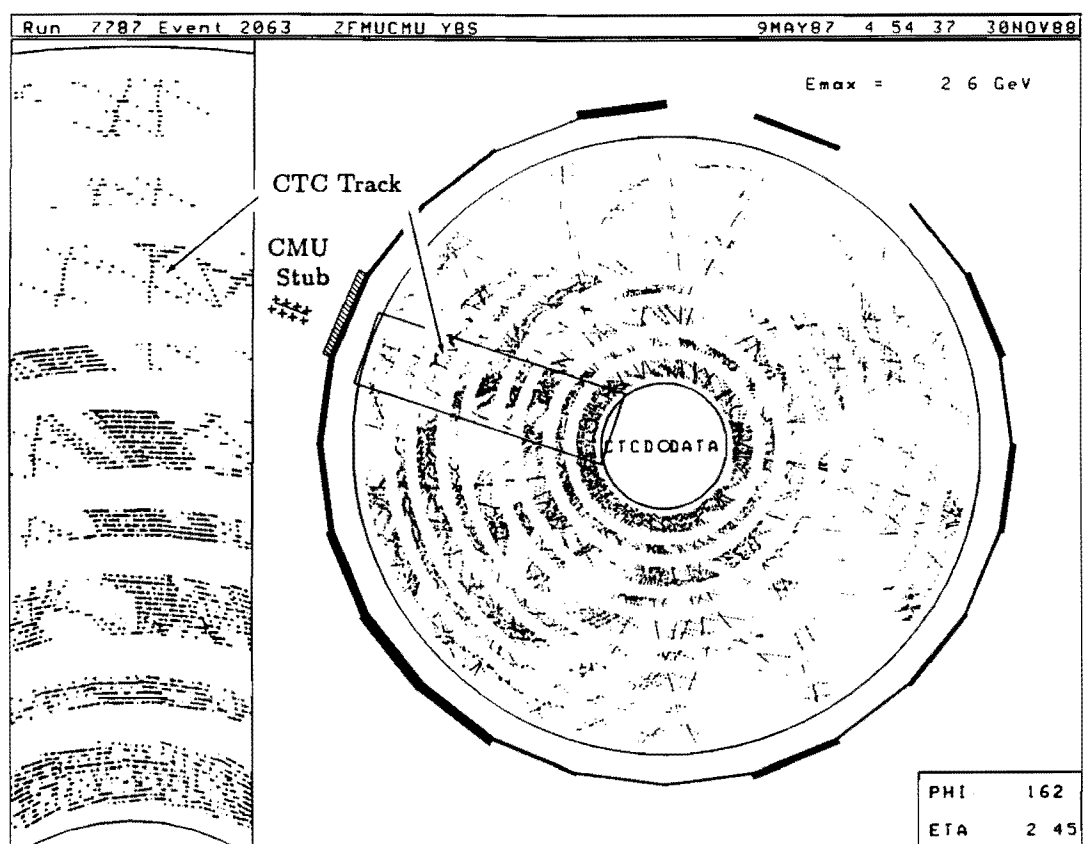


Figure 6.2: Central muon track inside the central tracking chamber.

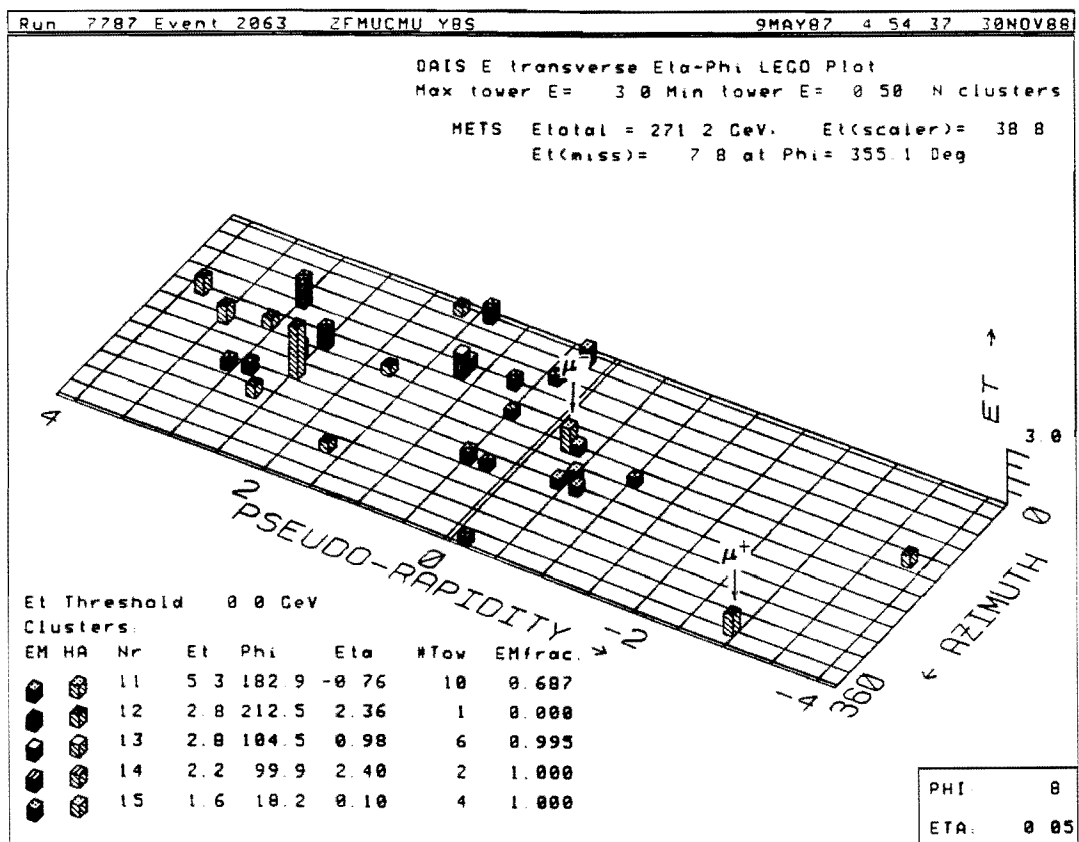


Figure 6.3: E_T lego plot for the Z^0 event.

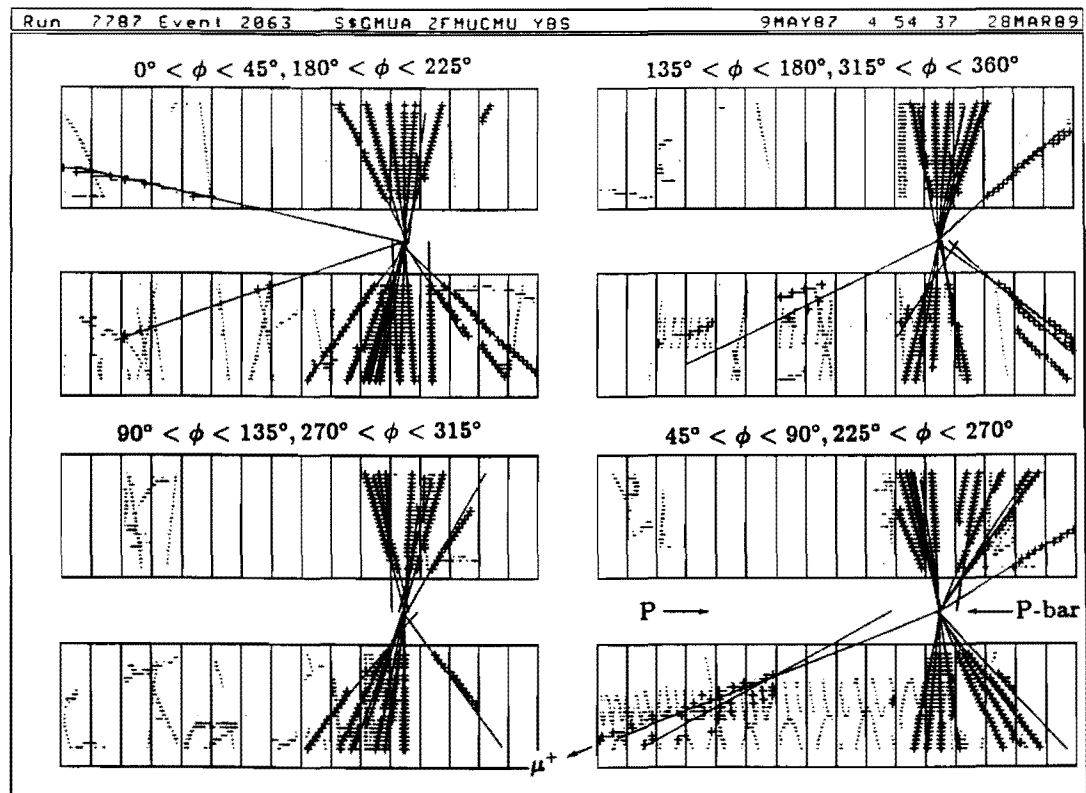


Figure 6.4: Forward muon track in the VTPC.

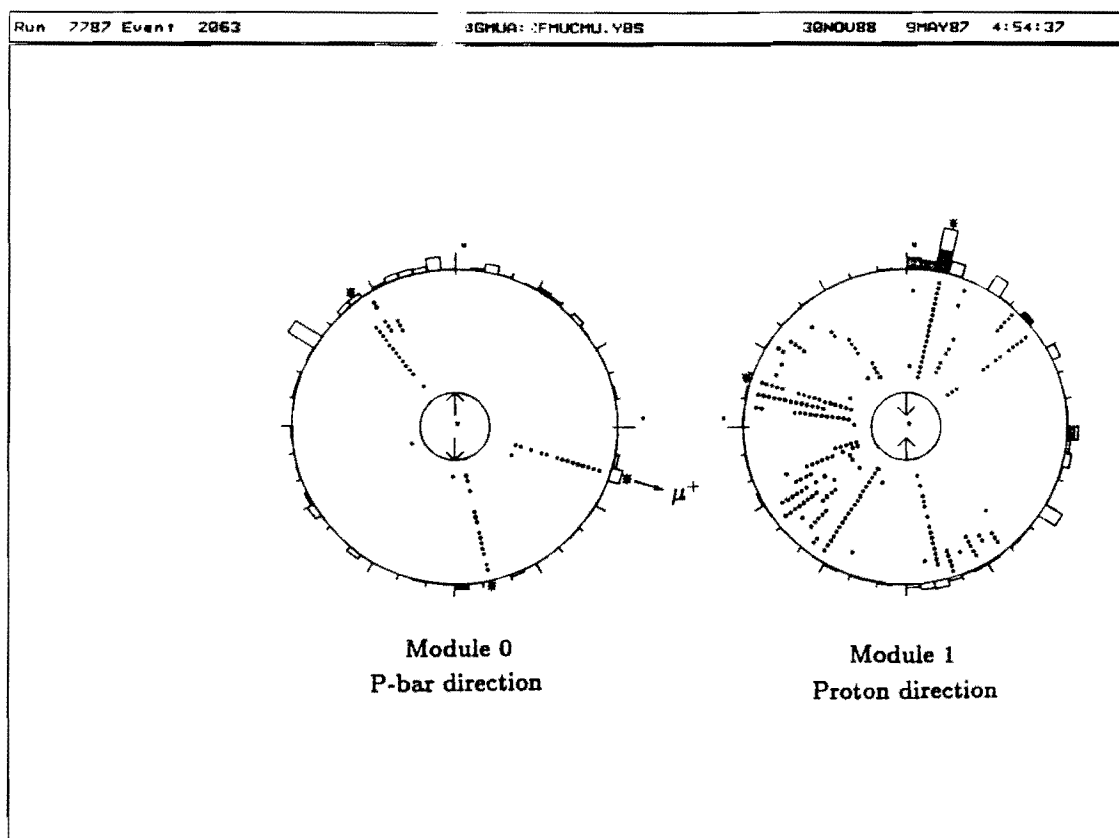


Figure 6.5: FTC azimuthal segment corresponding to the forward muon.

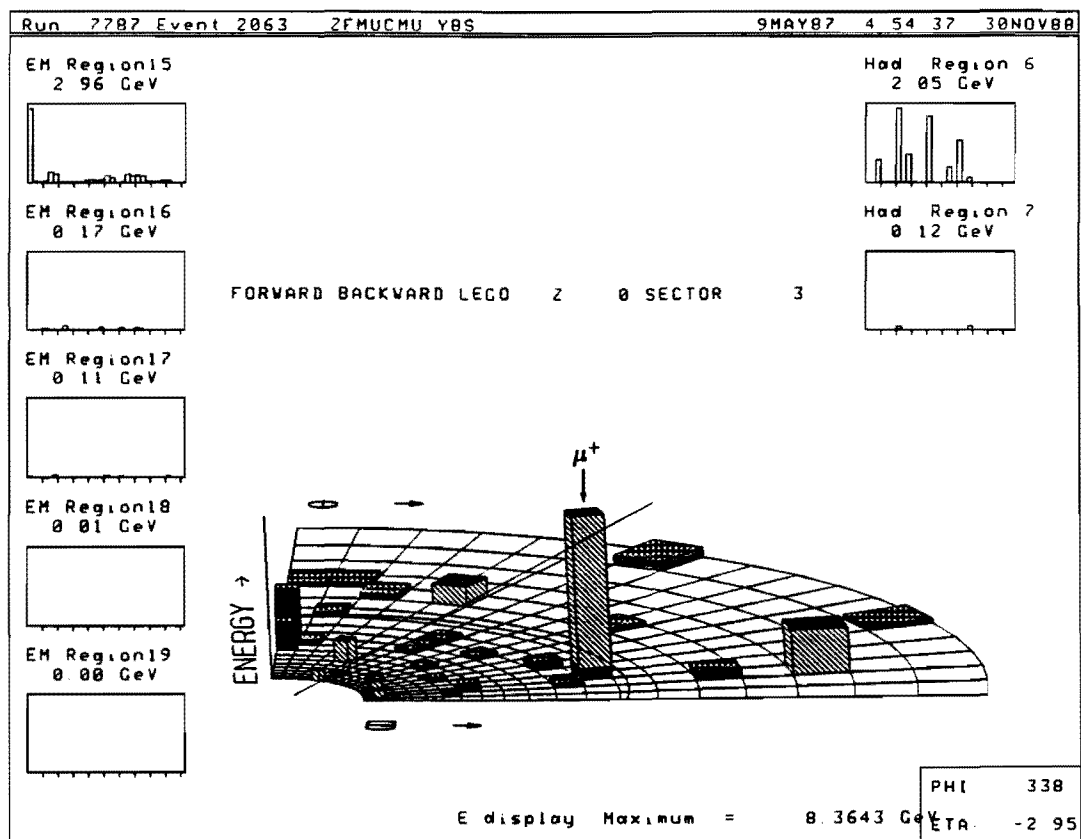
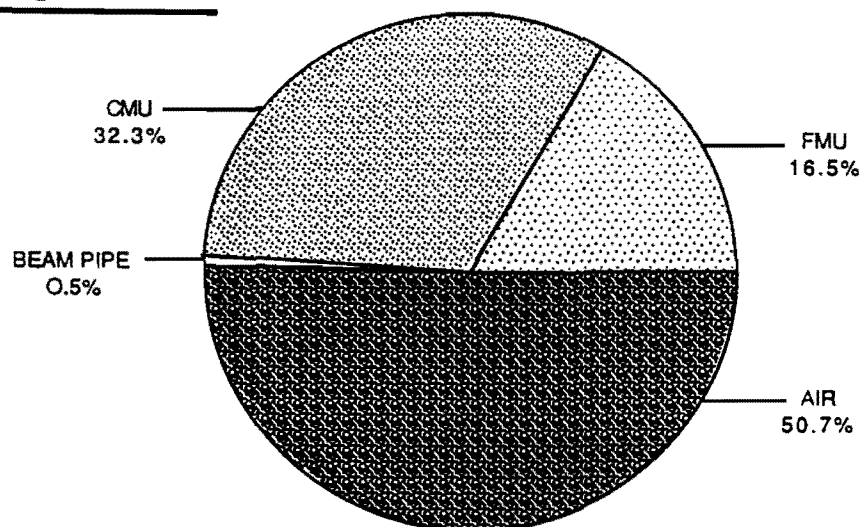


Figure 6.6: Muon energy deposition in the forward calorimeters.

$W \rightarrow \mu \nu$



$Z \rightarrow \mu \mu$

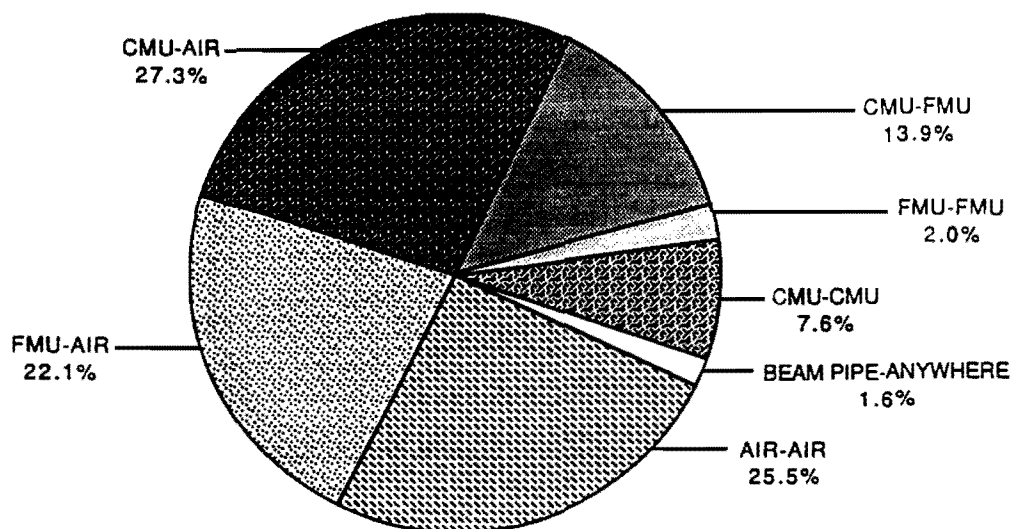


Figure 6.7: CDF muon acceptance for W^\pm and Z^0 boson decay.

Chapter 7

Conclusions

A lot was learned about the forward muon system in the 1987 Tevatron collider run. Valuable operational experience was gained with all aspects of the system. The trigger rates were measured for the first time and the unexpected accelerator backgrounds were encountered. CDF as a whole learned how to live together and take data together on its maiden voyage into the unknown physics possibilities at the highest-ever center-of-mass energy of 1.8 TeV.

In Chapter 1, we described some of the known physics mechanisms for producing both single and multi-muon events in the forward region. These mechanisms include muons from weak boson decay ($W \rightarrow \mu\nu, Z^0 \rightarrow \mu^+\mu^-$), Drell-Yan production ($q\bar{q} \rightarrow \gamma^* \rightarrow \mu^+\mu^-$), and heavy quark decays. It is for the measurement of the muon production from these processes, and any unknown ones, that the FMU system was built.

Chapter 2 saw a detailed description of the many parts of the forward muon system. The large area use of electrodeless drift chambers, state-of-the-art TDC electronics, and a constant p_T threshold trigger are some of the distinguishing features. In many ways, the forward muon system is a prototype detector for forward region physics at the proposed Superconducting Super Collider (SSC). It is hoped that this description will be useful to the designers of those systems.

In Chapter 3, we started with a discussion of the trigger rates and the beam fragment background source. In spite of a strongly prescaled trigger, a significant sample of forward muon events were collected. This data sample was then analyzed to extract a signal of real forward muons. Various cuts were applied to achieve a sample of some 480 forward muon candidates. The expected forward muon signals were observed in the vertex time projection chamber and the plug and forward calorimetry. Monte Carlo simulation was used to test the track reconstruction program. Results of this test were compared to hand-calculations and agreement was found in several cases. Finally, dead channel and efficiency corrections were determined and an inclusive forward muon spectrum was presented.

Forward muon backgrounds were described in Chapter 4. The dominant background source to emerge was pion and kaon decay-in-flight, with all other backgrounds relatively negligible. A hand-calculation to determine the expected yield from decay-in-flight was presented and a Monte Carlo simulation procedure was outlined to determine the actual shape of the decay muon spectrum.

In Chapter 5, we compared our data sample p_T spectrum with the simulated decay-in-flight background. An excess of muons with $p_T > 4 \text{ GeV}/c$ was observed and several events containing jet activity, possibly indicating heavy quark decay, were discovered. The number of muon+jet events was found to agree with expectations from bottom quark decay and the muon transverse momentum relative to the jet axis was also consistent with a bottom quark decay source. The muon p_T spectrum was then normalized and compared to CDF minimum bias and UA1 muon spectra.

The first observation of the decay $Z^0 \rightarrow \mu^+\mu^-$ at $\sqrt{s} = 1.8 \text{ TeV}$ was presented in Chapter 6. The signals from several CDF detectors were shown for this exciting event. A value of the cross section $\sigma \cdot \text{BR}(Z^0 \rightarrow \mu^+\mu^-)$ was given and was found to be in agreement with expectations.

The forward muon system has begun its journey into the exciting physics potential of the Tevatron collider program. With the experience and understanding gained from the 1987 run, the trip will be a smoother one and will yield many more physics results.

Appendix A

CDF Coordinate System

CDF uses the following coordinate system convention:

- The positive z-axis is along the direction of the proton beam.
- The positive y-axis is vertically upwards.
- The positive x-axis is horizontally pointing away from the Tevatron ring.
- The polar angle θ is defined from the positive z-axis.
- The azimuthal angle ϕ is defined in the x-y-plane perpendicular to the beam.

0° is along the positive x-axis and 90° is along the positive y-axis.

The coordinate system is shown in Figure A.1. The quantities p_T and E_T always refer to the vector component perpendicular to the z or beam axis.

The pseudorapidity is calculated using: $\eta = -\ln(\tan(\theta/2))$.

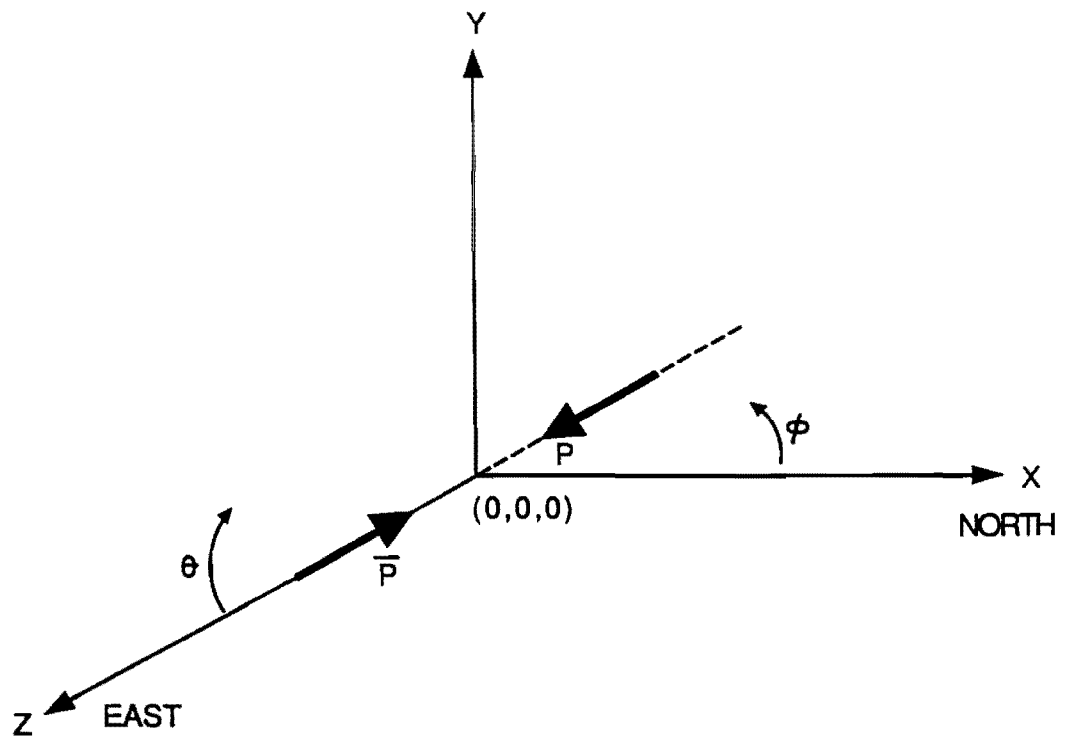


Figure A.1: The CDF coordinate system.

Appendix B

Forward Muon Tracking Code

Here we describe the algorithm used to locate and fit forward muon tracks. As an example, we consider the track shown in Figure B.1 (see Appendix C for a description of the FMU display). It is a good 6-hit track with consistent pad hits and an associated counter pair. There is also a matched VTPC track and energy in the projected calorimeter tower. We now want to go through the manipulations of taking the raw wire hit times and reconstructing a muon track.

B.1 TDC Data Manipulations

Figure B.2 shows the hit time data as it appeared in the PSL TDCs for the octant containing the track. The data was located in three TDCs, one for each chamber plane, and divided into six RAMs (Random Access Memories) within a TDC unit. The output is in LIFO (Last In, First Out) format so that the earliest

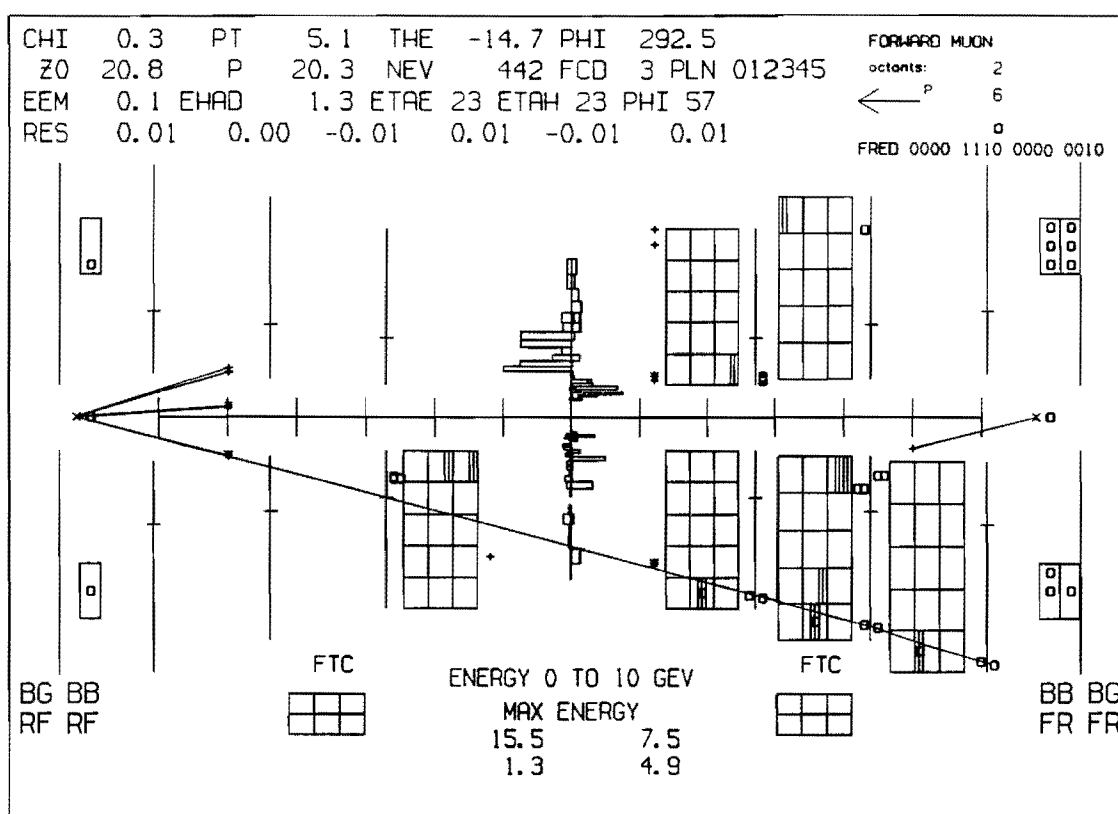


Figure B.1: Sample track to demonstrate the FMU track-fitting.

		RAM 4 STOP CLOCK WORDS		RAM# CLOCK TIME WIRE NO.		CLOCK TAP TIME TIME		RAM# CLOCK TIME WIRE NO.		CLOCK TAP TIME TIME		RAM 4 START CLOCK WORDS	
FRONT PLANE TDC	RAM 4 →	009F4FFF	009F0000	001D4FDF	001D3FFF	001C4FDF	001C000F	00004FFF	00000000				
	RAM 5 →	009F5FFF	009F0000	005C5FFD	005C007F	00005FFF	00000000						
MIDDLE PLANE TDC	RAM 1 →	009F1FFF	009F0000	003A1F7F	003A0FFF	001C1F7F	001C1FFF	00001FFF	00000000				
	RAM 4 →	009F4FFF	009F0000	004B4FDF	004B00FF	00004FFF	00000000						
	RAM 5 →	009F5FFF	009F0000	002E5BFF	002E00FF	00285FFD	00281FFF	00275FFD	0027000F				
		00195BFF	00197FFE	00185BFF	0018001F	00005FFF	00000000						
REAR PLANE TDC	RAM 4 →	009F4FFF	009F0000	00414FBF	0041003F	00004FFF	00000000						
	RAM 5 →	009F5FFF	009F0000	003E5FFB	003E3FFE	003D5FFB	003D001F	00005FFF	00000000				

Figure B.2: Hit time data as it appeared in the PSL TDC for our sample track.

data within a RAM is written further into the RAM. Considering the data in the front chamber plane and referring to the upper right-hand corner of Figure B.2, we have two hexadecimal words in RAM# 4 known as the "START CLOCK" marker words which were written when the TDC clock started its oscillation period. The bit pattern of these marker words is unique and they were used to locate the beginning of hit time data for the current event inside a RAM. The next two hexadecimal words to the left correspond to a drift time measurement. The four left-most digits of each hexadecimal word contain the clock time in units of 10 nanoseconds. For this hit, the clock time was $001C = 280$ nanoseconds. In the left-most word the RAM number is written in the 4th digit (in this case the RAM# is 4) and the next three hexadecimal digits contain twelve bits, one for each of the twelve inputs into the RAM. A wire hit is recorded by setting the corresponding bit to zero. The wire hit pattern is $FDF = 1111\ 1101\ 1111$, showing that the 6th wire (reading from the right) in RAM# 4 has registered a hit. Using Table B.1 we see that this corresponds to chamber wire number 53, where we have assigned the vertex-closest or coordinate wire plane within a chamber to have wire numbers 0 through 55 and the neighboring ambiguity wire plane to have numbers 56-95. The wire numbers for both wire planes start with their smallest value (0 for the coordinate plane and 56 for the ambiguity plane) near the beamline and increase with radius. Due to the way in which the chambers were cabled, the wire numbers do not increase consecutively within a TDC unit. The remaining four hexadecimal digits of the right-most hit word

RAM#	RAM Wire#	Chamber Wire#	RAM#	RAM Wire#	Chamber Wire#
0	1	0	4	1	48
0	2	1	4	2	49
0	3	2	4	3	50
0	4	3	4	4	51
0	5	4	4	5	52
0	6	5	4	6	53
0	7	6	4	7	54
0	8	7	4	8	55
0	9	8	4	9	88
0	10	9	4	10	89
0	11	10	4	11	90
0	12	11	4	12	91
1	1	12	5	1	92
1	2	13	5	2	93
1	3	14	5	3	94
1	4	15	5	4	94
1	5	16	5	5	56
1	6	17	5	6	57
1	7	18	5	7	58
1	8	19	5	8	59
1	9	20	5	9	60
1	10	21	5	10	61
1	11	22	5	11	62
1	12	23	5	12	63
2	1	24	6	1	64
2	2	25	6	2	65
2	3	26	6	3	66
2	4	27	6	4	67
2	5	28	6	5	68
2	6	29	6	6	69
2	7	30	6	7	70
2	8	31	6	8	71
2	9	32	6	9	72
2	10	33	6	10	73
2	11	34	6	11	74
2	12	35	6	12	75
3	1	36	7	1	76
3	2	37	7	2	77
3	3	38	7	3	78
3	4	39	7	4	79
3	5	40	7	5	80
3	6	41	7	6	81
3	7	42	7	7	82
3	8	43	7	8	83
3	9	44	7	9	84
3	10	45	7	10	85
3	11	46	7	11	86
3	12	47	7	12	87

Table B.1: Mapping of RAM wire# to chamber wire#.

contain what is known as the “tap time”. As discussed in Chapter 2, in order to achieve 1 nanosecond resolution, the TDC uses a tapped delay line with data inputs into a memory known as the “vernier RAM”. As a pulse propagates to the left down the delay line (Figure B.3), bits are set and its “picture” is taken (i.e. the bit pattern is recorded) on the next clock cycle. The earlier a pulse arrives, the further to the left it will travel before its “picture” is taken. And, by the same token, a pulse which arrives later travels a shorter distance down the delay line and will have fewer bits set in the vernier RAM memory. Thus, from the pattern of bits, the arrival time of the pulse, which can come before or after the current clock cycle, is measured to 1 nanosecond accuracy. Figure B.3 shows that a tap time of zero is taken to be at the center of the delay line or for a bit pattern of 00FF. Other tap times are positive or negative offsets depending on the arrival time of the pulse relative to the clock cycle. The tap time for this hit was 000F = +4 nanoseconds. Thus, we find that a hit occurred on chamber wire# 53 at $280 + 4 = 284$ ns into the clock oscillation period. Moving to the left in RAM# 4, we see that the next hit is also on wire# 53 with a time of $001D + 3FFF = 290 + -6 = 284$ ns, exactly the same as the first hit. This is simply our first pulse propagating down the delay line and being measured on the next clock cycle. Hits such as these are easy to recognize since they are on the same wire as the first hit and have a time equal to that of the initial hit. Such redundant hits are not used in the track-finding and only the initial hit is retained. Finishing up RAM# 4, we have the remaining two hexadecimal words which are known as

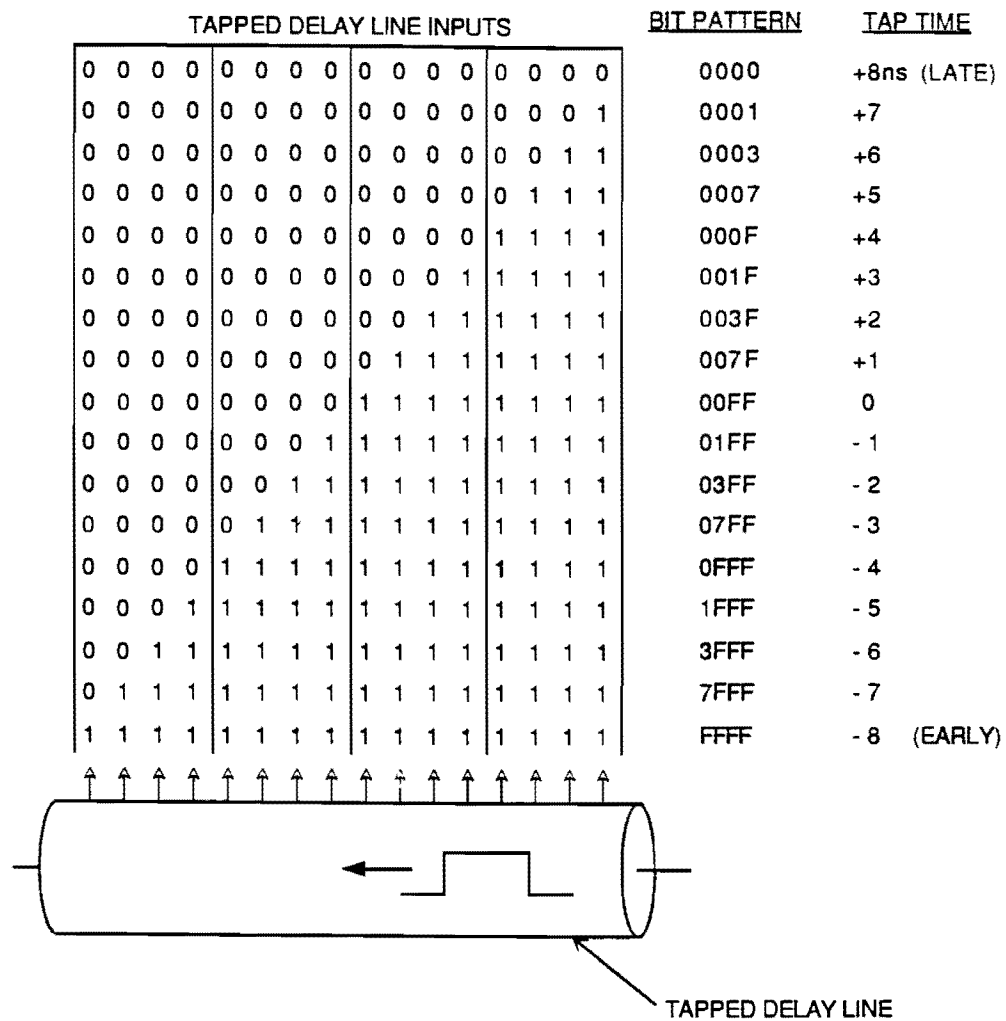


Figure B.3: Delay line operation and tap time offsets.

the “STOP CLOCK” marker words. These are written at the end of the clock oscillation period to indicate that there was no more data in the RAM for this event. The clock time value $009F = 1590$ nanoseconds gives the total TDC clock oscillation time.

As mentioned in Chapter 2, the TDC data is read out by the SSP and reformatted into a more convenient form before being written to tape. Figure B.4 shows the result of the SSP reformatting for the octant containing our sample track. The TDC data itself is stored on tape in an array-like structure known as a YBOS data bank [85]. The name of the particular YBOS bank containing the TDC data is the “FMUD” bank. Figure B.4 shows the data from the FMUD bank for the octant containing our sample track. Looking at the upper left-hand corner of Figure B.4, we see that the first dataword in the octant is simply a three for the three planes in the octant. The next four words contain pointers in the lower half-word to the TDC data in each of the three chamber planes as well as an end-of-data pointer. The upper half-words contain the total number of words in each plane. As an example, let us consider the pointer for data in the front plane. It is a five and so counting from the beginning of the bank (upper left-hand corner of the figure) and starting with zero (of course!), we find the first START CLOCK word for RAM# 4 which was discussed in our description of TDC data above. Continuing on we find the second START clock word as well as the two (one real, one redundant) hits found above and the RAM# 4 STOP CLOCK words all oriented now in FIFO (First In, First Out) order. So, the TDC

#PLANES ↓ RAM# CLOCK TIME WIRE NO.	# WORDS IN THIS PLANE ↓ POINTER TO DATA IN THE FRONT PLANE	POINTER TO DATA IN THE MIDDLE PLANE	POINTER TO DATA IN THE REAR PLANE	END OF DATA POINTER	START OF FRONT PLANE DATA ↓ RAM 4 START CLOCK WORDS	CLOCK TIME	TAP TIME
00000003 001C4FDF	000E0005 001D3FFF	001C0013 001D4FDF	000E002F 009F0000 START OF MIDDLE PLANE DATA ↓ 00000000	0000003D 009F4FFF	00000000 00005FFF	001C000F	005C007F
005C5FFD	009F0000	009F5FFF	00000000	00001FFF	001C1FFF	001C1F7F	003A0FFF
003A1F7F	009F0000	009F1FFF	00000000	00004FFF	004B00FF	004B4FDF	009F0000
009F4FFF	00000000	00005FFF	0018001F	00185BFF	00197FFE	00195BFF	0027000F START OF REAR PLANE DATA ↓ 00000000
00275FFD	00281FFF	00285FFD	002E00FF	002E5BFF	009F0000	009F5FFF	00000000
00004FFF	0041003F	00414FBF	009F0000	009F4FFF	00000000	00005FFF	003D001F
003D5FFB	003E3FFE	003E5FFB	009F0000	009F5FFF			

Figure B.4: Reformatted TDC data stored in the FMUD bank for our sample track.

data from the three planes in an octant has been combined using data pointers and re-ordered (FIFO versus LIFO) courtesy of the SSP. Table B.2 shows the result of decoding the wire and hit times for our sample track octant as well as some t_0 corrections we now want to describe.

The first observation for Table B.2 is that we have found ten hits, six on our sample track and two pairs of double wire hits in the inner HOPU region, in agreement with Figure B.1. Now, to obtain the actual drift time in the chamber cell from the TDC hit time, we first perform a global t_0 subtraction of 190. ns, which eliminates the cable delay from the collision hall to the counting room.[86] This global t_0 value and the reciprocal drift velocity we will use were obtained from the following method. Using Figure B.5a, we can write the relation:

$$R_C + v_D t_C + \Delta R = R_A - v_D t_A, \quad (\text{B.1})$$

or, after a little manipulation:

$$t_C + t_A = \frac{1}{v_D}(R_A - R_C - \Delta R), \quad (\text{B.2})$$

where t_C and t_A are the t_0 subtracted drift times and ΔR is gotten from the track angle and the wire plane separation. The sum of the measured times, T , is related to the t_0 subtracted times by:

$$T = t_C + t_A + 2t_0. \quad (\text{B.3})$$

Substituting into Equation B.2, we obtain:

$$t_0 = \frac{1}{2}\left(T - \frac{1}{v_D}(R_A - R_C - \Delta R)\right). \quad (\text{B.4})$$

A similar equation can be written for the case of the coordinate hit below the wire (Figure B.5b). Equation B.4 was simultaneously fit for t_0 and $1/v_D$ using data from our sample. The best fit gave $t_0 = 190. \text{ ns}$ and $1/v_D = 193. \text{ ns/cm}$, where the last value is in agreement with test beam results.

There is next a correction due to the fact that the CLR timing signal, which causes the TDCs to receive the 10 nanosecond clock cycles from the continuously running TDC clock and begin the time digitization process, can come anywhere within the 10 nanosecond clock cycle. In order to determine the starting time of the digitization process to within the desired 1 nanosecond accuracy, the arrival time of CLR within the 10 nanosecond clock cycle must be measured. Since CLR starts the time measurements, we can't measure that signal directly but use instead the arrival time of the STOP signal which was fixed in time relative to CLR. Recall from Chapter 2 that the STOP signal comes after the CLR signal and causes the TDC clock to run for a preset number of cycles to finish the time measurement for the current event. The event by event variation of the arrival time of the STOP signal within the TDC clock cycle is shown in Figure B.6 for both the east and the west sides of the detector since each side had its own TDC clock. These distributions should have equal occupancy in each of the one nanosecond bins over a ± 5 nanosecond range centered about the mean value and the variation in occupancy is due to jitter in the STOP/CLR time difference and internal delay differences within the TDC. For our data sample, the average value of STOP was measured and using this as the reference, a correction was made

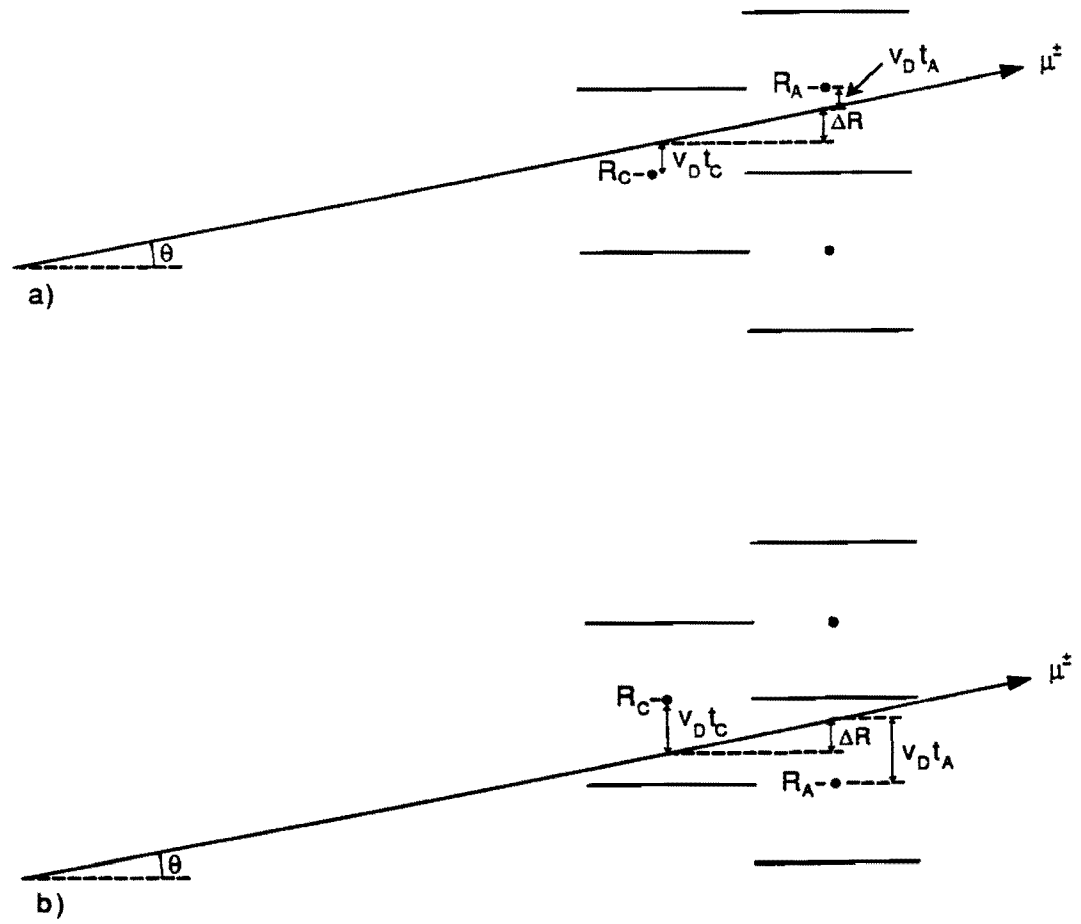


Figure B.5: Method for obtaining the global t_0 offset and reciprocal drift velocity.

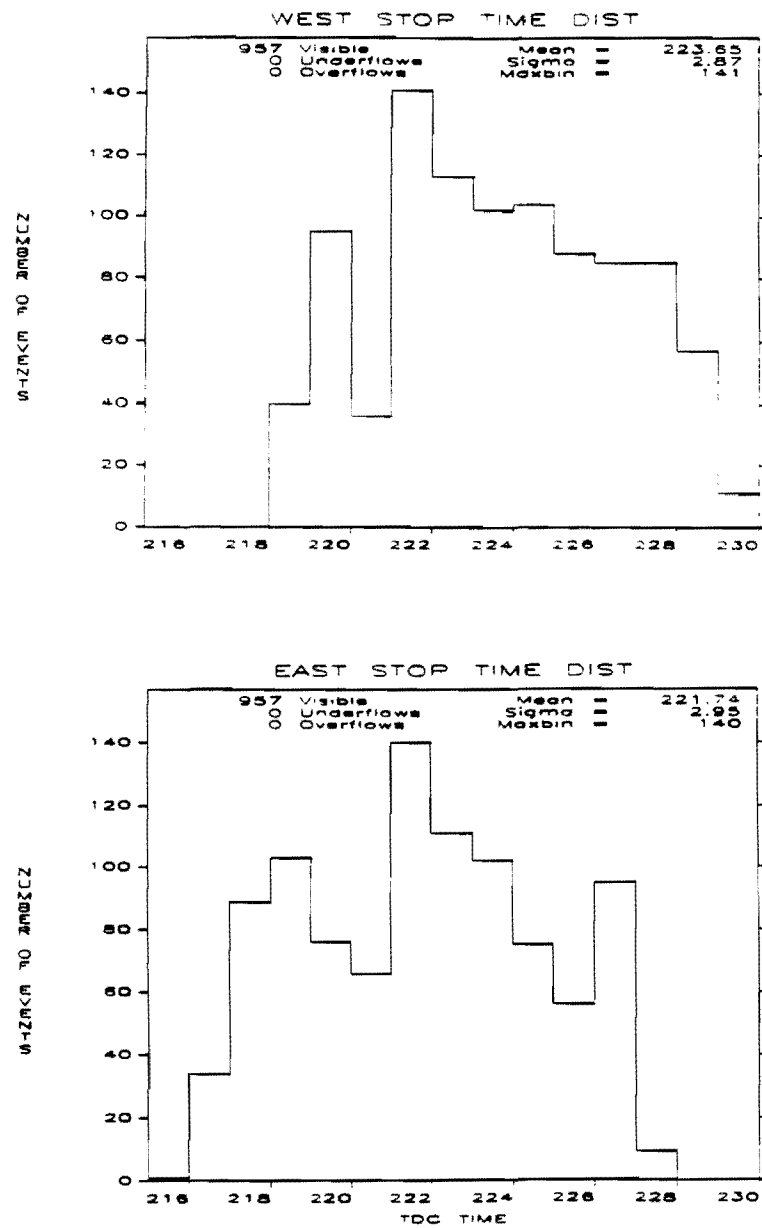


Figure B.6: STOP signal arrival time variation for our data sample.

for each event relative to this average. For example, from the FMTD data bank where the STOP arrival times are stored in the same format as the TDC hit data, the east STOP time was 218 ns and the west STOP time was 220 ns. Since our sample track is on the west side of the FMU system and the average of the west STOP time distribution in Figure B.6 is 223.65 ns, the clock phase correction is $223.65 - 220 = 3.65$ ns, as shown in Table B.2. The next drift time correction in Table B.2 is for the time-of-flight (TOF) between the different chamber planes. With a chamber plane separation of 168.0 cm and taking the front plane as the reference, the time-of-flight between planes requires an additional

$$168.0 \text{ cm} \times \frac{1.0 \text{ ns}}{29.98 \text{ cm}} = 5.6 \text{ ns.} \quad (\text{B.5})$$

The difference in cable delays between chamber cells at different radii is also another t_0 correction. Assuming $\beta = 0.58$ for the signal cable, the signal propagation delay for a chamber wire at radius R in a chamber plane with maximum radius R^{OUT} is:

$$\text{cable delay} = \frac{1}{\beta c} (R^{\text{OUT}} - R), \quad (\text{B.6})$$

where $R^{\text{OUT}} = 278.0, 325.0, 372.0$ cm for the front, middle, and rear chamber planes, respectively. The final t_0 correction is the delay due to signal propagation down the sense wire itself. Assuming $\beta = 0.66$ for the sense wire, this correction takes the form:

$$\text{wire delay} = 0.0505 \frac{L}{2}, \quad (\text{B.7})$$

where L is the wire length in centimeters.

All of the t_0 corrections are shown in Table B.2 and after the appropriate addition or subtraction of each correction to the TDC time, a value for the corrected time is shown for each hit. The corrected time is then divided by the reciprocal drift velocity of 193. ns/cm to obtain an integer value for the drift distance in units of 50 microns. For example, for the front plane hit on wire 53 at a TDC time of 284. nanoseconds, we obtain the following corrected drift time:

$$\text{corrected time} = 284. - 190. + 3.65 - 0.0 - 0.88 - 1.82 = 94.95 \text{ ns}$$

and a drift distance in 50 micron units of:

$$\text{drift distance} = (94.95 \text{ ns}/193. \text{ ns/cm})(200. \text{ 50 micron units/cm}) = 98,$$

which is the value shown in Table B.2. This information was stored in another YBOS data bank known as the “FMUE” bank and the operation of taking the raw TDC hit time and converting it to a drift distance was known as a “Data-to-Element” conversion. With the muon hit positions in hand, we now examine the algorithm used to fit the forward muon tracks and determine their momentum.

B.2 Track-finding Procedure

Hit pattern recognition in the chamber wires was performed as follows. The FMUE bank was searched for at least 5 out of a possible 6 hits within a user-specified vertex-pointing tower road. Each such candidate track formed a FMQW data bank. For example our track in Figure B.1 contains six hits pointing toward

the event vertex. Thus, the six hits composing the track with their wire numbers and drift distances were written into a FMQW bank. Other similar patterns of hits, say from another muon in the case of a dimuon event, would be written in a separate FMQW bank.

Using these banks, the left-right hit ambiguity was resolved in each chamber plane where possible and the absolute radius and z position of each hit was written to another data bank called the FMPW bank. If the left-right hit ambiguity was unresolved due to a missing coordinate or ambiguity hit for example, hits for both signs of drift were included in the FMPW bank. There was one FMPW bank for each FMQW bank. In the case of our sample track, there was good position matching on a plane-by-plane basis between the coordinate and ambiguity hits and the left-right ambiguity was resolved in each case.

The determination of the azimuth of a candidate track was done by first assigning all wire hits to the center of the chamber for which there existed an unambiguous counter hit pair. For some events more than one counter pair was present, and for other events there was no counter pair due to counter inefficiency. In either case, the wire hits were then assigned to the center of the first (smallest azimuth) chamber in the octant by default. To improve the azimuthal position of the candidate track, each wire hit was associated with at most two separate strip hits at the same radius. If no match was available or if more than two strip associations were possible, no associations were made and the wire hit retained its initial azimuth assignment. The track-finding required that the plane-by-plane

wire position azimuths as determined by the strips be consistent with the user-specified strip road. Strip inefficiency did not cause the track to be lost unless a strip hit caused the wire hit to be assigned to an azimuth inconsistent with the strip road. For example, in Figure B.7a we see that the strip hits, indicated by the shaded boxes, are consistent with a strip road of width 1. That is, the strip hits from any two planes match in azimuth to within one strip position. In Figure B.7b however, the front and rear plane strip hits are two strips apart and do not satisfy a strip road of width 1 requirement. Real muons are expected to scatter in azimuth by less than one strip position and strip hits separated in azimuth by more than one strip indicate that the associated wire hits are inconsistent with the passage of a muon.

The forward muon track-finding procedure [87] operated off of the hits in the FMPW bank and selected either a matched pair or a single hit from each of the front, middle, and rear planes within the tower road. All such combinations were fit and a track segment or “FMUS” bank was created for each new track satisfying a user-specified χ^2 cut. In the case where two segments shared a common hit and both satisfied the χ^2 cut, the segment with the smallest χ^2 per degree of freedom was kept and the other one was discarded.

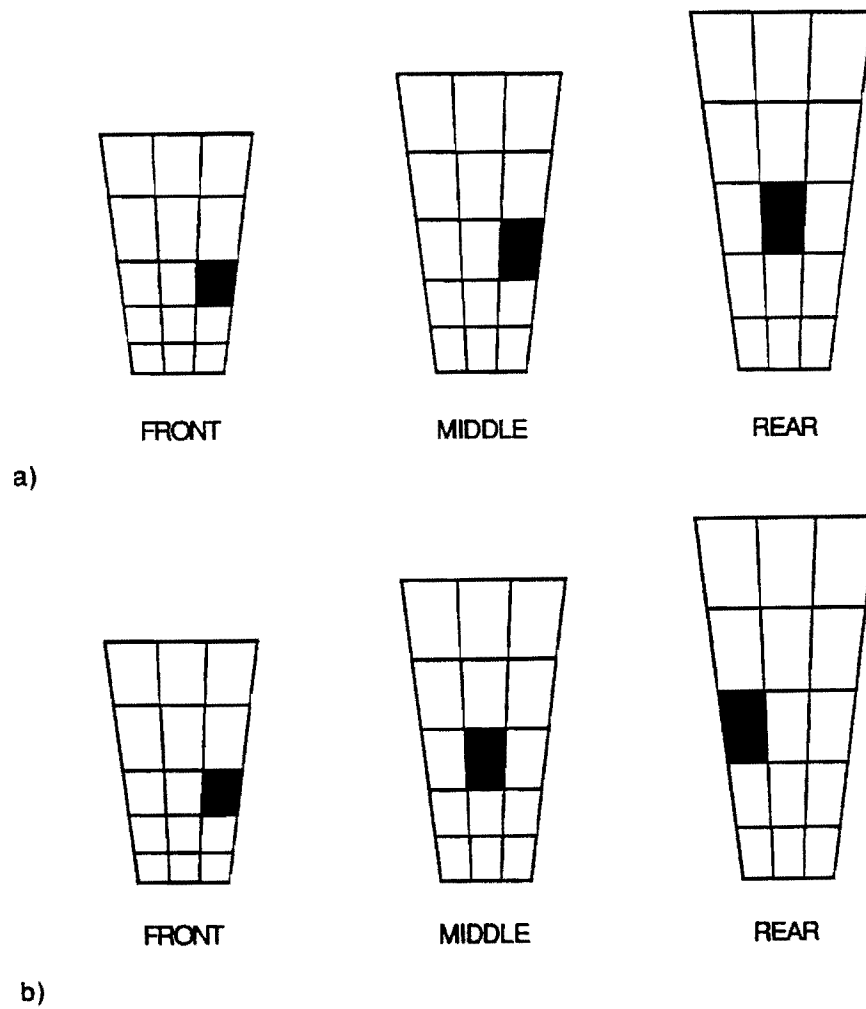


Figure B.7: a) Strip hits consistent with a strip road of width 1. b) Strip hits failing a strip road of width 1 requirement.

B.3 Track-fitting Algorithm

Initial estimates of the track parameters were determined from a fit to the parabolic equation:

$$r = r_0 + \tan\theta_0 z + \frac{1}{2}k(z - z')^2, \quad (\text{B.8})$$

where z' was the distance to the front face of the first toroid and the track parameters were r_0 , the impact parameter at the vertex position, $\tan\theta_0$, the initial polar angle of the track, and k , the charge divided by the momentum (also known as the “curvature”). The quadratic term was only used in regions of magnetic field. As shown in Figure B.8, the gaps were ignored in this estimation and the field region was taken to be from the front toroid face through the rear chamber plane position. A fourth track parameter, the azimuthal angle of the track, was determined from the counters when possible, otherwise from strip information, as discussed above. A Least-Squares algorithm was used to perform the fit. This was done by minimizing the χ^2 variable given (in matrix notation) by:

$$\chi^2 = (R - r)^T V_R^{-1} (R - r), \quad (\text{B.9})$$

where R is track position measurements, r is the fitted position values and a function of the track parameters r_0 , $\tan\theta_0$, and k , which we will denote collectively as “ α ”, and V_R is the covariance matrix of R . For our sample track, the hit positions contained in the FMPW bank are shown in Table B.3.

For the case of a linear Least Squares model such as we have here, one can

Plane #	Wire #	TDC Time (ns)	Global t0 (ns)	Clock Phase (ns)	Plane TOF (ns)	Cable Delay (ns)	Wire Delay (ns)	Corr. Time (ns)	Drift Dist. (50 μ m)
0	53	284.	-190.	+3.65	-0.0	-0.88	-1.82	94.95	98
0	93	921.	-190.	+3.65	-0.0	-0.65	-1.84	732.16	758
1	19	275.	-190.	+3.65	-5.6	-12.59	-0.75	69.71	72
1	19	576.	-190.	+3.65	-5.6	-12.59	-0.75	370.71	384
1	53	750.	-190.	+3.65	-5.6	-1.09	-2.12	554.84	574
1	62	243.	-190.	+3.65	-5.6	-13.72	-0.61	36.72	37
1	93	394.	-190.	+3.65	-5.6	-0.79	-2.15	199.11	206
1	62	460.	-190.	+3.65	-5.6	-13.72	-0.61	253.72	262
2	54	652.	-190.	+3.65	-11.2	-0.57	-2.50	451.38	467
2	94	613.	-190.	+3.65	-11.2	-0.27	-2.54	412.64	427

Table B.2: TDC data t0 corrections.

Wire Plane	Hit Number	Radial Position (cm)	Z Position (cm)	Position Error (cm)	Phi Position (degrees)
0	1	262.258	-974.509	0.050	5.105
1	2	262.858	-976.739	0.050	5.105
2	3	309.635	-1142.517	0.050	5.105
3	4	310.294	-1144.747	0.050	5.105
4	5	364.354	-1310.797	0.050	5.105
5	6	365.099	-1313.027	0.050	5.105
Vertex	7	0.000	20.810	0.1	0.000

Table B.3: Sample track hit positions.

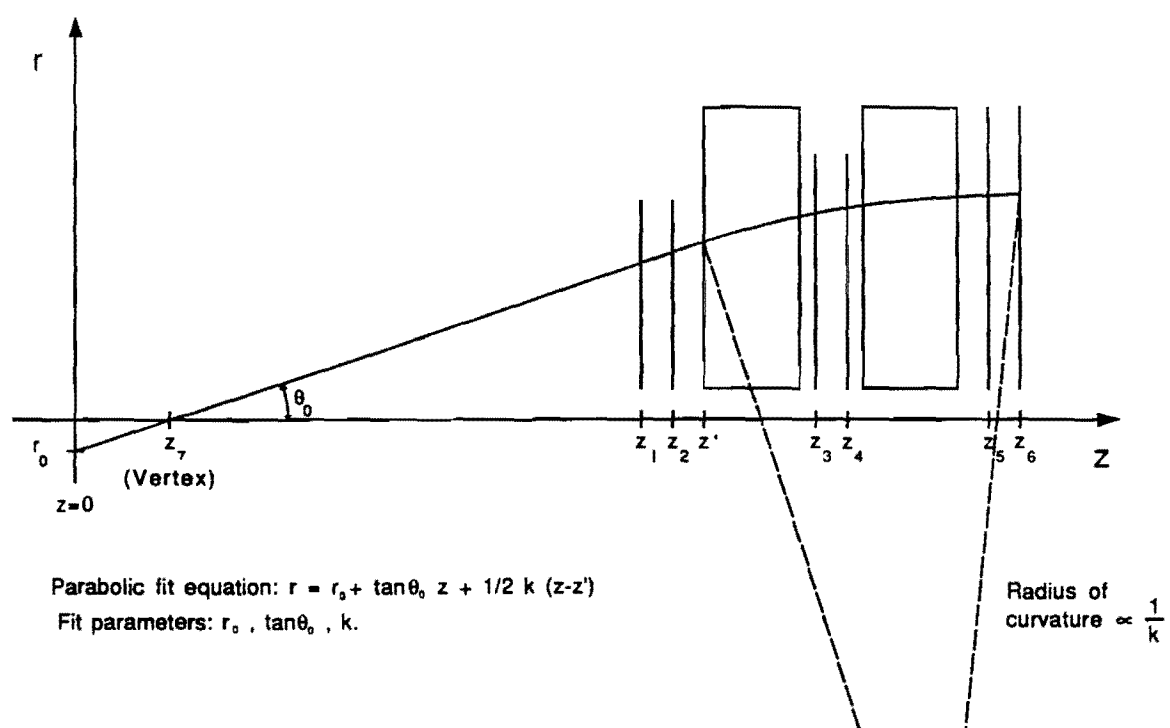


Figure B.8: Initial track parameter estimation.

write Equation B.8 in the matrix form $\mathbf{r} = \mathbf{A}\alpha$:

$$\begin{bmatrix} r_1 \\ r_2 \\ r_3 \\ r_4 \\ r_5 \\ r_6 \\ r_7 \end{bmatrix} = \begin{bmatrix} 1 & z_1 & 0 \\ 1 & z_2 & 0 \\ 1 & z_3 & \frac{1}{2}(z_3 - z')^2 \\ 1 & z_4 & \frac{1}{2}(z_4 - z')^2 \\ 1 & z_5 & \frac{1}{2}(z_5 - z')^2 \\ 1 & z_6 & \frac{1}{2}(z_6 - z')^2 \\ 1 & z_7 & 0 \end{bmatrix} \begin{bmatrix} r_0 \\ \tan\theta_0 \\ k \end{bmatrix}.$$

Equation B.9 then becomes:

$$\chi^2 = (\mathbf{R} - \mathbf{A}\alpha)^T \mathbf{V}_R^{-1} (\mathbf{R} - \mathbf{A}\alpha). \quad (\text{B.10})$$

Taking the derivative of Equation B.10 in order to determine the track parameters α for which χ^2 is a minimum, we have:

$$\nabla_{\alpha} \chi^2 = -2(\mathbf{A}^T \mathbf{V}_R^{-1} \mathbf{R} - \mathbf{A}^T \mathbf{V}_R^{-1} \mathbf{A} \alpha). \quad (\text{B.11})$$

Setting this equation equal to zero and solving for α , we find the solution:

$$\alpha = (\mathbf{A}^T \mathbf{V}_R^{-1} \mathbf{A})^{-1} \mathbf{A}^T \mathbf{V}_R^{-1} \mathbf{R}, \quad (\text{B.12})$$

where for our sample track \mathbf{R} is a column vector containing the radial hit posi-

tions,

$$R = \begin{bmatrix} 262.258 \\ 262.858 \\ 309.635 \\ 310.294 \\ 364.354 \\ 365.099 \\ 0.000 \end{bmatrix},$$

the matrix A is given by,

$$A = \begin{bmatrix} 1.000 & -974.509 & 0.000 \\ 1.000 & -976.739 & 0.000 \\ 1.000 & -1142.517 & 8387.386 \\ 1.000 & -1144.747 & 8678.677 \\ 1.000 & -1310.797 & 44341.671 \\ 1.000 & -1313.027 & 45008.240 \\ 1.000 & 20.810 & 0.000 \end{bmatrix},$$

and, ignoring multiple scattering in the initial fit, the measurement covariance matrix V_R is diagonal with elements consisting of the position errors squared (in

units of 10^{-2}cm^2):

$$V_R = \begin{bmatrix} 0.250 & 0.000 & 0.000 & 0.000 & 0.000 & 0.000 & 0.000 \\ 0.000 & 0.250 & 0.000 & 0.000 & 0.000 & 0.000 & 0.000 \\ 0.000 & 0.000 & 0.250 & 0.000 & 0.000 & 0.000 & 0.000 \\ 0.000 & 0.000 & 0.000 & 0.250 & 0.000 & 0.000 & 0.000 \\ 0.000 & 0.000 & 0.000 & 0.000 & 0.250 & 0.000 & 0.000 \\ 0.000 & 0.000 & 0.000 & 0.000 & 0.000 & 0.250 & 0.000 \\ 0.000 & 0.000 & 0.000 & 0.000 & 0.000 & 0.000 & 1.000 \end{bmatrix},$$

where the chamber resolution is $500\text{ }\mu\text{m}$ and the error on the vertex is 1.0 mm .

Performing the matrix multiplications given in Equation B.12, we obtain the following first estimate for the track parameters α :

$$\alpha = \begin{bmatrix} r_0 \\ \tan\theta_0 \\ k \end{bmatrix} = \begin{bmatrix} 5.261\text{ cm} \\ -0.264 \\ 2.952 \times 10^{-4}\text{ cm}^{-1} \end{bmatrix}.$$

Using the formula:

$$p = 2.9979 \times 10^{-4} \frac{qB}{k \cos\theta_0}, \quad (\text{B.13})$$

where p is in GeV/c , B is in kilogauss and k is in cm^{-1} , and with a magnetic field value of 17.5 kilogauss at the track entrance to the front toroid, we find a value for the momentum:

$$p = 18.4\text{ GeV}/c. \quad (\text{B.14})$$

An empirical correction is then made from a Monte Carlo simulation where it was

found that the reconstructed momentum was 20% higher than the generated momentum due to the gap (field-free region) between the toroids which was ignored in the parabolic fit.[88] Multiplying the above value by 0.8, the initial estimate for the momentum of our sample track is then

$$p = 14.7 \text{ GeV}/c. \quad (\text{B.15})$$

With these initial track parameters, the tracking algorithm then refits the track taking into account multiple scattering and energy loss in the calorimeters and toroids. This is done using a constrained Least-Squares fit [89] in which the event vertex (which was included before) and/or an initial track angle at the vertex from a matching VTPC track is used as a constraint. The χ^2 minimization equation then takes the form (again in matrix notation):

$$\chi^2 = (R - r)^T V_R^{-1} (R - r) + 2\lambda^T (B\alpha - b), \quad (\text{B.16})$$

where R , r , V_R , and α have the same meanings as above and the Lagrange multipliers, λ , have been introduced to handle the linear constraints $B\alpha - b = 0$. With $r = A\alpha$, we compute the derivatives:

$$\begin{aligned} \nabla_{\alpha} \chi^2 &= -2(A^T V_R^{-1} R - A^T V_R^{-1} A\alpha) + 2B^T \lambda = 0, \\ \nabla_{\lambda} \chi^2 &= 2(B\alpha - b) = 0. \end{aligned} \quad (\text{B.17})$$

Introducing $C \equiv A^T V_R^{-1} A$ and $c \equiv A^T V_R^{-1} R$, we have:

$$\begin{aligned} C\alpha + B^T \lambda &= c, \\ B\alpha &= b. \end{aligned} \quad (\text{B.18})$$

If the inverse of C exists, we can multiply the first equation by BC^{-1} and substitute for $B\alpha$ from the last equation to obtain:

$$b + BC^{-1}B^T\lambda = BC^{-1}c. \quad (B.19)$$

Defining $V_B \equiv BC^{-1}B^T$, we solve for λ :

$$\lambda = V_B^{-1}(BC^{-1}c - b), \quad (B.20)$$

and substitute into Equations B.18 to obtain an expression for the fit parameters α :

$$\alpha = C^{-1}c - C^{-1}B^TV_B^{-1}(BC^{-1}c - b). \quad (B.21)$$

We note here that b is a function of α from Equations B.18 so that an iterative procedure was necessary in order to determine the track parameters for which χ^2 given by Equation B.16 was a minimum. The input to the procedure was the track parameters from the parabolic fit. Using the initial values for the parameters r_0 , $\tan\theta_0$, and k , the muon was projected up to the front toroid face and stepped through the toroid in ten equal steps. The change in radius of the muon Δr due to the magnetic field after a step Δz is given by:

$$\Delta r = \frac{1}{k}(1 - \sqrt{1 - 2k\tan\theta_0\Delta z - (k\Delta z)^2}), \quad (B.22)$$

which reduces to Equation B.8 for $2k\tan\theta_0\Delta z + (k\Delta z)^2 \ll 1$. The curvature k ($=q/p$) was corrected for energy loss in the toroid steel after each step in exactly the same way as that for energy loss in a hadron calorimeter given below. The

multiple scattering of the muon was accounted for by the modification of the measurement covariance matrix to allow for multiple scattering correlations and errors. After passing through the front toroid, the muon was projected to the rear toroid face and then through the rear toroid. At each measurement plane, the residual was calculated and the χ^2 for the current set of fit parameters was computed using Equation B.16. Figure B.9 shows schematically the propagation of the muon track through the system. Small offsets $d\alpha$ were then added to the fit parameters one-by-one and the track was repropagated through the system for each offset addition to determine the new fitted positions r_{NEW} at each wire plane. The matrix A was calculated as the change in the fitted positions divided by the added offset to the track parameters:

$$A = \frac{dr}{d\alpha}, \quad (\text{B.23})$$

or in matrix notation:

$$A(I,J) = \sum_{I=1}^{\text{\#points}} \sum_{J=1}^{\text{\#parameters}} \frac{r_{\text{NEW}}(I) - r_{\text{OLD}}(I)}{\Delta\alpha(J)}, \quad (\text{B.24})$$

where in the first iteration r_{OLD} was obtained from the parabolic fit. Using this equation the matrix A was determined. All other necessary matrices were computed and a new set of track parameters were calculated using Equation B.21. The multiple scattering error was recomputed using the new fit momentum and the track was repropagated to determine the residuals and a new χ^2 . This χ^2 was then compared to the χ^2 from the previous pass. If the χ^2 value or the new fit parameters were unchanged through the third decimal place on this iteration, the

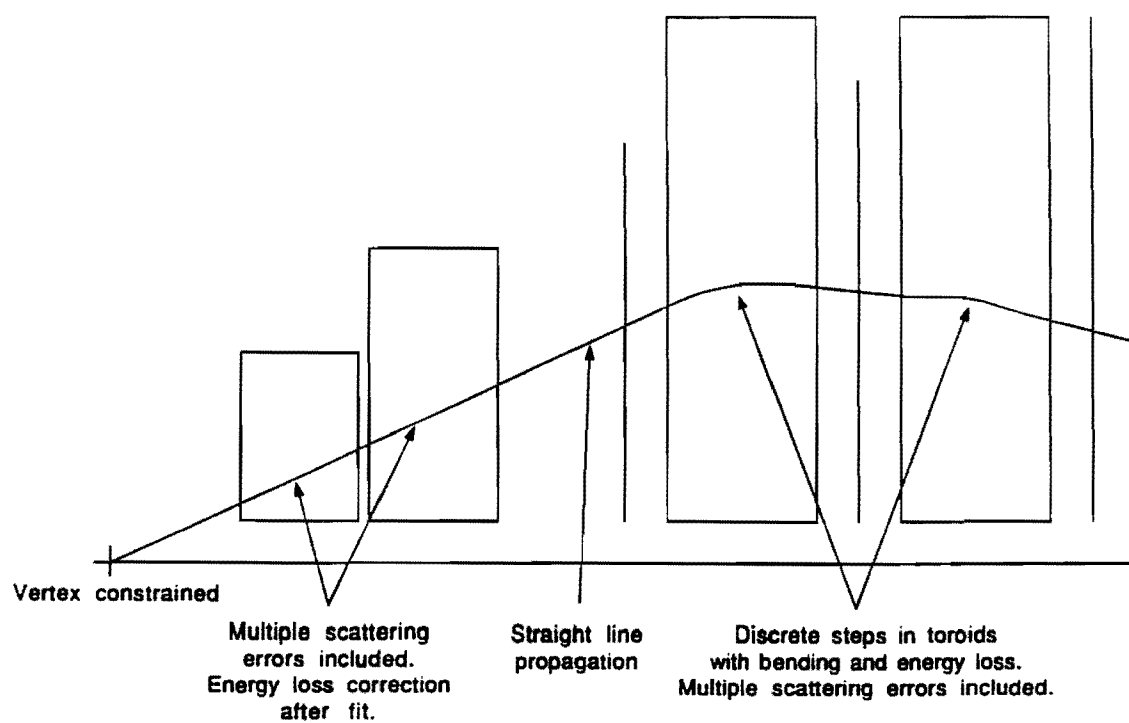


Figure B.9: Muon track propagation through the FMU system.

fit was finished. If not, the matrix A was computed again using Equation B.24, a new set of fit parameters were determined and the propagation and χ^2 comparison process was repeated. Figure B.10 shows the iterative fit procedure. For our sample track only three trials were required for the fit to converge, suggesting that the parabolic fit gave a good estimate of the final track parameters.

The multiple scattering deflection of the muon was handled by modifying the measurement covariance matrix V_R to be a sum of diagonal terms given by the chamber resolution and multiple scattering plus off-diagonal terms due solely to multiple scattering. The multiple scattering contribution to the I th and J th elements is given by:

$$V_R^{MS}(I, J) = \delta R_I \delta R_J, \quad (B.25)$$

where δR_I and δR_J are the deviations of the real trajectory from the ideal trajectory at z_I and z_J respectively, i.e. the deviations caused by multiple scattering. Figure B.11 shows the multiple scattering deflections in each of the material regions. The deviation δR_I is influenced by all scatters of angle θ_K at coordinates z_K with $z_K < z_I$. We can write:

$$\delta R_I = \sum_{K < I} \theta_K (z_I - z_K). \quad (B.26)$$

Similarly, the deviation δR_J is influenced by all scatters of angle θ_L at coordinates z_L with $z_L < z_J$,

$$\delta R_J = \sum_{L < J} \theta_L (z_J - z_L). \quad (B.27)$$

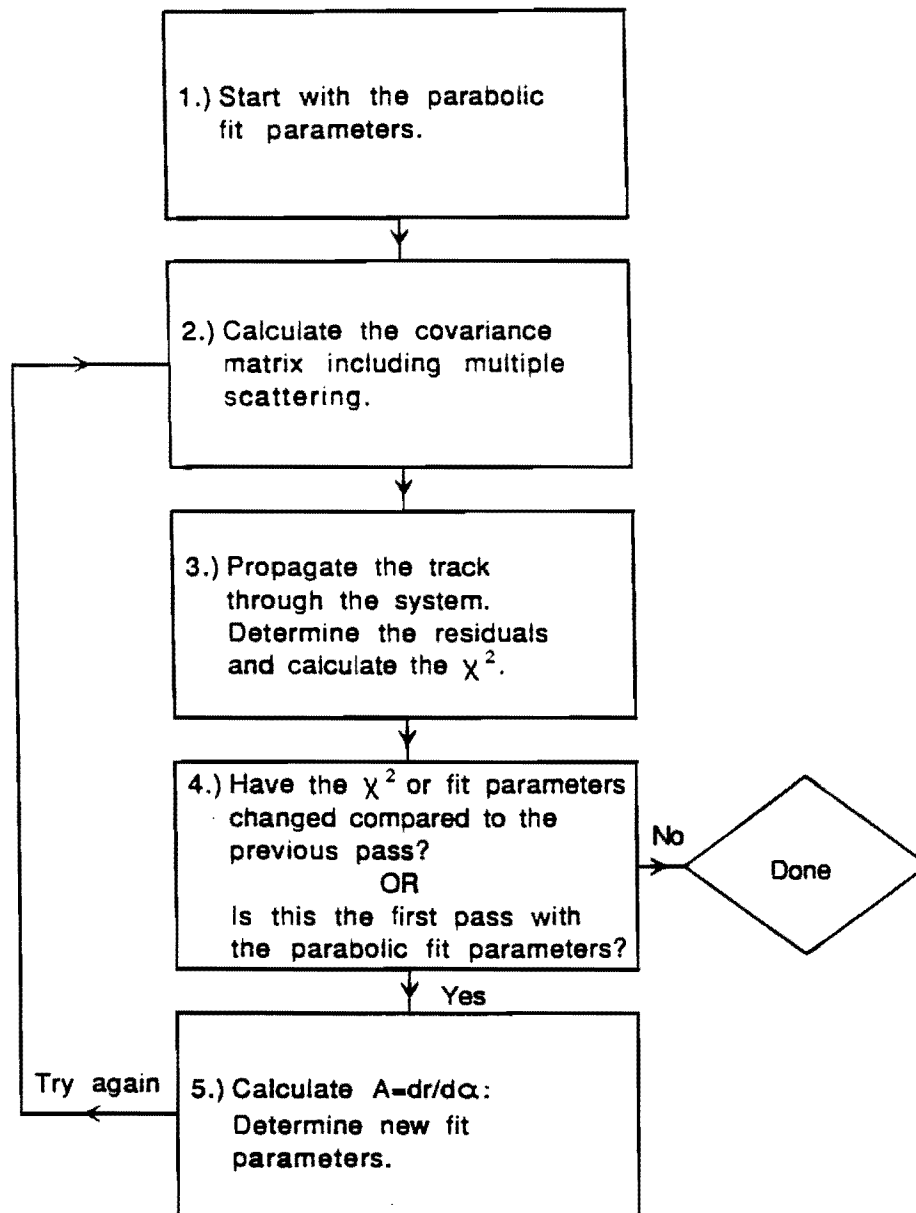


Figure B.10: Iterative fit procedure flowchart.

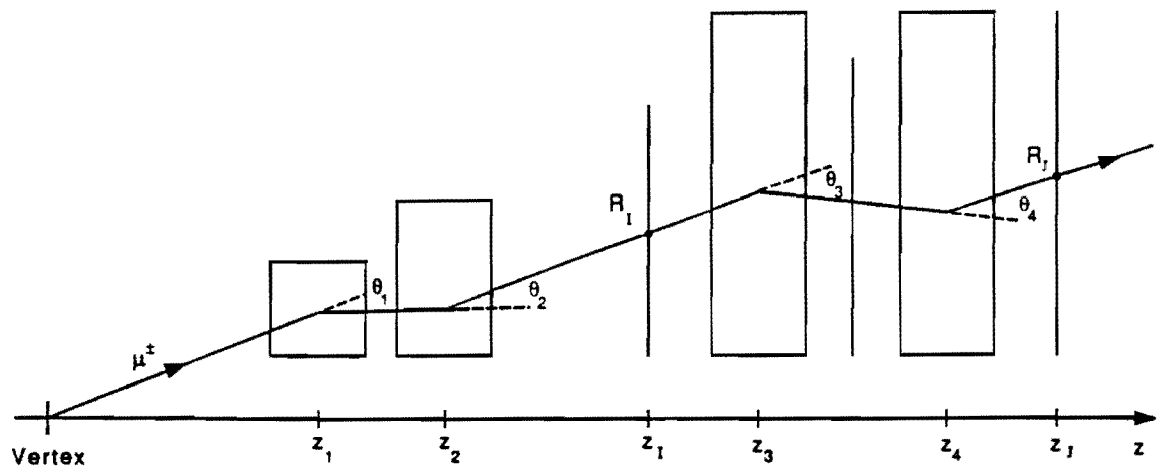


Figure B.11: Multiple scattering covariance calculation.

Combining the two expressions, we obtain:

$$\begin{aligned}\delta R_I \delta R_J &= \sum_{K < I} \sum_{L < J} \theta_K \theta_L (z_I - z_K)(z_J - z_L) \\ &= \sum_{K < \min(I, J)} \theta_K^2 (z_I - z_K)(z_J - z_K),\end{aligned}\quad (\text{B.28})$$

since either θ_K or $\theta_L = 0$ for $K \neq L$ (i.e. there is no multiple scattering correlation between a pair of points if one of the points is measured before the scattering occurs) [90]. The angle θ_K is given by the familiar formula for the plane-projected scattering angle due to multiple scattering:

$$\theta_K = \frac{0.0141}{p\beta} \sqrt{L_K/L_{\text{RAD}}} [1 + \frac{1}{9} \log_{10}(L_K/L_{\text{RAD}})], \quad (\text{B.29})$$

where L_K/L_{RAD} is the thickness of the scattering medium in units of radiation lengths as shown in Table B.4. Multiple scattering is accounted for in both the electromagnetic and hadron calorimeters through which the muon passes (either the plug or forward calorimeters) and the two toroidal magnets. Including multiple scattering, the measurement covariance matrix V_R had the following elements on the last fit iteration:

$$V_R = \begin{bmatrix} 39.482 & 39.606 & 48.987 & 49.113 & 58.510 & 58.636 \\ 39.606 & 39.735 & 49.144 & 49.270 & 58.697 & 58.824 \\ 48.987 & 49.144 & 61.198 & 61.363 & 73.873 & 74.041 \\ 49.113 & 49.270 & 61.363 & 61.534 & 74.096 & 74.265 \\ 58.510 & 58.697 & 73.873 & 74.096 & 91.246 & 91.479 \\ 58.636 & 58.824 & 74.041 & 74.265 & 91.479 & 91.719 \end{bmatrix},$$

where now we consider only six fitted points since the vertex is included as a constraint in the matrices B and b:

$$B = \begin{bmatrix} 1.000 & 20.810 & 0.000 \\ 0.000 & 0.000 & 0.000 \end{bmatrix}, b = \begin{bmatrix} 0.000 & 0.000 \\ 0.000 & 0.000 \end{bmatrix}.$$

We note that the two rows in B correspond to the two possible constraints. The vertex constraint which we are using is given in the first row and the track angle at the vertex constraint which we are not considering here is indicated by the zeros in the second row. Performing the matrix multiplication $B\alpha = b$ results in the equation:

$$r_0 + z_{\text{vertex}} \tan \theta_0 = 0, \quad (\text{B.30})$$

illustrating the vertex constraint requirement.

From $A = dr/d\alpha$ as described above, the matrix A for the final fit is given by:

$$A = \begin{bmatrix} 1.000 & -974.509 & 0.000 \\ 1.000 & -976.739 & 0.000 \\ 1.000 & -1143.614 & 51.211 \\ 1.000 & -1145.876 & 52.694 \\ 1.000 & -1316.586 & 245.869 \\ 1.000 & -1318.903 & 249.356 \end{bmatrix},$$

and the fit parameters are:

$$\alpha = \begin{bmatrix} r_0 \\ \tan \theta_0 \\ k \end{bmatrix} = \begin{bmatrix} 5.452 \text{ cm} \\ -0.262 \\ 5.864 \times 10^{-2} (\text{GeV}/c)^{-1} \end{bmatrix},$$

where we have rescaled the curvature k using Equation B.13 so that $p = q/k$. The resulting value of the momentum for our sample track is:

$$p = 17.0 \text{ GeV}/c \quad (\text{B.31})$$

with a χ^2 of 0.28.

There is one final correction and that is for the muon energy loss in the calorimeters. Energy loss in the toroids was already taken into account in the track propagation procedure in a way identical to the following for the calorimeters. Recall the well-known Bethe-Bloch equation for the ionization energy loss of a charged particle in a material medium:

$$\frac{dE}{dx} = \frac{DZ\rho}{A\beta^2} \left[\ln\left(\frac{2m_e\gamma^2\beta^2c^2}{I}\right) - \beta^2 \right], \quad (\text{B.32})$$

where $D = 0.3070 \text{ MeV cm}^2/\text{g}$, and Z , A , ρ , and I are the atomic number, atomic weight, density, and ionization potential of the medium, respectively. Using Table B.5 for the material properties, substituting in $p = m\gamma\beta c$, taking $\beta = 1$ and realizing that dx is along the track so that $dx = \Delta z / \cos\theta_0$, we have for the muon energy loss in an electromagnetic calorimeter:

$$(\Delta E)_{\text{EM}} = 1.379 \times 10^{-3} \frac{\Delta z}{\cos\theta_0} (2\ln(p) + 10.594) \text{ GeV}, \quad (\text{B.33})$$

and a hadronic calorimeter:

$$(\Delta E)_{\text{HAD}} = 1.125 \times 10^{-3} \frac{\Delta z}{\cos\theta_0} (2\ln(p) + 11.627) \text{ GeV}, \quad (\text{B.34})$$

where Δz is the calorimeter material thickness in centimeters. For our sample

Scattering Medium	Scattering Index K	z_K (cm)	L_K/L_{RAD}	$p\theta_K$ (GeV/c radians)
PEM	1	201.	16.39	0.0648
PHA	2	299.	57.95	0.1284
FEM	1	662.	25.71	0.0827
FHA	2	829.	78.24	0.1510
Front Toroid	3	1063.	56.82	0.1275
Rear Toroid	4	1216.	56.82	0.1275

Table B.4: Multiple scattering parameters.

Energy Loss Medium	Material Type	Atomic Number Z	Atomic Weight A	Density ρ (g/cm ³)	Ionization Potential I (eV)	Thickness Δz (cm)
PEM	Pb	82	207.19	11.35	844.4	9.2
PHA	Fe	26	55.85	7.87	300.3	102.0
FEM	Pb	82	207.19	11.35	844.4	14.4
FHA	Fe	26	55.85	7.87	300.3	137.7
Front Toroid	Fe	26	55.85	7.87	300.3	100.0
Rear Toroid	Fe	26	55.85	7.87	300.3	100.0

Table B.5: dE/dx energy loss parameters.

track $\theta_0 = 165.3^\circ$, which is 14.7° from the beamline or in the plug calorimeter region. Thus, using the values for the material thickness Δz for the PEM and PHA from Table B.5 and taking $p = 17.0 \text{ GeV}/c$, we have:

$$(\Delta E)_{\text{EM}} = 0.2 \text{ GeV} \quad (\text{B.35})$$

and

$$(\Delta E)_{\text{HAD}} = 2.1 \text{ GeV}. \quad (\text{B.36})$$

Our sample track also happened to clip the forward hadron calorimeter with an energy loss of 1.0 GeV . Adding these energy losses to our fitted momentum result, we have for the final momentum of our sample muon:

$$p = 20.3 \text{ GeV}/c. \quad (\text{B.37})$$

This concludes the momentum measurement part of the tracking code. It should be pointed out that the residual distribution from this fitting process is very broad due to the fact that multiple scattering was *not* included in the track propagation routine but instead was accounted for in the covariance matrix. The residual distribution after the fitting process is shown in Figure B.12. The momentum measurement is reliable because multiple scattering errors have been included, but the resulting residual distribution is distorted. Figure B.13 illustrates the difference that may arise in the actual and fitted trajectories due to multiple scattering. The effect on the residual values can be quite large, particularly for the relatively low momentum muons in our sample. To obtain a residual

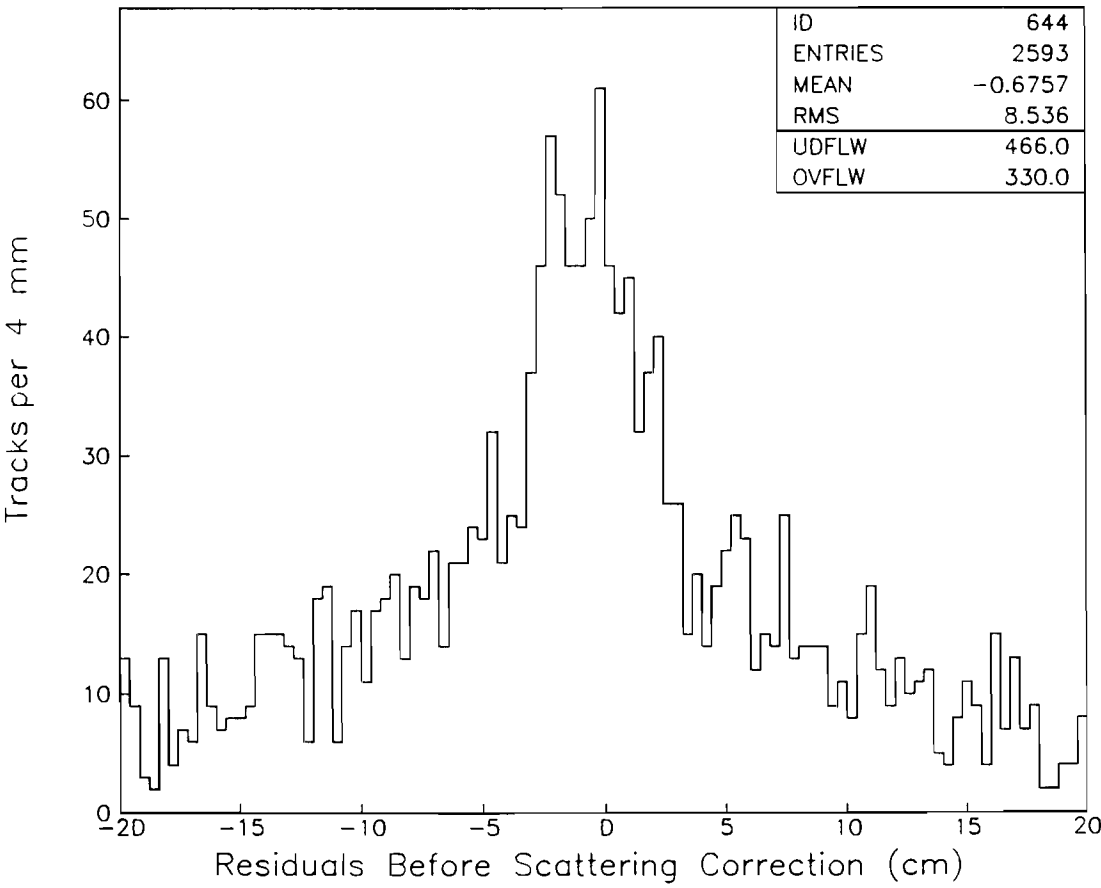


Figure B.12: Residual distribution before including the multiple scattering correction.

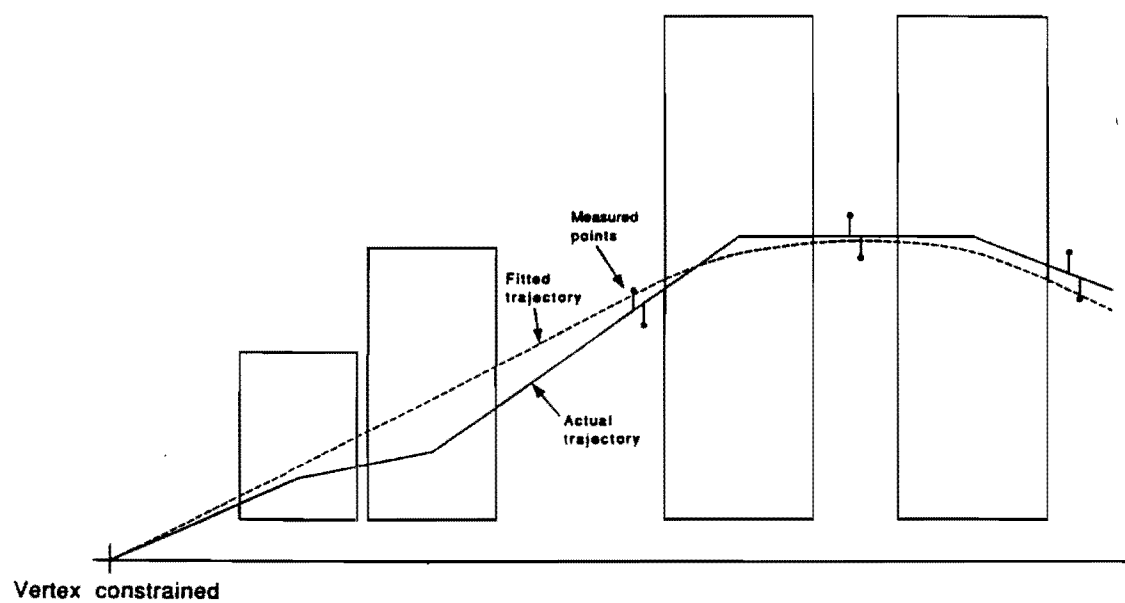


Figure B.13: Difference in the actual and fitted trajectories due to multiple scattering.

distribution which reflects the chamber position measurement error alone, we use the fact that the above method, in which we include the effects of multiple scattering in the covariance matrix, is completely equivalent to introducing discrete scatters in the material regions and writing the χ^2 as a sum of two terms, the first term which includes only detector errors and the second which handles the discrete scattering [91,92]:

$$\chi^2(\alpha, \Theta) = \chi_1^2 + \chi_2^2, \quad (\text{B.38})$$

where

$$\chi_1^2(\alpha, \Theta) = (\mathbf{R} - \mathbf{r}(\alpha, \Theta))^T \mathbf{V}_C^{-1} (\mathbf{R} - \mathbf{r}(\alpha, \Theta)) \quad (\text{B.39})$$

and

$$\chi_2^2(\alpha, \Theta) = \Theta^T \mathbf{S}^{-1} \Theta. \quad (\text{B.40})$$

Here, χ^2 and the fit positions \mathbf{r} are written explicitly as functions of the track parameters α and scattering angles Θ . The matrix \mathbf{V}_C is the covariance matrix of detector measurement errors and \mathbf{S} is the covariance matrix of scattering angles. Both matrices are diagonal and \mathbf{V}_C is similar to \mathbf{V}_R in the parabolic fit and contains elements consisting of the chamber resolution squared, while \mathbf{S} has elements equal to θ_K^2 for each discrete scatter K with θ_K given by Equation B.29 above. A linear expansion of $\mathbf{r}(\alpha, \Theta)$ yields:

$$\mathbf{r}(\alpha, \Theta) = \mathbf{A}\alpha + \mathbf{F}\Theta, \quad (\text{B.41})$$

where $\mathbf{A} = \partial \mathbf{r} / \partial \alpha$ and $\mathbf{F} = \partial \mathbf{r} / \partial \Theta$. Substituting the expansion into Equa-

tion B.38, we have:

$$\chi^2(\alpha, \Theta) = (R - (A\alpha + F\Theta))^T V_C^{-1} (R - (A\alpha + F\Theta)) + \Theta^T S^{-1} \Theta. \quad (\text{B.42})$$

We can solve for the best-fit scattering angles by taking the derivative of χ^2 and setting it equal to zero:

$$\frac{\partial \chi^2}{\partial \Theta} = -F^T V_C^{-1} (R - A\alpha) + (F^T V_C^{-1} F + S^{-1}) \Theta = 0. \quad (\text{B.43})$$

Let $X \equiv F^T V_C^{-1} F + S^{-1}$ and solve for Θ :

$$\Theta = X^{-1} F^T V_C^{-1} (R - A\alpha). \quad (\text{B.44})$$

Substituting for Θ into Equation B.41, the residuals due to the chamber resolution alone are given by:

$$R - r(\alpha, \Theta) = (1 - F X^{-1} F^T V_C^{-1}) (R - A\alpha), \quad (\text{B.45})$$

where we see clearly the subtraction of the contribution from multiple scattering displacement to the residuals. Applying this correction, we see that the residual distribution has narrowed appreciably (Figure B.14) and now reflects more directly the chamber measurement error.

It should be mentioned that the tracking algorithm is reasonably flexible and allows for the following user-specified track-finding parameters:

- Track search lower and upper trigger wire number boundaries;
- Track search lower and upper octant number boundaries;
- Width of tower road in units of trigger cells;

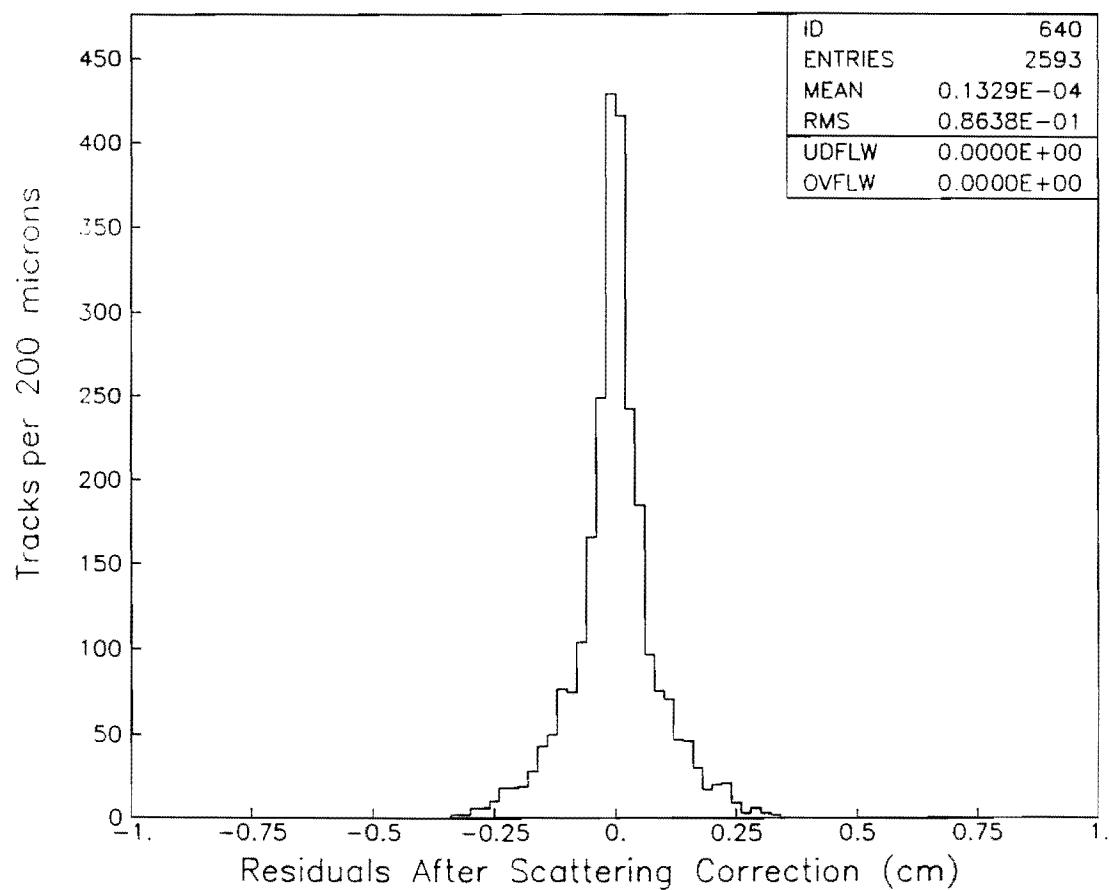


Figure B.14: Residual distribution after the multiple scattering correction. (Same as Figure 3.33.)

- Width of road in strip azimuth;
- Minimum number of hits on the track;
- Coordinate/ambiguity match distance;
- Cut on number of hit combinations allowed in a tower road;
- χ^2 cut.

As mentioned above, the following track-fitting options are also available:

- Event vertex constraint;
- Multiple scattering covariance model;
- Initial polar angle constraint from a matching VTPC track.

Appendix C

Forward Muon Display

Here we describe the forward muon event display used for handscanning events in this thesis. This display has been very useful for providing an overall understanding of the properties of events containing forward muons.[93]

Figure C.1 shows a good, clean 6-hit forward muon track. In this display, the east and west sides of the FMU system have been merged to provide space for information. The vertex for tracks heading to the west, such as our muon track, is on the left side of the display and similarly east-going tracks have a vertex on the right. The horizontal line in the middle is located at the beamline position and sets the display distance scale with a 1.0 meter separation between ticks. Hit information is shown for the octant in which a forward muon track was found plus the octant which is 180° opposite in azimuth. Including both the east and west sides of the system, a total of four octants are displayed. The octant numbers

are listed in the upper right-hand corner. By inspection, our muon track is in octant 6.

The vertical lines in each octant show the position of the three drift chamber planes. Coordinate wire hits are displayed on the vertex-nearest side of the line and the ambiguity wire hits on the other side. For each wire hit a symbol is drawn at the radial position of the wire. Multiple hits on a wire are drawn horizontally next to each other. The small horizontal tick on the drift chamber plane line indicates the inner and outer HOPU boundary. We see that the muon track in Figure C.1 is located in the outer HOPU region and contains six hits.

In-time (beam-beam) and out-of-time (beam-gas) scintillation counter hits for both the front and rear planes are shown at the left- and right-hand edges of the display. These are represented by symbols identical to those used for the wire hits. The counter at the smallest azimuth position in the octant has its hits drawn closest to the beamline with successive counter hits in the octant drawn thereafter. For example, the front counter at the smallest azimuth in octant 6 recorded an in-time (BB) hit and both front and rear counters in the middle of the octant also recorded hits.

The forward muon strip hits are displayed using a rectangular grid which is drawn only for those octants containing strip hits. The three chambers in an octant are each segmented into three strips in azimuth by five strips in radius. Each box in the grid is one chamber in azimuth (15°) by one strip in radius. The azimuth of a chamber within an octant, or a strip within a chamber, increases

with the distance from the corresponding vertex. Strip hits are denoted by a partially-filled box and strips associated with a wire hit also have the wire hit symbol superimposed on them. For our muon track in octant 6, there is a strip hit on the middle strip in the middle chamber in the front and middle planes and a hit on the first strip in the rear plane.

The vertex time projection chamber (VTPC) segments are drawn at the vertex positions. Since the VTPC octants are rotated 22.5° relative to the FMU octants, segments from two matching VTPC octants are shown. These segments are then projected to the front chamber plane and their location is recorded with a symbol. From the closeness of the projected symbol to our muon track in octant 6, we see that there is a matching VTPC segment for this track.

The forward tracking chamber (FTC) segments for the octant are displayed in a fashion similar to that for the strips. The two rows of three boxes represent the upper and lower octants, respectively. A partially-filled box denotes an FTC segment at the corresponding 5° azimuth position. In Figure C.1, we see that there is an FTC segment which matches the azimuth of the strip hits for the forward muon track.

Information about the reconstructed track, including fit parameters and residuals as well as the projected muon calorimeter tower indices and energies, are displayed in the upper left-hand corner of Figure C.1. The calorimetry energy summed in azimuth for the octant is shown as a lego plot in the middle of the display. The energy scale is from 0 to 10 GeV with larger energies clipped to the

10 GeV size. The maximum electromagnetic or hadronic single tower energy is displayed at the bottom for each of the four octants. The lego display is drawn such that the forward muon track should roughly pass through the projected calorimetry tower. For the case of a dimuon event (either a forward-forward or a forward-central dimuon), the invariant mass of the muon pair and its error would be shown in the lower left-hand corner of the display.

The CDF FRED trigger logic bits are shown bit by bit in the upper right-hand corner. The 5th bit corresponded to the FMU Level 1 trigger during the 1987 run and the 14th bit was used to record that the FMU trigger caused the event to be read out.

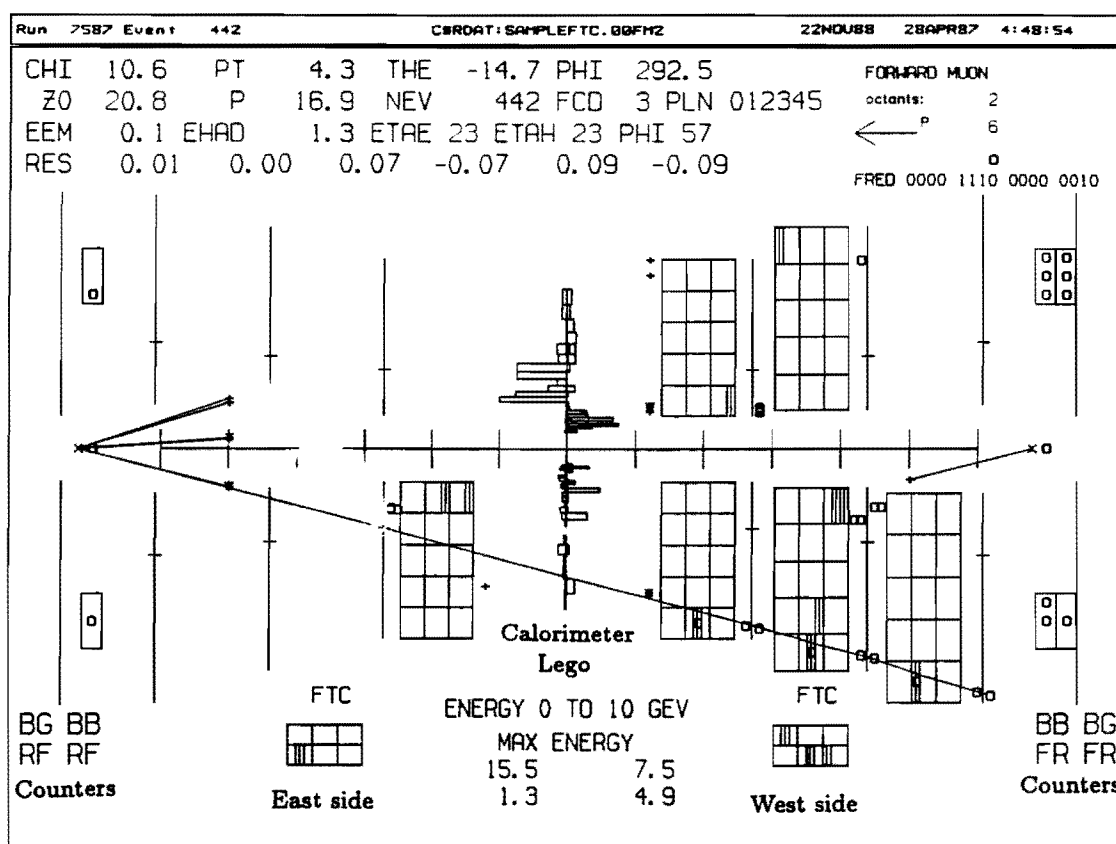


Figure C.1: A forward muon event picture

Bibliography

- [1] S.L. Glashow, Nucl. Phys. 22 (1961) 579;
S. Weinberg, Phys. Rev. Lett. 19 (1967) 1264;
A. Salam, in Elementary Particle Theory: Relativistic Groups and Analyticity (Nobel Symposium No. 8), edit by N. Svartholm, Almqvist and Wiksell, Stockholm (1968) 367.
- [2] A treatment of Standard Model topics in various forms and levels of sophistication can be found in the following textbooks:
D. H. Perkins, *Introduction to High Energy Physics*, third edition, (Addison-Wesley, Menlo Park, California, 1987);
G. Kane, *Modern Elementary Particle Physics*, (Addison-Wesley, Redwood City, California, 1987);
F. Halzen and A. D. Martin, *Quarks and Leptons*, (Wiley, New York, 1984);
V. Barger and R. J. N. Phillips, *Collider Physics*, (Addison-Wesley, Redwood City, California, 1987);
C. Quigg, *Gauge Theories of Strong, Weak, and Electromagnetic Interac-*

- tions, (Benjamin/Cummings, Reading, Massachusetts, 1983).
- [3] Design Report for the Fermilab Collider Detector Facility (CDF), (1981) (unpublished).
 - [4] M. Kobayashi and T. Maskawa, Prog. Theor. Phys. 49 (1973) 652.
 - [5] S. L. Glashow et al., Phys. Rev. D2 (1970) 1285.
 - [6] P. W. Higgs, Phys. Lett. 12 (1964) 132; Phys. Rev. 145 (1966) 1156.
 - [7] A. Astbury et al. (UA1 Collaboration), *A 4π Solid-Angle Detector for the SPS Used as a Proton-Antiproton Collider at a Centre-of-Mass Energy of 540 GeV*, preprint CERN/SPSC 78-06 (1978).
 - [8] G. Arnison et al. (UA1 Collaboration), Phys. Lett. 122B (1983) 103.
 - [9] G. Arnison et al. (UA1 Collaboration), Phys. Lett. 126B (1983) 398.
 - [10] M. Banner et al. (UA2 Collaboration), Phys. Lett. 122B (1983) 476.
 - [11] F. Abe et al. (CDF Collaboration), Phys. Rev. Lett. 62 (1989) 1005.
 - [12] E. L. Berger et al., Phys. Rev. D40 (1989) 83.
 - [13] T. Müller et al. (UA1 Collaboration), preprint CERN-EP/88-48 (1988).
 - [14] J. Ransdell, Ph.D. thesis, University of California, Riverside, 1987 (unpublished).

- [15] N. Ellis et al. (UA1 Collaboration), preprint CERN-EP/88-12 (1988).
- [16] C. Peterson et al., Phys. Rev. D27 (1983) 105.
- [17] R. Ansari et al. (UA2 Collaboration), Phys. Lett. 186B (1987) 452.
- [18] C. Albajar et al. (UA1 Collaboration), Z. Phys. C37 (1988) 489.
- [19] G. Arnison et al. (UA1 Collaboration), Phys. Lett. 147B (1984) 241.
- [20] G. Bauer, Ph.D. thesis, University of Wisconsin, Madison, 1986 (unpublished).
- [21] S. D. Drell and T. M. Yan, Phys. Rev. Lett. 25 (1970) 316.
- [22] C. Albajar et al. (UA1 Collaboration), Phys. Lett. 209B (1988) 397.
- [23] G. Zweig, CERN Report 8419/Th412, 1964.
- [24] C. Albajar et al. (UA1 Collaboration), Phys. Lett. 200B (1988) 380.
- [25] G. Arnison et al. (UA1 Collaboration), Phys. Lett. 155B (1985) 442.
- [26] H.-G. Moser, Ph.D. thesis, RWTH Aachen, Aachen, 1987 (unpublished).
- [27] C. Albajar et al. (UA1 Collaboration), Phys. Lett. 186B (1987) 237.
- [28] C. Albajar et al. (UA1 Collaboration), Phys. Lett. 213B (1988) 405.
- [29] C. Albajar et al. (UA1 Collaboration), Phys. Lett. 186B (1987) 247.

- [30] L. M. Lederman, in *Particles and Detectors* 108, 165 (Springer-Verlag, 1986).
- [31] Design Report for the Tevatron I Project, (1984) (unpublished).
- [32] P. Martin et al., in *Proc. of the 12th Particle Accelerator Conference*, Washington, D. C. (1987).
- [33] R. Johnson et al., in *Proc. of the 12th Particle Accelerator Conference*, Washington, D. C. (1987).
- [34] F. Abe et al. (CDF Collaboration), Nucl. Inst. Meth. A271 (1988) 387.
- [35] G. Drake et al., Nucl. Inst. Meth. A269 (1988) 68.
- [36] E. Barsotti et al., Nucl. Inst. Meth. A269 (1988) 82.
- [37] D. Amidei et al., Nucl. Inst. Meth. A269 (1988) 51.
- [38] J. T. Carroll et al., Nucl. Inst. Meth. A263 (1988) 199.
- [39] F. Snider et al., Nucl. Inst. Meth. A268 (1988) 75.
- [40] M. Atac et al., Nucl. Inst. Meth. A269 (1988) 40.
- [41] Y. Fukui et al., Nucl. Inst. Meth. A267 (1988) 280.
- [42] W. C. Carithers et al., CDF-368 (1985) (unpublished).
- [43] G. Brandenburg et al., Nucl. Inst. Meth. A267 (1988) 257.
- [44] S. Cihangir et al., Nucl. Inst. Meth. A267 (1988) 249.

- [45] H. Frisch et al., CDF-250 (1984) (unpublished).
- [46] K. Byrum et al., Nucl. Inst. Meth. A268 (1988) 46.
- [47] L. G. Pondrom, in *Proc. of the SSC/LHC Muon Detection Workshop*, Madison, Wisconsin (1985).
- [48] D. Carlsmith et al., CDF-518 (1987) (unpublished).
- [49] J. Allison et al., Nucl. Inst. Meth. A201 (1982) 341.
- [50] L. G. Pondrom, in *Proc. of the CDF Forward Detectors Workshop*, Madison, Wisconsin (1984).
- [51] M. Aguilar-Benitez et al. (Particle Data Group), Phys. Lett. 170B (1986) 57.
- [52] B. Rossi, *High Energy Particles*, (Prentice-Hall, New York, 1952), p. 72.
- [53] M. A. Thompson et al., IEEE Trans. Nucl. Sci. NS-35 (1988) 184.
- [54] *IEEE Standard FASTBUS Modular High-Speed Data Acquisition and Control System*, The Institute of Electrical and Electronics Engineers, Inc., New York (1985).
- [55] H. Brafman et al., IEEE Trans. Nucl. Sci. NS-32 (1985) 336;
F. Kirsten et al., CDF-312 (1985) (unpublished).
- [56] G. Drake et al., IEEE Trans. Nucl. Sci. NS-33 (1986) 92.

- [57] D. L. Carlsmith, CDF-308 (1985) (unpublished).
- [58] K. Eggert et al. Nucl. Inst. Meth. A176 (1980) 217.
- [59] G. Bauer et al. Nucl. Inst. Meth. A253 (1987) 179.
- [60] C. Ghesquiere, Proc. of "Forward Production of High-mass Flavours at Collider Energies", Paris, (1979) 283.
- [61] T. Hansl, Proc. of "Forward Production of High-mass Flavours at Collider Energies", Paris, (1979) 257.
- [62] B. van Eijk, Ph.D. thesis, University of Amsterdam, Amsterdam, 1987 (unpublished).
- [63] T. M. Liss, CDF-552 (1987) (unpublished).
- [64] G. P. Yeh, CDF-596 (1987) (unpublished).
- [65] The author would like to thank K. Byrum and C. Wendt for help in the scanning effort.
- [66] C. Haber, LBL/CDF 87-02 (1987) (unpublished).
- [67] J. Bellinger, private communication.
- [68] David A. Smith and Hans B. Jensen, CDF-707 (1988) (unpublished).
- [69] A. Bodek, preprint UR-911 (1985).

- [70] F. S. Merritt et al., Nucl. Inst. Meth. A245 (1986) 27.
- [71] F. Abe et al. (CDF Collaboration), Phys. Rev. Lett. 61 (1988) 1819.
- [72] F. Abe et al. (CDF Collaboration), in *Pseudorapidity Distributions of Charged Particles Produced in $\bar{p}p$ Interactions at $\sqrt{s} = 630$ and 1800 GeV*, to be submitted to Phys. Rev. Lett.
- [73] A. V. Tollestrup, CDF-584 (1987) (unpublished).
- [74] T. W. Markiewicz, in *Proc. of the XXIII International Conference on High Energy Physics*, Berkeley, California (1986).
- [75] M. Banner et al. (UA2 Collaboration), Phys. Lett. 122B (1983) 322.
- [76] G. J. Alner et al. (UA5 Collaboration), Nucl. Phys. B258 (1985) 505.
- [77] A. P. McManus (E735 Collaboration), private communication.
- [78] C. Albajar et. al. (UA1 Collaboration), Z. Phys. C37 (1988) 489.
- [79] W. Beenakker et al., Phys. Rev. D40 (1989) 54.
- [80] F. James, preprint CERN 72-21 (1972).
- [81] T. Westhusing, Ph.D. thesis, University of Illinois, Urbana-Champaign, Illinois, 1988 (unpublished).
- [82] L. M. Lederman et al., Phys. Rev. Lett. 37 (1976) 1374.

- [83] F. E. Paige and S. D. Protopopescu, preprint BNL-38034 (1986).
- [84] K. Yasuoka, in *Proc. of the 7th Topical Workshop on Proton-Antiproton Collider Physics*, Batavia, Illinois (1988).
- [85] D. Quarrie, CDF-356 (1988) (unpublished).
- [86] R. Handler, private communication.
- [87] D. Carlsmith, University of Wisconsin-Madison, was the principal author of the forward muon tracking code used in this thesis.
- [88] D. Carlsmith, private communication.
- [89] A. G. Frodesen et al., *Probability and Statistics in Particle Physics*, (Universitetsforlaget, Oslo, Norway, 1979).
- [90] W. Matt, Ph.D. thesis, Max-Planck Institut für Physik und Astrophysik, München, 1972 (unpublished).
- [91] P. Billoir et al., Nucl. Inst. Meth. A241 (1985) 115.
- [92] P. Billoir, Nucl. Inst. Meth. A225 (1984) 352.
- [93] A. Beretvas, Fermi National Accelerator Laboratory, and D. Carlsmith, University of Wisconsin-Madison, are the authors of this display.